






Universitat Autònoma de Barcelona

**ADVERTIMENT.** L'accés als continguts d'aquesta tesi queda condicionat a l'acceptació de les condicions d'ús establertes per la següent llicència Creative Commons:  [http://cat.creativecommons.org/?page\\_id=184](http://cat.creativecommons.org/?page_id=184)

**ADVERTENCIA.** El acceso a los contenidos de esta tesis queda condicionado a la aceptación de las condiciones de uso establecidas por la siguiente licencia Creative Commons:  <http://es.creativecommons.org/blog/licencias/>

**WARNING.** The access to the contents of this doctoral thesis it is limited to the acceptance of the use conditions set by the following Creative Commons license:  <https://creativecommons.org/licenses/?lang=en>

PhD Thesis

# Generalized Hydrodynamic Heat Transport in Semiconductors

**Author:**

Albert Beardo Ricol

**Directors:**

Dr. Francesc Xavier Alvarez Calafell

Dr. Javier Bafaluy Bafaluy



**Universitat Autònoma  
de Barcelona**

Department of Physics

08193 Bellaterra, Barcelona

September 2nd, 2021



# Acknowledgment

I feel fortunate to have joined the Statistical Physics group of the UAB during my PhD training, since I have benefited from the different perspectives, tools, and understanding contributed by many excellent researchers, present and past, to whom I will always remain grateful. In particular, I acknowledge Francesc Xavier Alvarez for your leadership, guidance and mentoring, and for showing me true commitment to research along with courage to propose new approaches and surpass the difficulties. I acknowledge Javier Bafaluy for your experience and mentoring. I appreciate your advice and your patience on solving my endless doubts and uncertainties. I acknowledge Juan Camacho for your invaluable contributions to this thesis, for your rigor and your patience on instructing me on mathematical reasoning and analysis. Finally, I also want to acknowledge Lluç Sendra for your generosity, your enthusiasm, and your unconditional support in both the good and the bad moments. Working with you all over the last four years has been extremely enriching and stimulating.

I am also deeply grateful to professors Ali Shakouri, Margaret Murnane, Konstantinos Termentzidis, Marisol Martín-González, Sebastián Reparaz, and Tim Myers, for giving me the opportunity to collaborate with your respective research groups. As a result, I have met many excellent researchers from whom I learned so much. I want to specially mention Josh Knobloch, Begoña Abad, Travis Frazer, Brendan McBennett, Matt Hennessy, Sami Alajlouni and Paul Desmarchelier. I truly enjoyed our long and fruitful respective collaborations. Moreover, I want to thank Javier Cristín and Axel Masó, with whom I shared the office, the suffering, and the victories, together with Lluç.

To conclude, I thank all the friends and family who have supported me throughout my time in the UAB. Brother, mom, and dad, thanks for always being there supporting me. Jen, thank you for being at my side during all this time. I'm grateful for all the experiences we went through together, and for the experiences to come.



## Abstract

This thesis presents a unifying description of a variety of experiments on micro- and nano-scale heat transport in semiconductors like silicon or germanium. A hydrodynamic-like heat transport model is used to predict the non-diffusive thermal response of complex systems in technologically relevant situations, like the process of energy release from nanostructured heat sources towards a semiconductor substrate. The model does not use geometry-dependent or fitted parameters, but use intrinsic material properties that can be calculated from first principles. Small-size and high-frequency effects are captured through the use of specific boundary conditions, thus resulting in a practical tool for complex microelectronic device design. Since hydrodynamic modeling is not the state-of-the-art approach to describe standard semiconductors like silicon, special care is devoted to quantitatively determine the applicability of the model, and multiple experiments using different techniques are considered and studied in a unifying way. As a result, previously unreported non-Fourier phenomena in materials like silicon or germanium is identified and demonstrated (e.g. second sound in rapidly varying thermal fields or multiple decay times characterizing the evolution of nano-structured heaters). Furthermore, the hydrodynamic description is compared with alternative modern frameworks describing size and frequency effects in semiconductor heat transport, and a summarized overview of the theoretical background, namely non-equilibrium thermodynamics and kinetic theory, is presented. In light of the extensive experimental evidence provided, this thesis demonstrate the predictive capability of hydrodynamic-like thermal transport modeling in semiconductors within a certain range of applicability that is well beyond the diffusive regime.

# Contents

<b>1</b>	<b>Introduction</b>	<b>7</b>
<b>2</b>	<b>Heat Transport</b>	<b>10</b>
2.1	Boltzmann Transport Equation . . . . .	11
2.2	Collision Operator and Conservation Laws . . . . .	15
2.3	Approximation Methods in Kinetic Theory . . . . .	22
2.4	Extended Irreversible Thermodynamics . . . . .	24
2.5	Ballistic effects . . . . .	28
<b>3</b>	<b>Phonon Hydrodynamics</b>	<b>34</b>
3.1	Phonon hydrodynamics in the collective regime . . . . .	34
3.2	Generalized hydrodynamic heat transport . . . . .	35
3.3	Transport equations . . . . .	39
3.4	Boundary Conditions . . . . .	40
3.5	Parameters . . . . .	46
3.6	Thermoelastic coupling . . . . .	49
3.7	Thermoelectric coupling . . . . .	51
<b>4</b>	<b>Thin films and Thermal Gratings</b>	<b>54</b>
4.1	Non-local effects . . . . .	54
4.2	Effective thermal conductivity of compact and holey Silicon films . . . . .	55
4.3	Relaxation of optically induced thermal gratings in Silicon films . . . . .	59
4.4	Discussion on the Hydrodynamic Model Applicability . . . . .	60
<b>5</b>	<b>Linear and circular heat sources on Silicon substrate: Full field thermorefectance maps</b>	<b>66</b>
5.1	Thermorefectance Imaging . . . . .	66
5.2	Room Temperature measurements . . . . .	68
5.3	Low Temperature measurements . . . . .	76
<b>6</b>	<b>Frequency Domain Thermorefectance</b>	<b>79</b>
6.1	Failure of Effective Fourier Theory in FDTR . . . . .	79
6.2	Non-Fourier response in Silicon . . . . .	81
6.3	Non-Fourier response in Germanium . . . . .	87

<b>7</b>	<b>1D- and 2D- confined nanostructure cooling in Silicon substrate: EUV-scatterometry technique</b>	<b>89</b>
7.1	Non-local Effects and Hydrodynamic Region . . . . .	92
7.2	Thermal Decay Analysis: Diffusion vs Hydrodynamics . . . . .	97
7.3	Two-Box Model for Heater Thermal Decay . . . . .	100
7.4	Derivation of the Two-Box Model . . . . .	105
<b>8</b>	<b>Bismuth Telluride nanowire networks for thermoelectric applications</b>	<b>111</b>
8.1	Effective thermal conductivity of the 3D Bi <sub>2</sub> Te <sub>3</sub> nanowire networks	112
8.2	Seebeck coefficient of the 3D Bi <sub>2</sub> Te <sub>3</sub> nanowire networks . . . . .	116
<b>9</b>	<b>Second sound in Germanium in a rapidly varying temperature field</b>	<b>118</b>
9.1	Memory effects . . . . .	118
9.2	Frequency Domain Thermorefectance in the absence of metallic transducers . . . . .	123
9.3	Thermorefectance Signal Analysis . . . . .	124
9.4	Experimental Signatures of Wave-like Heat Transport . . . . .	127
9.5	Diffusion of Hot Electrons and Influence of the Pump and Probe Penetration Depths . . . . .	132
9.6	1D-Limit of the HHE and Influence of the Spot Size . . . . .	134
9.7	Influence of Metallic Transducers . . . . .	139
<b>10</b>	<b>Computational Experiments</b>	<b>141</b>
10.1	Deviational energy Monte Carlo BTE simulations . . . . .	141
10.2	Non-equilibrium Molecular Dynamics . . . . .	152
<b>11</b>	<b>Mathematical Methods</b>	<b>159</b>
11.1	Finite Elements . . . . .	159
11.2	Analytical solutions and validation . . . . .	162
<b>12</b>	<b>Conclusions</b>	<b>165</b>
<b>13</b>	<b>List of Publications</b>	<b>168</b>



# 1 Introduction

The number of transistors on a microprocessor chip has been doubled every two years since the information-technology revolution in the 1960s. This exponential increase, known as Moore's law, has been translated into the miniaturization of electronic devices along with an improvement of its performance, thus giving rise to high-speed internet, the smartphone and many other engines that modified the way we consume, we access to information, or we interact among ourselves. However, the success of the electronic industry on producing new technologies directly impacting to our daily life has recently reached a critical limitation: the inefficient thermal response of current nanostructured circuitry in silicon devices [1]. In other words, the heat that is unavoidably generated by a dense distribution of electronic components can not be efficiently evacuated from the devices, thus limiting its efficiency and lifetime. Unfortunately, current knowledge of thermal transport phenomena is insufficient to develop strategies to surpass this limit.

The origin of the problem is that fabrication techniques scaled the characteristic sizes of the chips down to the mean free paths of the phonons, which are microscopic energy carriers in semiconductors [2]. At these scales, the interaction of the phonon population with the system boundaries is critical for predictive modeling, and the simple models governing the evolution at the macroscale, like the Fourier's law, breaks down. The dominant state-of-the-art techniques to model heat transport are based on predicting the phonon dynamics in terms of the Boltzmann Transport equation (BTE) and kinetic theory. Since the BTE can be fully characterized using first principles calculations in infinite crystals [3, 4], such self-contained frameworks pursue a mechanical description of the system, with avoiding the use of phenomenological or fitting parameters. In this context, most of the effort is focused on developing smart and efficient ways to solve the BTE, and thermodynamic considerations have been usually relegated to a set of requirements that the solutions must fulfill. These approaches are usually intended to characterize the apparently reduced thermal conductivity or enhanced interfacial resistance observed in nanostructured semiconductor systems, with maintaining the same simple relations between macroscopic quantities that apply in the bulk, like the Fourier's law relating the heat flux and the temperature field. This reductionist perspective has had limited success in predicting experimental observations at the nanoscale, due to the complexity of the BTE and the difficulties on integrating the influence of boundaries or external energy sources within the microscopic description.

The tradition of the Statistical Physics group of the Universitat Autònoma de Barcelona does not follow the dominant school of thought. It was originated by the pioneering works by David Jou, José Casas-Vázquez, and Georgy Lebon, who developed a framework to extend the use of thermodynamic concepts and restrictions to non-equilibrium situations, the so-called Extended Irreversible Thermodynamics (EIT) theory [5]. The EIT is a guide to simplify the microscopic or kinetic description of the system into generalized mesoscopic mod-

els without missing the fundamental physical information contained in the BTE. It is assumed that the complete microscopic description is not necessary to successfully model the experiments, but the control of the slowly relaxing thermodynamic magnitudes like the heat flux is sufficient. The key advantage of this approach is that size or frequency effects are captured through the use of appropriate boundary conditions rather than with the use of effective parameters in the transport equations. In consequence, this framework is perfectly suited for engineering applications, since arbitrary complex geometries and conditions are accessible.

This thesis combines both disciplines, kinetic theory and non-equilibrium thermodynamics, to provide a unifying description of a variety of experiments on nanoscale thermal transport in standard semiconductors like silicon. The specific model proposed, known as Kinetic Collective Model (KCM), was first envisioned by F. Xavier Alvarez and it is based in the seminal work by R. A. Guyer and J. A. Krumhansl [6]. It consists of a non-Fourier description of heat transport that resembles mass transport in fluid dynamics, and it is simple enough to be used by engineers for microelectronic device design [7]. Recently, hydrodynamic phenomena in nanoscale heat transport has been theoretically and experimentally demonstrated for some exotic materials at low temperatures [8]. The main goal of this thesis is to show that this behavior is generally obtained in a wider range of materials and for room temperature applications. Therefore, special care has been taken here to discuss and analyze the applicability of the model and to unify the description of different phenomena observed by different groups using different experimental techniques in a variety of materials and temperatures.

From a more general point of view, this thesis argues for the need of refined mesoscopic descriptions to complement and contrast the available microscopic models, which are based in axiomatic sets of fundamental rules. It is obvious that the information provided by such microscopic frameworks, including molecular dynamics simulations, is valuable. However, such approaches are limited by the computational capabilities, and, most importantly, are usually difficult to interpret since all the microscopic information is included and mixed. Thermal transport in solids is a paradigmatic example of the limitations of the reductionist approach, since it involves the dynamics of an overwhelmingly high number of atoms vibrating around their crystal lattice equilibrium positions, whereas experiments only access to the evolution of few averaged magnitudes. Usually, understanding is associated to the capacity of simplifying the description of certain phenomena in compact physical models only including the relevant degrees of freedom, rather than to expensive numerical calculations solving complex models including all the microscopic information. Therefore, it is risky to trust that progress in physics depends on the evolution of our computing capabilities, and that the efforts must be only focused on improving the computing efficiency. These considerations motivate the main objective of this thesis, which is the empirical validation of the simplest thermal transport model with predictive power at the nanoscale.

The thesis is organized as follows. In Chapter 2, we introduce the most relevant theories describing heat transport in semiconductors and we show the difficulties and achievements on describing the thermal behavior of nanoscopic systems. In Chapter 3, we introduce the widely accepted theory of phonon hydrodynamics for some specific materials at low temperatures, and we argue its general applicability on standard semiconductors like silicon for room temperature applications. Furthermore, we compactly show all the transport equations, boundary conditions, and parameters required for experimental modeling and microelectronic device design. Chapters 4 to 9 contain the experimental validation of the hydrodynamic model in a variety of situations and materials including silicon, germanium, and bismuth telluride. This is the result of multiple international collaborations with different research groups, and represents the most important part of the thesis. Chapter 10 aims to provide microscopic interpretation of phonon hydrodynamics phenomenology with the use of alternative methods like a Monte Carlo solver of the BTE and non-equilibrium molecular dynamics simulations. In Chapter 11, implementation and validation of the mathematical technique used, namely the Finite Elements solver of the generalized heat transport equations, is shown. Finally, Chapter 12 is devoted to concluding remarks.

## 2 Heat Transport

Two centuries ago, Joseph Fourier proposed a law to describe thermal conduction in terms of the local temperature  $T$  and the energy flux  $\mathbf{q}$ :

$$\mathbf{q} = -\kappa \nabla T, \quad (1)$$

where  $\kappa$  is a material property known as the thermal conductivity. This phenomenological law can be combined with the energy conservation equation:

$$c \frac{dT}{dt} = -\nabla \cdot \mathbf{q}, \quad (2)$$

being  $c$  the specific heat, to characterize the thermal evolution of solids. However, as it will be defended in this thesis, Eq. 1 needs to be refined to achieve predictive thermal modeling of nowadays electronic devices. Fundamental derivation from microscopic grounds and generalization of these equations along with the methods to calculate its parameters has been the subject of intensive research study for decades.

Crystal solids like Silicon store thermal energy due to the capability of the atoms to vibrate around their lattice sites. The transport of this internal energy is not easily interpreted in terms of the individual atom kinetics and neighboring interaction, and switching to collective models is required [9]. From a different perspective, the energy of the solid is distributed among the normal modes of vibration of the crystal as a whole. Remarkably, this interpretation allows calculating the specific heat  $c$  of the solid relating the temperature and the lattice kinetic and potential energy (Debye model). These normal modes can be interpreted as standing waves in the crystal accumulating energy.

The lattice vibrational field can be described by the Hamiltonian including the (harmonic) interatomic potential, whose quanta is referred to as phonon [9, 10]. The phonons are intuitively interpreted as traveling wave-packets with defined energy and wave-vector. The translational symmetry of the lattice Hamiltonian allows its quantization in terms of the phonon states belonging to the first Brillouin zone of the reciprocal lattice. In this picture, the solid is considered as a gas of excitations (or phonons) which carry a significant amount of energy. Transport phenomena is then more easily approachable by treating phonons as particles and using concepts of the kinetic theory of gases [2, 11, 12]. It is important to remark that phonons are the quanta of the Hamiltonian assuming an harmonic interatomic potential. However, the interatomic potential includes higher order terms (anharmonicities), which means that the phonons are not eigenstates of the actual Hamiltonian and, thus, the phonon population evolves in time due to transitions from different states. In the kinetic theory framework, this is interpreted as scattering between phonons.

The phonon gas interpretation permits the use of the Boltzmann Transport equation (BTE) to predict the non-equilibrium evolution of the thermal energy of the solid in terms of the non-equilibrium phonon distribution function (see

sections 2.1, 2.2, and 2.3). As it will be shown, this fundamental equation and its projections allow connecting the microscopic properties of the phonon population (which can be calculated from first principles using Density Functional Theory [3, 4, 13–15]), to the characterization of mesoscopic transport properties like the thermal conductivity  $\kappa$  in equation 1. Furthermore, generalized mesoscopic transport equations beyond Fourier's can be obtained [16–19].

The kinetic interpretation of heat transport is parallel to alternative approaches based in non-equilibrium thermodynamics [5]. As discussed in section 2.4, the generalization of the notion of local entropy and the second principle of thermodynamics is the guide to obtain refined mesoscopic thermal descriptions, and serves as a filter for physically acceptable transport models [20].

Nowadays, both the kinetic and the thermodynamic approaches are focused to provide predictive tools for heat management in modern electronic devices. The extreme miniaturization of these devices and the high frequency clock-rates drive the systems to non-equilibrium conditions where phenomenological transport models like Eq. 1 breakdown [21, 22]. In such conditions, the phonon scattering rates and mean free paths become comparable to the system scales, and the models should be refined to include boundary effects. In section 2.5, we discuss different approaches to include size and frequency effects at different levels of description, and we present the use of hydrodynamic-like heat transport models as the simplest framework with predictive capabilities.

## 2.1 Boltzmann Transport Equation

We assume that there exists a distribution function  $f_{\mathbf{k}}(\mathbf{r}, t)$ , which quantifies the number of phonons in the neighborhood of position  $\mathbf{r}$  at time  $t$  in the state (or mode)  $\mathbf{k}$ , which also denotes the phonon wave-vector. The state  $\mathbf{k}$  is characterized by a frequency  $\omega$  and a polarization  $p$ . To simplify the notation, the state  $(\mathbf{k}, p)$  is simply denoted as  $\mathbf{k}$  throughout this thesis. In equilibrium at temperature  $T$ , the distribution function is the Bose-Einstein distribution [10]:

$$f_{\mathbf{k}}^{\text{eq}}(T) = \frac{1}{e^{\hbar\omega_{\mathbf{k}}/\kappa_B T} - 1}, \quad (3)$$

where  $\kappa_B$  and  $\hbar$  are the Boltzmann and reduced Planck constants, respectively. Out of equilibrium, the distribution function evolves due to two distinct mechanisms. On one hand, the phonons move at its group velocity  $\mathbf{v}_{\mathbf{k}} = \frac{\partial\omega_{\mathbf{k}}}{\partial\mathbf{k}}$  (drift). On the other hand, the phonons interact with other phonons or with defects in the lattice as a consequence of the anharmonicity of the Hamiltonian, which tends to restore equilibrium (collisions). By invoking detailed balance we obtain the BTE for phonons:

$$D(f_{\mathbf{k}}) \equiv \frac{\partial f_{\mathbf{k}}}{\partial t} + \mathbf{v}_{\mathbf{k}} \frac{\partial f_{\mathbf{k}}}{\partial \mathbf{r}} = C(f_{\mathbf{k}}), \quad (4)$$

where we denoted  $D$  and  $C$  as the drift and collision operators, respectively. Note that, in contrast to the BTE for electrons, in the previous equation the influence of external fields is not required. The nonlinear form of the collision opera-

tor precludes directly using Eq. 4 for applications. For illustration, we show here the general form of  $C$  if only considering the simplest (and most important) kind of collisions (i.e. the three-phonon transitions):

$$C(f_{\mathbf{k}}) = \int \int \frac{d\mathbf{k}' d\mathbf{k}''}{(2\pi)^3} \left[ \left( f_{\mathbf{k}} f_{\mathbf{k}'} (1 + f_{\mathbf{k}''}) - (1 + f_{\mathbf{k}}) (1 + f_{\mathbf{k}'}) f_{\mathbf{k}''} \right) \Omega_{\mathbf{k}, \mathbf{k}'}^{\mathbf{k}''} + \right. \\ \left. + \frac{1}{2} \left( f_{\mathbf{k}} (1 + f_{\mathbf{k}'}) (1 + f_{\mathbf{k}''}) - (1 + f_{\mathbf{k}}) f_{\mathbf{k}'} f_{\mathbf{k}''} \right) \Omega_{\mathbf{k}}^{\mathbf{k}', \mathbf{k}''} \right], \quad (5)$$

where  $\Omega_{\mathbf{k}, \mathbf{k}'}^{\mathbf{k}''}$  is the scattering rate between two incident phonons  $\mathbf{k}$  and  $\mathbf{k}'$  resulting in an outgoing phonon  $\mathbf{k}''$ , and  $\Omega_{\mathbf{k}}^{\mathbf{k}', \mathbf{k}''}$  is the scattering rate between one incident phonons  $\mathbf{k}$  resulting in two outgoing phonons  $\mathbf{k}'$  and  $\mathbf{k}''$ . Remarkably, recent studies pointed out that, in some specific materials like boron arsenide, the role of higher order transitions involving four phonons is necessary [23, 24]. Moreover, transitions due to mass defects (or isotopic impurities) must be also accounted for. Fortunately, it is possible to calculate the transition probabilities from first principles by using perturbation theory and the Fermi's Golden rule [9]. The required (periodic) Hamiltonian is obtained using the Density Functional Theory (DFT) [3, 4, 14, 25, 26]. In brief, an adequate pseudopotential is assumed for the crystal lattice, and the relaxed state is determined by computing the state of minimum energy. Then, the total energy of a portion of the lattice (or supercell) is calculated when perturbing the position of two or more atoms with respect to its equilibrium positions. This allows to calculate the harmonic and anharmonic interaction force constants between the atoms, which characterize the Hamiltonian [27, 28]. The harmonic part of the Hamiltonian allows constructing fundamental properties of the phonons like the dispersion relation, which relates the wave-vector and the frequency of each phonon mode. The anharmonic part is required to calculate the rates  $\Omega$  with the use of the Fermi's Golden rule. It is worth to note that this celebrated rule ensures conservation of energy between the initial and final states, so the BTE with the full collision operator conserves the energy. More details about the different transitions and the influence of conservation laws in the scattering processes can be found in section 2.2.

The applicability of the BTE demands some simplifying assumptions due to the complex nonlinear form of operator  $C$ . If we restrict ourselves to situations close enough to local equilibrium, we can simplify Eq. 4 by linearizing the perturbation around equilibrium:

$$f_{\mathbf{k}} \approx f_{\mathbf{k}}^{\text{eq}} + \frac{f_{\mathbf{k}}^{\text{eq}} (f_{\mathbf{k}}^{\text{eq}} + 1)}{\kappa_B T} g_{\mathbf{k}}, \quad (6)$$

where  $g_{\mathbf{k}}$  is a linear deviation with respect to local equilibrium i.e. proportional to a certain perturbation like  $\nabla T$ . By using Eq.6 in Eq. 5, and neglecting the nonlinear terms, one can obtain the linearized collision operator [9],

$$C(f_{\mathbf{k}}) = \int \int \frac{d\mathbf{k}' d\mathbf{k}''}{(2\pi)^3} \left[ (-g_{\mathbf{k}} - g'_{\mathbf{k}} + g''_{\mathbf{k}}) W_{\mathbf{k}, \mathbf{k}'}^{\mathbf{k}''} + \frac{1}{2} (-g_{\mathbf{k}} + g'_{\mathbf{k}} + g''_{\mathbf{k}}) W_{\mathbf{k}}^{\mathbf{k}', \mathbf{k}''} \right], \quad (7)$$

where  $W$  are functions of the equilibrium distributions and the scattering rates  $\Omega$ , weighted by a delta function ensuring energy conservation in each transition [29].

### Relaxation Time Approximation

In section 2.2, an extended discussion about the different approaches to deal with the collision operator and obtain physical insight from the BTE is provided. However, it is illustrative to first consider the Relaxation Time Approximation. This phenomenological approach is based in assuming that each phonon mode relaxes independently at a given rate due to collisions. More specifically, each phonon mode exponentially relax towards equilibrium as if the rest of the population was in equilibrium ( $g'_k = g''_k = 0$  in Eq. 7). By denoting as  $\Omega_{\mathbf{k}}^{\mathbf{k}'}$  the transition rate from  $\mathbf{k}$  to mode  $\mathbf{k}'$  through all the phonon scattering processes, this approximation eliminates the off-diagonal elements in operator  $C$ , which reads:

$$C(f_{\mathbf{k}}) = -\frac{f_{\mathbf{k}} - f_{\mathbf{k}}^{\text{eq}}}{\tau_{\mathbf{k}}}, \quad (8)$$

where  $\tau_{\mathbf{k}}$  are the independent phonon life times (i.e. the characteristic time the phonon mode  $\mathbf{k}$  needs to relax towards equilibrium). From Eq. 7, we have

$$\frac{1}{\tau_{\mathbf{k}}} = \int \frac{d\mathbf{k}'}{(2\pi)^3} \Omega_{\mathbf{k}}^{\mathbf{k}'}. \quad (9)$$

Usually, the relaxation times are approximated by combining the momentum-destroying phonon-phonon (Umklapp) scattering time, the scattering time due to mass defects in the lattice, and the momentum-conserving phonon-phonon (Normal) scattering time, by using a Matthiessen's rule. The first important drawback of the RTA is that conservation of energy in collisions is no longer guaranteed, which leads to nonphysical results in some situations [30, 31]. However, the simplification of operator  $C$  allows straightforward interpretation of the transport phenomena. For example, the RTA framework allows defining the notion of phonon mean free path (MFP)  $\Lambda_{\mathbf{k}} = v_{\mathbf{k}}\tau_{\mathbf{k}}$ , which is the average distance an excited non-equilibrium phonon travels before colliding. As we will discuss in section 2.5, the phonon MFP is a crucial concept in many interpretations of the role of size and frequency effects in thermal transport experiments. However, the results presented in this thesis challenge the physical validity of this simplified picture of the phonon kinetics at the nanoscale (see Chapter 4 for details).

Nevertheless, the RTA has been shown useful to predict with remarkable accuracy the thermal conductivity of many materials in the absence of boundary effects. For illustration, here we show a simple derivation of Fourier's law and a microscopic expression for the thermal conductivity within the RTA for isotropic 3D materials [11]. We start from the linear BTE using the RTA form of the collision operator (Eq. 8):

$$\frac{\partial f_{\mathbf{k}}}{\partial t} + \mathbf{v}_{\mathbf{k}} \frac{\partial f_{\mathbf{k}}}{\partial \mathbf{r}} = -\frac{f_{\mathbf{k}} - f_{\mathbf{k}}^{\text{eq}}}{\tau_{\mathbf{k}}}. \quad (10)$$

Now, we assume there is a stationary temperature gradient in the  $x$  direction. Hence, the distribution function will solely vary in this direction. We now assume that  $\frac{df_{\mathbf{k}}}{dx} \approx \frac{df_{\mathbf{k}}^{\text{eq}}}{dx}$ . This is a rough assumption only valid for very smooth temperature profiles in the absence of other perturbations like an inhomogeneous heat flux profile. In fact, avoiding this approximation will be crucial to derive higher order transport equations beyond Fourier's law as discussed in section 3.2. We have,

$$f_{\mathbf{k}} = f_{\mathbf{k}}^0 - \tau_{\mathbf{k}} v_{\mathbf{k}}^x \frac{\partial f_{\mathbf{k}}^0}{\partial T} \frac{\partial T}{\partial x}. \quad (11)$$

Now we input 11 in the microscopic definition of the total heat flux

$$\mathbf{q} = \int \frac{d\mathbf{k}}{(2\pi)^3} f_{\mathbf{k}} \mathbf{v}_{\mathbf{k}} \hbar \omega_{\mathbf{k}}. \quad (12)$$

and we obtain the transport equation 1 with the thermal conductivity being

$$\kappa = \frac{1}{3} \int \frac{d\mathbf{k}}{(2\pi)^3} c_{\mathbf{k}} \tau_{\mathbf{k}} \mathbf{v}_{\mathbf{k}}^2 \quad (13)$$

where  $c_{\mathbf{k}} = \hbar \omega_{\mathbf{k}} \frac{\partial f_{\mathbf{k}}^{\text{eq}}}{\partial T}$  is the specific heat of mode  $\mathbf{k}$ . Note that we used that the contribution of the equilibrium distribution function to the heat flux is null. It should also be noted that the integration over  $v_{\mathbf{k}}^x$  is the same as the integration over  $v_{\mathbf{k}}^y$  or  $v_{\mathbf{k}}^z$  in isotropic materials, so the integration over  $(v_{\mathbf{k}}^x)^2$  is equivalent to 1/3 of the integration over  $\mathbf{v}_{\mathbf{k}}^2$ .

Moreover, the simplified RTA-BTE framework (Eq. 10) has been extensively used to study more complex non-equilibrium situations including boundary conditions through different numerical solvers [32–39]. In section 10.1, we implemented a Monte Carlo solver of the RTA-BTE [32] to compare with the hydrodynamic heat transport description used for experimental modeling in Chapters 4 to 9.

### Iterative BTE solver

It is also worth mentioning the iterative solvers of the linear BTE beyond the RTA (i.e. using the complete form of  $C$  without neglecting the off-diagonal terms) in the presence of homogeneous (and small) temperature gradients [14, 28]. The full version of the linear collision operator (Eq. 7) in the BTE is used. Moreover, the non-equilibrium part of the phonon distribution is assumed to be solely dependent on a temperature gradient in steady state conditions. Finally, a linear relation between  $\nabla T$  and  $\mathbf{q}$  (Fourier's law) is imposed. With all, an expression for the thermal conductivity can be obtained

$$\kappa^{ij} = \frac{1}{\kappa_B T^2 V N} \sum_{\mathbf{k}} f_{\mathbf{k}}^{\text{eq}} (f_{\mathbf{k}}^{\text{eq}} + 1) (\hbar \omega_{\mathbf{k}})^2 v_{\mathbf{k}}^i v_{\mathbf{k}}^j F_{\mathbf{k}}^j, \quad (14)$$

where  $i = x, y, z$  are the three spatial directions,  $V$  is the volume of the unit cell,  $N$  is the number of  $\mathbf{k}$ -points, and  $F_{\mathbf{k}}^j$  is the perturbation of phonon mode  $\mathbf{k}$  in the



direction  $j$  (proportional to  $g_{\mathbf{k}}$ ). The perturbation  $F_{\mathbf{k}}^j$  is obtained by iteratively solving the linear BTE with the non-diagonal form of  $C$  (expression 7). First,  $F_{\mathbf{k}}^j$  is taken equal to  $\tau_{\mathbf{k}}v_{\mathbf{k}}^j$  (RTA case). Starting from this initial guess,  $F_{\mathbf{k}}^j$  is iteratively obtained and takes the form  $\tau_{\mathbf{k}}(v_{\mathbf{k}}^j + \Delta_{\mathbf{k}}^j)$ . Note that, for isotropic materials, tensor  $\kappa^{ij}$  in eq. 14 is proportional to the identity. This method provides accurate bulk thermal conductivity values that, in some materials like graphene, significantly improve the agreement to experimental bulk (intrinsic) values, with respect to expression 13.

Furthermore, some numerical methods have been recently proposed to obtain solutions of the linear BTE also including the off-diagonal terms in the Collision operator and including boundary conditions [40–42].

## 2.2 Collision Operator and Conservation Laws

As stated above, it is difficult to deal with the collision operator in the BTE because collisions mix the phonon modes in a complicated way until the phonon distribution is relaxed back to equilibrium. In this section we show how the use of fundamental conservation laws can be used to manipulate the linearized BTE and extend its applicability.

First, it is important to distinguish the different kinds of phonon collisions included in operator  $C$ . The phonons populating the mode  $\mathbf{k}$  have a defined energy  $\hbar\omega_{\mathbf{k}}$  and a defined crystal momentum  $\hbar\mathbf{k}$ . All collisions conserve energy. Hence, in a three phonon collision involving modes  $\mathbf{k}, \mathbf{k}'$  resulting in mode  $\mathbf{k}''$  it is satisfied that

$$\omega_{\mathbf{k}} + \omega'_{\mathbf{k}} = \omega''_{\mathbf{k}}, \quad (15)$$

and in a three phonon collision involving mode  $\mathbf{k}$  resulting in modes  $\mathbf{k}', \mathbf{k}''$  it is satisfied that

$$\omega_{\mathbf{k}} = \omega'_{\mathbf{k}} + \omega''_{\mathbf{k}}. \quad (16)$$

In contrast, the conservation of crystal momentum is not guaranteed in the collisions. Due to the translational symmetry of the lattice Hamiltonian, the phonon with wave-vector  $\mathbf{k}$  can not be distinguished from the phonon with wave-vector  $\mathbf{k} + \mathbf{G}$ , being  $\mathbf{G}$  a reciprocal lattice vector. In fact, the latter phonon (lying outside the first Brillouin zone) has no physical meaning in a discrete medium such as the crystal lattice (i.e. there are not enough atoms to propagate a vibration of such short wavelength). In other words, the maximum crystal momentum that can be carried throughout the lattice is determined by the phonons inside the first Brillouin zone. Hence, we can distinguish two different scattering mechanisms. On one hand, there are Normal processes, which conserve the crystal momentum:

$$\mathbf{k} = \mathbf{k}' + \mathbf{k}'', \quad (17)$$

or

$$\mathbf{k} + \mathbf{k}' = \mathbf{k}''. \quad (18)$$

On the other hand, there are Resistive processes, where the crystal momentum of the resulting phonons is reduced due to its wave-vector being rewritten in terms of  $\mathbf{G}$

$$\mathbf{k} = \mathbf{k}' + \mathbf{k}'' + \mathbf{G}, \quad (19)$$

or

$$\mathbf{k} + \mathbf{k}' = \mathbf{k}'' + \mathbf{G}. \quad (20)$$

Therefore, if we imagine a situation where Resistive processes were lacking, collisions would not be able to relax the momentum of the phonon population, and a certain perturbation would propagate at infinite distances (i.e. we would have an infinite thermal conductivity). Notice that, in the RTA, Normal and Resistive collisions are not distinguished, thus introducing a systematic underprediction of the thermal conductivity in bulk situations. This partially explains the discrepancies on the  $\kappa$  values obtained by using the RTA and the Iterative solutions of the BTE in some materials like graphene, since the latter properly include the conservation of momentum in Normal collisions. Moreover, this explains why the RTA provide satisfactory predictions in materials where Normal collisions do not dominate, like Silicon or germanium. Resistive processes include a portion of the phonon-phonon interactions (Umklapp) and also interactions with mass defects (i.e. presence of lattice impurities or dislocations). Distinguishing Normal and Resistive collisions has been shown very useful to obtain simplified models from the BTE and to identify a rich variety of phenomenology in different materials and temperatures.

### Callaway's Model

One of the most celebrated models beyond the RTA is the Callaway's Model [43]. This phenomenological model is based in the incapability of Normal collisions to relax the distribution back to equilibrium. Instead, Normal collisions relax the distribution towards a non-equilibrium situation with a non-null invariable crystal momentum. It is assumed that there is a mode-dependent Normal relaxation time  $\tau_{\mathbf{k}}^N$  and a mode-dependent Resistive relaxation time  $\tau_{\mathbf{k}}^R$ . Callaway's operator  $C$  reads:

$$C(f_{\mathbf{k}}) = -\frac{f_{\mathbf{k}} - f_{\mathbf{k}}^{\text{eq}}}{\tau_{\mathbf{k}}^R} - \frac{f_{\mathbf{k}} - f_{\mathbf{k}}^4}{\tau_{\mathbf{k}}^N}, \quad (21)$$

being  $f_{\mathbf{k}}^4$  the displaced Bose-Einstein distribution:

$$f_{\mathbf{k}}^4 = f_{\mathbf{k}}^{\text{eq}} + \frac{\hbar}{\kappa_B T} f_{\mathbf{k}}^{\text{eq}} (f_{\mathbf{k}}^{\text{eq}} + 1) \lambda_{\mathbf{k}} \cdot \mathbf{u}, \quad (22)$$

where  $\mathbf{u}$  is known as the drift velocity and quantifies the amount of crystal momentum density, and  $\lambda_{\mathbf{k}}$  is a mode-dependent function. The form of  $f_{\mathbf{k}}^4$  can be derived in the limit where Resistive collisions are lacking with using maximization of entropy arguments [9, 18]. Function  $\lambda_{\mathbf{k}}$  is determined in situations with an homogeneous temperature gradient by imposing that Normal collisions preserve the crystal momentum [43]:

$$\int \hbar \mathbf{k} \frac{f_{\mathbf{k}} - f_{\mathbf{k}}^4}{\tau_{\mathbf{k}}^N} d\mathbf{k} = 0. \quad (23)$$

This model allows more accurate calculation of the bulk thermal conductivity with respect to the RTA in materials where Normal collisions are important, like graphene or diamond. Moreover, numerical solvers of the BTE-RTA introduced in the previous subsection have been adapted to solve the linearized BTE using the Callaway's operator also including complex boundary conditions [44–47]. Remarkably, this has been shown useful to model non-Fourier behavior like the Drifting second sound [48] or the presence of heat vortex [49] (see more details in Chapter 10).

### Theory of Relaxons

So far, we have considered the solutions of the linearized BTE in terms of the basis of phonon modes, which are the eigenvectors of the Drift operator (i.e. with a well defined velocity). However, it is possible to switch to a different basis determined by the eigenvectors of the collision operator [50]. A simple variable change can be used to symmetrize operator  $C$ . Then, the eigenbasis elements of the symmetrized operator  $\tilde{C}$  are linear combinations of phonons known as relaxon modes  $|\theta^\alpha\rangle$  with eigenvalue  $\Omega^\alpha$  (where  $\alpha$  is the relaxon index) [15]:

$$\tilde{C}|\theta^\alpha\rangle = \Omega^\alpha|\theta^\alpha\rangle. \quad (24)$$

The relaxon modes are not eigenvectors of the drift operator and, hence, we do not have a defined velocity for each relaxon. In other words, the independent movement of the phonon modes at different velocities cause transitions between relaxons. Therefore, in this basis, the inverse of the diagonal elements of  $\tilde{C}$  are the relaxation times of each relaxon  $1/\Omega^\alpha$ . Hence, no approximations are needed to rigorously introduce the notion of relaxation times of the distribution in this basis. Moreover, identification of the relaxons with macroscopic quantities like the heat flux is possible, thus leading to microscopic insight of the evolution of relevant thermodynamic quantities. The relaxon framework was used by Robert J. Hardy [50] to propose the microscopic conditions to unlock the thermal wave propagation as described by the Maxwell-Cattaneo equation [51] including memory effects. This transport equation predicts an exponential decay for the heat flux, which allows direct interpretation of this non-Fourier signature in terms of the BTE in the relaxon basis. These ideas are developed in section 9.1, and then used for experimental modeling in the same Chapter.

More recently, a kinetic theory of relaxons has been developed to refine the ab initio calculation of the bulk thermal conductivity [15]. An arbitrary deviation from equilibrium of the  $\mathbf{k}$ -mode ( $\Delta\tilde{f}_{\mathbf{k}} = \tilde{f}_{\mathbf{k}} - \tilde{f}_{\mathbf{k}}^{\text{eq}}$ ) can be expressed in terms of relaxons:

$$\Delta\tilde{f}_{\mathbf{k}}(\mathbf{r}, t) = \sum_{\alpha} a_{\alpha}(\mathbf{r}, t)|\theta_{\mathbf{k}}^{\alpha}\rangle \quad (25)$$

where  $|\theta_{\mathbf{k}}^{\alpha}\rangle$  is the projection of relaxon  $\alpha$  on phonon mode  $\mathbf{k}$ , and coefficients  $a_{\alpha}$  are the relaxon occupation numbers. The linearized BTE can also be expressed

in terms of relaxons:

$$\begin{aligned} & \sqrt{\frac{c}{\kappa_B T^2}} \left( \frac{\partial T(\mathbf{r}, t)}{\partial t} \langle \theta^0 | \theta^\alpha \rangle + \nabla T(\mathbf{r}, t) \cdot \langle \theta^0 | \mathbf{v} | \theta^\alpha \rangle \right) \\ & + \frac{\partial a_\alpha(\mathbf{r}, t)}{\partial t} + \sum_{\alpha'} \langle \theta^\alpha | \mathbf{v} | \theta^{\alpha'} \rangle \cdot \nabla a_{\alpha'}(\mathbf{r}, t) = -\Omega^\alpha a_\alpha(\mathbf{r}, t) \end{aligned} \quad (26)$$

where  $c$  is the total specific heat. As stated above, the previous equation provides a simple and accurate picture of the role of collisions in relaxing the distribution in terms of relaxation times. However, the drift operator couples different relaxon modes, thus increasing the complexity. Nevertheless, if we consider an steady-state situation and an homogeneous temperature gradient in an infinite crystal, the resulting perturbation is homogeneous ( $\nabla a_\alpha(\mathbf{r}, t) = 0, \forall \alpha$ ). Hence, the relaxons have a well defined velocity  $\nu_\alpha \equiv \langle \theta^0 | \mathbf{v} | \theta^\alpha \rangle$ , and Eq. 26 becomes simplified:

$$\sqrt{\frac{c}{\kappa_B T^2}} \nabla T(\mathbf{r}, t) \cdot \nu_\alpha = -\Omega^\alpha a_\alpha(\mathbf{r}, t). \quad (27)$$

Now using the microscopic definition of the heat flux (Eq. 12), and the relation between phonon and relaxon occupation numbers, we obtain an expression for the thermal conductivity:

$$\kappa = \frac{1}{3} \sum_{\alpha} c \nu_\alpha^2 / \Omega^\alpha. \quad (28)$$

By using first principles calculations, the previous expression has been shown to provide accurate predictions for the bulk thermal conductivity of materials like graphene [15], in which the RTA infrapredicts the experimental value.

The theory of relaxons has been also used to derive a generalized Fourier's law with a time and space dependent thermal conductivity for situations with an inhomogeneous temperature gradient [52]. Furthermore, derivation of transport equations beyond Fourier has been proposed in this framework to consider more complex non-equilibrium situations with an inhomogeneous temperature gradient or heat flux profiles [18, 53]. The method in [18] is based in solving the linearized BTE around the displaced distribution 22 including first order perturbations, and predicts the emergence of non-local and memory effects in collective materials like graphite or diamond, where Normal collisions dominate. However, this approach predicts negligible non-Fourier effects in a kinetic material like silicon at room temperature, which is in conflict with the main results of the present thesis. Predicting the thermal behavior of silicon is not possible if assuming the displaced distribution as initial ansatz for the BTE. In materials like silicon, a different approach is needed to connect the microscopic properties of the distribution with continuous models [19]. Alternative BTE solutions predicting significant hydrodynamic effects in silicon are presented in section 3.2. Moreover, extensive experimental evidence of hydrodynamic behavior in Silicon is presented in Chapters 4 to 7, and further justification using computational experiments can be found in Chapter 10.

## Guyer-Krumhansl framework

A similar perspective was adopted by R. A. Guyer and J. A. Krumhansl to develop his seminal work [6, 54], which significantly contributed to extract physical insight from the BTE for phonons with the use of fundamental conservation laws. The symmetrized collision operator may be divided into two parts:

$$\tilde{C} = \tilde{N} + \tilde{R}, \quad (29)$$

where  $\tilde{N}$  contains the Normal scattering processes and  $\tilde{R}$  the Resistive ones. The Guyer-Krumhansl framework is based in developing a solution of the BTE for isotropic materials in terms of the eigenvectors of operator  $\tilde{N}$  [6]. Since  $\tilde{N}$  modifies neither the energy nor the crystal momentum of the population, there are four independent distribution functions which are eigenvectors of  $\tilde{N}$  with null eigenvalue: The zero-order element  $|\eta_0\rangle$ , related to the deviational energy (which is also eigenvector of  $R$  with null eigenvalue), and the three first-order elements  $|\eta_{1i}\rangle$ , related to the total crystal momentum in the three spatial directions  $i = x, y, z$ , respectively:

$$|\eta_0\rangle = \mu[2 \sinh(x/2)]^{-1} \quad (30)$$

$$|\eta_{1i}\rangle = \lambda_i k_i [\kappa_B T 2 \sinh(x/2)]^{-1} \quad (31)$$

where  $k_i$  is the component  $i$  of the wave-vector  $\mathbf{k}$ ,  $x = \frac{\hbar\omega}{\kappa_B T}$ , and  $\mu, \lambda_i$  are normalizing constants. The higher order elements with non-null eigenvalue are all included in  $|\eta_2\rangle$ . The hyperbolic sinus appear as a result of the BTE symmetrization. An arbitrary perturbation of the distribution function  $\tilde{f}(\mathbf{r}, t)$  can be expressed as

$$\Delta\tilde{f}(\mathbf{r}, t) = a_0(\mathbf{r}, t)|\eta_0\rangle + \sum_i a_{1i}(\mathbf{r}, t)|\eta_{1i}\rangle + \mathbf{a}_2(\mathbf{r}, t)|\eta_2\rangle, \quad (32)$$

where coefficients  $a$  are the occupation numbers in the new basis. Remarkably, for isotropic media and assuming a dispersionless single phonon branch (single polarization) with Debye velocity  $v$ , the most important thermodynamic magnitudes can be directly related with the basis elements [6]. The deviational energy density with respect to the average thermal energy reads

$$\epsilon(\mathbf{r}, t) = \frac{\kappa_B T}{\mu} a_0(\mathbf{r}, t) \quad (33)$$

and the heat flux components  $i = x, y, z$  read

$$q_i = \frac{\kappa_B T \hbar v^2}{\lambda_i} a_{1i}(\mathbf{r}, t) \quad (34)$$

Furthermore, in this basis, it is possible to explicitly impose that  $\tilde{R}$  conserves the energy of the distribution and  $\tilde{N}$  conserves both the energy and the momentum. The BTE in matricial form reads

$$\left( \begin{bmatrix} 0 & 0 & 0 \\ 0 & R_{11} & R_{12} \\ 0 & R_{12} & N_{22} + R_{22} \end{bmatrix} - \begin{bmatrix} D_{00} & D_{01} & 0 \\ D_{10} & D_{11} & D_{12} \\ 0 & D_{21} & D_{22} \end{bmatrix} \right) \begin{bmatrix} a_0 \\ \mathbf{a}_1 \\ \mathbf{a}_2 \end{bmatrix} = \begin{bmatrix} 0 \\ 0 \\ 0 \end{bmatrix}. \quad (35)$$

The matrix elements of the Drift operator  $D$  are the time and space derivatives acting over the combination of phonon modes represented by each eigenvector of  $\tilde{N}$ . Using equations 33 and 34, the first row of 35 leads to the energy conservation equation 2. Moreover, the second and third rows of 35 can be combined to obtain the analog to a momentum balance equation:

$$D_{11}\mathbf{a}_1 + D_{10}a_0 = [R_{11} - (R_{12} - D_{12})(N_{22} + R_{22} - D_{22})^{-1}(R_{21} - D_{21})]\mathbf{a}_1. \quad (36)$$

Let us define the relaxation operator  $\tau$  encompassing all the Collision operator elements in the previous equation:

$$\tau = [R_{11} - (R_{12} - D_{12})(N_{22} + R_{22} - D_{22})^{-1}(R_{21} - D_{21})]^{-1}. \quad (37)$$

From Eq. 36 and using equations 37, 33, 34, it is possible to obtain the general transport equation

$$- (\mu\hbar v^2/\lambda)^2 c \nabla T = \frac{\partial \mathbf{q}}{\partial t} + \tau_{11}^{-1} \mathbf{q}, \quad (38)$$

where  $\tau_{11}$  is the diagonal element of operator  $\tau$  associated to the first-order element  $|1\rangle$  (which is a linear combination of eigenvectors  $|\eta_{1x}\rangle, |\eta_{1y}\rangle, |\eta_{1z}\rangle$ ).

Now it is possible to derive a refined expression for the bulk thermal conductivity in steady-state conditions ( $D_{11} = D_{22} = \frac{\partial}{\partial t} = 0$ ) with an homogeneous temperature gradient ( $D_{12} = 0$  and  $D_{21} = 0$ ). In such situation,

$$\tau = [R_{11} - (R_{12})(N_{22} + R_{22})^{-1}(R_{21})]^{-1}. \quad (39)$$

In [6], the previous expression is analyzed in the limiting cases where Normal collisions dominate  $N \gg R$  (collective regime), and where Resistive collisions dominate  $N \rightarrow 0$  (kinetic regime). Identification of the  $R$  and  $N$  elements are then proposed to satisfy the expected behavior in the different limits:

$$N_{22} \rightarrow 1/\tau_N, \quad (40a)$$

$$R_{11} \rightarrow \langle 1 | \tau_R^{-1}(\mathbf{k}) | 1 \rangle, \quad (40b)$$

$$R_{22} \approx R_{11}, \quad (40c)$$

$$(R^{-1})_{11} \rightarrow \langle 1 | \tau_R(\mathbf{k}) | 1 \rangle. \quad (40d)$$

being  $\tau_N$  and  $\tau_R$  the Normal and Resistive relaxation times. Note that  $\tau_N$  does not depend on the momentum of the distribution  $\mathbf{k}$ , whereas  $\tau_R$  depend on the momentum, so it depends on the specific excited phonon modes contributing to the deviation with respect to equilibrium. The explicit expressions for the different projections in 40 can be found in [6]. Using 40, the expression 39 for operator  $\tau$  reads

$$\tau = \langle 1 | \tau_R^{-1}(\mathbf{k}) | 1 \rangle \left[ \frac{\tau_N + \langle 1 | \tau_R^{-1}(\mathbf{k}) | 1 \rangle^{-1}}{\tau_N \langle 1 | \tau_R(\mathbf{k}) | 1 \rangle} \right], \quad (41)$$

and the thermal conductivity can be identified from 38 as

$$\kappa = \frac{1}{3} c v^2 [\tau_K (1 - \Sigma) + \tau_C \Sigma], \quad (42)$$

where  $c$  is the total specific heat, and  $\Sigma = \frac{1}{1+\tau_N/\tau_K}$  is a switching factor measuring the ratio of Resistive scattering rate to Normal scattering rate. We denoted the kinetic relaxation time  $\tau_K = \langle 1|\tau_R(\mathbf{k})|1\rangle$  and the collective relaxation time  $\tau_C = \langle 1|\tau_R^{-1}(\mathbf{k})|1\rangle^{-1}$ .

Some physical insight can be obtained from the previous expression for the thermal conductivity, which, in contrast to RTA, properly includes the role of the Normal collisions. Even though these collisions do not directly contribute to the thermal resistance (note that for  $R \rightarrow 0$  we have  $\kappa \rightarrow \infty$ ), its influence modify the total thermal conductivity of the system. In fact, Eq. 42 can be interpreted as a weighted sum of the thermal conductivity in a purely kinetic situation ( $N \rightarrow 0$ ) and in a collective situation ( $N \gg R$ ). In the kinetic limit, the phonon modes relax independently towards equilibrium through different scattering rates, like the RTA assumes. In the collective situation, many Normal collisions take place between each Resistive collision, thus redistributing the momentum which was lost. Hence, the distribution relax collectively due to the phonon modes with higher Resistive scattering rates being populated through Normal scattering involving the phonon modes with weak Resistive scattering. This collective evolution is characterized by a globally defined relaxation time ( $\tau_C$ ) for the momentum of all the phonon modes.

An alternative derivation of the refined expression 42 for the thermal conductivity can be obtained using maximization of entropy arguments in each regime [55]. The key idea is that the optimization of entropy production is achieved independently mode by mode in the kinetic limit, whereas it is achieved collectively by all the modes in the collective limit. Moreover, the resulting thermal conductivity (Eq. 42) values for different materials and temperatures have been successfully validated with experiments using first principles calculations of the relaxation times [56].

The Guyer-Krumhansl formalism can be also used to derive generalized transport equations beyond Fourier's law for transient situations with an inhomogeneous gradient of temperature. The derivation is obtained in the collective regime (Normal dominating collisions) for isotropic materials. From Eq. 38 and using the properties of the operators  $R, N$  in the collective limit, a hydrodynamic-like heat transport equation resembling the Navier-Stokes equation for fluids can be obtained [6]:

$$\tau_C \frac{\partial \mathbf{q}}{\partial t} + \mathbf{q} + \kappa_C \nabla T = \ell_C^2 (\nabla^2 \mathbf{q} + 2\nabla \nabla \cdot \mathbf{q}) \quad (43)$$

where  $\kappa_C = \frac{1}{3}cv^2\tau_C$  and  $\ell_C^2 = \frac{1}{5}v^2\tau_N\tau_C$ . Detailed analysis of this transport equation and its implications is provided in [54]. It is worth remarking that the mentioned original derivation of the phonon hydrodynamic model was obtained in the limit of Normal dominating collisions (i.e. the collective regime) as further discussed in section 3.1. However, recent derivations from the BTE extended its applicability beyond this regime as shown in section 3.2, where eq. 43 is generalized. In Chapters 4 to 9 we provide extensive evidence of the applicability of the previous transport equation along with the appropriate boundary conditions

and ab initio parameters to model nanoscale experiments in silicon or germanium at room temperature, where Normal collisions do not dominate.

## 2.3 Approximation Methods in Kinetic Theory

The approaches introduced in the previous section are mainly aimed to calculate the intrinsic (bulk) thermal conductivity appearing in eq. 1. Its applicability is limited to infinite crystals (as compared to the phonon mean free paths) under homogeneous perturbations like a constant gradient of temperature, where the diffusive description is valid. However, extensive experimental evidence has shown the breakdown of Fourier's law with the bulk thermal conductivity to explain non-equilibrium effects in current electronic devices, which include nanoscale heat sources and boundaries [21, 22, 57, 58]. Consequently, refined treatment of the BTE is required to include the effects of higher order perturbations like an inhomogeneous heat flux profile in the macroscopic transport equations.

The non-equilibrium distribution function  $f$  provides a complete picture of the state of the phonon gas. However, such detailed information is not necessarily required to control and manipulate the thermal response of semiconductor systems. Instead, one can switch to the description of the moments of the phonon distribution function, whose tensorial components read

$$M_{i_1, \dots, i_n}^n = \int d\mathbf{k} \hbar \omega_{\mathbf{k}} v_{\mathbf{k}}^{i_1} v_{\mathbf{k}}^{i_2} \dots v_{\mathbf{k}}^{i_n} f_{\mathbf{k}}, \quad (44)$$

with  $n$  denoting the order of the moment.

Interestingly, the lower order moments can be directly related to physical quantities like the total energy ( $n=0$ ) or the total heat flux ( $n=1$ ). Moreover, the same projections can be applied to the BTE to obtain an independent equation for each moment. Therefore, full description of the phonon population evolution can be obtained in terms of the moments. This description is in principle as complex as the usual description (in which we have a different equation for each phonon mode). Note that the drift operator increases the order of any given moment and the collision operator also mix the different moments, so the different projections of the BTE are strongly coupled. However, this alternative description has some important advantages. First, conservation of energy can be directly imposed by using that the energy is a collision invariant in the zeroth order BTE projection, as used in section 2.2 to simplify the BTE in eq. 35. Second and most important, the variational principle and entropic arguments can be used to drastically simplify the system of BTE projections by neglecting the higher order moments [9], thus providing simple macroscopic transport equations suitable for experiment modeling.

The celebrated H-theorem states that the entropy production due to collisions is always positive [59]. Consequently, any free evolving non-equilibrium distribution irreversibly tends to the maximum entropy state (i.e. the equilibrium



described by the distribution 3). It may be assumed that this irreversible evolution consists on fast jumps between intermediate states that maximize the entropy of the system at different length or time scales, before the equilibrium is reached. Accordingly, these intermediate states, known as pseudoequilibrium states, would describe a stable non-equilibrium situation during a short enough time interval after an external perturbation, or within a small enough region close to an external source. For example, consider a nanoscale energy source releasing heat to a semiconductor substrate. Within a region below the source and smaller than the average phonon mean free path, the scarcity of collisions preclude that the system can locally reach equilibrium. Hence, this region is described by a certain non-equilibrium state accommodating to the imposed heat flux profile, with locally maximizing the entropy production. Note that, in principle, such pseudoequilibrium state strongly depends on the form of the external perturbations, and it is unknown. However, for non-extreme non-equilibrium situations (i.e. for small enough Knudsen numbers), it is natural to assume that the pseudoequilibrium is only dependent on the lowest order moments of the distribution. Microscopically, there are many microstates that can accommodate to the constraint imposed by the presence of a heat flux ( $M^1 \neq 0$ ), which forces an asymmetry of the phonon density flux in a given direction. In contrast, the higher order moments impose more complex constraints and asymmetries to the distribution, thus drastically reducing the number of available microstates. Hence, the larger the amount of excited higher order moments, the larger the probability that any given collision modifies the global macrostate towards equilibrium. Therefore, the relaxation of higher order moments imply a faster production of entropy than the relaxation of the lower order ones. In consequence, collisions tend to relax much faster the higher order moments, and, hence, the distribution function rapidly falls into a pseudoequilibrium state where only the low order moments survive. The existence and identification of such pseudoequilibrium states is crucial to simplify the microscopic description. As demonstrated in [9], the variational principle ensures that approximated solutions of the BTE can be restricted to the subspace determined by the pseudo-equilibrium. The relaxation of the rest of the distribution can be assumed to be infinitely fast, and hence it can be excluded from the description. This conceptual framework is fundamental for the derivation of generalized transport equations (see examples in section 3.2). The crucial point is to successfully select an appropriate pseudoequilibrium.

There is a variety of methods to properly manipulate the non-equilibrium distribution function and the BTE to obtain macroscopic transport equations [12]. Such equations, complemented by the balance equations for the conserved quantities, provide a closed description of the system evolution. Standard derivations were originally meant to model mass transport in fluids, and mainly include the Chapmann-Eskog [60] and the Grad methods [61]. The Chapman-Eskog method is based in expanding the distribution function in terms of the Knudsen number, with using only the conserved magnitudes as independent variables for the distribution. For small enough Knudsen, this method leads to the Navier-Stokes equation for fluids or the Fourier's law for thermal transport. Higher order expansions lead to unstable equations like the Burnett ones. Conversely, the

Grad's method directly include the moments to the description as new variables and makes use of the associated BTE projections. To properly close the resulting coupled system of equations, this approach is usually limited to the first 13 moments or 26 moments. The resulting equations provide stable solutions, but its complexity usually preclude including the required boundary conditions for direct comparison with experiments. Furthermore, the two methods can be combined to derive a regularized form of the Grad equations, which are explicitly restricted to the manifold generated by a pseudoequilibrium function [12]. The basic idea is to include the spatial and time derivatives of the moments into the description to close the system.

The regularized method with assuming appropriate ansatz for the pseudoequilibrium inspire different derivations of generalized heat transport equations from the BTE. Specifically, in [16], the regularized method is used to derive an hydrodynamic equation resembling the original Guyer-Krumhansl equation 43 for arbitrary situations beyond the collective regime

$$\tau_R \frac{\partial \mathbf{q}}{\partial t} + \mathbf{q} + \kappa \nabla T = \ell^2 (\nabla^2 \mathbf{q} + \frac{1}{3} \nabla \nabla \cdot \mathbf{q}), \quad (45)$$

along with the associated pseudoequilibrium distribution function

$$f = f^{\text{eq}} + \frac{3}{c\bar{v}^2} \frac{\partial f^{\text{eq}}}{\partial T} q_i \bar{v}_i + \frac{\bar{\tau}_R}{c} \frac{\partial q_i}{\partial x_i} \frac{\partial f^{\text{eq}}}{\partial T} - \frac{3\bar{\tau}_R}{c\bar{v}^2} \bar{v}_i \bar{v}_j \frac{\partial q_i}{\partial x_j} \frac{\partial f^{\text{eq}}}{\partial T}, \quad (46)$$

where  $\bar{\tau}_R$ ,  $\bar{v}$ , and  $\ell$  represent an averaged phonon relaxation time, velocity, and mean free path, respectively. Moreover, alternative derivations of the previous transport equation and the associated pseudoequilibrium distribution have been recently obtained using a modified version of the regularized method [19].

It is worth to mention that the access to the pseudoequilibrium distribution function allows to derive consistent boundary conditions using simple kinetic arguments (see section 3.4), which is the crucial requirement for predictive modeling of heat transport at the nanoscale. Alternatively, other approaches include the external perturbations explicitly in the perturbed distribution that is inserted in the BTE [17, 62], thus leading to alternative generalized transport models also capturing size and frequency effects.

## 2.4 Extended Irreversible Thermodynamics

Full microscopic description of transport phenomena is precluded due to the overwhelmingly high number of degrees of freedom involved. Hence, as shown in the previous sections, microscopic theories are usually manipulated to lead to simpler mesoscopic or macroscopic descriptions based on few averaged magnitudes. Such descriptions consist of well-known conservation laws (e.g. eq. 2) along with phenomenological or approximated constitutive (transport) equations (e.g. eq. 1 or eq. 45) to close the system. In this section we show how

non-equilibrium thermodynamics [5, 63] informs about the validity and robustness of the required constitutive equations.

From a macroscopic point of view, the key independent variables are the conserved magnitudes in the system (e.g. mass, momentum, or energy). The simplest extension of thermodynamics to the non-equilibrium is the Classical Irreversible Thermodynamics (CIT) framework [64], in which the evolution of the non-conserved variables (like the flux of a conserved one) is assumed to be extremely fast, so one can treat them as dependent functions of the conserved magnitudes and its gradients. Accordingly, the system can be assumed to locally behave as in equilibrium. This means that the fundamental thermodynamic relations (like the Gibbs equation for the entropy) can be formulated locally in terms of the same set of variables that globally describe the equilibrium. The CIT approach is only reasonable in situations close to the global equilibrium, where the perturbations are sufficiently slow or homogeneous. However, in this thesis we consider small and fast excitations comparable to the characteristic sizes and times of the microscopic evolution (i.e. the phonon mean free paths and collisions times). In such conditions, the relaxation time of some non-conserved magnitudes like the energy flux is comparable to the duration of the perturbation in space or time, so more general frameworks are required. One of the available theories beyond the notion of local equilibrium is the Extended Irreversible Thermodynamics (EIT) [5], which is based in treating all the slowly evolving magnitudes as independent variables that are explicitly included in the thermodynamic relations. As it will be shown, this formulation allows generalizing the second principle of the thermodynamics, thus providing insight of the physically acceptable forms of the constitutive (transport) equations and boundary conditions far from equilibrium. This generalization can be used to inspect many non-equilibrium processes like fluid dynamics [65] or phase transformations [66]. For illustration, here we restrict the discussion to thermal transport phenomena in solids with no external volumetric energy sources [20, 67–69].

### Classical Irreversible Thermodynamics for diffusive heat transport

According to the hypothesis of local equilibrium, the entropy density  $s$  only depends on the local internal energy, so the Gibbs equation reads

$$ds = T^{-1} du, \quad (47)$$

in which  $T = (\partial s / \partial u)^{-1}$  is the local temperature and  $u = cT$  is the local internal energy per unit volume. The time derivative of eq. 47 can be combined with the conservation equation 2 to obtain an entropy balance equation

$$\frac{ds}{dt} = -\nabla \cdot (T^{-1} \mathbf{q}) - T^{-2} \mathbf{q} \cdot \nabla T. \quad (48)$$

Eq. 48 can be expressed as

$$\frac{ds}{dt} + \nabla \cdot \mathbf{J}_s = \sigma_s, \quad (49)$$

where

$$\mathbf{J}_s = T^{-1} \mathbf{q} \quad (50)$$

is the entropy flux, and

$$\sigma_s = -T^{-2} \mathbf{q} \cdot \nabla T \quad (51)$$

is the entropy production. The entropy flux can be either positive or negative since it represents the internal transport of entropy between contiguous parts of the system. Conversely, as imposed by the second principle of thermodynamics, the entropy production can not be negative ( $\sigma_s \geq 0$ ), since it represents the generation of entropy in a given location. This constrain imposes some physical limitations for the transport equation required to complement the conservation equation 2 for a self-contained description of the system. For example, according to the CIT (based in eq. 47), the Fourier's law 1 with a defined-positive thermal conductivity  $\kappa$  satisfies that  $\sigma_s \geq 0$  according to expression 51 ( $\sigma_s = \kappa (\frac{|\nabla T|}{T})^2 \geq 0$ ). As it will be shown below, analogous justification of generalized transport equations would require generalized notions of entropy beyond local equilibrium.

### Extended Irreversible Thermodynamics for generalized heat transport

The EIT is based in treating the dissipative fluxes like the energy flux  $\mathbf{q}$  as independent variables. The method can be generalized by including higher-order variables like the flux of the energy flux in the description. It is assumed that the entropy of the system locally depends both on conserved magnitudes and non-conserved (but slowly evolving) magnitudes. The resulting entropy is assumed to be additive and a convex function, and its general formulation can be found in [5]. Here, for simplicity, we restrict ourselves to the linear version of this theory for isotropic materials, in which the temperature  $T$  retains its local character. Specifically, we use the simplified form proposed in [20], where the entropy is a function of the internal energy  $u$ , the heat flux  $\mathbf{q}$ , and the traceless symmetric part of the heat flux gradient  $\nabla \mathbf{q}_s^0 = \frac{1}{2}(\nabla \mathbf{q} + (\nabla \mathbf{q})^T) - \frac{1}{3}(\nabla \cdot \mathbf{q})\mathbb{I}$ , with the superindex  $T$  denoting the transposed tensor. The resulting generalized Gibbs relation reads

$$ds = T^{-1} du + \frac{\partial s}{\partial \mathbf{q}} \cdot \mathbf{q} + \frac{\partial s}{\partial (\nabla \mathbf{q}_s^0)} : \nabla \mathbf{q}_s^0, \quad (52)$$

and we denote  $\frac{\partial s}{\partial \mathbf{q}} = -T^{-2} \mathbf{a}(u, \mathbf{q}, \nabla \mathbf{q}_s^0)$  and  $\frac{\partial s}{\partial (\nabla \mathbf{q}_s^0)} = -T^{-2} B(u, \mathbf{q}, \nabla \mathbf{q}_s^0)$ . We assume now the simplest linear relation for the unknown vector  $\mathbf{a} = a\mathbf{q}$  and the tensor  $B = b\nabla \mathbf{q}_s^0$ , with  $a, b$  being scalars. In order to explore possible forms of generalized transport equations in good agreement with the second principle, the physical identification of coefficients  $a$  and  $b$  is not indispensable. Nevertheless, such parameter identification is possible by envisioning connections with microscopic theories (like the approximation methods in kinetic theory discussed in the previous section) as shown in [20]. With these assumptions, the generalized Gibbs equation 52 reads

$$ds = \frac{1}{T} du - \frac{a}{T^2} \mathbf{q} \cdot d\mathbf{q} - \frac{b}{T^2} \nabla \mathbf{q}_s^0 : d\nabla \mathbf{q}_s^0. \quad (53)$$

Since the entropy corresponding to local equilibrium (eq. 47) is the maximum entropy, it is reasonable to assume that  $a > 0$  and  $b > 0$ . Accordingly, the integrated form of equation 53 indicates that the presence of a heat flux reduce

the total entropy of the system, and this reduction is enhanced if the heat flux is non-homogeneously distributed. This is consistent with the microscopic notion of entropy, which is proportional to the number of microstates that can accommodate to a given macrostate defined by the averaged variables. The presence of a heat flux introduce some asymmetry in the phonon distribution, forcing a higher amount of energy carriers to flow in a specific direction, thus reducing the amount of available microstates with respect to the equilibrium. Furthermore, some of these microstates are not consistent with an increasing heat flux in some direction, so that more constraints are imposed on the distribution function and the entropy is further reduced in the presence of a heat flux gradient.

Tensor  $\nabla \mathbf{q}_s^0$  is contained in the flux of the energy flux. The time-derivative of this higher-order perturbation is assumed to be negligibly small in front of lower order perturbations like  $\frac{d\mathbf{q}}{dt}$  within most of the derivations of generalized heat transport equations [16, 19]. Hence, in our context, the time derivative of eq. 53 can be reduced to

$$\frac{ds}{dt} = \frac{1}{T} \frac{du}{dt} - \frac{a}{T^2} \mathbf{q} \cdot \frac{d\mathbf{q}}{dt}. \quad (54)$$

Now, in analogy to the CIT procedure shown in the previous subsection, we combine eq. 54 and the energy conservation eq. 2 to obtain the balance equation for the entropy:

$$\frac{ds}{dt} = -\nabla \cdot (T^{-1} \mathbf{q}) - T^{-2} \mathbf{q} \cdot \nabla T - \frac{a}{T^2} \mathbf{q} \cdot \frac{d\mathbf{q}}{dt}. \quad (55)$$

To use the second principle, identification of the entropy flux and the entropy production from the previous equation through some method along with identification of the coefficients  $a, b$  is required. Then, all the possible constitutive equations beyond Fourier's law (i.e. involving higher-order terms) can be discriminated from the unphysical ones by imposing  $\sigma_s \geq 0$ . For example, it is possible to show that the hydrodynamic heat transport equation 45, which will be used throughout this thesis to model a variety of experiments, is consistent with the second principle. As shown in [20], we can identify parameters  $a, b$  by comparing eq. 53 with the kinetic definition of the entropy density for bosons [20, 70, 71],

$$s = -\kappa_B \int [f \ln(f) - (1+f) \ln(1+f)] d\mathbf{k}, \quad (56)$$

where  $f$  is the non-equilibrium distribution function 46 bijectively related to the hydrodynamic equation (see section 2.3). We obtain  $a = \frac{\tau}{\kappa}$  and  $b = \frac{2\tau\ell^2}{\kappa}$ . Moreover, we can obtain the entropy flux by using its kinetic definition [20, 70, 71]

$$\mathbf{J}_s = -\kappa_B \int \mathbf{v}_k [f \ln(f) - (1+f) \ln(1+f)] d\mathbf{k}. \quad (57)$$

By identifying the entropy flux (eq. 57) in eq. 55, and with the use of eq. 49 and the hydrodynamic transport equation 45, yields to the entropy production  $\sigma_s$  according to the phonon hydrodynamic model:

$$\sigma_s = \frac{\mathbf{q} \cdot \mathbf{q}}{\kappa T^2} + \frac{2\ell^2}{\kappa T^2} \nabla \mathbf{q}_s^0 : \nabla \mathbf{q}_s^0. \quad (58)$$

It can be seen that, for positive-defined thermal conductivities  $\kappa$ , the non-negativeness of the entropy generation is explicitly ensured. Therefore, the hydrodynamic transport equation is consistent with the second principle in the framework of the EIT.

Remarkably, similar methods can be used to test the physical validity of the required boundary conditions to model heat transport experiments at the nanoscale. In particular, the validity of the boundary conditions used in this thesis (see section 3.4) is demonstrated in [20].

## 2.5 Ballistic effects

Current semiconductor devices have characteristic sizes comparable to the average phonon MFP at room temperature. Moreover, the computing clock-rates are approaching the phonon scattering rates. Therefore, boundary and high-frequency effects play a crucial role in the thermal evolution of current micro electronic devices [1]. Fortunately, the improvement of experimental techniques has allowed researchers to probe the thermal response of a wide number of materials at nanoscale sizes. As a general qualitative trend, the apparent thermal conductivity is reduced at the nanoscale with respect to the bulk thermal conductivity values if Fourier's law is assumed [72–75]. The main goal of this thesis is to validate a predictive model based in the phonon hydrodynamic framework introduced in sections 2.3 and 2.4 to capture such nanoscale effects using a variety of experiments. For contextualization purposes, in this section we introduce some alternative approaches to explain the same or similar experiments, with highlighting the connections and discrepancies with the hydrodynamic transport description. We limit the discussion to the models directly compared with the hydrodynamic model along this thesis and, hence, some widely used and remarkable models like the Dual Phase Lag Model [76–79] or the Thermomass Model [80–82] are not introduced here.

### Casimir Regime

The Casimir regime [83] is the limit where the system characteristic size  $L$  is much larger than the average phonon MFP ( $L > \bar{\Lambda} = \bar{v}\bar{\tau}$ ). In such conditions, the phonon relaxation time of a given mode  $\mathbf{k}$  is reduced and may be approximated by the averaged scattering time with the boundaries  $L/v_{\mathbf{k}}$  in the kinetic expression of the thermal conductivity 13. This approach provides a simple explanation for the reduction of the effective thermal conductivity observed in experiments. Due to the weak temperature dependence of the phonon velocities, the temperature dependence of the thermal conductivity is the same as the specific heat one in this limit, thus we have  $\kappa \propto c \propto T^{-3}$  at low temperatures [9]. This behavior was originally observed at cryogenic temperatures, where the phonon MFPs are larger. Nowadays, this limit can be reached in simple structures like nanowires [84] even at higher temperatures [85].

Understanding the transition from the Casimir limit to the diffusive behavior, where the bulk thermal conductivity and Fourier's law apply (no size effects), has been the subject of intensive research for many years. One simple approach within the RTA framework is to combine the boundary scattering time  $L/v_{\mathbf{k}}$  with the Umklapp scattering time using a Mathiessen rule. However, this oversimplified picture does not allow to properly model the diffusive to ballistic transition. Moreover, complex devices usually include more than one characteristic size comparable to the phonon MFPs, so more sophisticated theories are required.

### **Ballistic Suppression of Phonons and Mean Free Path spectroscopy**

The development of first principles calculation techniques to characterize the collision operator has been crucial to obtain the intrinsic thermal conductivity of many materials without fitting parameters [3, 4]. Furthermore, the notion of the phonons MFPs within the RTA allowed the development of microscopic frameworks aimed to model the influence of system boundaries on the transport of heat by the different phonon modes. One of this models is the ballistic phonon suppression and the MFP spectroscopy [86–88]. The simplest version of this model is based in the use of an effective Fourier's law with removing the contribution to the thermal conductivity of the phonon modes with MFP larger than the system characteristic length  $L$  [74, 75, 89, 90]. This proposal has been used in many experimental modelizations, with remarkable results in alloy semiconductors like SiGe [75, 90]. It has been also used to model the thermal conductivity of Silicon thin films [88] or the phase lag between an harmonic optical excitation and the oscillating thermal response in Frequency-domain thermoreflectance (FDTR) experiments in Silicon [89]. Other authors have used the notion of mean free path spectroscopy to characterize the apparent interfacial thermal resistance observed during the relaxation of nanoscale heaters on Silicon substrate [57, 91, 92]. Discussion about the applicability of this framework in Silicon in these particular experiments and comparison with the phonon hydrodynamics predictions is provided in Chapters 4, 6, and 7, respectively.

There is a variety of derivations from the BTE of geometry-dependent suppression functions of ballistic phonons to explain the thermal conductivity reduction due to size or frequency effects [93–95]. To illustrate this kind of interpretations, we focus here in the work by A. A. Maznev et. al [95] due to its simplicity and physical insight. Consider the thermal relaxation of a sinusoidal temperature distribution (or thermal grating) in 1D with wave-number  $q$ . It is reasonable to assume that phonons with MFPs larger than the grating period  $2\pi/q$  behave differently than the rest of the phonons. Let us then distinguish the dynamics of the low-frequency phonons (large MFP), which do not locally follow the temperature gradients, and the high-frequency phonons, which behave diffusively due to its MFP being much smaller than the characteristic scale of the perturbation  $2\pi/q$ . The low-frequency phonons will be described by the non-equilibrium distribution  $f$  obeying the BTE-RTA and the high frequency-ones will be described by a temperature  $T$  obeying Fourier's law. The interaction

between the two subsets of phonon modes is the following: On one hand, the energy of the low-frequency phonons that relax due to scattering is a heat source for the temperature encompassing the energy of the high-frequency phonons and, on the other hand, the local equilibrium of the low-frequency phonons is determined by the local temperature  $T$ . This can be expressed using the diffusion equation for  $T$  (combination of equations 1 and 2 including a source term) coupled with the BTE-RTA 10 for  $f$ :

$$c \frac{\partial T}{\partial t} = \kappa_r \frac{\partial^2 T}{\partial x^2} + \int d\mathbf{k} \int_0^{\omega_0} d\omega \frac{f - f^{\text{eq}}(T)}{\tau_\omega} \hbar\omega, \quad (59a)$$

$$\frac{\partial f}{\partial t} + v^x \frac{\partial f}{\partial x} = - \frac{f - f^{\text{eq}}(T)}{\tau_\omega} \quad (59b)$$

where  $\kappa_r = \frac{1}{3} \int_{\omega_0}^{\omega_{\text{max}}} d\omega c_\omega v_\omega \Lambda_\omega$  is the kinetic conductivity of the high-frequency phonon modes, and  $\omega_0$  is the threshold frequency distinguishing the two subsets. The specific heat  $c$  in Eq. 59 is approximately the total specific heat and the temperature  $T$  can be identified with the total thermal energy, since the main contribution to the specific heat comes from the high-frequency phonon modes. The exact value of  $\omega_0$  does not significantly modify the model outputs. According to Eq. 59, the dominant relaxation mechanism for low-frequency phonons occurs via their absorption or radiation by the thermal reservoir. This is based in the fact that the three-phonon scattering involving one low-frequency phonon and two high-frequency phonons from the thermal reservoir is the dominant Resistive mechanism relaxing the low-frequency phonons. These low-frequency phonons do not locally follow the temperature gradients (i.e. do not contribute to the thermal conductivity) and uniformly inject energy to the thermal reservoir of high-frequency phonons, whose diffusive behavior ultimately relax the inhomogeneous temperature distribution. Interestingly, by resolving the transient evolution of the system (eq. 59) considering the grating with wave-vector  $q$  as the initial temperature distribution, one can identify the effective thermal conductivity displayed by the system

$$\kappa_{\text{ef}}(q) = \frac{1}{3} \int_0^{\omega_{\text{max}}} d\omega A(q\Lambda) c_\omega v_\omega \Lambda_\omega, \quad (60)$$

where  $A(q\Lambda)$  is a suppression function for the thermal conductivity contribution of low-frequency (or ballistic) phonons, which reads

$$A(q\Lambda) = \frac{3}{q^2 \Lambda^2} \left( 1 - \frac{\arctan(q\Lambda)}{q\Lambda} \right). \quad (61)$$

This interpretation is inspired by previous frameworks like the ballistic-diffusive equations [96–98], which originally divided the distribution function into two parts: One associated to the ballistic phonons originating from the boundaries and the other to the scattered and excited carriers undergoing diffuse transport. The suppression function 61 leads to the notion of MFP spectroscopy, i.e. the possibility of characterizing the MFP spectrum from thermal conductivity measurements in simple experiments like the relaxation of optically induced thermal



gratings [74, 88, 90]. This has been shown useful to predict the thermal conductivity in semiconductor alloys like SiGe [90]. However, as it will be discussed in Chapters 4 and 6, this approach based in Fourier's law and the notion of cumulative thermal conductivity in terms of the MFPs is in conflict with some experimental measurements in pure materials. Moreover, recent work [99], examine the reliability of the MFP spectroscopy framework from a theoretical point of view. It is shown that a given cumulative thermal conductivity does not correspond to a unique relaxation-times function for the phonon modes, in the sense that more than one distribution of MFPs can result in the same cumulative thermal conductivity.

### Lévy Flights

At the macroscale, where Fourier's law with the bulk thermal conductivity is valid, the phonon MFP are negligible as compared to the system sizes. Hence, one can describe the phonon dynamics as a Brownian motion, which ultimately leads to the macroscopic diffusive behavior of heat. At the nanoscale, this microscopic picture is not adequate due to ballistic effects. The Truncated Lévy Flights formalism [30, 100] is specially designed to identify and interpret the deviations with respect to heat diffusion at the nanoscale in semiconductor alloys like SiGe or InGaAs [101].

Consider the instantaneous injection of a planar pulse in a semiconductor at the position  $z = 0$  and time  $t = 0$ . We assume that the system response is restricted to the cross-plane direction  $z$ , and close to the reference equilibrium situation at temperature  $T_0$  ( $\Delta T = T - T_0 \ll T_0$ ). In such conditions, the linearized BTE equation in 1D under the RTA can be projected by the phonon energy to obtain:

$$\frac{\partial g_{\mathbf{k}}}{\partial t} + v_{\mathbf{k}}^z \frac{\partial g_{\mathbf{k}}}{\partial z} = -\frac{g_{\mathbf{k}} - c_{\mathbf{k}} \Delta T(z, t)}{\tau_{\mathbf{k}}} + \frac{c_{\mathbf{k}}}{c} \delta(z) \delta(t), \quad (62)$$

where  $g_{\mathbf{k}} = \hbar \omega_{\mathbf{k}} (f_{\mathbf{k}} - f_{\mathbf{k}}^{\text{eq}}(T_0))$  is the deviational energy with respect to equilibrium. Now we perform Fourier spatial transformation ( $z \leftrightarrow \xi$ ) and Laplace temporal transformation ( $t \leftrightarrow s$ ) of Eq. 62:

$$G_{\mathbf{k}}(\xi, s) = \frac{c_{\mathbf{k}}(\Delta T(\xi, s) + \frac{\tau_{\mathbf{k}}}{c})}{1 + s\tau_{\mathbf{k}} + i\xi \Lambda_{\mathbf{k}}^z} \quad (63)$$

where  $i$  is the imaginary unit, and  $\Lambda_{\mathbf{k}}^z = v_{\mathbf{k}}^z \tau_{\mathbf{k}}$  is the projected mean free path in the  $z$  direction. As discussed in 2.1, one of the main drawbacks of the RTA is that energy conservation is not guaranteed. This can be rectified by explicitly imposing energy conservation on the evolution of  $G_{\mathbf{k}}$ :

$$\sum_{\mathbf{k}} \frac{1}{\tau_{\mathbf{k}}} (G_{\mathbf{k}} - c_{\mathbf{k}} \Delta T) = 0. \quad (64)$$

Combining 63, 64, and assuming isotropy in the  $z$  direction, we obtain:

$$P(\xi, s) \equiv c \Delta(\xi, s) = \frac{\sum_{\mathbf{k}^z > 0} c_{\mathbf{k}} \Psi_{\mathbf{k}}(\xi, s)}{\sum_{\mathbf{k}^z > 0} \frac{c_{\mathbf{k}}}{\tau_{\mathbf{k}}} (1 - \Psi_{\mathbf{k}}(\xi, s))} \quad (65)$$

where

$$\Psi_{\mathbf{k}}(\xi, s) = \frac{1 + s\tau_{\mathbf{k}}}{(1 + s\tau_{\mathbf{k}})^2 + (\xi\Lambda_{\mathbf{k}}^z)^2}. \quad (66)$$

Equation 65 predicts the evolution of the perturbed system in the Fourier-Laplace space. It can be shown [30] that  $P(\xi, s)$  is the characteristic function of a random-walk process associated to the probability in real space  $P(z, t)dz$  of finding the injected energy pulse in the location  $[z, z + dz]$  at time  $t$ . One can imagine an instrument that determines if a given location at a certain time is perturbed with respect to a reference equilibrium situation or not. The probability of detecting a deviation is  $P(z, t)dz$ , which locally reflects the evolution of the injected energy. Then, the analysis of the statistical moments of  $P(z, t)$  for different materials and temperatures allow distinguishing different transport regimes.

Due to the symmetry of the studied problem around the  $z = 0$  position, the first derivative vanish ( $\frac{dP(z, t)}{dz} = 0$ ). The mean-square displacement  $\sigma(s)$  of  $P(z, t)$  characterizes the spatial extend of the injected thermal energy in average. From 65, we have

$$\sigma^2(s) = \frac{2}{s^2} \frac{\sum_{\mathbf{k}} \frac{c_{\mathbf{k}} v_{\mathbf{k}}^z \Lambda_{\mathbf{k}}^z}{(1+s\tau_{\mathbf{k}})^2}}{\sum_{\mathbf{k}} \frac{c_{\mathbf{k}}}{1+s\tau_{\mathbf{k}}}}. \quad (67)$$

The mathematical construction  $\sigma(s)$  is physically resembling the thermal penetration depth used to analyze Frequency Domain Thermoreflectance experiments in Chapters 6 and 9. It can be easily shown that for  $s \rightarrow 0$  (long time scales with respect to the relaxation times  $\tau_{\mathbf{k}}$ ), one obtains in real space  $\sigma^2(t) \rightarrow 2t\kappa/c$ , which corresponds to the thermal penetration depth according to Fourier's law (diffusive regime). In the opposed limit  $s \rightarrow \infty$  (small time scales with respect to  $\tau_{\mathbf{k}}$ ), one obtains  $\sigma^2(t) \rightarrow (\bar{v}^z t)^2$ , which corresponds to ballistic propagation of energy at the average phonon velocity  $\bar{v}^z$  (no collisions). The transition between the two limits using ab initio phonon properties is the subject of study in [30, 100], and informs about the emergence of size effects in different materials and temperatures. Specifically, an intermediate regime for alloys is identified as superdiffusive transport or Lévy stable process [102, 103], for which a fractal diffusivity can be defined. Therefore, this model allows distinguishing the thermal response of alloy materials like SiGe or InGaAs from pure materials like silicon (see discussion in section 4.4).

### Hydrodynamic effects in heat transport: From diffusive to ballistic regimes

The phonon hydrodynamic framework is widely known to apply at low temperatures in specific materials like graphene, where Normal collisions dominate. In such conditions, the size and frequency effects lead to a non-Fourier regime, where phenomena beyond the diffusive description like the second sound or the Poiseuille heat flux profile have been predicted and observed [8, 48, 104, 105]. As discussed in section 2.2, the Guyer-Krumhansl formalism leads to a generalized heat transport equation 43 resembling the Navier-Stokes equation for fluids in this regime.

The use of generalized transport equations predicting hydrodynamic behavior of heat (eq. 45) have been also proposed to describe size and frequency effects at arbitrary temperatures in general semiconductors like silicon within extended non-equilibrium thermodynamics frameworks [67, 68, 106]. More recently, a full ab initio version of the hydrodynamic heat transport model for general semiconductors have been derived from the linearized BTE [19].

The main idea is that the ballistic effects introduced in the previous subsections can be captured in a unified way by introducing a single characteristic length and time scales in the transport equations, with the use of appropriate boundary conditions [69, 107]. The resulting non-Fourier phenomenology captures the effective reduction of the thermal conductivity due to size effects as a nonlocal effect (see section 4.1). Moreover, the model predicts deviations from Fourier's law due to memory effects at high excitation frequencies (see section 9.1). In contrast to the usual effective Fourier framework, the hydrodynamic equation parameters like the thermal conductivity or the non-local length are intrinsic material properties (i.e. geometry independent). The complete set of transport equations, boundary conditions, and the microscopic expressions for the parameters depending on the phonon relaxation times and dispersion relations can be found in sections 3.3,3.4, and 3.5, respectively.

The new contribution contained in this thesis is an extensive experimental validation of this generalization of phonon hydrodynamics to situations where Normal collisions do not dominate (Chapters 4 to 9), along with a microscopic interpretation and comparison with alternative approaches like a Monte Carlo solver of the BTE, or non-equilibrium Molecular Dynamics simulations (Chapter 10).

### 3 Phonon Hydrodynamics

At low temperatures or in specific 2D materials, momentum-preserving (Normal) phonon collisions dominate over the Resistive ones. Hence, the momentum of the phonon population is mainly destroyed due to collisions with the boundaries of the system, in perfect analogy with the momentum of the particles in a fluid. In such extreme conditions, the phonon distribution function can be characterized by a mode-independent drift velocity (eq. 22), and the emergence of non-diffusive heat transport phenomena like the Drifting second sound or the Poiseuille heat flux profile have been predicted and experimentally observed [8]. In consequence, generalized transport equations beyond Fourier's law like the Guyer-Krumhansl equation 43 are required at the mesoscopic level of description [6, 105, 108, 109]. This is the standard and well-established (collective) phonon hydrodynamic regime.

Recently, it has been shown that phonon hydrodynamic phenomena is not restricted to the collective regime [16, 19]. For high enough excitation frequencies compared to the average Resistive collision rate or in nanoscale regions with size comparable to the Resistive mean free path, nonlocal and memory effects in heat transport are unlocked, also leading to hydrodynamic-like heat transport as described by the Guyer-Krumhansl equation. Therefore, phonon hydrodynamics is not specific of some exotic materials at low temperatures, but it is a useful framework to understand the diffusive to ballistic transition in arbitrary materials and temperatures. The main objective of this thesis is to provide extensive experimental evidence supporting this perspective. In particular, this chapter contextualizes and details the generalized phonon hydrodynamic model which is then used to describe a variety of experiments in Chapters 4 to 9.

In section 3.1 we summarize the most important predictions and observations of hydrodynamic behavior in the collective regime. In section 3.2, we introduce the generalized phonon hydrodynamic framework, which is derived from the BTE. Sections 3.3, 3.4, and 3.5 contain the required model equations, boundary conditions and parameter values for different materials and temperatures, respectively. Finally, sections 3.6 and 3.7 are devoted to show the thermoelectric and thermoelastic couplings to the model equations, respectively.

#### 3.1 Phonon hydrodynamics in the collective regime

The momentum is a conserved magnitude during collisions between particles in a fluid. Hence, mass transport in a flowing fluid is due to the transport of particles with a drift velocity, and the total momentum is only modified due to scattering with boundaries. Microscopically, the distribution function deviates from equilibrium and accommodate to the displaced Maxwell distribution characterized by the drift velocity. In general, this microscopic picture is not analogous to the transport of heat in semiconductors because intrinsic resistive phonon scattering (Umklapp, impurities) destroys crystal momentum. However, at very low

temperatures or in some specific materials like graphene, momentum-preserving collisions dominate and the destruction of momentum due to phonon-phonon Resistive collisions is weak. In analogy to fluids, in such conditions the distribution of phonons accommodate to the displaced Bose-Einstein distribution 22.

The mesoscopic description of heat transport in the collective regime requires the use of generalized hydrodynamic-like transport equations beyond the diffusive description [7, 8]. As discussed in section 2.2, by splitting the Collision operator in the Normal and Resistive parts in the BTE, and by assuming weak Resistive scattering, one obtains the Guyer-Krumhansl equation 43 for heat transport including memory and nonlocal effects. In [108], solutions of the BTE using the displaced distribution function (Eq. 22) as ansatz lead to similar hydrodynamic equations. Moreover, in [50] the same ansatz leads to the Maxwell-Cattaneo transport equation [51] predicting the emergence of wave-like heat transport. Therefore, demonstrating the abundance of Normal collisions with respect to Resistive collisions using First Principles calculations is considered an indication of the phonon hydrodynamic regime. Alternatively, identification of the displaced distribution function for phonons from solutions of the BTE in some specific non-equilibrium situations has been considered a clear signature of phonon hydrodynamic behavior [104, 110, 111].

The hydrodynamic transport equations were already introduced in sections 2.2 and 2.3. All the details about these equations along with its parameters and the required boundary conditions will be introduced in detail in the following sections. However, an important consideration is in order at this point: The hydrodynamic transport equations reduce to Fourier's law for sufficiently small excitation frequencies or for homogeneous perturbations as compared to the characteristic phonon life times and mean free paths. Therefore, the election of the material and the temperature range is not enough to unlock hydrodynamic behavior even in the collective regime, but the spatial or temporal experimental time scales should be reduced enough in order to unlock nonlocal or memory effects, respectively, as predicted by the transport equations. Accordingly, phonon hydrodynamics can be identified through characteristic non-diffusive behavior in the appropriate non-equilibrium situations. Paradigmatic examples include the Poiseuille heat flux profile [110–112] and the peculiar trend of the thermal conductivity with system size, known as Knudsen minimum [104, 113], or the Drifting second sound propagation [48, 54, 114–116].

## 3.2 Generalized hydrodynamic heat transport

The microscopic picture of phonon hydrodynamics associated to the displaced distribution may lead to believe that hydrodynamic-like heat transport is restricted to the collective regime. However, as we experimentally justify in this thesis, the same hydrodynamic heat equation 45 also apply to kinetic materials like silicon or germanium at room temperature, that is, even in materials and temperatures where Normal collisions do not dominate. Therefore, if the

phonon population is accommodated to the displaced distribution function 22 due to the abundance of Normal collisions, then macroscopic hydrodynamic-like heat transport is obtained as explained in the previous section, but the inverse implication is not true.

In fact, early theoretical works envisioned that the emergence of this kind of behavior is not necessarily restricted to situations where Normal collisions dominate. For example, in the pioneering works by Hardy and others [50, 117] the wave-like heat propagation in the collective regime is regarded to as Drifting second sound to distinguish it from second sound not associated to the displaced phonon distribution, the so-called Driftless second sound. It was shown that the key requirement for the emergence of thermal waves is the slow relaxation of the heat flux as compared to the experimental time scales (i.e. a pseudo-equilibrium situation characterized by the heat flux relaxing significantly slower than the rest of the perturbation). Specifically, alternative solutions of the BTE without imposing the dominance of Normal collisions also lead to non-diffusive transport due to memory effects. Moreover, deviations from diffusive transport due to non-local effects have been also proposed to interpret and unify the description of nanoscale heat transport experiments beyond the collective regime, both in transient and steady-state situations [16, 69]. According to this vision, phonon hydrodynamics is expected in certain non-equilibrium conditions in arbitrary semiconductors, rather than associated to some specific materials in narrow temperature windows. In other words, hydrodynamic transport is unlocked by the external perturbation and the boundary conditions, rather than the material intrinsic properties.

The generalized use of hydrodynamic-like transport equations to model small size or high frequency effects in semiconductors is extensively motivated in previous work [7, 67, 68, 106, 118]. This approach has a twofold theoretical motivation: On one hand, the hydrodynamic transport equation 45 is consistent with the second principle of thermodynamics within the EIT framework [20] as discussed in section 2.4. On the other hand, the postulation of a pseudo-equilibrium distribution function depending on few macroscopic variables like the heat flux and its first derivatives leads to solutions of the BTE consistent with macroscopic hydrodynamic transport equations [19] as discussed in section 2.3. In fact, the crucial advantage of the generalized hydrodynamic model in front of purely microscopic models is the consistency between the non-equilibrium distribution satisfying the BTE, and the mesoscopic transport equations resulting from zeroth and first order projections of the BTE. Importantly, the non-equilibrium distribution function allows obtaining the appropriated boundary conditions for the transport equations by using simple kinetic arguments like detailed energy balance in the boundary [119].

Justifying the applicability of the Guyer-Krumhansl equation 45 beyond the collective regime from microscopic grounds, and obtaining microscopic (*ab initio*) expressions for its parameters in terms of the phonon properties has been the subject of intensive research during the last years. Here we summarize three different proposals leading to the generalized hydrodynamic model.

## Kinetic Collective Model

The Kinetic Collective Model (KCM) is the original and simplest phenomenological model for the generalized hydrodynamic transport parameters [55, 56, 120–122]. It is inspired by the original Guyer-Krumhansl work [6]. As discussed in the last subsection of 2.2, by distinguishing Normal and Resistive processes in the Collision operator, the bulk thermal conductivity can be written as an interpolation between the collective and the kinetic limit (expression 42) with the interpolation factor  $\Sigma = \frac{1}{1+\tau_N/\tau_K}$ . The KCM is based in assuming that the rest of equation parameters in the transport eq. 45 can be obtained for situations beyond the collective regime by interpolation in a similar way:

$$\ell^2 = \ell_K^2(1 - \Sigma) + \ell_C^2\Sigma, \quad (68)$$

$$\tau = \tau_K(1 - \Sigma) + \tau_C\Sigma, \quad (69)$$

where  $\ell_C, \tau_C, \tau_K$  were already introduced in section 2.2, and the non-local length in the pure kinetic regime  $\ell_K$  is postulated as an averaged phonon mean free path [120].

Remarkably, the ab initio calculation of the non-local length according to expression 68 agrees quite well with the more refined expressions shown below (which are derived from the BTE) but fails to estimate the heat flux relaxation time  $\tau$ . In section 3.5, we compare the parameter values for different materials and temperatures according to the different models. Since this simple model is adequate to calculate the most important parameters (i.e. the thermal conductivity and the non-local length) in this thesis the generalized hydrodynamic model is referred to as KCM for historical reasons. However, more reliable expressions for the equation parameters for arbitrary materials and temperatures can be found below. Moreover, note that this proposal derives neither the generalized transport equation nor the non-equilibrium distribution function from the BTE, so the derivations in the following subsections are necessary to obtain a consistent framework for experimental modeling including boundary conditions.

### **Derivation from the BTE assuming a mode-independent relaxation time, identical phonon branches and the Debye approximation.**

An explicit derivation of the hydrodynamic heat transport equation 45 was recently proposed in [16] by a perturbation expansion of the BTE around the nonequilibrium distribution obtained by the maximum-entropy principle, with slight modification of the dimensionless equation coefficients on its right-hand side with respect to the original derivation [6]. The derivation is based in standard approximation methods in kinetic theory (section 2.3). Specifically, the regularized moment method combining some advantages of the Grad's and the Chapman-Eskog approaches is used. Importantly, the mode-independent Relaxation Time Approximation is assumed to model the Collision operator, so the conservation of momentum in Normal collisions is neglected. This indicates that hydrodynamic heat transport phenomena as described by eq. 45 is not necessarily a consequence of Normal dominant collisions, and hence it can be used

beyond the collective regime. Moreover, a mode-independent velocity is also assumed for all the phonon distribution.

Due to the use of mode-independent properties, this derivation does not provide microscopic expressions for the equation parameters that can be calculated from first principles. The authors of [16] propose to use a non-local length equivalent to the median of the phonon MFP spectrum. They show that the corresponding value for Silicon at room temperature ( $\sim 190$  nm) allows to model the effective thermal conductivity of thin films or the relaxation of optically-induced thermal gratings. In fact, this value is very close to the ab initio calculated non-local length value using the microscopic expressions provided by the more general derivation introduced below. Moreover, the authors also show validation of the generalized hydrodynamic model using energy-based Monte Carlo simulations of the BTE with a mode-independent relaxation time [32]. An extended validation considering the same microscopic framework is presented in section 10.1. Finally, the form of the non-equilibrium (pseudoequilibrium) distribution function consistent with the hydrodynamic transport equation is obtained (eq. 46), thus allowing the derivation of consistent boundary conditions.

### **Derivation from the BTE assuming a general Collision operator and general phonon dispersion relations**

The most general derivation to date of the hydrodynamic equation from the linearized BTE is shown in [19]. This work is the core of the PhD thesis by Lluç Sendra, which will be published in the forthcoming years.

In this case, no assumptions are made to simplify the Collision operator and the full phonon dispersion relation with multiple branches is assumed. The model is based in expanding the phonon distribution on appropriate macroscopic variables, so that the unknowns are now the mode-dependent prefactors of the macroscopic quantities. This view generalizes the approach of [14], where the perturbation is set proportional to a constant temperature gradient and the mode-dependent prefactor is found through some method. The crucial difference is the choice of the quantities characterizing the macroscopic nonequilibrium state or pseudoequilibrium (see section 2.3). It is proposed that for finite Knudsen numbers the nonequilibrium perturbation depends on the heat flux  $\mathbf{q}$  and its first derivatives in time and space, considered as independent variables:

$$f_{\mathbf{k}} = f_{\mathbf{k}}^{\text{eq}} + \beta_{\mathbf{k}} \cdot \mathbf{q} + \gamma_{\mathbf{k}} \cdot \frac{\partial \mathbf{q}}{\partial t} + G_{\mathbf{k}} : \nabla \mathbf{q} \quad (70)$$

where  $\beta_{\mathbf{k}}, \gamma_{\mathbf{k}}, G_{\mathbf{k}}$  are unknown mode-dependent weight functions to be determined. By using the microscopic definitions of the heat flux and the energy, the transport equations can be obtained by projecting the BTE around the distribution 70. The equation parameters are functions of the distribution weights, which can be calculated for a general Collision operator with the use of the mode-dependent BTE [19]. Therefore, this method provides the distribution function required to describe complex non-equilibrium situations (i.e. the weights in 70). This is necessary to derive the boundary conditions consistent with the hydrodynamic heat transport equations. Moreover, the expressions for the equation



parameters in the hydrodynamic transport equations used to model experiments are obtained for general Collision operators  $C$ , thus avoiding the use of any fitting parameter. Iterative methods [14, 28] analogous to the ones introduced in section 2.1 to calculate the thermal conductivity can be used to obtain the weights and the equation coefficients without simplifying  $C$  (see full expressions in [19]). For simplicity, here we show these expressions assuming a simplified  $C$  operator under the RTA approximation, which is accurate for most of the (kinetic) materials considered in this work, in which Normal collisions are not dominant. Defining the phonon phase velocity  $v_{\mathbf{k}}^p = \omega_{\mathbf{k}}/|\mathbf{k}|$  and  $\langle x_{\mathbf{k}} \rangle = \int \hbar \omega_{\mathbf{k}} \partial_T f_{\mathbf{k}}^{\text{eq}} x_{\mathbf{k}} d\mathbf{k}/c$  as the average of quantity  $x_{\mathbf{k}}$ , the thermal conductivity expression reads

$$\kappa = \frac{1}{3} c \langle v_{\mathbf{k}}^2 \tau_{\mathbf{k}} \rangle, \quad (71)$$

so the thermal conductivity within the RTA (expression 13) is recovered. The non-local length expression reads

$$\ell^2 = \frac{1}{5} \frac{\langle \tau_{\mathbf{k}}^2 v_{\mathbf{k}}^3 / v_{\mathbf{k}}^p \rangle}{\langle v_{\mathbf{k}} / v_{\mathbf{k}}^p \rangle}, \quad (72)$$

and the heat flux relaxation time expression reads

$$\tau = \frac{\langle v_{\mathbf{k}}^2 \tau_{\mathbf{k}}^2 \rangle}{\langle v_{\mathbf{k}}^2 \tau_{\mathbf{k}} \rangle}. \quad (73)$$

Finally, coefficient 1/3 in 45, or 2 in 43, become also a material and temperature dependent property denoted as  $\alpha$ . According to the present derivation, the expression for this coefficient is

$$\alpha = 2 - \frac{5 \langle v_{\mathbf{k}}^2 \tau_{\mathbf{k}} \rangle \langle \tau_{\mathbf{k}} v_{\mathbf{k}} / v_{\mathbf{k}}^p \rangle}{3 \langle \tau_{\mathbf{k}}^2 v_{\mathbf{k}}^3 / v_{\mathbf{k}}^p \rangle} - \frac{\kappa(\tau - \langle \tau_{\mathbf{k}} \rangle)}{c \ell^2}. \quad (74)$$

In section 3.5, we show the ab initio calculated values according to the previous expressions for different materials and temperatures, which are used to experimentally validate the generalized hydrodynamic model in Chapter 4 to 9.

### 3.3 Transport equations

According to the most general derivation introduced in the previous section and detailed in [19], the generalized hydrodynamic model is based in the energy conservation and the heat flux transport equations for the heat flux  $\mathbf{q}$  and the temperature  $T$ :

$$c \frac{dT}{dt} = -\nabla \cdot \mathbf{q} + Q, \quad (75)$$

$$\tau \frac{\partial \mathbf{q}}{\partial t} + \mathbf{q} + \kappa \nabla T = \ell^2 (\nabla^2 \mathbf{q} + \alpha \nabla \nabla \cdot \mathbf{q}), \quad (76)$$

where  $c$  is the specific heat per unit volume,  $\tau$  is the heat flux relaxation time 73,  $\kappa$  is the thermal conductivity 71,  $\ell$  is the non-local length 72, and  $\alpha$  is a dimensionless coefficient 74. All these parameters are intrinsic material properties only dependent on temperature. Its microscopic expressions in terms of the phonon lifetimes and velocities are derived from the BTE and provided in the previous section. The exact values for a variety of materials of interest at different temperatures is provided in section 3.5. Note that, in contrast to the original derivation of the hydrodynamic equation where  $\alpha=2$  (see expression 43),  $\alpha$  is a material-dependent property. Finally,  $Q$  denote an external power density source. The Finite Element implementation of the equation is shown in section 11.1.

Equation 76 adds a non-local term (proportional to  $\ell^2$ ) and a memory term (proportional to  $\tau$ ) to Fourier's law. For large enough system sizes and slow enough perturbations, the diffusive description is recovered. The interplay between the two kinds of non-Fourier effects is the subject of detailed study in this thesis. Non-local effects explain the reduction of the thermal conductivity in micro and nanoscopic systems (see section 4.1). Memory effects explain deviations from the diffusive behavior in the form of thermal waves (see section 9.1). However, the latter effects only emerge in the absence of the former ones. Therefore, non-locality dominates the thermal response in most of the experiments (Chapters 4, 5, 6, 7, and 8), and only one experiment, in which non-local effects vanish, is explained through memory effects (Chapter 9).

It is important to remark a couple of crucial differences between mesoscopic hydrodynamic phenomena in heat transport, and the standard description of fluids based in the Navier-Stokes equations. On one hand, intrinsic resistive phonon collisions are never completely avoided in a realistic material. Hence, viscous or non-local effects due to system boundaries or external perturbations are confined in regions comparable to the average resistive mean free path characterized by  $\ell$ . Conversely, in fluids the momentum is strictly conserved in particle collisions so viscous effects have infinite range (note that the coefficient of viscosity in fluids is not a length). On the other hand, the advective term present in the Navier-Stokes equations is substituted by the diffusive term  $\mathbf{q}$  in 76, so mesoscopic heat transport is always analogous to laminar (non-turbulent) fluid flow. As it will be shown throughout the thesis, this leads to important differences between viscous effects in heat transport and in fluids.

### 3.4 Boundary Conditions

As explained above, the parameters appearing in the transport equations are intrinsic material properties only dependent on temperature. Size and frequency effects are captured through appropriate boundary conditions that can be implemented in realistic geometries using Finite Elements. In this section we show how the boundary conditions can be derived from microscopic arguments by requiring that, at the boundary, the net balance of a macroscopic quantity due to incoming and outgoing phonons must be equal to the macroscopic quantity prescribed by the macroscopic equation. Therefore, the transport equation is consis-

tently related to the boundary conditions through the non-equilibrium distribution function. Here we discuss the required conditions for modeling in Chapters 4 to 10. In section 11.1, we show the corresponding Finite Element implementation.

### Free Surfaces

At the nanoscale, heat conduction is the dominant energy transport mechanism in semiconductors. Radiation and convection are neglectable and, hence, the insulation condition is assumed in all the free surfaces:

$$\mathbf{q} \cdot \mathbf{n} = 0, \quad (77)$$

where  $\mathbf{n}$  is the boundary normal vector pointing towards the semiconductor domain.

The transport equation 76 is a second order differential equation, meaning that the heat flux in the boundary is prescribed by two independent boundary conditions. Hence, a condition for the heat flux tangential to the boundary  $\mathbf{q}_t (= \mathbf{q} - (\mathbf{q} \cdot \mathbf{n})\mathbf{n})$  is also required, which allows modeling of the heat flux reduction close to the surface due to momentum destruction in phonon-boundary scattering. In analogy with the flow of rarefied gases with large Knudsen number, a Maxwell's slip boundary condition [123–125] with characteristic length of order  $\ell$ , may be used for the heat flux tangential to the boundary  $\mathbf{q}_t$  [16, 69, 126]. This boundary condition can be obtained using the non-equilibrium distribution function 46 and kinetic theory [16, 119, 127], by imposing the balance equation for the flux of the heat flux in the boundary. At the microscopic level of description, this condition reads

$$\int_{\Omega} f_{\mathbf{k}} \phi \mathbf{v}_{\mathbf{k}} d\mathbf{k} = \int_{\Omega^-} f_{\mathbf{k}}^- \phi \mathbf{v}_{\mathbf{k}} d\mathbf{k} + \int_{\Omega^+} f_{\mathbf{k}}^+ \phi \mathbf{v}_{\mathbf{k}} d\mathbf{k}, \quad (78)$$

where  $\mathbf{k}$  is the phonon wave vector,  $\Omega$  denotes the whole wave vector space, and  $\Omega^-$  and  $\Omega^+$  are the hemispherical wave vector space satisfying  $\mathbf{k} \cdot \mathbf{n} < 0$  (incident phonons) and  $\mathbf{k} \cdot \mathbf{n} > 0$  (out-going phonons), respectively. The balanced magnitude in this case is the heat flux  $\phi = \hbar \omega_{\mathbf{k}} \mathbf{v}_{\mathbf{k}}$ . The microscopic balance condition 78 can be used for other macroscopic field variables to obtain different (but physically consistent) boundary conditions, as shown in the next subsection. The crucial point is to use appropriate distribution functions for the incident and out-going phonons in good consistency with the macroscopic transport equation (eq. 76 in our case). The distribution function of the incident phonons towards the interface from the semiconductor  $f^-$  follows the non-equilibrium distribution function 46, referred to as  $f$ . Moreover, the distribution function of reflected phonons  $f^+$  is composed by the specularly reflected ones following  $f$ , and the diffusely reflected phonons, which are assumed to thermalize at the boundary (i.e. are described by the local equilibrium distribution 3). Accordingly,

$$f_{\mathbf{k}}^- = f_{\mathbf{k}}, \quad (79a)$$

$$f_{\mathbf{k}}^+ = p f_{\mathbf{k}'}^- + (1 - p) f_{\mathbf{k}}^{\text{eq}}, \quad (79b)$$

where  $\mathbf{k}' = \mathbf{k} - 2(\mathbf{k} \cdot \mathbf{n})\mathbf{n}$  (specular phonons bounce), and  $p$  is the fraction of specularly reflected phonons

$$p = \frac{\sum_{\mathbf{k}} c_{\mathbf{k}} e^{-\pi \left( \frac{4\pi\eta \cos(\theta)}{\lambda_{\mathbf{k}}} \right)^2}}{\sum_{\mathbf{k}} c_{\mathbf{k}}}, \quad (80)$$

with  $\eta$  being the average height of the boundary roughness defects,  $c_{\mathbf{k}}$  and  $\lambda_{\mathbf{k}}$  the specific heat and the wave length of the phonon mode with wave vector  $\mathbf{k}$ , respectively, and  $\theta$  the angle of incidence obtained from the normal vector to the surface  $\mathbf{n}$  and the wave vector using  $\cos(\theta) = \frac{\mathbf{n} \cdot \mathbf{k}}{|\mathbf{k}|}$ . The previous expression is based in basic arguments from geometrical optics [9]. Furthermore, it is assumed that the phonons that do not collide specularly are absorbed and remitted by the boundary, which acts like a black body for  $p = 0$ . This assumption is extensively used in the literature [2, 119] and provides good agreement both with experiments (see section 4.2) and numerical simulations of the phonon dynamics (see section 10.1). Nevertheless, alternatives based in non-thermalizing diffusive scattering [128] or enhanced diffusive scattering due to the naturally grown amorphous layers [129] have also been proposed.

Introducing the distributions 79a and 79b in 78, and with the use of the heat flux transport equation 76, leads to the slip boundary condition [16]:

$$\mathbf{q}_t = C\ell \nabla \mathbf{q}_t \cdot \mathbf{n}, \quad (81)$$

where  $\mathbf{n}$  points towards the semiconductor, and  $C$  is a dimensionless constant that can be defined in terms of the specularity  $p$  (eq. 80):

$$C = \frac{1+p}{1-p}. \quad (82)$$

Accordingly, purely diffusive phonon scattering in boundaries corresponds to  $C = 1$  and purely specular phonon scattering corresponds to  $C \rightarrow \infty$ . Notice that, at high temperatures, diffusive scattering strongly dominates even in smooth surfaces like the ones used in state-of-the-art experiments. As a reference, in Silicon above 100K, values of  $C$  larger than 2 require  $\eta < 0.2$  nm.

Note that the present framework avoids the use of phenomenological models for the boundary conditions like generalized Casimir [53] or Fuch-Sondheimer [129, 130] conditions, since full consistency between the transport equation, the non equilibrium distribution function and the boundary conditions is achieved. Taking into account the strong influence of the boundary condition on relevant model outputs like the relation between the thermal conductivity and the size or the temperature [41], this robustness is crucial for predictive modeling of nanoscale thermal transport. Further analysis of the slip boundary condition 81 and its implications can be found in sections 4.1 and 4.2.

It is also worth mentioning that the slip boundary condition 81 facilitates the interpretation of size effects in heat transport due to the possibility of establishing analogies with the theory of rarefied gases and fluid mechanics at the nanoscale

[131]. In particular, possible generalizations of the slip boundary condition including higher order terms or including back-scattering effects could be used to phenomenologically interpret experimental data or pursue generalizations of the present model. For example, it is reasonable to assume that the extra term appearing in the generalized Maxwell's slip condition for non-flat surfaces [123]

$$\mathbf{q}_t = C\ell (\nabla \mathbf{q}_t \cdot \mathbf{n} + \nabla \mathbf{q}_n \cdot \mathbf{t}), \quad (83)$$

also plays a role in phonon transport. Hence, we show the Finite Element implementation of this refined boundary condition in section 11.1. However, in the experiments including curved surfaces that are considered in this thesis, this refinement is shown to be negligible (see section 4.2).

### Metal-Semiconductor Interfaces.

Electronic devices usually include metallic nanocomponents which release heat to a semiconductor substrate. Therefore, this situation has been extensively reproduced in experiments as shown in Chapters 5, 6 and 7. The heat carriers in metals are electrons, with extremely small mean free paths, so that non-local or memory effects are negligible in front of the non-Fourier effects expected in commonly used semiconductors like Silicon. Therefore, diffusive heat transport (and the corresponding simplified non-equilibrium distribution function) is assumed in the metal region.

We proceed now to show the boundary conditions connecting a semiconductor domain (hydrodynamic-like transport) with a metal domain (Fourier-like transport). Consider the interface normal vector  $\mathbf{n}$  pointing towards the semiconductor. First, continuity of the normal heat flux to the interface should be satisfied:

$$\mathbf{q} \cdot \mathbf{n} = \mathbf{q}_\Gamma \cdot \mathbf{n}, \quad (84)$$

where sub-index  $\Gamma$  denotes the metallic domains.

Microscopically, the balance equation for the energy flux at the interface (i.e.  $\phi = \hbar\omega_{\mathbf{k}}$  in eq. 78) along the normal direction implies that

$$q^x = \int_{\Omega} f_{\mathbf{k}} \hbar\omega_{\mathbf{k}} v_{\mathbf{k}}^x d\mathbf{k} = \int_{\Omega^-} f_{\mathbf{k}}^- \hbar\omega_{\mathbf{k}} v_{\mathbf{k}}^x d\mathbf{k} + \int_{\Omega^+} f_{\mathbf{k}}^+ \hbar\omega_{\mathbf{k}} v_{\mathbf{k}}^x d\mathbf{k} \quad (85)$$

where  $\mathbf{k}$  is the phonon wave vector,  $\Omega$  denotes the whole wave vector space, and  $\Omega^-$  and  $\Omega^+$  are the hemispherical wave vector space satisfying  $\mathbf{k} \cdot \mathbf{n} < 0$  and  $\mathbf{k} \cdot \mathbf{n} > 0$  respectively. The normal direction is denoted by the index  $x$ .

Similar to the previous subsection, the distribution function of the incident phonons towards the interface from the semiconductor  $f^-$  follow the non equilibrium distribution function 46, referred to as  $f$ . Moreover, the distribution function of reflected phonons  $f^+$  is composed by the specularly reflected ones following  $f$  and the diffusely reflected phonons, which are in equilibrium at some contact temperature  $T_C$ . Accordingly,

$$f_{\mathbf{k}}^- = f_{\mathbf{k}}, \quad (86a)$$

$$f_{\mathbf{k}}^+(v_{\mathbf{k}}^x) = p f^-(-v_{\mathbf{k}}^x) + (1-p) f_{\mathbf{k}}^{\text{eq}}(T_C), \quad (86b)$$

where  $p$  is the fraction of specularly reflected phonons (see expression 80) and  $T_C$  is an instrumental parameter to define the equilibrium situation of the diffusely reflected phonons in the interface going towards the semiconductor.

In the metal region, we assume Fourier heat transport. The corresponding non-equilibrium distribution function  $f_\Gamma$  reads

$$f_\Gamma = f^{\text{eq}} + \frac{3}{c^\Gamma(\mathbf{v}^\Gamma \cdot \mathbf{v}^\Gamma)} \frac{\partial f^{\text{eq}}}{\partial T} \mathbf{v}^\Gamma \cdot \mathbf{q}. \quad (87)$$

Again, we impose energy balance at the interface:

$$q^x = \int_{\Omega} f_{\mathbf{k}\Gamma} \hbar \omega_{\mathbf{k}} v_{\mathbf{k}}^{x\Gamma} d\mathbf{k} = \int_{\Omega^+} f_{\mathbf{k}\Gamma}^- \hbar \omega_{\mathbf{k}} v_{\mathbf{k}}^{x\Gamma} d\mathbf{k} + \int_{\Omega^-} f_{\mathbf{k}\Gamma}^+ \hbar \omega_{\mathbf{k}} v_{\mathbf{k}}^{x\Gamma} d\mathbf{k} \quad (88)$$

where  $f_\Gamma^-$  and  $f_\Gamma^+$  are the incident and outgoing phonon distribution functions satisfying conditions (86a) and (86b), respectively. Notice that  $T_C$  is also used to define the equilibrium distribution of the diffusely reflected phonons going towards the metal.

Current fabrication techniques generate significant roughness defects in metal-semiconductor interfaces. Hence, according to 80, for experimental modeling we assume  $p = 0$  (purely diffusive reflections). Now, by using the non-equilibrium distribution functions (46) and (87) in the balance equations (85, 88) with identifying  $T_C$  we obtain the boundary condition

$$T - T_\Gamma = (\gamma^{-1} + \gamma_\Gamma^{-1})(-\mathbf{q} \cdot \mathbf{n} + \boldsymbol{\epsilon} \cdot \mathbf{q}) + \gamma^{-1}(\beta \nabla \cdot \mathbf{q} - \nabla \mathbf{q} : \chi) \quad (89)$$

where the ab initio calculated coefficients read for  $i = x, y, z$ :

$$\gamma = \frac{\bar{v}c}{4}, \quad (90a)$$

$$\gamma_\Gamma = \frac{\bar{v}^\Gamma c^\Gamma}{4}, \quad (90b)$$

$$\epsilon_i = \int_{\Omega^-} \hbar \omega_{\mathbf{k}} v_{\mathbf{k}}^x \frac{3}{c_{\mathbf{k}}(\mathbf{v}_{\mathbf{k}} \cdot \mathbf{v}_{\mathbf{k}})} \frac{\partial f_{\mathbf{k}}^{\text{eq}}}{\partial T} v_{\mathbf{k}}^i d\mathbf{k} = \frac{1}{2} \delta_{ix}, \quad (90c)$$

$$\beta = \int_{\Omega^-} \hbar \omega_{\mathbf{k}} v_{\mathbf{k}}^x \frac{\tau_{\mathbf{k}}}{c_{\mathbf{k}}} \frac{\partial f_{\mathbf{k}}^{\text{eq}}}{\partial T} d\mathbf{k}, \quad (90d)$$

$$\chi_{ij} = \int_{\Omega^-} \hbar \omega_{\mathbf{k}} v_{\mathbf{k}}^x \frac{3\tau_{\mathbf{k}}}{c_{\mathbf{k}}(\mathbf{v}_{\mathbf{k}} \cdot \mathbf{v}_{\mathbf{k}})} \frac{\partial f_{\mathbf{k}}^{\text{eq}}}{\partial T} v_{\mathbf{k}}^i v_{\mathbf{k}}^j d\mathbf{k}. \quad (90e)$$

By introducing these coefficients in (89) we obtain the temperature-jump boundary condition

$$T - T_\Gamma = -\frac{1}{2}(\gamma^{-1} + \gamma_\Gamma^{-1})\mathbf{q} \cdot \mathbf{n} + \gamma^{-1}(\beta \nabla \cdot \mathbf{q} - \nabla \mathbf{q} : \chi). \quad (91)$$

The parameter values (90) for different materials and temperatures can be found in section 3.5. Let us define the coefficient  $R_{\text{min}} \equiv (\gamma^{-1} + \gamma_\Gamma^{-1})/2$  denoting the thermal boundary resistance for perfect contact (i.e. total surface contact

in the interface) assuming diffusive reflections. Therefore, it can be considered as a lower bound for the thermal resistance. This estimation of the interfacial resistance is equivalent to the Diffusive Mismatch Model (DMM) [132]. To obtain an adequate boundary condition for a realistic non-perfect contact area, we adjust the coefficient multiplying the normal heat flux, which we denote by  $R$ :

$$T - T_{\Gamma} = -R\mathbf{q} \cdot \mathbf{n} + \gamma^{-1}(\beta\nabla \cdot \mathbf{q} - \nabla\mathbf{q} : \chi). \quad (92)$$

The  $R$  value is typically 2 or 3 times larger than the lower bound  $R_{\min}$  at each temperature (see section 3.5). The actual contact area at the interface is usually unknown. Hence, it is not possible to quantitatively validate such correction to account for a non-perfect contact area. However, this correction is an intrinsic property for each specific sample fabrication conditions i.e. it is temperature-, size-, and frequency-independent. Therefore, as it will be shown in this thesis, it is always possible to characterize  $R/R_{\min}$  at low frequencies or high sizes in experiments, where non-Fourier effects are negligible. The resulting values used for experimental modeling are in good agreement with modern reviews characterizing metal-semiconductor interface properties [133] (see section 3.5).

Equation 92 is the usual Kapitza interface condition along with two non-local terms. As discussed in Chapter 4, the influence of these extra terms is only relevant at low temperatures or for very small interface sizes. Finally, we note that a second boundary condition for the heat flux in the semiconductor domain is required (non-Fourier heat conduction). Hence, the Slip boundary condition 81 is also imposed to determine the tangential component of the heat flux in the semiconductor side of the interface.

At this point it is important to note that, to simplify the calculations, the boundary conditions 81 and 91 are derived using the non-equilibrium distribution function 46 obtained in [16], which is not the most general derivation of the hydrodynamic heat transport model (see discussion in 3.2). Refinement of the microscopic expressions for the parameters 90 would be obtained by using the solution of the BTE 70 for general collision operators and dispersion relations instead of 46. However, such refinement is expected to be negligible here due to the dominance of the Kapitza term in condition 91 in all the considered experiments.

For illustration, in Figure 1 we show the boundary conditions and transport equations required to model a metallic transducer built on top a semiconductor substrate. These are the exact situation required to model FDTR experiments in Chapter 6. The same interface conditions are used in Chapters 5 and 7.

### Auxiliary conditions

In order to compare with experiments or numerical simulations (Chapter 10) some auxiliary boundary conditions are required, like periodic boundary conditions for the heat flux between two boundaries with imposing a temperature difference, or isotherm boundary conditions. The corresponding numerical implementation can also be found in section 11.1.

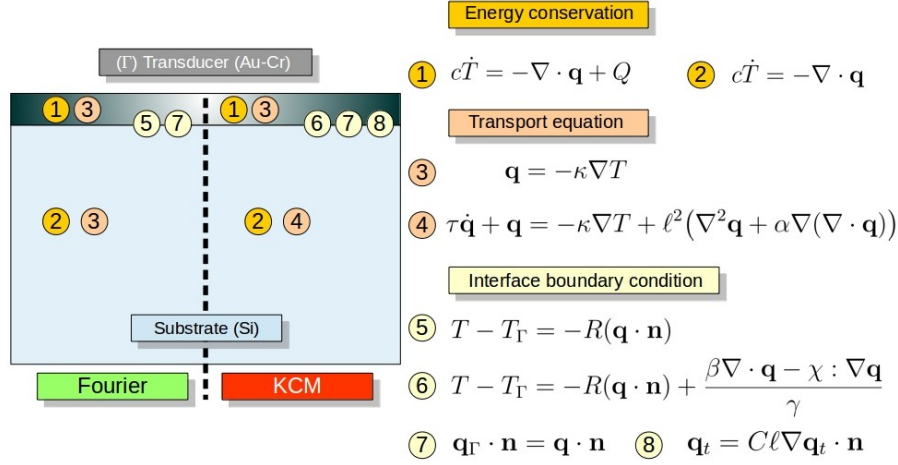


**Figure 1:** *Reproduced from [134].* Schematic illustration of transport equations and interface boundary conditions for a semiconductor substrate with a metallic transducer on top. The interface normal vector  $\mathbf{n}$  points toward the semiconductor. The substrate heat flux tangential component is denoted by  $\mathbf{q}_t$ , and subindex  $\Gamma$  refers to the transducer domain in the boundary conditions.

### 3.5 Parameters

In this section we show the parameter values for the transport equations and boundary conditions for different temperatures and materials (Ge, Si, Bi<sub>2</sub>Te<sub>3</sub>) according to the microscopic expressions shown in 3.2 and 3.4, respectively. We also show the required parameters to model the metallic transducers in experiments (Au/Cr, Au, Ni).

#### Transport Equations

On one hand, the thermal conductivity and the specific heat used to model experiments are the bulk values, which are shown in Figure 2 for Ge and Si at different temperatures. Note that in Chapter 5 we consider highly doped Silicon samples, so the used thermal conductivity in this specific case is slightly smaller as characterized from experiments. On the other hand, in Figure 3 we show the required non-Fourier parameters for the same materials as obtained from ab initio calculations.

The phenomenological expression 68 and the more refined expression 72 provide very similar values for the non-local length [19]. In Figure 3 we also show the non-local length values used for experimental modeling in Si and Ge in Chapters 4 to 7. It can be seen that the ab initio calculations are consistent with the parameter values used, thus validating the generalized hydrodynamic model presented in section 3.2. In the same experiments, memory effects are negligible and, hence, the heat flux relaxation time values can not be simultaneously validated. Finally, to model experiments in the Bi<sub>2</sub>Te<sub>3</sub> nanostructures at room temperature (Chapter 8), the non-local length and the thermal conductivity values used are 55 nm and 2.2 W/(m·K), respectively.



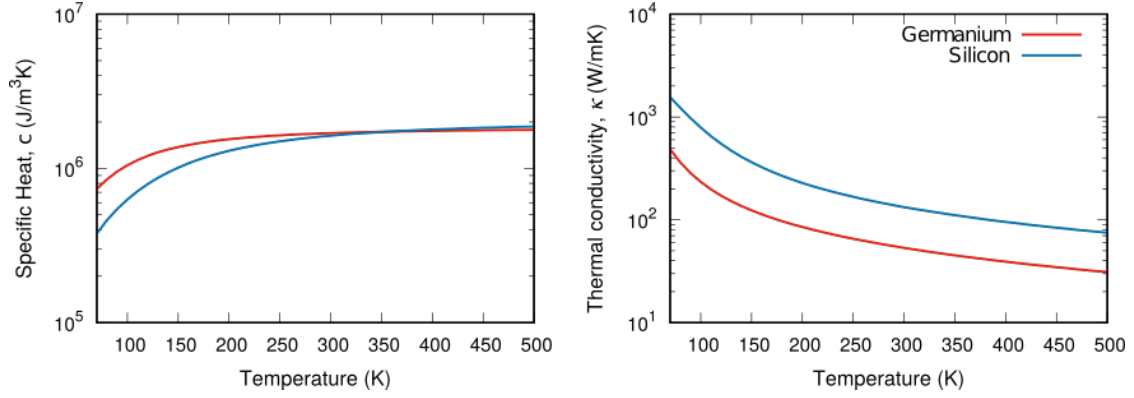


**Figure 2:** Specific heat  $c$  and thermal conductivity  $\kappa$  for Germanium (red) and Silicon (blue) at different temperatures.

The phenomenological expression 69 can not be used to estimate the heat flux relaxation time, so the refined expression 73 is required. Remarkably, the heat flux relaxation time  $\tau$  is one order of magnitude larger than the usual relaxation time  $\langle\tau_k\rangle$  obtained using the specific heat as the averaging weight over phonon modes. Therefore, according to the generalized hydrodynamic model, memory effects emerge at smaller excitation frequencies than expected in previous work [50]. This is experimentally demonstrated for germanium in Chapter 9, where the heat flux relaxation time values fitted to experimental data are compared with the ab initio calculations at different temperatures (see Figure 47). This comparison is not displayed here because the model used in 9 is a reduced version of the generalized hydrodynamic model with only including memory effects.

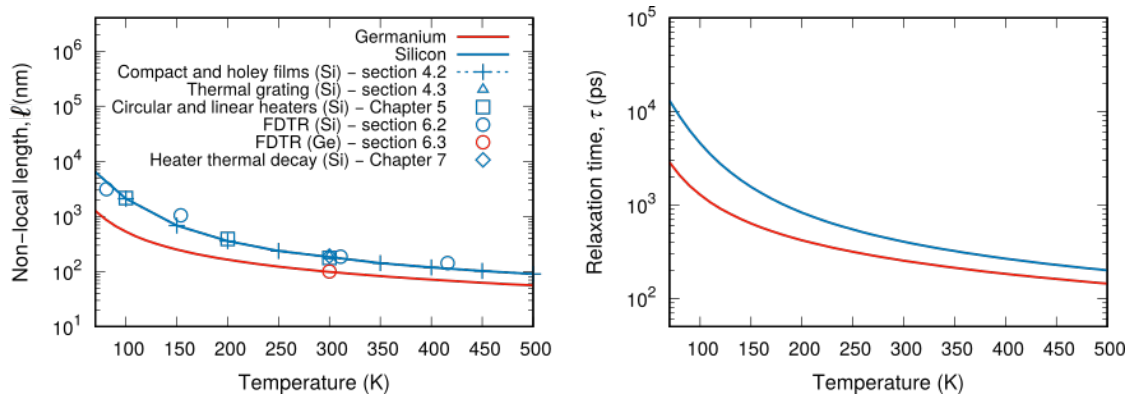


**Figure 3:** Non-local length  $\ell$  and heat flux relaxation time  $\tau$  for Germanium (red) and Silicon (blue) at different temperatures. The non-local length values used to model experiments are also shown.

It is also worth to mention the role of doping in the non-Fourier parameter values. All the calculations were done assuming natural doping abundances, as required for experiments, except in Chapter 5. In this specific experiment, the samples are doped, and the thermal conductivity decreases as characterized

**Table 1:** Thermal properties of metallic transducers used for experimental modeling.

	Gold (5)	Nickel (7)	Gold/Chromium (6)
Specific Heat $c$ [ $\text{Jm}^{-3}\text{K}^{-1}$ ]	-	$4 \cdot 10^6$	$2.5 \cdot 10^6$
Conductivity $\kappa$ [ $\text{Wm}^{-1}\text{K}^{-1}$ ]	310	91	110

from experiments. Conversely, the non-local length is not strongly modified due to doping since the phonon modes that are more influenced by impurities have small contribution to the non-local length (expression 72). Hence, the non-local length value for natural samples displayed in Fig. 3 is also used for the doped samples in Chapter 5.

As discussed in section 3.2, the original Guyer-Krumhansl derivation [6] predicted  $\alpha = 2$ , and more recent derivations beyond the collective regime with some simplifying assumptions like a mode-independent relaxation time [16] predicted  $\alpha = 1/3$ . In contrast, the most recent general derivation [19] treats  $\alpha$  as an intrinsic material property, which at room temperature is close to 1. For experimental modeling, a value of  $\alpha = 1/3$  is assumed. The only exception is the study of the thermal grating relaxation in section 4.3, where this parameter has a dominant effect and the refined value  $\alpha=1$  is used as obtained from expression 74. In other experiments, refinement of this parameter from  $1/3$  to 1 would not cause significant effects. It does not appear in the description of stationary experiments in section 4.2 and Chapters 5, and 8 (where  $\nabla \nabla \cdot \mathbf{q} = 0$ ), and its influence in transient experiments is usually weak. In particular, the heater relaxation experiments in Chapter 7 are dominated by shear viscosity and the role of volume viscosity and parameter  $\alpha$  is very minor. In the FDTR experiment (Chapter 6), volume viscosity plays a significant role, and the use of  $\alpha = 1$  would slightly enhance the differences between Fourier and the hydrodynamic model, and would imply a slight modification of the experimentally characterized TBR. Nevertheless, the phenomenology and interpretation provided in Chapter 6 is not altered by changing this parameter value from  $1/3$  to 1.

Moreover, in some experiments the introduction of metallic transducers is required to electrically or optically perturb the system. Heat conduction is dominated by electrons in the transducers (diffusive transport). The material properties used in experiments for these transducers is shown in Table 1.

### Boundary conditions

The coefficients of the generalized temperature jump boundary condition 92 can also be calculated ab initio. In Table 2 we show the required values for Silicon at different temperatures studied in experiments. Tensor  $\chi$  is diagonal and  $\chi_{yy} = \chi_{zz}$ , with  $x$  denoting the interfacial normal direction pointing toward the substrate. We also indicate the upper bound of the Si contribution to the interfacial conductance  $\gamma$  assuming a perfect contact with diffusive reflections. As discussed in 3.4 and in good agreement with the DMM [132], considering the corresponding upper bound of the transducer contribution ( $\gamma_{\Gamma}$  in 91), we esti-

**Table 2:** Silicon parameter values of the temperature jump boundary condition 92 according to expressions 90 used for experimental modelization in Chapter 4.

	415 K	300 K	150 K	80 K
$\gamma$ [MW m <sup>-2</sup> K <sup>-1</sup> ]	1145	1068	732	359
$\beta$ [nm]	-14	-21	-87	-745
$\chi_{xx}$ [nm]	-21	-31	-129	-1066
$\chi_{yy}$ [nm]	-11	-16	-66	-586

mate a lower bound for the thermal boundary resistance  $R_{\min} = (\gamma^{-1} + \gamma_T^{-1})/2$ . In this thesis, we consider three experiments including metal-silicon interfaces and we characterize the intrinsic TBR values  $R$  in each case. The actual  $R$  values are larger than  $R_{\min}$  due to the interface defects:

- Section 5 (Au-ox-Si): The TBR is extremely large ( $R=20 \cdot 10^{-9} \text{Km}^2/\text{W}$ ) due to the presence of a thick oxide layer of 20 nm, which precludes comparison with  $R_{\min}$ .
- Section 7 (Ni-Si):  $R=2.25 \cdot 10^{-9} \text{Km}^2/\text{W}$  and  $R/R_{\min}=3.11$ .
- Section 6 (Cr-Si):  $R=1.77 \cdot 10^{-9}, 1.87 \cdot 10^{-9}, 2.6 \cdot 10^{-9}, 5.15 \cdot 10^{-9}$  [Km<sup>2</sup>/W], at  $T=415, 300, 150, 80$  [K], respectively. The correcting factor  $R/R_{\min}=2.71$  is temperature-independent since it only captures geometrical defects.

The reported values are in good agreement with recent reviews [133] characterizing a variety of metal-semiconductor interfaces fabricated using similar techniques than the ones considered here.

The slip coefficient used in all the experiments is  $C = 1$  corresponding to fully diffusive reflections. This corresponds to the expected behavior at not extremely low temperatures taking into account the typical defects in surfaces and interfaces obtained by current fabrication methods (see expression 80). In section 4.2, we also show the influence of modifying the  $C$  coefficient on the thermal conductivity of thin films.

### 3.6 Thermoelastic coupling

One of the key advantages of the present model is its easy coupling with other physical phenomena. In this section we detail the thermoelastic coupling, which is required to compare with experiments in Chapter 7.

The elastic evolution is governed by Newton's mechanics:

$$\rho \frac{\partial^2 \mathbf{u}}{\partial t^2} = \nabla \cdot \sigma, \quad (93)$$

where  $\sigma$  is the stress tensor,  $\mathbf{u}$  the displacement vector and  $\rho$  the mass density. To obtain the expression for  $\sigma$  including thermal expansion we follow [135], and we

consider a second order expansion of the Helmholtz free energy density with a linear term on temperature, which reads

$$F(T) = F_0(T) - K\alpha_M(T - T_0)\nabla \cdot \mathbf{u} + \mu \left( \frac{1}{2} \left( \frac{\partial u_i}{\partial x_k} + \frac{\partial u_k}{\partial x_i} \right) - \frac{1}{3} \delta_{ik} \nabla \cdot \mathbf{u} \right)^2 + \frac{1}{2} K (\nabla \cdot \mathbf{u})^2, \quad (94)$$

being  $\alpha_M$  the linear coefficient of thermal expansion, and

$$K = Y_0/(3 - 6\nu) = \lambda + \frac{2}{3}\mu \quad (95)$$

the modulus of compression, which can be expressed in terms of the Lamé coefficients  $\lambda, \mu$  or the Poisson ratio  $\nu$  and the Young's modulus  $Y_0$ . The sum over all the  $i, k$  components is implicit in the third term of the right-hand-side in 94.

Now, assuming local equilibrium, we can use the thermodynamic relation between the free energy density and the Stress Tensor [135] to obtain

$$\sigma_{ik} = -K\alpha_M(T - T_0)\delta_{ik} + K\delta_{ik}\nabla \cdot \mathbf{u} + \mu \left( \frac{\partial u_i}{\partial x_k} + \frac{\partial u_k}{\partial x_i} - \frac{2}{3}\delta_{ik}\nabla \cdot \mathbf{u} \right). \quad (96)$$

The previous Stress Tensor can be used to model the elastic evolution of Niquel nanoheaters in Chapter 7. However, we use an anisotropic version of the Stress Tensor for the Silicon substrate to account for the structural defects produced during the fabrication of the nanoheaters [136]. All details and the mechanical parameter values can be found in Chapter 7.

In order to obtain the mechanical coupling in the thermal equations we consider the amount of heat absorbed per unit time in unit volume

$$-\nabla \cdot \mathbf{q} = T \frac{\partial s}{\partial t} \quad (97)$$

where  $s$  is the entropy per unit volume. Now we use another thermodynamic relation

$$s(T) = -\frac{\partial F(T)}{\partial T} = s_0(T) + K\alpha_M\nabla \cdot \mathbf{u}. \quad (98)$$

We note that

$$\frac{\partial s_0}{\partial t} = \frac{\partial s_0}{\partial T} \frac{\partial T}{\partial t}, \quad (99)$$

where  $\partial s_0/\partial T$  is equivalent to  $c/T$  provided  $\nabla \cdot \mathbf{u} \simeq 0$  (i.e. at constant volume). Using 98 and 99 in 97 we obtain the energy conservation equation 75 including the thermal coupling

$$c \frac{dT}{dt} = -\nabla \cdot \mathbf{q} - \alpha_M K T \frac{\partial}{\partial t} \nabla \cdot \mathbf{u}. \quad (100)$$

In the original derivation of the phonon hydrodynamic model [6] an analogous coupling between the elastic and thermal fields is obtained, in which a phonon internal pressure  $p_t$  is defined. With the notation introduced here,

$$p_t = \alpha_M K T. \quad (101)$$

Moreover, in [6], a mechanical coupling is also obtained for the heat transport equation. Specifically, it is shown that the hydrodynamic transport equation 76 includes an extra term and reads:

$$\tau \frac{\partial \mathbf{q}}{\partial t} + \mathbf{q} = -\kappa \nabla T + \ell^2 (\nabla^2 q + \alpha \nabla \nabla \cdot \mathbf{q}) + \frac{3\kappa}{c} p_t \nabla \nabla \cdot \mathbf{u}. \quad (102)$$

This correction (i.e. the last term in the previous equation) is derived by taking into account the local dependence of the phonon dispersion relations on the local compression/dilatation of the elastic field [137]. The basic idea is that the energy of a phonon with a given frequency may change between contiguous regions with different strain due to the local modification of the dispersion relations, thus leading to an energy flux. In the experiments in Chapter 7 the uncorrected version of the heat transport equation 76 is used, since the influence of the extra term in 102 is found to be negligible in the specific situations considered.

### 3.7 Thermoelectric coupling

In many semiconductor experiments, including the role of electrons is crucial to proper modelization of metallic transducers (Chapter 5), or the thermoelectric phenomena (Chapter 8). Hydrodynamic transport effects for electrons [138, 139] are neglected in this thesis, because we focus in the length scales where non-local effects and memory effects emerge for phonons. Due to the mean free path of phonons being larger than the electrons mean free path, we can approximate electron transport using the classical description in all the considered situations. Moreover, we only explicitly include electron transport in steady-state experiments, so no transient effects are discussed here.

The stationary conservation equation for the electrical current  $\mathbf{J}$  in the absence of volumetric charge sources reads:

$$\nabla \cdot \mathbf{J} = 0. \quad (103)$$

Scattering between free electrons and the body of the conductor (usually atomic ions) randomize its direction of motion. Thus, the electrical energy required to increase the kinetic energy of electrons and generate a current density  $\mathbf{J}$  is gradually and irreversibly transferred to thermal energy. This is known as Joule's heating. At the mesoscopic level of description, a power density

$$Q = \rho \mathbf{J} \cdot \mathbf{J}, \quad (104)$$

is introduced in the energy conservation equation 75, where  $\rho$  is the electrical resistivity. In the thermoreflectance map experiments discussed in Chapter 5, an electrical current is imposed through the metallic nanostructured transducers, thus injecting energy by Joule's heating 104 that is finally evacuated towards the semiconductor substrate.

Moreover, the reversible conversion of temperature differences to electric voltage and viceversa (Seebeck-Peltier effect) has upmost importance in semiconductor physics due to its wide range of applications [140]. This effect is caused by

the coupling between equilibrium phonons and electrons, which results in an spontaneous tendency of the charge carriers to diffuse from hot to cold (Seebeck effect). This phenomena is characterized by the Seebeck coefficient  $S$  [141, 142]. Accordingly, the thermal gradients are coupled with an electric field  $\mathbf{E}$  such that,

$$\rho\mathbf{J} = \mathbf{E} - S\nabla T. \quad (105)$$

The reverse phenomenon of generating/removing heat due to the presence of an electric field is known as Peltier effect, and it is characterized by the Peltier coefficient  $\Pi$  [141]. Due to the microscopic reversibility of the electron and phonon motions (i.e. the time-reversibility of the trajectories of electrons and phonons), the phenomenological laws for the Seebeck and Peltier effects are symmetric and, hence, the associated coefficients are simply related through the well-known Onsager relation  $\Pi = TS$ . Consequently, characterization of one of these coefficients fully characterizes the thermoelectric performance of a device. It is worth mentioning that the momentum transferred due to collisions between non-equilibrium phonons and electrons can enhance the Seebeck effect due to the existence of a heat flux flowing from hot to cold. This is known as the phonon drag contribution to the Seebeck coefficient. Naturally, an equivalent effect can enhance the Peltier effect due to the phonons dragged along by the electric current. Here we will not consider the phonon drag contribution, since we focus on room temperature experiments where this effect is assumed to be negligible.

In Chapter 8, we study the thermoelectric response of a system of interconnected Bi<sub>2</sub>Te<sub>3</sub> nanowire networks at room temperature. In contrast to the other semiconductors studied in this thesis, Bismuth Telluride is not a good electrical insulator, so that it is a good candidate to study thermoelectric energy conversion phenomena. Importantly, a significant contribution of free electrons to the thermal conductivity must be accounted for. We use the empirical Wiedemann-Franz law, which provides a relation between the electronic contribution to the thermal conductivity  $\kappa_e$  and the electrical conductivity  $\rho^{-1}$ :

$$\rho\kappa_e = LT, \quad (106)$$

where  $L = 2.44 \cdot 10^{-8} \text{W}\Omega\text{K}^{-2}$  is known as the Lorentz number.

Improving the thermoelectric efficiency of a device for applications is based in optimizing the electrical/thermal energy conversion along with reducing the capability of the system to homogenize the temperature field due to heat conduction. Typical applications are aimed to generating electrical energy from waste heat or cooling using electric fields. The thermoelectric efficiency is compactly quantified by the  $zT$  figure of merit:

$$zT = \frac{S^2 T}{\kappa\rho}, \quad (107)$$

where  $\kappa$  is the sum of the phononic and electronic contributions to the thermal conductivity. Note that smart nanostructuring of materials like Bi<sub>2</sub>Te<sub>3</sub> to sizes comparable to the phonon MFP is a way to reduce the phononic contribution to

the thermal conductivity with maintaining its electrical conductivity, and hence it is a promising strategy to increase the  $zT$  [143, 144]. This approach is discussed using experiments in Chapter 8.

## 4 Thin films and Thermal Gratings

In this Chapter we show that the hydrodynamic heat transport model presented in sections 3.3, 3.4, 3.5 reproduces the thermal behavior of Silicon at the nanoscale in the simplest cases of study through the emergence of non-local effects. Specifically, we model the stationary effective conductivity of compact and holey films within a large range of temperatures, and the transient relaxation of thermal gratings at room temperature. We use these experiments to quantitatively determine the applicability of the model, and we compare it with other approaches like the ballistic suppression of phonons.

### 4.1 Non-local effects

It is well known that extracting thermal energy from semiconductor samples with reduced characteristic sizes is more difficult than from bulk materials [2]. This observation is generally attributed to the role of phonon-boundary scattering, and it is usually interpreted as a ballistic effect due to the apparent mean free paths of some phonon modes being larger than the system sizes. In previous works, an effective form of Fourier's law with a reduced thermal conductivity [74, 75, 89, 90] or a size-dependent thermal boundary resistance [57, 91, 92] has been used to model experimental observations of size effects. These effective interfacial resistances or conductivities are interpreted in terms of the spectral contribution of the phonon modes. As discussed in section 2.5, it is usually assumed that the phonon modes with mean free paths larger than the system characteristic sizes do not contribute to the thermal conductivity. This interpretation has been shown to capture the effective thermal conductivity in alloys like SiGe [90], and relies on the apparent multiscale nature of the phonon mean free path spectrum according to the RTA collision operator neglecting off-diagonal terms (see section 2.1).

Here we show that the generalized hydrodynamic framework provides an alternative interpretation of experimental data through the emergence of nonlocal effects with a single characteristic length scale  $\ell$ , which is much smaller than the longest MFP ( $\ell \simeq 190$  nm in Si at 300 K). This length scale informs about the range of the heat flux correlations in space, thus orienting about the system sizes where boundary effects are noticeable. As discussed in section 3.2, the solutions of the BTE and the transport equations are obtained in terms of the lower-order moments of the non-equilibrium phonon distribution function. Therefore, the resulting transport equation has only one characteristic length scale, and the length scales associated to higher orders do not appear in the description. The underlying assumption is that the evolution of the higher moments is instantaneous as compared to the evolution of the lower-order moments (like the heat flux) in experiments (see section 2.3). This interpretation justifies why a single length scale allows describing the collective evolution of the whole phonon distribution. This length scale is calculated using the microscopic information of the phonon modes, and even the RTA can be used to simplify the expression for this



parameter [19]. The crucial idea is that the only length scale that manifests in experiments is the scale of the heat flux evolution (i.e. the non-local length), and the phonon modes do not independently evolve with its own mean free path in complex non-equilibrium situations. In other words, direct modeling of the BTE within the RTA (i.e. modeling the independent dynamics of each phonon mode with distinct mean free paths) is inadequate because these multiple length scales are not manifested in the description of the thermodynamic variables (i.e. the experimental observables). Conversely, since the number of length scales in the transport equation is already determined by the slowly evolving pseudo-equilibrium function  $\bar{f}_0$  in the hydrodynamic model, the integrated coefficients in the corresponding BTE projections like the thermal conductivity or the non-local length can be quantified assuming the simplified RTA collision operator  $\hat{C}$  for materials like Si.

The distinct characteristic of the hydrodynamic description of size effects is thus the use of a single length to model kinetic materials like Silicon. Furthermore, the full Poiseuille heat flux profile predicted in the collective regime in other materials like graphene (see section 3.1) can be also mesoscopically described by the generalized hydrodynamic model. Nonlocal effects are mesoscopically modeled through the Laplacian term in Eq.76, and emerge in regions where the heat flux profile is not homogeneous. This occurs in multiple relevant situations like transiently heated samples, in nanostructured materials or, more generally, close to the system boundaries. In those regions, the Laplacian of the heat flux is not null, which leads to a reduction of the local heat flux with respect to the bulk situation for a given temperature gradient (i.e. lower local effective thermal conductivities). This phenomena is analogous to viscosity in fluids as described by the Navier-Stokes equation. However, in contrast to fluids, the characteristic size of this viscous effect is the non-local length, and for large enough system sizes the diffusive (Fourier) description is naturally recovered. Moreover, other new phenomena like heat vorticity is predicted.

## 4.2 Effective thermal conductivity of compact and holey Silicon films

Multiple experiments have shown that the energy flowing in bulk Silicon for a given temperature gradient is significantly reduced if the same temperature gradient is imposed in samples with nanoscale or microscale characteristic sizes [73, 145–149]. Here we show that these experiments can be modeled using the hydrodynamic heat transport equations within a certain applicability range. Specifically, we solve the energy conservation equation 75 and the hydrodynamic transport equation 76 to obtain the heat flux and temperature profiles in thin and holey Silicon films [122]. Periodic boundary conditions are imposed in the ends of the sample unit cell with fixing a temperature difference  $\Delta T$ . Moreover, insulation 77 and slip heat flux 81 conditions are imposed in all the free surfaces. The equation parameter values can be found in section 3.5 and the details of the Finite Element implementation of the equations and boundary conditions can be

found in section 11.1.

In contrast to the description based in Fourier's law, the hydrodynamic model predicts the emergence of the so-called boundary layers, which are regions of size  $2\ell$  surrounding the system boundaries where the heat flux is reduced (see Figures 4 and 6c). In these regions the heat flux profile resembles the Poiseuille velocity profile observed in fluids due to viscous effects. However, the heat flux is non-null in the boundary according to the slip boundary condition 81. In materials where normal-collisions dominate, such as graphene, the analogy with fluids is clear because the phonon momentum is only destroyed in the boundaries and a common drift velocity appears due to the conservation of momentum under the intrinsic (normal) collisions. In kinetic materials like Silicon, where normal collisions do not dominate, the emergence of a boundary layer is also due to the conservation of momentum, but this time is due to the relative absence of Resistive intrinsic collisions. The phonons generated in the boundary layer have an average mean free path smaller than the phonons generated in the bulk of the sample, and hence its ability to contribute to the longitudinal heat flux is reduced. Therefore, a heat flux inhomogeneous profile is also observed even though there is not a preserved magnitude (except the energy) in the collision mechanisms. Most importantly, at the mesoscopic level of description both situations are described by the Laplacian term in the hydrodynamic heat equation 76. We note that this phenomenology is also predicted from numerical solutions of the BTE in similar non-equilibrium conditions [44].

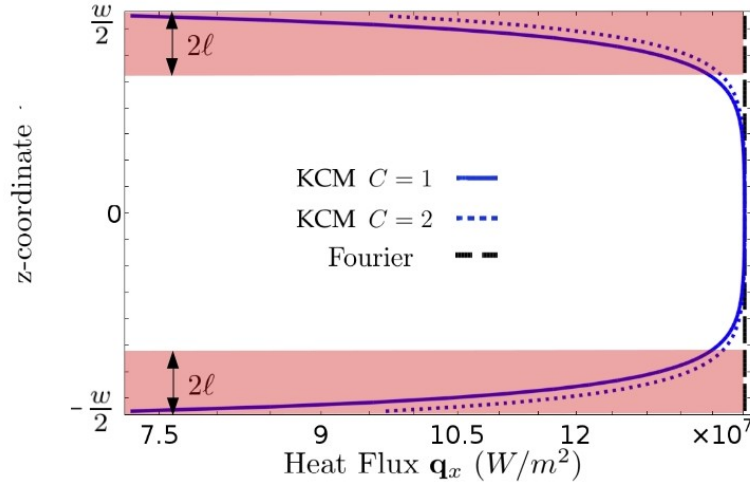


**Figure 4:** *Reproduced from [122].* Heat flux profile for a Silicon thin film of width  $w = 3 \mu\text{m}$  at  $T = 300 \text{ K}$  predicted by Fourier (dashed line) and KCM (solid line). The reduction of  $\mathbf{q}$  at the boundaries in the KCM has a nonlocal effect of characteristic size  $2\ell$ , which is the cause of the effective thermal conductivity reduction. We refer to this region (indicated in red) as boundary layer.

As discussed in section 3.4, the characteristic size of the boundary defects as compared to the phonon wave-lengths determine the fraction of specular phonon-boundary reflections  $p$  (see expression 80), which is introduced in the

slip boundary condition 81 through the specular coefficient  $C = \frac{1+p}{1-p}$ . In smooth enough surfaces the fraction  $p$  is increased, which imply an increase of coefficient  $C$  that results in a larger heat flow in the boundaries as illustrated in Figure 4. Note that the size  $2\ell$  of the boundary layers is determined by the intrinsic collisions and do not depend on boundary properties like the  $C$  value.

To validate that the heat flux reduction in the boundary layers quantitatively predicts the influence of system boundaries observed in experiments, we define the global effective thermal conductivity of the sample

$$\kappa_{\text{ef}} = \frac{\int_{\Gamma} |q| d\Gamma}{S \nabla T}, \quad (108)$$

where  $\Gamma$  is a cross section transversal to the temperature gradient and  $S$  its area. In Figure 5 we compare model predictions with experimental data in thin films with different thickness  $w$  [73, 145–147]. Specifically, in 5a we show comparison of  $\kappa_{\text{ef}}$  at room temperature by modifying  $w$ . In 5b we show comparison at different temperatures for three films with different thickness  $w$ . For high temperatures, diffusive boundary reflections ( $C = 1$ ) can be assumed so as to predict the effective thermal conductivity of the samples considered. However, the authors of the experimental works [73, 145–147] estimate a small average roughness-defect height  $\eta$  in the samples, which has a significant effect on  $\kappa_{\text{ef}}$  at lower temperatures. Hence, consistent with Refs. [73, 145–147], here we assume  $\eta = 0.3$  nm to calculate the specular parameter  $C$ . Using Eqs. 82 and 80 we obtain a constant specular parameter  $C = 1.5$  above 100K, which improves the prediction at low temperatures.

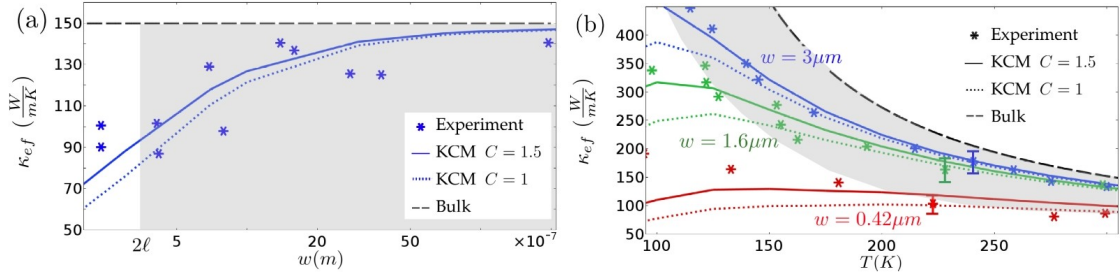


**Figure 5:** Reproduced from [122]. Thin films experimental and predicted thermal conductivities versus: (a) width at room temperature, and (b) temperature for different widths. In both panels the KCM applicability region ( $w > 2\ell$ ) is indicated in gray.

A distinct advantage of the mesoscopic hydrodynamic model is that it can be used in arbitrary complex geometries using the same Finite Element implementation (see section 11.1). In Figure 6b, we show that the model is also able to predict the experimental conductivity reduction in holey films with similar characteristic sizes [149] (the exact sizes of the considered holey films are indicated in Figure 6a). Note that purely diffusive phonon-boundary scattering ( $p = 0$ ;  $C = 1$ ) is assumed for holey films because the reported surface defects have sizes much larger than 0.3 nm in these samples [149]. Moreover, in good

agreement with experimental data, the model predictions are not significantly modified by considering staggered patterns for the hole positions. Finally, we note that the generalized Slip Boundary condition 83 introduced in section 3.4 includes an extra term which is non-null in curved surfaces, as the ones present in the holey films. However, no significant effect in the predicted  $\kappa_{\text{ef}}$  has been observed for the present samples.

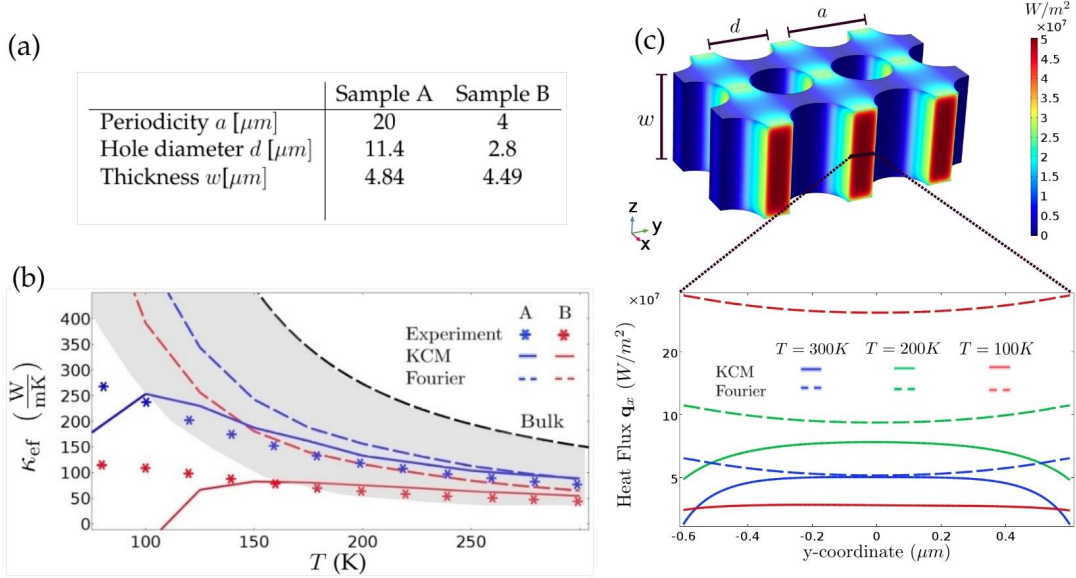


**Figure 6:** *Reproduced from [122].* (a) Geometric properties of the two different holey Silicon membranes considered. (b) The experimental thermal conductivities vs temperature are compared with the KCM and Fourier predictions. The KCM applicability region is indicated in gray. (c) Comparison between the Fourier and KCM heat flux profiles along the line intersecting the centre of two contiguous pores in the holey film B at different temperatures.

We note that the model predictions agree with experimental data in the cases where the smallest system length scale  $L$  is larger than  $2\ell$ . These regions of applicability are denoted in gray color in Figures 5 and 6. This corresponds to situations where the boundary layers do not completely intersect with each other, i.e. the non-local effects from disconnected boundaries are not overlapped. Therefore, the breakdown of the model with intrinsic equation parameters occurs for small enough sample sizes at a given temperature, or at low temperatures in a given sample due to the increase in the non-local length value (see section 3.5). The failure of the model is attributed to the use of a single length scale  $\ell$  to characterize the non-local effects, which is not adequate in extreme ballistic conditions because of the requirement of higher order moments in the transport equations (along with its characteristic length scales). More discussion about the validity limits of the model can be found below.

Furthermore, it is worth to remark that these experiments indicate the inadequacy of the ballistic phonon suppression picture in Silicon. Note that the experimental thermal conductivity of a Silicon thin film at room temperature with

thickness larger than  $1 \mu\text{m}$  is very close to the bulk thermal conductivity [73, 145–147], which is in good agreement with the hydrodynamic model. However, the contribution to the thermal conductivity of the phonon modes with mean free path larger than  $1 \mu\text{m}$  is  $\sim 30\%$  [3, 148].

### 4.3 Relaxation of optically induced thermal gratings in Silicon films

Other paradigmatic experiment where non-Fourier behavior has been observed is the transient relaxation of optically induced thermal gratings (i.e. sinusoidal temperature profiles with period  $L$ ) in semiconductor substrates [74, 90, 150]. We focus on the experiments reported in [74], where a 400nm-thick Silicon film have been considered at room temperature. Due to the laser extinction length being much larger than the film thickness, the initial temperature profile is homogeneous in the cross-plane direction, and the thermal transport is restricted to 1D along the thermal gradient direction.

By combining the energy conservation equation 75 and Fourier's law 1, it is easy to show that the relaxation of the sinusoidal temperature profile (its homogenization) has a characteristic decay rate

$$\gamma = \frac{\kappa \xi^2}{c}, \quad (109)$$

where  $\xi = 2\pi/L$ . Hence, Fourier theory predicts a quadratic raise of the decay rate as a function of  $L^{-1}$ . As shown in Figure 7, the experimental functional dependence of  $\gamma$  on  $L$  is not quadratic, so Fourier theory breaks down. We note that, as shown in the previous section, a 400nm-thick Si film at room temperature has a reduced effective thermal conductivity. However, effective Fourier modeling using this reduced thermal conductivity does not reproduce the experimentally observed decay rates for small grating periods  $L$  comparable to  $\ell$  (see Fig. 7).

In this experiment, by substituting Fourier's law by the hydrodynamic heat equation 76, two different viscous effects that contribute to reduce the effective thermal conductivity displayed by the system are predicted. On one hand, the global thermal conductivity is reduced due to the presence of the heat flux boundary layers introduced in section 4.2, which capture the steady-state thermal response of the film. This effect can be also reproduced using an effective Fourier's law with a reduced thermal conductivity. On the other hand, by reducing the grating period  $L$  to values close to  $\ell$  ( $\xi^2 > 4 \mu\text{m}^{-2}$ ), an extra viscous effect emerges according to Eq. 76. In these cases the heat flux flows from hot to cold regions that are separated small distances comparable to  $\ell$ . Thus the nonlocal term in 76 increases, which limits the amount of heat flux flowing and slows down the homogenization of the initial temperature profile. This extra nonlocal effect is the responsible of the reduction of the hydrodynamic decay rate with respect to the effective Fourier solution (which only captures the influence of the small film thickness), and allows capturing the functional dependence between

$\gamma$  and  $L$  for small grating periods as shown in Fig. 7. We used Finite Element solutions of the model equations (see section 11.1). However, simple analytic solutions for this particular case of study can be found in [120]. Again, we used the ab initio calculated parameter values for eq. 76 shown in section 3.5. Due to the relevance of volume viscosity in this kind of 1D system, we used here  $\alpha=1$  as predicted by the most general derivation of the hydrodynamic heat equation [19].

This experiment has been extensively used for inferring the phonon MFP distribution and the cumulative thermal conductivity within the effective Fourier framework in materials like Silicon. Furthermore, derivation of the corresponding ballistic phonon suppression function has been derived considering the present non-equilibrium situation as described in section 2.5. However, the applicability of the hydrodynamic model, which makes use of a single characteristic length  $\ell$  much smaller than a significant fraction of phonon MFPs in Si, seems to be at odds again with these previous interpretations.

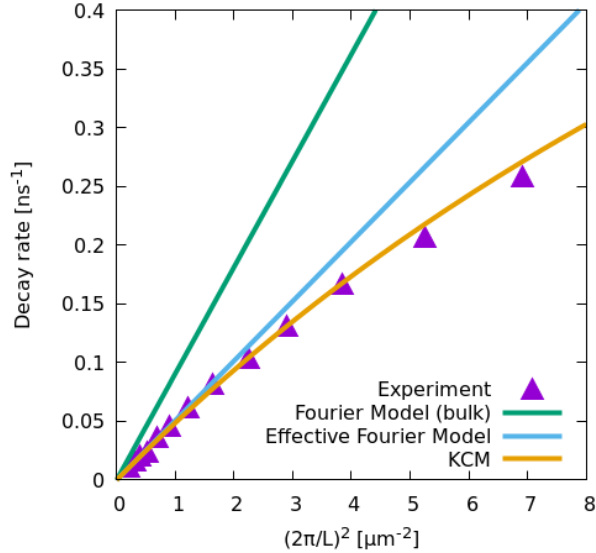


**Figure 7:** Decay rates of a thermal grating with period  $L$  induced in a 400nm-thick Silicon film at room temperature. We compare experimental data, the bulk Fourier model, the effective Fourier model using the reduced thermal conductivity displayed by the same film in steady-state, and the hydrodynamic model (KCM) predictions.

#### 4.4 Discussion on the Hydrodynamic Model Applicability

One important consequence of the applicability of the hydrodynamic model in these experiments is the breakdown of the ballistic suppression of phonons introduced in section 2.5. In standard materials like Silicon the mean free path spectrum span from the nanometer to the tens of microns length scales as derived from first principles within the RTA approximation. However, the thermal

conductivity of the system is only reduced when the system size approaches  $\ell$ , so the suppression of phonons with  $\text{MFP} \gg \ell$  is not manifested. This is a clear indication that the mean free path spectrum predicted by the RTA can not be directly extrapolated to the nanoscale in complex non-equilibrium situations. In other words, the phonon modes do not behave independently with its own mean free path, but a single collective length scale emerges. This discrepancy can be interpreted in terms of the simplifications used in the ballistic suppression model, which assumes that each phonon mode relax to equilibrium independently, i.e. assuming that the rest of the modes are in equilibrium. Even though the collision rates are calculated from first principles in infinite crystals, the resulting relaxation times and mean free paths are constructions which are not necessarily physical at the nanoscale in arbitrary materials and temperatures. In fact, the relaxation time of a given mode can only be defined locally since it depends on the local non-equilibrium situation of the rest of the distribution, which invalidates assuming  $g'_k = g_k = 0$  in expression 7.

However, other approaches beyond RTA based in the theory of relaxons, provide a generalized Fourier law with a size-dependent thermal conductivity qualitatively similar to the effective conductivity obtained by suppressing phonons using the MFP spectrum (from RTA) [52]. More specifically, derivations with a non-diagonal collision operator also predict a significant reduction of the thermal conductivity for system sizes of  $1 \mu\text{m}$  in Si at room temperature. One possible explanation for this is the simplification of the influence of the drift operator on the distribution function, which is only explicitly dependent on the temperature gradient in [52]. This contrasts to other analysis of the BTE [19].

The ballistic suppression model failure in Silicon is supported by extensive experimental evidence in similar conditions [73, 145–149]. Some authors [95, 148] attributed the discrepancies between the ballistic suppression model and experiments to the Akhieser’s damping. Remarkably, this refinement is not required within the hydrodynamic framework. Moreover, taking the previous experiments into account, the experimental evidence of the apparent suppression of phonons with large MFP in Silicon provided in [88, 150] should be analyzed carefully. In [150], a model with enhanced specular effects is introduced to justify the reduction of the thermal conductivity of the films. However, the measured system response can be explained using the bulk thermal conductivity for all the considered films if no enhanced specular effects are assumed (i.e. all the grating relaxation times in Figure 1 of [150] can be explained using the bulk conductivity of Si). In [88], a perfect agreement between experimental data and the suppression function model is reported. However, the experiments are not carried out at the same temperature for different system size due to the energy introduced by the probe laser, and the measurement temperatures are significantly higher than room temperature. Therefore, direct comparison using the ab initio MFP spectrum at 300K for Si might not be appropriate.

The hydrodynamic model resolves these inconsistencies and successfully predicts the transition from a purely diffusive system response to the first stages of the ballistic regime in non-alloys. In fact, the predictive power of a model

based in a single length scale is the most important signature of hydrodynamic transport in kinetic materials like Silicon. Nevertheless, when the distance between two disconnected boundaries (denoted by  $L$ ) is small enough, systematic deviations are observed in experiments with respect to the hydrodynamic description with ab initio equation coefficients (see Figures 5 and 6). Specifically, the model applies for Silicon if and only if  $L > 2\ell$  (gray regions). Remarkably for applications, this condition allows reducing the interface connecting the semiconductor and a metallic heater to arbitrary small sizes. For example, in Chapter 7 we model the thermal response of isolated heaters as small as 20 nm. Moreover, note that an analogous applicability condition could be formulated in terms of the heat flux relaxation time  $\tau$  and the frequency of an external excitation. Most of the experiments in silicon or germanium that we consider in the following chapters fall within this regime of applicability, with few exceptions where the ab initio hydrodynamic model systematically breaks down: In Chapter 5 the model fails to describe small circular heaters at very low temperatures; In Chapter 9, the external perturbation size is extremely small and, as it will be shown, non-local effects must be completely neglected; In Chapter 7 we study a system of close-packed arrays of heaters which, in some cases, is beyond the applicability regime and the model fails. However, the use of reduced and geometrically-defined effective values for the non-local length is shown to successfully model that particular cases. This last observation opens the door to use the generalized hydrodynamic model out of the applicability regime to provide phenomenological interpretations of experimental data. Finally, we note that the applicability condition can be slightly relaxed in Bi<sub>2</sub>Te<sub>3</sub> samples, as discussed in Chapter 8.

The failure of the model for large Knudsen numbers may be related to the influence of excited higher-order moments <sup>44</sup> in the distribution function. These moments can not relax fast enough in extremely fast or confined situations. Hence, removing them from the description, as done in [19] (see section 3.2), is not adequate. In previous work, the influence of higher-order moments is interpreted as an effective reduction of the non-local length [68]. This is similar to the apparent reduction of the thermal conductivity within a Fourier description due to non-local effects (associated to first- and second-order moments). Moreover, this is qualitatively consistent with the mentioned experimental modeling beyond the applicability regime in Chapter 7, where the non-local length needs to be systematically reduced with respect to the ab initio calculated value.

### **Size effects in the collective regime: The Poiseuille heat flux profile and Knudsen minimum**

From a kinetic point of view, the synchronized phonon response, which suppress the manifestation of a multiscale phonon MFP spectrum and allows the use of a single length scale  $\ell$ , may attenuate at very large Knudsen numbers, where most of the MFPs are larger than the system characteristic sizes according to RTA. It is possible that in such conditions some of the phonons behave independently, and the hydrodynamic description breaks down. In materials like Silicon, where the Normal and Resistive MFPs are comparable, the range of applicability



is shown to be restrictive. However, in collective materials like graphene, the Normal MFP is much smaller than the Resistive MFP. In such conditions, the hydrodynamic description may hold beyond the applicability regime determined for silicon. Moreover, a full Poiseuille-like heat flux profile in perfect analogy to fluids is expected rather than the emergence of disconnected heat flux boundary layers in opposed system contours (see Fig. 4), thus leading to characteristic phenomena:

In systems with characteristic size  $L$  significantly larger than the average Resistive phonon-phonon mean free path  $\Lambda_R$ , the randomization of phonon momentum, which cause a finite thermal conductivity, is mainly due to phonon-phonon scattering, and the thermal conductivity is size-independent (diffusive limit). In systems with characteristic size smaller than most of the phonon mean free paths (both Normal  $\Lambda_N$  and Resistive  $\Lambda_R$ ), the randomization of phonon momentum is due to phonon-boundary scattering. In such situation, the mean free path is temperature-independent and it is  $\propto L$  (Casimir or ballistic limit). Hence, according to expression 13, the thermal conductivity is proportional to the system size and its temperature dependence is solely determined by the specific heat (at low temperatures is  $\propto T^3$ ). The transition between both limits by increasing the size of the system can be microscopically interpreted in the collective regime. For appropriate materials and temperatures, the Normal mean free path is smaller than the Resistive mean free path and, consequently, for some system sizes the phonons only experience Normal phonon-phonon collisions ( $\Lambda_R > L > \Lambda_N$ ). In such cases, all the phonon momentum is destroyed in the boundaries and a Poiseuille heat flux profile associated to the phonon drift velocity is expected, in perfect analogy to the fluid velocity profile in a pipe [110–112]. Furthermore, a peculiar dependence of the thermal conductivity (i.e. the Knudsen minimum) is predicted and experimentally observed: When the system size is increased to values close to the normal mean free path ( $L \sim \Lambda_N$ ), the phonon-boundary scattering rate increases because the low-frequency phonons traveling in the longitudinal direction suffer normal collisions that deviate its direction. This cause a reduction of the momentum-destroying mean free path and, hence, the thermal conductivity is reduced. When the system size is further increased but it is still smaller than the Resistive phonon-phonon mean free path, the phonons experience a large number of Normal collisions, which effectively increase the distance they travel before losing its momentum by colliding to the boundaries. This produces an effective increase of both the momentum-destroying mean free path and the resulting thermal conductivity. Therefore, a non-monotonous trend in the thermal conductivity is obtained by increasing the system size. The minimum of the thermal conductivity is known as the Knudsen minimum in analogy to fluids [104, 113]. Experimental evidences [112] and numerical studies [41, 47, 104] of this peculiar thermal conductivity trend with system size and temperature are available in the literature.

Further investigation is required to determine the applicability of the mesoscopic hydrodynamic model with ab initio calculated parameters in the collective regime to predict this kind of effects. For example, it is still pendant to model the

graphene experimental thermal conductivity at low temperatures and small system sizes using the present hydrodynamic model with *ab initio* coefficients. It also remains unclear if the mesoscopic hydrodynamic model can capture peculiar phenomena like the Knudsen minimum.

Note that the particular influence of the boundaries leading to the Knudsen minimum is specific of the collective regime, since in kinetic materials like Si the Resistive and the Normal mean free paths are always comparable. However, the generalized hydrodynamic framework utilized in this thesis also predicts non-homogeneous heat flux profiles beyond the collective regime due to the presence of boundaries or inhomogeneous external excitations, which also allow interpreting the thermal conductivity dependence on system size and temperature in silicon as has been shown in section 4.2. Moreover, these profiles are also explicitly obtained in numerical BTE simulations (e.g. [44]) beyond the collective regime. Therefore, we conclude that the absence of characteristic phenomena like the Knudsen minimum in some material does not invalidate the hydrodynamic description of size effects in kinetic materials.

### Size effects in alloys

In this thesis we focus on non-alloys like silicon. For alloy materials like SiGe or InGaAs, there are strong evidences of the applicability of the ballistic suppression of phonon modes [90], or multiscale Lévy Flight transport [30], which contrasts with the hydrodynamic description based in a single length scale. Interestingly, the latter framework, which is introduced in section 2.5, has been shown to distinguish the thermal response of such alloys and silicon. In Figure 8, we show the characteristic thermal penetration depth  $\sigma(t)$  with respect to the external excitation timescale (Eq. 67) at room temperature for different materials using its *ab initio* calculated properties [30]. Remarkably, the alloys (SiGe and InGaAs) present a distinct regime in between the ballistic and diffusive limits (i.e. for intermediate frequencies  $s$ ), where a well defined power law behavior of  $\sigma^2(t)$  with fractional exponent is obtained ( $\sigma^2(t) \sim t^{1.34}$ ). In contrast, this intermediate regime is not obtained for a non-alloy semiconductor like Silicon. The intermediate regime observed for alloys is identified as superdiffusive transport or Lévy stable process [102, 103], for which a fractal diffusivity can be defined. This behavior can be clearly distinguished from Fourier transport, and it was experimentally confirmed using laser transient thermoreflectometry measurements [100]. The existence of this Lévy flight behavior is linked with a certain slope of the cumulative thermal conductivity, which is not obtained in non-alloys. This signature could be related with the manifestation of the multiscale nature of the phonon MFP spectrum in alloys due to the independent evolution of the phonon modes through collisions with the alloying atoms. This collisions completely dominate over Normal processes and may destroy all the collective behavior. Conversely, this multiscale behavior is inhibited in other semiconductors like Silicon, where Normal collisions are present, and the cumulative thermal conductivity can not be used to interpret experimental observations. Nevertheless, it is worth to note that some authors identified Lévy flight transport

in Silicon in extremely small systems [151], which are beyond the applicability of the hydrodynamic model. This might be an indication of the emergence of ballistic effects (i.e. the independent behavior of the different modes) in front of hydrodynamic (collective) behavior at sufficiently large Knudsen numbers.

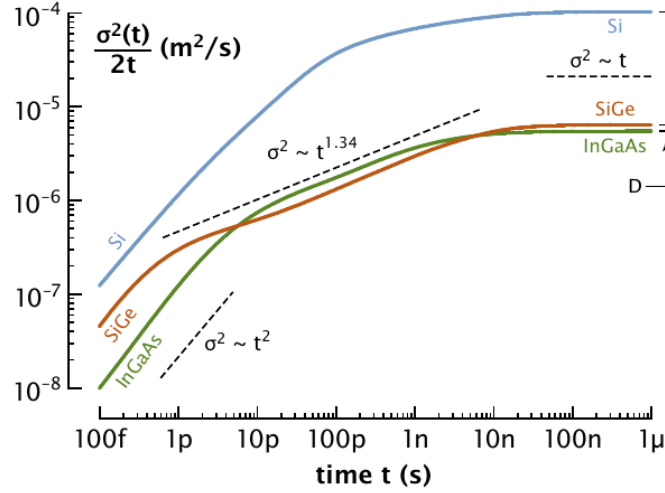


**Figure 8:** *Reproduced from [30].* Normalized mean-square displacement of the thermal energy 65 using ab initio relaxation times and velocities for InGaAs, SiGe, and Si at room temperature. The two alloys (InGaAs and SiGe) display de Lévy flight intermediate regime, whereas an abrupt transition between the diffusive and ballistic limits is observed in Silicon.

According to these results, the mainly studied materials in this thesis (i.e. semiconductor non-alloys) do not display a clear Lévy Flight behavior (at least for not extremely high Knudsen numbers). Consistently, the influence of nano heaters on Silicon substrate [152] can be described using the ab initio hydrodynamic model based in a single length scale as shown in the next Chapter. Conversely, the same experiment in InGaAs required the use of geometry-dependent thermal conductivities [21]. This may be a signature of the multiscale Lévy-Flight behavior in an alloy like InGaAs, which precludes the use of full ab initio hydrodynamic modeling in this material. However, it is worth to note that the inclusion of nonlocal effects within the hydrodynamic framework was still required to effectively model the experiment in [21]. Therefore, future work should be aimed to integrate the Lévy flights and the hydrodynamic frameworks to further understand the peculiarities of heat transport in alloys and the influence of hydrodynamic effects in this kind of materials [121].

## 5 Linear and circular heat sources on Silicon substrate: Full field thermorefectance maps

In collaboration with Birck Nanotechnology Center (University of Purdue)

In this Chapter we study the process of heat release from metallic nanostructures towards a Silicon substrate in steady-state conditions at different temperatures. Importantly for applications, it is shown that the inefficient cooling of the heaters can be fully understood by properly distinguishing the resistive effects arising from the metal-semiconductor interface and the non-local effects influencing the heat conduction in the substrate. Specifically, we use Thermorefectance imaging (TRI) to examine the steady-state spatial temperature distribution of electrically-heated Au structures built on Silicon substrates (see Figure 9). These measurements are extremely relevant since local information about the thermal response is obtained in a technologically relevant device configuration. As it will be shown here, the obtained thermal maps allow identifying clear non-Fourier signatures on the substrate heat conduction mechanisms close to the heater [152].

### 5.1 Thermorefectance Imaging

Thermorefectance imaging (TRI) is a high-resolution, non-contact optical imaging technique where the local relative change in the sample's reflection coefficient varies as a function of local temperature [21, 153]. The change in reflectivity depends on the calibrated thermorefectance coefficient ( $C_{TH}$ ), which is a function of the illumination wavelength, the sample's material, and surface characteristics. Once the  $C_{TH}$  is known, the relative change in the sample's surface reflectivity ( $\Delta R/R$ ) can be translated to a precise temperature change ( $\Delta T$ ) relative to the experimental ambient temperature.

A green ( $\lambda=530$  nm) narrow-band LED illuminates the sample's full field-of-view (the LED wavelength is chosen to maximize the detected reflectivity signal). The LED is pulsed which provides the ability to obtain thermal images with up to 50 ns resolution. By controlling the LED timing, the transient and steady-state thermal response of the imaged devices can be probed. The sampling duration of the LED (probe) was set to 25  $\mu s$ , time-delayed to capture the steady-state temperature at the end of the 500  $\mu s$  stress pulse. A CCD camera synchronized with the electrical excitation pulse-train quantifies the relative change in the sample's reflectivity ( $\Delta R/R$ ) in each cycle. Some time averaging (over multiple cycles) is required to improve the signal-to-noise ratio of the thermal image. The thermal images acquired for the Au structures were averaged for 1-5 minutes yielding a typical resolution of 0.1 K.

The  $C_{TH}$  calibrated values for Au and Si were measured to be  $-2.2 \cdot 10^{-4} \pm 5\%$   $K^{-1}$  and  $1.0 \cdot 10^{-4} \pm 5\%$   $K^{-1}$ , respectively. The  $C_{TH}$  calibration process was performed using methods similar to what is described in [154, 155]. To further val-

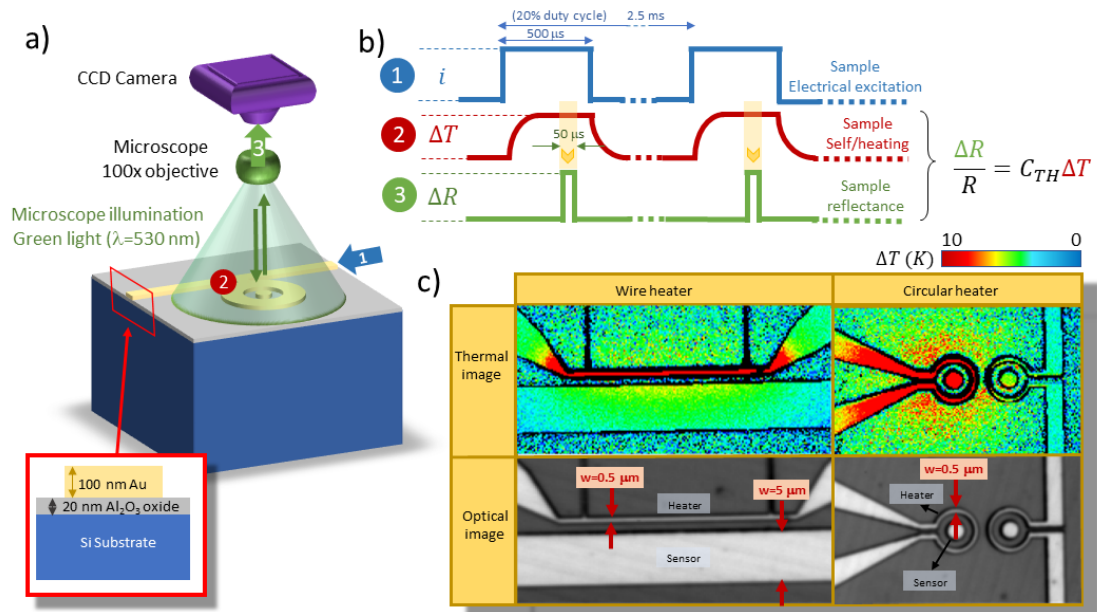


**Figure 9:** Reproduced from [152]. Overview of TRI experimental setup and outputs. (a) Experimental setup along with a cross-section of the imaged Au structures on top of a silicon substrate. (b) Sequence of events leading to a thermal image: (1) the device is electrically excited with a pulse-train; (2) the device self-heats, during the on-current state, due to Joule heating; and (3) the reflection coefficient for the tested device changes as a function of temperature. By controlling when to illuminate the sample, a CCD camera quantifies the thermally induced optical reflectivity variations between the on-current state and off state, which finally produces a 2D spatial temperature distribution (thermal image) of the top surface. (c) Typical system outputs, which are pairs of optical and thermal images, obtained for (left) Au wire-structure with a heater width of 0.5  $\mu\text{m}$ , and (right) Au circular-structure with a heater width of 0.5  $\mu\text{m}$ .

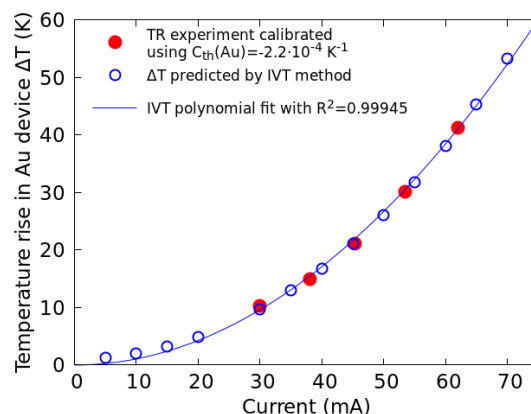


**Figure 10:** Reproduced from [152]. IVT calibration of the gold thermoreflectance coefficient for a wire-shaped heater device with  $W=1 \mu\text{m}$ .

idate the measurements and the  $C_{\text{TH}}$  for Au ( $C_{\text{TH}}^{\text{Au}}$ ), each device was calibrated using temperature-dependent current-voltage measurements (IVT). In the IVT, the average temperature of the Au structures is obtained at different current levels. By comparing the average temperature of the heater lines measured by IVT with that obtained by TRI, the  $C_{\text{TH}}^{\text{Au}}$  is extracted. To get temperature as a function of current in the IVT, the 4-wire electrical resistance is measured for each heater line at different current levels. Then, the linear approximation below is used to quantify the corresponding average temperature rise ( $T - T_0$ ) of the wire

$$r(T) = r_0(1 + \alpha(T - T_0)) \quad (110)$$

where  $r(T)$  is the measured 4-wire resistance at currents larger than zero,  $r_0$  is the resistance of the device at zero current (estimated from the slope of the IV-curve at small current levels), and  $\alpha$  is the temperature coefficient of resistance. Coefficient  $\alpha$  was experimentally measured and has values between 0.0026 and 0.0028  $\text{K}^{-1}$ , which agrees with reported literature values for thin Au conductors [156]. Figure 10 shows a sample IVT calibration for a 1  $\mu\text{m}$ -wide gold wire heater with an extracted  $C_{\text{TH}}^{\text{Au}} = -2.2 \cdot 10^{-4} \text{ K}^{-1}$ . This thermoreflectance coefficient is very stable under the temperature ranges considered in our experiments.

We analyze the thermal response of devices with varying the size and the shape of the heater, and also the ambient temperature using a cryostat. Two sets of samples (with circular- and wire- shaped heaters) with identical characteristic lengths are considered (see Fig. 9). Both groups of samples consist of gold heaters and thermometers (sensors) fabricated on a silicon (Si) substrate with an interfacial  $\text{Al}_2\text{O}_3$  layer of 20 nm. The gold structures have a fixed thickness of 100 nm and a variable width  $W$ , ranging from 10  $\mu\text{m}$  down to 400 nm. Each heater has a designed adjacent Au metallization to serve as a nearby thermometer sensor. The samples are placed in the focal plane of the microscope and are electrically excited (heated). A fixed electrical current intensity  $i$  is imposed through the Au heaters that introduces a power density distribution due to Joule's heating. The resulting stationary 2D temperature distribution of the top surface  $\Delta T$  is obtained by the change in its optical reflectivity  $\Delta R$  using the TRI technique.

## 5.2 Room Temperature measurements

To compare experimental measurements with theoretical predictions of the temperature field at some point  $\mathbf{r}_0$ , the effect of the optical blurring must be accounted for. Hence, we convolute the theoretically predicted surface temperature increase with the following transformation function [153, 157]:

$$f(\mathbf{r}) = \frac{1}{\sqrt{2\pi}} \exp\left(-\frac{(2.44|\mathbf{r}|/\lambda N)^2}{2}\right) \quad (111)$$

where  $N=(2\text{NA})-1$ , with  $\text{NA}=0.75$  (the numerical aperture), and  $\lambda=530 \text{ nm}$  (the probe wavelength used). The convolution reads

$$\Delta T(\mathbf{r}_0) = \frac{1}{gC_{\text{TH}}} \left( \int_{\text{Au}} d\mathbf{r} (T - T_0) C_{\text{TH}}^{\text{Au}} f(\mathbf{r} - \mathbf{r}_0) + \int_{\text{Si}} d\mathbf{r} (T - T_0) C_{\text{TH}}^{\text{Si}} f(\mathbf{r} - \mathbf{r}_0) \right) \quad (112)$$

where  $C_{\text{TH}}$  is  $C_{\text{TH}}^{\text{Si}}$  if  $\mathbf{r}_0$  is located in the substrate and  $C_{\text{TH}}^{\text{Au}}$  otherwise. The normalizing constant  $g = 2\pi\left(\frac{N\lambda}{2.44}\right)$ .

To reproduce the experimental temperature fields with geometry-independent parameters, we model the heat transport in the metal and semiconductor domains along with the interface effects using the hydrodynamic heat transport model presented in Chapter 3. The stationary current density  $\mathbf{J}$  distribution in the heaters is calculated to obtain the local power density introduced by Joule's heating using Eq. 103, 104, with imposing electrical insulation  $\mathbf{J} \cdot \mathbf{n} = 0$  in all the metal domains except in the heater terminals, where a total current intensity  $i$  is imposed. Importantly, we use the temperature-dependent electrical resistivity as experimentally characterized:

$$\rho(T) = \rho_0(1 + \alpha(T - 295)), \quad (113)$$

where  $\rho_0 = 29\Omega\cdot\text{nm}$  is the reference electrical resistivity at room temperature, and  $\alpha = 0.0027 \text{ K}^{-1}$ .

The thermal response of the gold regions can be described by Fourier's law (Eq. 1 with  $\kappa_{\text{Au}}=310 \text{ W/mK}$ ) and the energy conservation (Eq. 75) including the energy source 104. This is because the nonlocal (hydrodynamic) effects for heat carriers in metals (electrons) are not relevant at the size scales of our fabricated devices. However, in the Si substrate, heat carriers (phonons) have MFPs comparable to the geometry characteristic sizes. Therefore, refining the thermal transport equation of the substrate to include nonlocal effects is needed to describe the heat flux  $\mathbf{q}$  and the temperature  $T$ . We use the energy conservation equation 75 and the hydrodynamic heat transport Eq. 76.

Appropriate boundary conditions to model the free surfaces and the metal-semiconductor interface are also required. In both, the heater and the thermometer free surfaces, thermal insulation is imposed (Eq. 77). Moreover, there is a 20nm-thick oxide layer between the metal and the semiconductor. This layer obeys Fourier's law with conductivity  $\kappa_{\text{ox}} = 1 \text{ W/mK}$  (the experimental characterization of  $\kappa_{\text{ox}}$  is discussed below). In the metal-oxide interface, continuity of the heat flux and the temperature is imposed. In the oxide-silicon interface, we impose three conditions to connect Fourier and hydrodynamic transport. The first is continuity of the normal component of the heat (Eq. 84). The second is a temperature jump boundary condition that accounts for the non-equilibrium effects introduced by the interface (Eq. 92). Derivation of this boundary condition and the microscopic expression for the appearing coefficients can be found in section 3.4, and the required ab initio coefficient values for Silicon can be found in 3.5. In the present experiment, the main contribution to the temperature jump between the metal and the semiconductor is due to the presence of the oxide layer, which plays the role of the usual Kapitza interface resistance. Hence, for simplicity, we use  $R = 0$  in 92 and we capture all the intrinsic interface resistivity in the oxide thermal conductivity as explained below. Further reduction of the interface size  $W$  would be required to observe a significant contribution of the non-local (non-Kapitza) effects predicted by the boundary condition 92. The third interface condition is a slip boundary condition 81 for the tangential component of

the substrate heat flux with  $C=1$  (diffusive phonon-boundary scattering). Moreover, in the substrate-free surfaces, insulation 77 for the normal component of the flux and the slip boundary condition 81 for its tangential component are imposed. We note that the presence of heat flux boundary layers (see section 4.2) far away from the heat sources in the substrate top surface has a negligible effect in the present experimental conditions. Consistently, the value of  $C$  does not significantly modify the temperature profile predictions. Finally, the temperature of the substrate base is fixed to the reference ambient temperature.

All the parameters used in the transport equations and boundary conditions are geometry-independent. However, experimental characterization of the intrinsic thermal conductivities of the oxide layer and the silicon substrate are still required. To quantify those properties, we consider the experimental measurements of the largest geometry, with characteristic size  $W = 10 \mu\text{m}$  ( $\gg \ell$ ), in which the Laplacian term in Eq. 76 can be neglected, and the Fourier and the hydrodynamic description of heat conduction in the substrate are equivalent. Then, we extract the thermal conductivities by fitting the experimental observation to a Fourier model (see Figure 11). The resulting oxide conductivity is  $\kappa_{\text{ox}} = 1 \text{ W/mK}$ , and the silicon bulk conductivity is  $\kappa_{\text{Si}} = 130 \text{ W/mK}$ . The value for the Silicon thermal conductivity is slightly smaller than the one reported in 3.5. This is due to significant doping in the present samples. Finally, we use the values for  $\ell$  and the rest of ab initio parameters reported in 3.5, since no significant influence of the doping is expected.

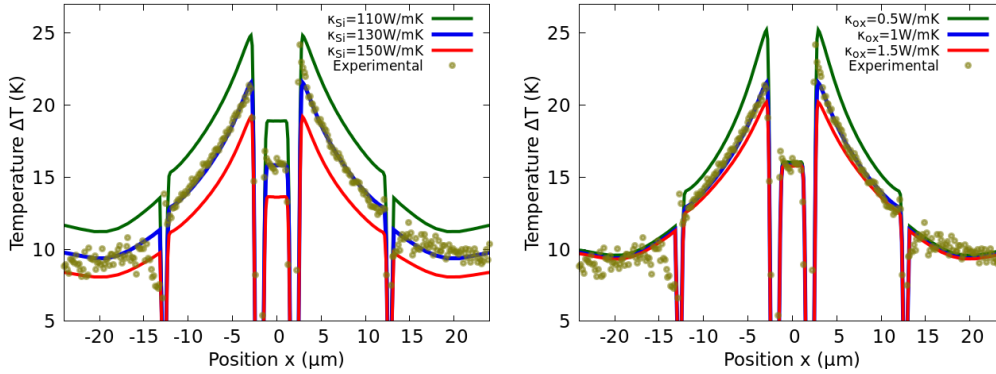


**Figure 11:** *Reproduced from [152].* Sample characterization at room temperature: Temperature profile dependence on the substrate thermal conductivity  $\kappa_{\text{Si}}$  with  $\kappa_{\text{ox}}=1 \text{ W/mK}$  (left), and on the oxide layer thermal conductivity  $\kappa_{\text{ox}}$  with  $\kappa_{\text{Si}}= 130\text{W/mK}$  (right), in the largest circular device  $W=10 \mu\text{m}$  according to Fourier's law (which in this case is equivalent to the hydrodynamic prediction).

In Fig. 12, we compare the experimental data (brown dots) with the hydrodynamic model predictions (red lines). The predictions using Fourier's law instead of Eq. 76 but also using the bulk thermal conductivity (blue lines) are also shown for illustration of the non-diffusive behavior observed in this experiments. For the largest widths ( $W = 10 \mu\text{m}$ ), the Fourier and the hydrodynamic model predictions coincide and match the experimental data (notice that from this result



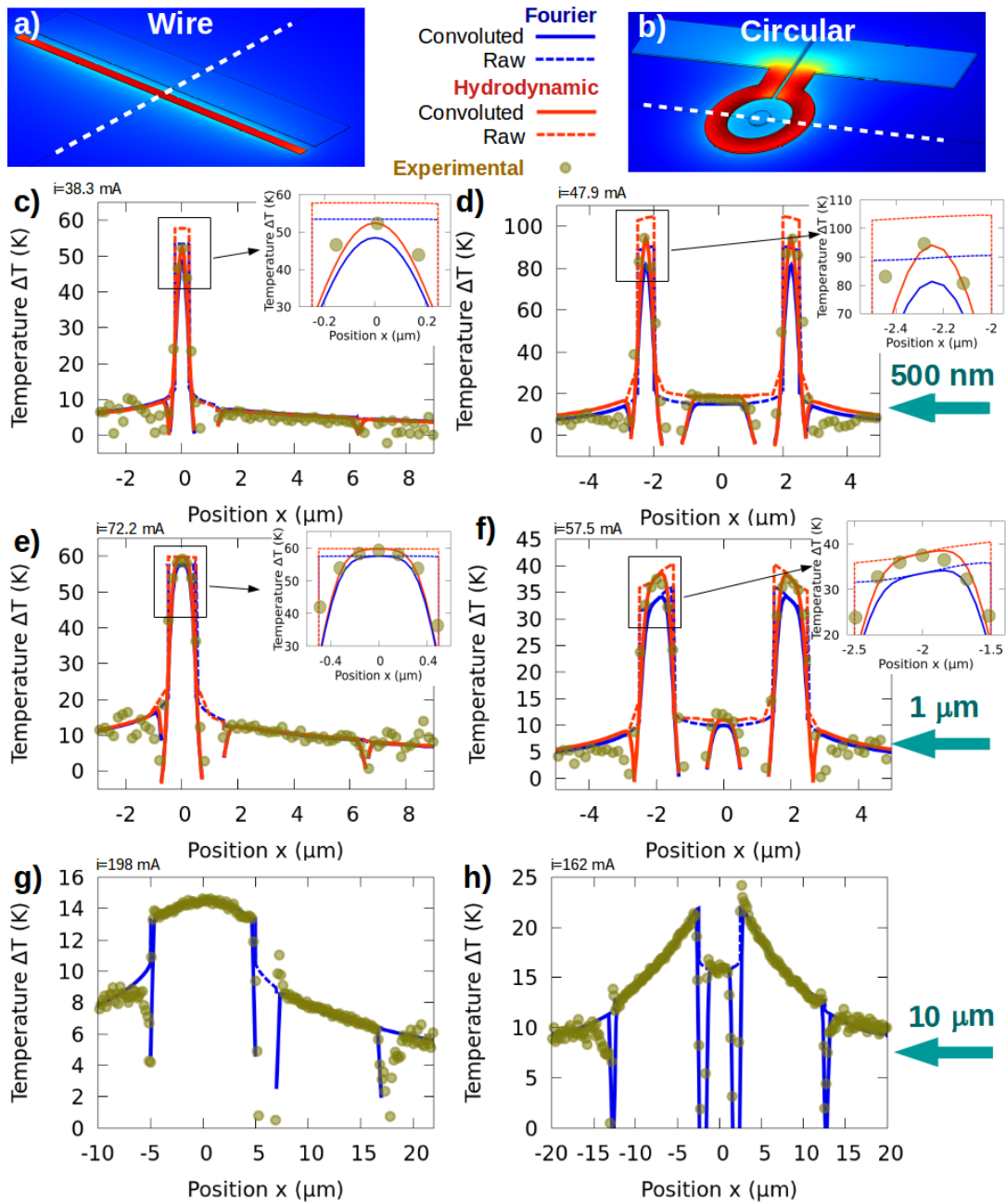


**Figure 12:** *Reproduced from [152].* Temperature-profile comparisons of experimental, Fourier bulk predictions, and hydrodynamic predictions (with geometry-independent parameters). Data plotted for wire and circular heater geometries of different sizes: 500 nm, 1  $\mu\text{m}$ , 10  $\mu\text{m}$  at room temperature. The left plots ((c), (e), and (g)) represent the temperature increase with respect to the reference temperature of 295 K in a cross-section of the wire geometry (a), and the right plots ((d), (f), and (h)) represent the temperature increase in a cross-section of the circular geometry (b). The dashed lines correspond to the temperature field predictions. The solid lines correspond to the predictions including the optical blurring effects of the experiment, i.e. the convoluted temperature fields 112.

we characterized the bulk thermal conductivities of silicon and the oxide layer as shown in Fig. 11). For this reason, in the largest samples (Figs. 11(g) and 11(h)), we have only represented the Fourier solution. By reducing the width of the heaters, the Fourier bulk prediction starts to deviate from the experimental data, whereas the hydrodynamic predictions still reproduce the measurements. Furthermore, the deviations from the bulk Fourier predictions are enhanced in the circular geometry. Samples with heater size  $W = 1 \mu\text{m}$  are of special interest (Figs. 11(e) and 11(f)) since for the wire device, similar solutions are obtained from Fourier and the hydrodynamic model, whereas in the circular device, the Fourier prediction deviates and does not match the experimental data. The heater shape effects observed in this experiment highlights the need for using a model with full 3D capabilities such as generalized phonon hydrodynamics. This issue has a dramatic impact on electronic device design, where parametric models based on size-dependent thermal conductivities are used, and the effects of the heat source shape are usually not considered.

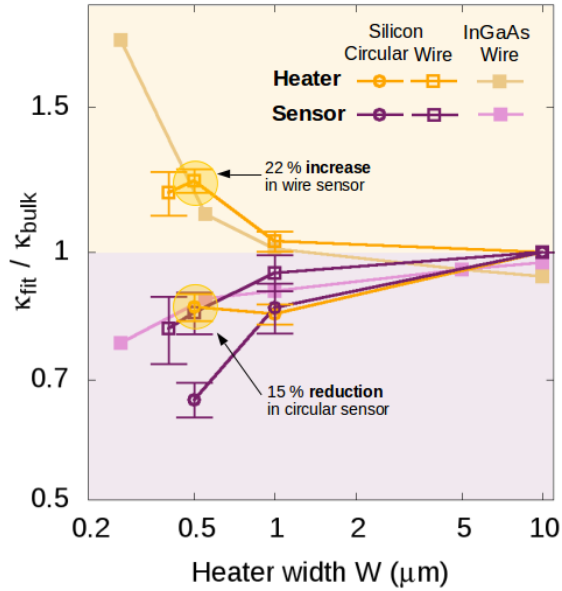


**Figure 13:** *Reproduced from* [152]. Normalized effective thermal conductivity,  $\kappa_{\text{fit}}/\kappa_{\text{bulk}}$ , required, in an effective Fourier description of the substrate, to reproduce the experimental temperature profile in the thermometer sensor (yellow) and in the heat source (purple). Both the wire (squares) and the circular structures (circles) are plotted. Two substrates are considered at room temperature: InGaAs (solid symbols) and Si (open symbols). The non-Fourier behavior displayed by this experiment not only depends on the heater size  $W$ , but also on the specific geometry of the metallic regions.

To highlight the non-Fourier behavior observed in this experiment, we show in Fig. 13 the effective substrate thermal conductivity ( $\kappa_{\text{fit}}$ ) required in Fourier to fit the experimental temperature profile in the thermometer (yellow) and the heater (purple), normalized by the bulk value ( $\kappa_{\text{bulk}}$ ). For illustration purposes, similar results of wire-shaped heaters on an InGaAs substrate (presented in [21]) are shown. The resulting fitted values depend on the size of the heater. For a

given sample, different values are needed to reproduce the experimental measurements at the heater and at the thermometer. Furthermore, the values required by the effective Fourier model are different for the circular and the wire configurations having the same size. This discrepancy is particularly evident if we compare the fits to the thermometer temperature profile. While for the circular device the thermal conductivity value needs to be reduced, for the wire device it needs to be increased.

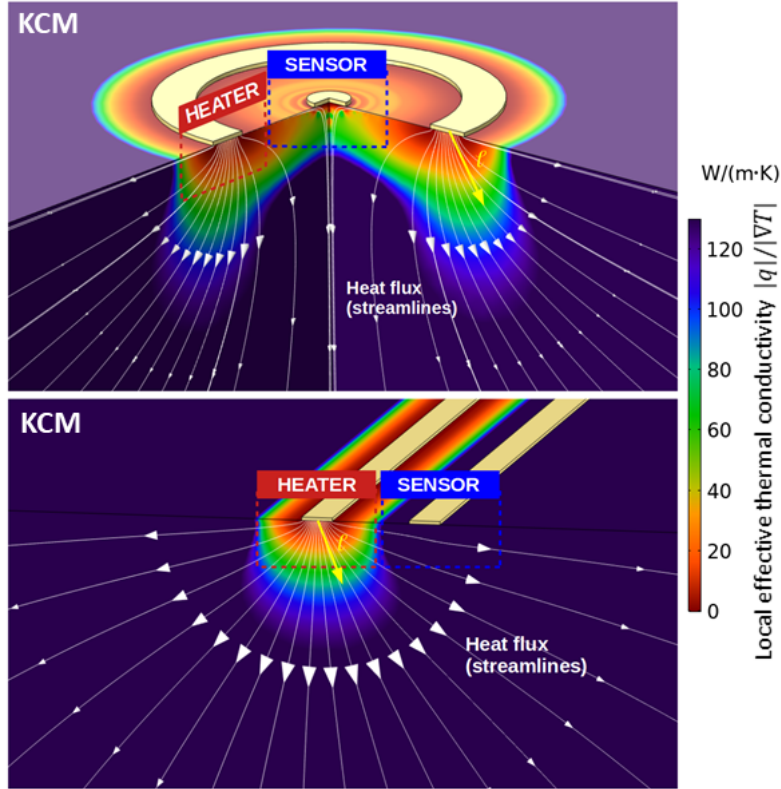


**Figure 14:** *Reproduced from [152].* Local effective thermal conductivity  $|q|/|\nabla T|$  calculated from the hydrodynamic stationary solution of the circular device cross-section (top) and the wire device cross-section (bottom). Below the heat sources, the inhomogeneities of the heat flux profile cause a viscous reduction of the energy released to the substrate, resulting in a reduced local thermal conductivity in both geometries. Below the sensor in the wire-device, the heat flux streamlines are straight so that the heat flux inhomogeneities (and viscous effects) are small, and the local thermal conductivity is not reduced. In contrast, below the sensor in the circular device, the streamlines are curved by symmetry, diminishing the heat-spreading efficiency and the local thermal conductivity. To highlight the effects of the non-homogeneous injection of heat flux to the substrate, this profile is obtained using  $C \rightarrow \infty$  in the boundary condition 81, thus avoiding the emergence of boundary layers on the substrate top surface away from the heaters.

In a region within the average MFP length scale close to the interface, the lack of resistive collisions favors the conservation of the heat flux initial direction (cross-plane). This geometric effect is mesoscopically captured through the Laplacian term in Eq. 76, and the nonlocal length  $\ell$ , and, hence, the hydrody-

dynamic model is able to reproduce the experimental data using fixed parameters values for all geometries and sizes  $W$  in contrast to Fourier, as shown in Fig. 12. Note that these results have a direct impact on electronic engineering, where thermal analysis is usually done using effective Fourier models. The lack of the characteristic length  $\ell$  in the Fourier description is the reason behind its breakdown at the nanoscale even in an effective way.

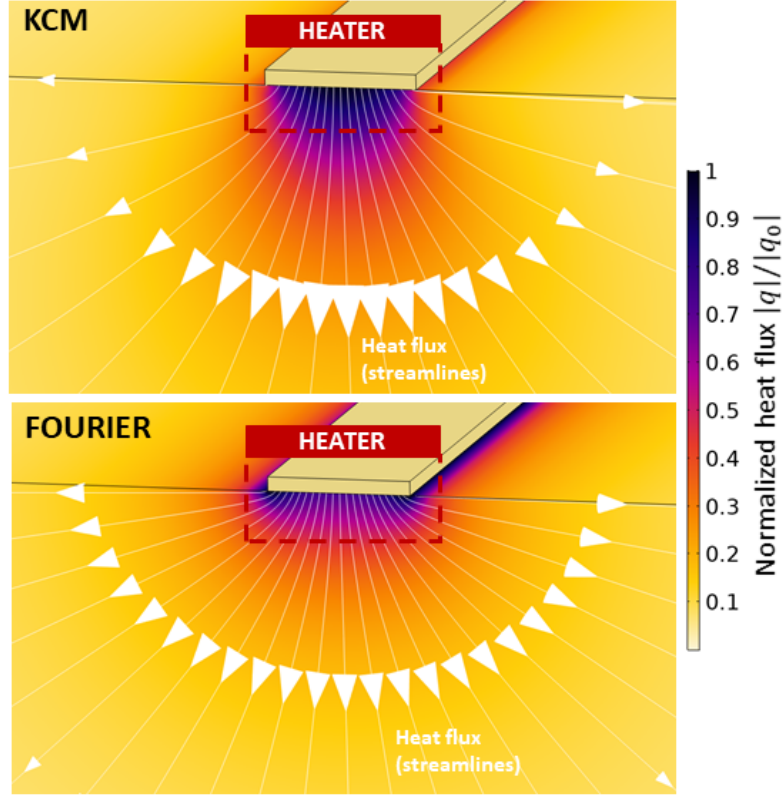


**Figure 15:** *Reproduced from [152].* Heat flux stationary profile normalized by the maximum heat flux value  $|q|/|q_0|$  below the heater according to the hydrodynamic (top), and to Fourier (bottom). In the hydrodynamic case, the reduction of the local thermal conductivity in the regions where the heat flux streamlines are curved causes a larger heat flux in the downward direction than in the in-plane direction. In contrast, Fourier's law predicts an isotropic substrate response.

At this point, it is important to indicate some differences that can be observed when comparing the present results based on silicon with the data for InGaAs presented in previous work [21]. For similar wire-shaped heaters deposited on InGaAs substrate, a fixed value of the nonlocal length ( $\ell$ ) was used, but, contrary to silicon, a size-dependent InGaAs thermal conductivity was required to reproduce the experiments. A possible explanation could be found in the relative importance of normal (momentum-conserving) and resistive phonon collisions in both materials. In Si, normal collisions reduce the width of the resistive phonon MFP spectrum, and the hydrodynamic description based on a single characteristic length  $\ell$  can be used. However, in a purely kinetic material like InGaAs, the

distribution of Resistive phonon MFPs is broader, and hence, thermal transport is better described by multi-scale models, such as the Lévy flight formalism [30, 100].

The finite elements solutions of the hydrodynamic model offer a way to understand the differences between the observed thermal response in the wire and in the circular devices. Two magnitudes are useful for this comparison: the local effective thermal conductivity  $|q|/|\nabla T|$  and the heat flux streamlines. In Fig. 14 and 15, we provide these two magnitudes, respectively, as obtained from the hydrodynamic stationary solutions. In the substrate region, under the heaters, the effective thermal conductivity is reduced in both geometries. We refer to this region as hydrodynamic region, and the reason for its appearance lies in the effects of the Laplacian term in Eq. 76. In the hydrodynamic region where this term is larger, that is, in the regions where the heat flux streamlines are curved, the effective thermal conductivity is reduced. On the contrary, out of the hydrodynamic region where straight streamlines are obtained, the Laplacian is negligible, and the bulk thermal conductivity value is recovered. By comparison of Eq. 76 with the standard hydrodynamic equation for fluids, we refer to this phenomenon as heat viscosity. Consequently, near the heaters, the heat flux is larger in the downward direction than in the in-plane direction. This prevents the heat from spreading in the in-plane direction in both the circular and the wire geometries and explains the apparent reduction in the substrate thermal conductivity when using the Fourier's law to model the heater thermal response. For illustration, in Figure 15, we also show the stationary heat flux profile below the heater, according to Fourier and to the hydrodynamic model, respectively. As expected, the Fourier heat flux profile is isotropic, whereas the hydrodynamic model predicts a larger heat flux in the downward direction.

In the sensor region, the hydrodynamic solutions show essential differences between wire and circular geometries. In Fig. 14, it can be observed that the heat flux streamlines under the wire sensor are straight, and, consequently, the local effective thermal conductivity does not change from the bulk value. However, the wire sensor is cooler than predicted by Fourier bulk. This apparent increase of the substrate thermal conductivity to fit the wire sensor temperature is observed because only a small fraction of energy reaches the sensor due to the reduced in-plane energy flow. In the circular device, a smaller fraction of energy is also being released from the heater to the thermometer along the in-plane direction. However, in this case, the cylindrical symmetry forces the heat flux streamlines to curve under the sensor to follow the downward direction, enhancing the viscous effects in that region and reducing the local effective thermal conductivity. Therefore, the energy is retained in the circular sensor, which leads to the apparent reduction of the substrate thermal conductivity according to Fourier's law.

### 5.3 Low Temperature measurements

Diffraction blurring in our experimental set up has been well characterized at room temperature as explained in the previous section. This is due to the finite numerical aperture of the imaging lens. When the sample is introduced in a liquid nitrogen cryostat for variable temperature measurements, there is additional blurring due to the fact that we do imaging through optical window with finite thickness. Fortunately, it is possible to characterize the cryostat window blurring effects in each sample by comparing thermoreflectance images with/without window at room temperature.

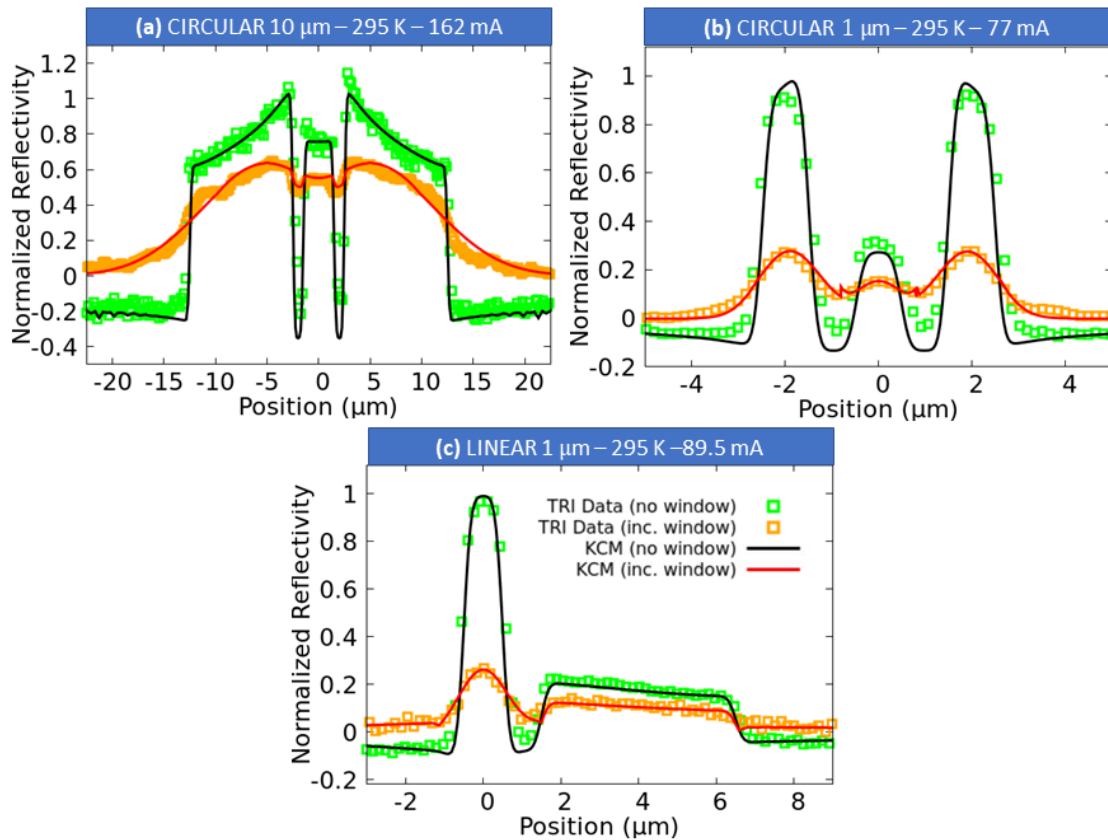


**Figure 16:** Effect of the thermostat window on the measurement of thermoreflectance profile at 295K. Green dots represent the experimental data without the lid window. Orange dots the measurements with the window lid in the same conditions as the green dots. Black line is the hydrodynamic prediction using ab-initio parameters. Red line is the convoluted profile using Gaussian functions with position-dependent variance. The same transformations are used to study the measurements at lower temperatures.

In Fig. 16, we show the room temperature raw measurements (normalized optical reflectivity) with (orange dots) and without (green dots) the cryostat window. The Gaussian convolution function 111, which does not depend on geometry, is applied to reproduce the measurements without the window (black line). Conversely, the model predictions are convoluted with a Gaussian function with a position-dependent fitted variance to reproduce the measurements

with window also at room temperature under the same current intensity (red line). The Gaussian variance is increased by moving away from the center of the images (the thermometer), and the the spatial dependency of the required variance is different for each geometry. Moreover, the weight of the signal coming from the substrate is almost eliminated to fit the experimental data. The blurring effects introduced by the cryostat window are not expected to be temperature-dependent. Therefore, the convolution obtained at room temperature for each geometry is applied to the model predictions at lower temperatures to compare with experimental data.

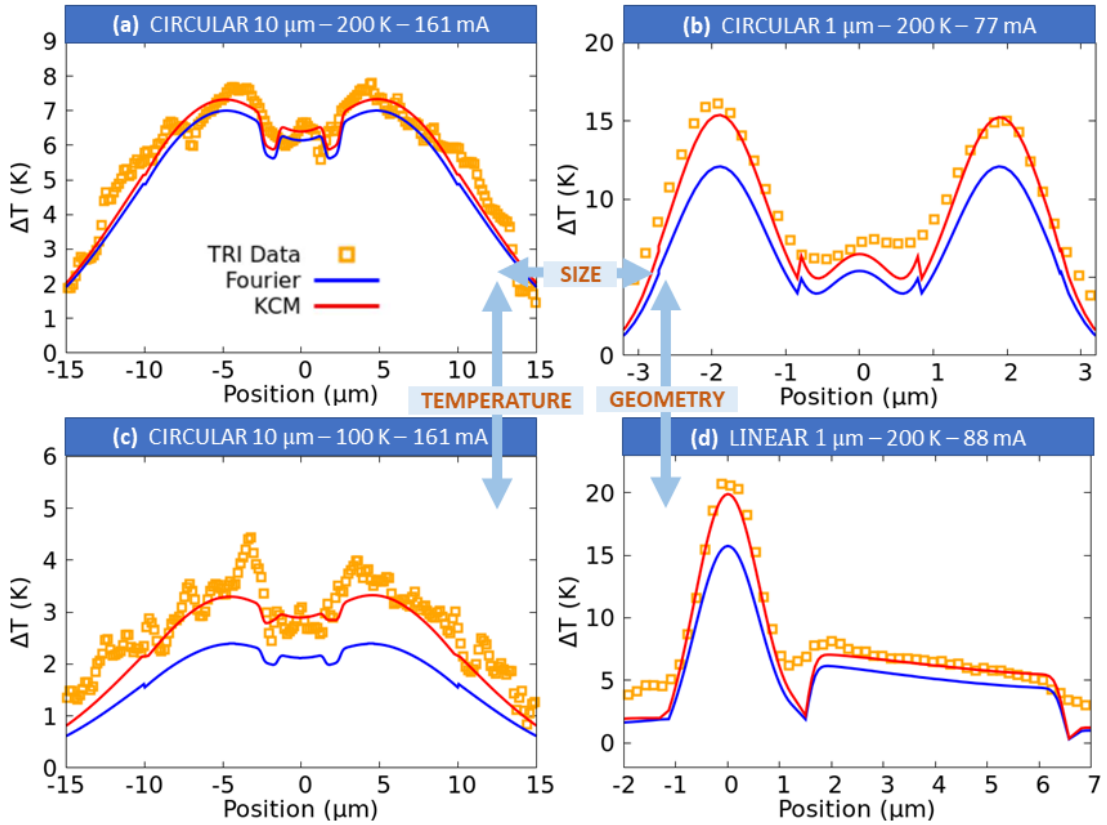


**Figure 17:** Stationary temperature increase on the surface of the sample obtained by the TRI setup (orange dots) and the results using Fourier's law (blue line) and eq. 76 (red line) in the substrate. a) Large circular heater (width  $W=10 \mu\text{m}$ ) at 200 K, b) Small circular heater (width  $W=1 \mu\text{m}$ ) at 200 K, c) Large circular heater (width  $W=10 \mu\text{m}$ ) at 100 K, d) Small linear heater (width  $W=1 \mu\text{m}$ ) at 200 K. The electrical current imposed in the heaters is indicated on top of each profile.

In Fig. 17 we provide the same comparison shown in Fig. 12 but at reduced temperatures. Exactly the same modeling explained in the previous subsection is used. Since the thermal conductivity strongly depends on the doping, we used values consistent with a sample displaying the thermal conductivity characterized at room temperature ( $\kappa_{\text{Si}}$  is 180 W/mK and 400 W/mK at 200 K and 100 K, respectively). The rest of the parameters values at the different temperatures can be found in section 3.5. At lower temperatures, non-Fourier effects are relevant

even in the large devices. Recall that, in our experiment, there is a 20 nm thick oxide layer between metal and substrate. This oxide layer has an extremely high thermal resistivity of  $20 \text{ nK}\cdot\text{m}^2/\text{W}$  that hinders the influence of a possible change in the TBR due to size or temperature variations. Nevertheless, the predictions using eq. 76 for the Si substrate and a fixed TBR value are found to explain the full temperature distribution for different device sizes and shapes. Indeed, size effects are accounted for through the Laplacian term in eq. 76 and, hence, they are decoupled from the resistive effects arising from the TBR. These results are consistent with the other experiments studied in this thesis (chapters 6 and 7), where the same hydrodynamic modeling together with TBR values very close to the Diffuse Mismatch Model [132] explain other experimental configurations including metal-semiconductor interfaces in the absence of thick oxide layers.

Finally, in Fig. 18 we show the normalized substrate thermal conductivity within the Fourier framework required to fit the temperature profile in the heater and in the sensor for the different samples at different temperatures. Note that the apparent conductivity depends on the region where the temperature profile is fitted - a signature of non-Fourier transport. In contrast, the hydrodynamic model captures the measured deviations with respect to the bulk thermal conductivity, which depend on the temperature, the size, and the heater shape. The only exception is the smaller circular geometry at 100K, where KCM predicts a temperature lower than the reference one in the sensor. This prediction is not observed in experiments and cannot be fitted using a Fourier's model. More details about the breakdown of KCM in such extreme situations are provided in section 4.4.

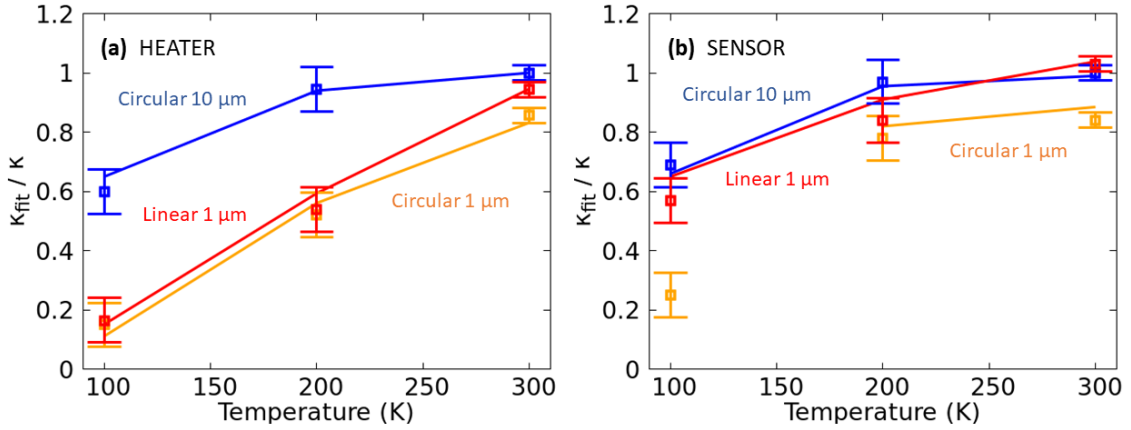


**Figure 18:** Normalized effective thermal conductivity to fit the temperature profile (a) in the heater, and (b) in the sensor, for different geometries and ambient temperatures. Comparison between experiments (squares) and hydrodynamic predictions (lines) is provided. The hydrodynamic prediction for the temperature in the sensor of the smaller circular geometry at 100K is lower than the reference temperature, and, hence, this case cannot be fitted using an effective Fourier model.



## 6 Frequency Domain Thermoreflectance

In collaboration with Centre de Recerca Matemàtica (CRM)

As explained in section 2.5 an effective form of Fourier's law with a reduced thermal conductivity or a size-dependent thermal boundary resistance has been widely used to interpret experimental observations of small size or high frequency effects. A paradigmatic example in which this approach has been applied are time-domain and frequency-domain thermoreflectance (TDTR/FDTR) experiments in which an oscillating laser heats a metal thin film (the transducer) on top of a semiconductor substrate, and the temperature evolution of the transducer is obtained by thermoreflectance techniques [22, 89, 158–162]. Specifically, these measurements have been interpreted as a way to measure the phonon mean free path spectrum and the cumulative thermal conductivity in the substrate because of the suppression of the modes with mean free paths larger than the thermal penetration depth. In this Chapter, we show that this picture is inadequate for a full description of this kind of experiments, and we propose the use of the hydrodynamic approach to successfully model all the experimentally observable magnitudes in silicon and germanium at different temperatures [134]. Moreover, we distinguish the role of the TBR between the transducer and the substrate from the non-Fourier heat conduction effects in the substrate. Consequently, we show that, in contrast to previous works using spectral or enhanced TBR values, the hydrodynamic description allows simple modeling of the interfaces with the use of frequency-independent TBR values very close to the DMM predictions.

### 6.1 Failure of Effective Fourier Theory in FDTR

We first motivate the use of non-Fourier heat transport models by demonstrating the inability of an effective Fourier model to reproduce the detailed temporal information obtained in FDTR experiments [89, 158]. In these experiments, a silicon substrate is heated with a sinusoidal laser pulse with frequency  $f$  and spot radius  $r_s=3.2 \mu\text{m}$ ; the thermal response is measured by a second laser with similar spot radius and compared with the original heating wave. To achieve this, the substrate is covered by a transducer of gold (64 nm in height) that absorbs the laser power through electron excitation and releases it to the substrate. From the amplitude of the temperature oscillations  $\Delta T$  in the transducer and the phase shift  $\varphi$  between the temperature response and the heating function, information about the TBR between materials and the thermal transport in the substrate can be obtained. The described experiment is very sensitive to the contact between the metal and the substrate. Hence, the authors include a thin layer of chromium between the gold and the silicon to reduce the TBR, thus making the experiment more sensitive to the substrate conduction [89]. To model the experiments, a Kapitza interface boundary condition with conductance  $210 \text{ MW m}^{-2}\text{K}^{-1}$  between the Au/Cr transducer and the Si substrate is assumed in [89]. This value is significantly smaller than the one expected at room temperature according to

the DMM. However, to analyze the effective Fourier modeling, we use the same conductance reported in [89].

In Fig. 19, we show the phase shift  $\varphi$  and the temperature amplitude  $\Delta T$  measurements compared with the results obtained using Fourier's law in the substrate with different values of the thermal conductivity. The blue line represents the results obtained using the bulk value of the thermal conductivity for the substrate. It can be seen that for very small frequencies the predictions for both  $\Delta T$  and  $\varphi$  agree with the experimental data, but as the frequency increases, both curves deviate from the data. In [89], this is interpreted in terms of an effective Fourier's law with a decreasing thermal conductivity with increasing frequency due to the ballistic suppression of phonon modes with MFP larger than the thermal penetration depth. The thermal penetration depth is defined as the depth at which the temperature increase due to the external excitation is attenuated by a factor  $1/e$ , and within the Fourier framework reads  $L_{\text{Si}} = \sqrt{\kappa_{\text{Si}}/(c_{\text{Si}}\pi f)}$ . In fact, to fit to the phase shift, the effective thermal conductivity must decrease with increasing frequency of the laser pulse beam, as shown in [89]. However, using this type of thermal conductivity leads to a poor fit to the temperature amplitude. To reproduce the reduction of the temperature amplitude  $\Delta T$ , the effective thermal conductivity for the substrate must increase with increasing frequency. In this case, the fit to the phase-shift curve becomes worse. The conclusion to this is that the use of a frequency-dependent effective thermal conductivity cannot simultaneously explain both experimental observables  $\varphi$ ,  $\Delta T$  at 311 K. This result indicates that the ballistic suppression of phonons is not an adequate framework to interpret the present experiments.

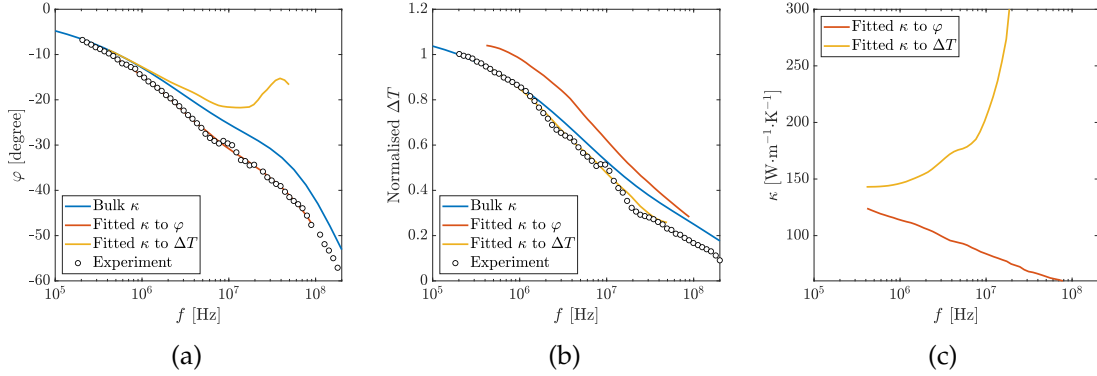


**Figure 19:** Reproduced from [134]. (a) Phase shift  $\varphi$  and (b) normalized temperature oscillation amplitude  $\Delta T$  as functions of the heating frequency  $f$  at 311 K. Curves denote predictions from effective Fourier models based on bulk and fitted values of the substrate thermal conductivity, the latter of which are shown in panel (c).

## 6.2 Non-Fourier response in Silicon

The hydrodynamic model is an alternative to describe the same experiment. As discussed in Chapter 5, generalization of the transport equation is only required to describe substrate conduction, where heat is mainly carried by phonons with a large mean free path and nonlocal effects are expected. For the transducer this change is not necessary, since in metals heat is mainly carried by electrons, which have a significantly shorter mean free path. Then, we use Eq. 76 and 75 for the substrate, and Eq. 1 and 75 including the laser heat source  $Q = Q_0 \sin(2\pi ft) \exp\left(\frac{-2r^2}{r_s^2}\right)$  in the transducer, where  $Q_0=1 \text{ Wm}^{-3}$ , and  $r$  is the radial coordinate. Regarding the boundary conditions, insulation is imposed in the transducer free surface 77. Moreover, continuity of the normal heat flux 84, the slip condition 81 for the tangential heat flux in the substrate, and the generalized temperature jump condition 92 are imposed in the interface. An schematic comparison of the transport equations and interface boundary conditions between the hydrodynamic and the Fourier's models is displayed in Fig. 1. All the parameters required in the transport equations and the boundary conditions for the substrate and the transducer, respectively, are provided in section 3.5, with the exception of the TBR that depends on the sample fabrication and should be experimentally characterized as explained below.

Figure 20 displays the hydrodynamic (KCM) and Fourier predictions for a given heating frequency. It shows that the nonlocal term included in the transport equation modifies the system thermal response with respect to Fourier. As it will be shown, these differences capture most of the phenomena observed in the FDTR experiment.

In Fig. 21, we show the corresponding hydrodynamic results for the phase shift  $\varphi$  at different temperatures 416, 311, 154, and 81 K compared with the experimental data [89] and the bulk Fourier prediction with the same thermal boundary resistance,  $R$ , as in the hydrodynamic description. For illustration, we also show that the bulk Fourier solutions with an increased TBR fitted to reproduce high-frequency measurements do not fit the low-frequency measurements. The normalized temperature oscillation amplitude  $\Delta T$  is also compared in Fig. 22 at the experimentally available temperature: 311 K. All quantities correspond to a weighted average across the surface of the transducer, computed using the Gaussian function of the probe beam as the weight according to the supplementary material of [158]. As displayed in the figures, the solutions of the model equations are obtained through two different methods in the present case: Finite Element methods (see section 11.1) and analytical methods (see section 11.2).

From Figs. 22 and 23 it can be observed that by using frequency-independent coefficients obtained from ab initio calculations of natural bulk Si (see section 3.5), we obtain good agreement between experiments and the KCM for both  $\varphi$  and  $\Delta T$ . In previous sections, it was shown that non-Fourier effects emerge in experiments involving small characteristic lengths comparable to the nonlocal length  $\ell$ . In the present case, the thermal penetration depth is the limiting length scale. By increasing the heating frequency, the penetration depth is reduced and

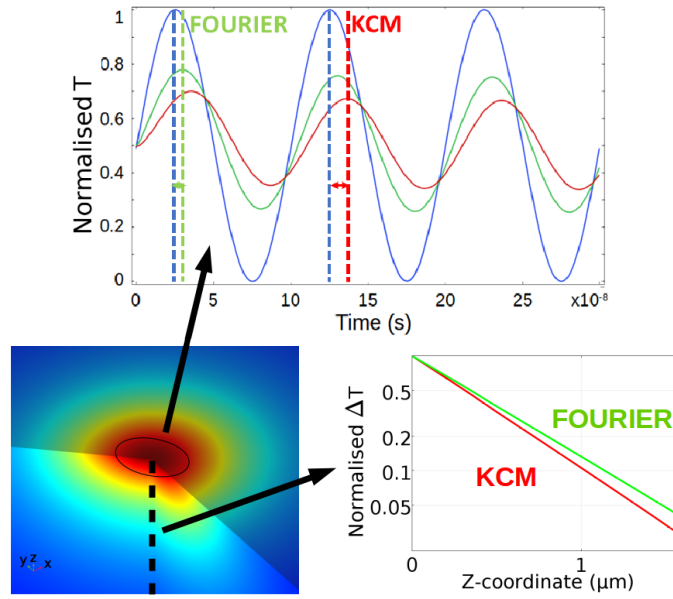


**Figure 20:** *Reproduced from [134].* Output obtained from the models for  $f=100$  MHz at 311 K. The top plot shows the heating energy density function (blue line) and the temperature evolution of the transducer surface according to bulk Fourier and the hydrodynamic (KCM) models, respectively. The right-bottom plot shows the amplitude of the temperature oscillations along the cross-plane direction.

non-Fourier effects become significant. For illustration, we include in the figures a blue shading indicating the range of frequencies for which the classical thermal penetration depth  $L_{\text{Si}} = \sqrt{\kappa_{\text{Si}}/(c_{\text{Si}}\pi f)}$  is larger than three times the microscopic characteristic length  $(1 + \alpha)\ell$ . Across the experimentally accessible range of frequencies, the memory term in the hydrodynamic equation 76 with coefficient  $\tau$  and the hydrodynamic corrections in the interface condition 92 only play important roles at temperature below 200 K and provide small corrections. The inclusion of the viscous (nonlocal) term with coefficient  $\ell^2$  in the heat transport equation is the main cause for the non-Fourier corrections. More specifically, the role of the volume viscosity term ( $\nabla\nabla \cdot \mathbf{q}$ ) is dominant in the present experiment, in front of the shear viscous term ( $\nabla \times (\nabla \times \mathbf{q})$ ) included in the Laplacian. This is due to the large value of the heating laser spot radius  $r_s \gg \ell$ , which cause shear viscous effects to be attenuated. This contrasts with other experiments where the size of the heat source is reduced to values similar to  $\ell$  (sections 7 or 5) and shear viscosity dominates. In consequence, the dominant term in the FDTR experiment is a purely transient term (note that it is null in steady-state situations like the ones described in section 4.2 or chapters 5, 8, because the energy conservation Eq. 75 reads  $\nabla \cdot \mathbf{q} = 0$ ).

The non-Fourier behavior predicted by KCM provides a description of the experimental data with a fixed set of parameters at different temperatures. In contrast, the Fourier-based description requires a nonphysically enhanced thermal boundary resistance  $R$  in order to fit the high-frequency measurements of the

phase shift, which leads to a poor fit at low frequencies, as can be seen in Fig. 21. In addition, the improved performance of the KCM allows for better modeling of the semiconductor-transducer TBR. In previous works using Fourier's law, a TBR that is dependent on the size of the contact has been used to interpret similar experimental results [57]. However, the resistance  $R$  is an intrinsic property determined only by the mismatch between the contact materials and the quality of the contact. Assuming no defects in the contact area of the interface and diffusive phonon reflections, a lower bound for the thermal boundary resistance  $R$  in the interface condition 92 is  $R_{\min} = (\gamma^{-1} + \gamma_{\Gamma}^{-1})/2$ , with  $\gamma$  and  $\gamma_{\Gamma}$  depending only on the specific heat and group velocities of the phonon modes in each material (a derivation of this lower bound using the hydrodynamic non-equilibrium distribution function can be seen in section 3.4). This thermal resistance arises from the phonon distribution function mismatch between chromium and silicon, and is in agreement with the diffuse mismatch model (DMM) [132]. Current fabrication processes do not allow perfect contact and hence the thermal resistance is larger than this lower bound. This is because the metal is sputtered on top of the substrate, which implies that the interface is not purely crystalline. We cannot quantitatively predict the value of  $R$  because of the lack of knowledge of the interface defects. However, it is natural to expect that the correction due to interface imperfections is temperature-independent. Consequently, we fitted a temperature-independent scaling factor with respect to the lower bound  $R/R_{\min} = 2.71$  in order to reproduce the experimental measurements at low frequencies (which do not depend on hydrodynamic effects, i.e., the bulk Fourier and the KCM predictions coincide, as can be seen in Fig. 21). This correcting factor is similar to the one obtained to characterize similarly fabricated samples in the experiments of Chapter 7. The rest of the terms in the interface boundary condition 92 are higher-order corrections derived from the non-equilibrium phonon distribution function describing the substrate close to the interface, as shown in section 3.4. These terms cause only small corrections in the present results.

A comment on the observed discrepancy at high temperatures and high frequencies  $f > 100$  MHz in Fig. 21 is in order. We modeled the Au/Cr transducer as a single domain with homogeneous properties. However, the presence of an interface between the 5-nm-thick chromium layer and the rest of the transducer influences the thermal response of the system at high frequencies, as suggested in [22]. In Fig. 23 we show alternative modeling results using the bulk Fourier and the hydrodynamic models considering detailed heat conduction in the transducer. Specifically, we assume that the energy deposition by the laser is restricted to the 5-nm-thick chromium layer due to the very weak electron-phonon coupling in Au as suggested in [22]. In addition, an extra Kapitza interface thermal resistance between the chromium layer and the rest of the transducer is expected. The thermal conductance value used for the Au-Cr interface is  $2 \text{ GWm}^{-2}\text{K}^{-1}$ , which is in reasonable agreement with previous work [22]. Therefore, complex heat transport in the transducer is a possible explanation for the extremely large phase shift measured at  $f > 100$  MHz. This refinement is only relevant at very high frequencies and, hence, does not significantly modify the phase-shift predictions at the experimentally accessible range of frequencies at low temperatures.

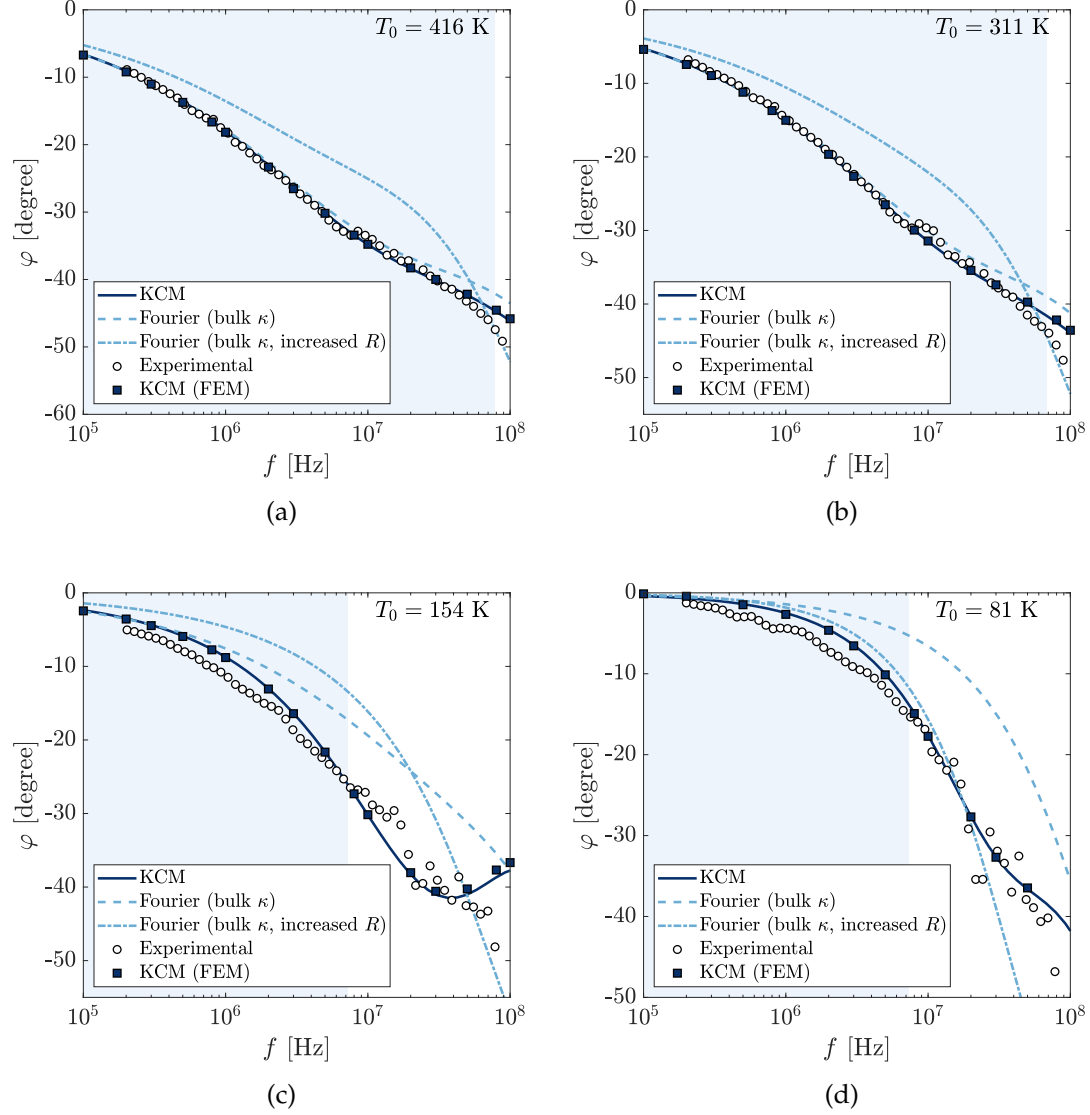


**Figure 21:** *Reproduced from [134].* Phase shift  $\varphi$  as a function of frequency  $f$  at (a) 416 K, (b) 311 K, (c) 154 K, and (d) 81 K. The hydrodynamic (KCM) and Fourier (bulk  $\kappa_{\text{Si}}$ ) solutions use a corrected TBR (denoted by  $R$ ), such that  $R/R_{\text{min}}=2.71$ , where  $R_{\text{min}}$  is the temperature-dependent TBR lower bound for Cr-Si interfaces reported in section 3.5. The Fourier (bulk  $\kappa_{\text{Si}}$ , increased  $R$ ) solution uses an enhanced TBR chosen to fit the high-frequency measurements, which leads to a poor fit at low frequencies. The agreement between the finite elements calculation (section 11.1) and the analytical solutions (section 11.2) is excellent.

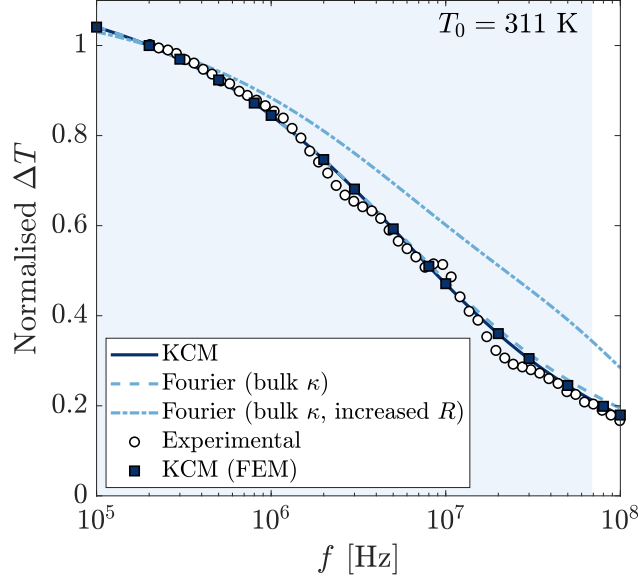


**Figure 22:** Normalized temperature amplitude  $\Delta T$  as a function of frequency  $f$  at 311 K using the different models specified in the caption of Fig. 21.

Furthermore, it only causes minor corrections to the obtained amplitude of the temperature oscillations. In particular, the result presented in Fig. 22 is almost the same.

The main effect of the nonlocal term of Eq. 76 is the modification of the thermal penetration depth as illustrated in Fig. 20. Analytical solutions to the model equations in the present case shed light on this previously unreported mechanism, and are provided in [134]. Specifically, they reveal that there are two modes of thermal transport, which are analogous to pressure (P-mode) and shear (S-mode) waves in viscoelastic media. The P-mode captures longitudinal flux waves that are irrotational (as in the case of Fourier's law), whereas the S-mode captures transverse flux waves that are divergence-free (and thus temperature-conserving). The transverse nature of the S-modes means they can only be a feature of three-dimensional heat conduction and would not be observed in one-dimensional models. Based on the analysis, we can define the penetration depths of the hydrodynamic P-modes and S-modes as  $L_P$  and  $L_S$ , respectively (see Fig. 24). Specific expressions for these penetration lengths can be found in [134]. The penetration depth  $L_S$  is proportional to the nonlocal length  $\ell$ . At low frequencies ( $f \ll \kappa_{\text{Si}}/(c_{\text{Si}}\ell^2)$ ), the penetration depth  $L_P$  is equivalent to  $L_{\text{Si}}$ , the classical penetration depth for Si derived from Fourier's law. However, at high frequencies ( $f > \kappa_{\text{Si}}/(c_{\text{Si}}\ell^2)$ ), the penetration depth  $L_P$  becomes proportional to  $\ell$  as well, with  $L_P/L_S \rightarrow (\alpha + 1)^{-1/2}$ , indicating that the penetration depth of both modes can become comparable. The coupling of both modes at high frequencies causes deviations in the thermal response of the substrate with respect to the classical description based on Fourier's law. Further analysis of the onset of these hydrodynamic heat transport effects can be found in [134].

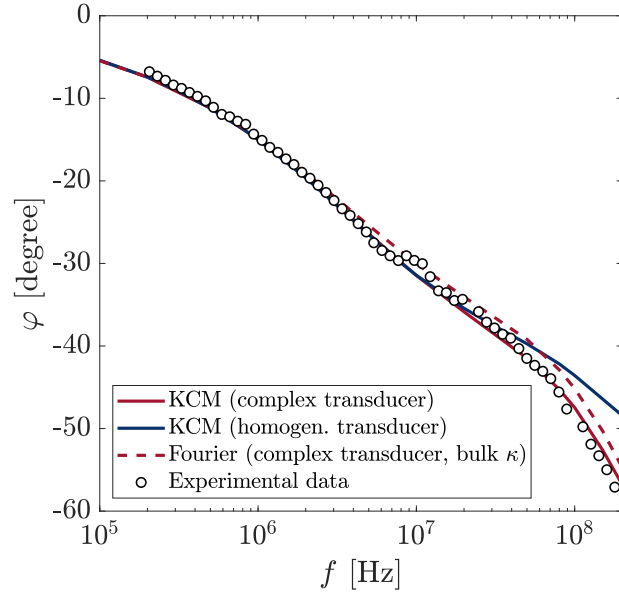


**Figure 23:** *Reproduced from [134].* Phase shift  $\varphi$  at 311 K as predicted from hydrodynamic (KCM) and Fourier models that consider the complex heat conduction in the Au/Cr transducer (purple line). The blue line corresponds to a numerical solution of the hydrodynamic model in which the Au/Cr transducer is modeled as a single homogeneous layer as in Fig. 21b.

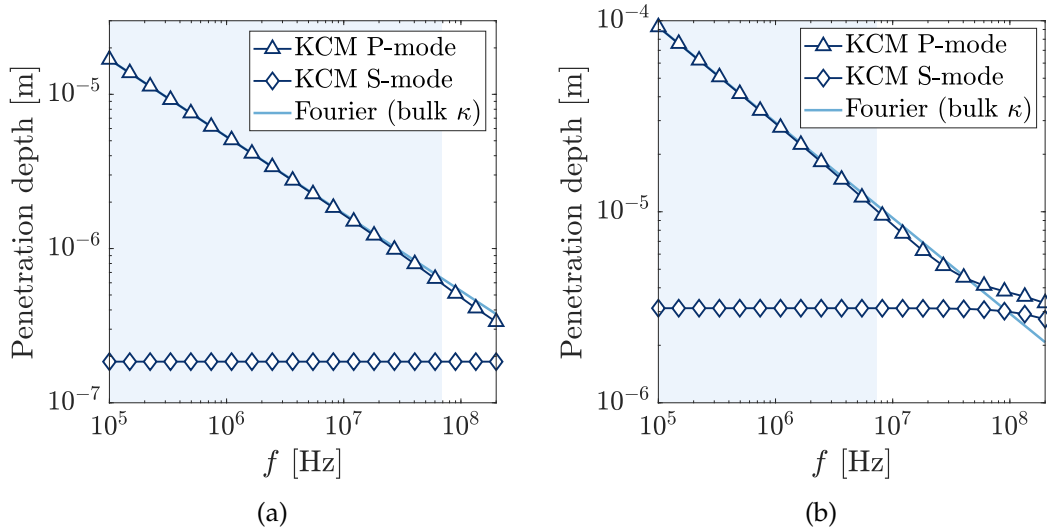


**Figure 24:** *Reproduced from [134].* The thermal penetration depths computed from Fourier and the hydrodynamic (KCM) models at (a) 311 K and (b) 81 K.



### 6.3 Non-Fourier response in Germanium

Sebastián Reparaz from the Institut de Ciències de Materials de Barcelona (ICMAB), repeated the same experiment in germanium at room temperature using similar laser spot radius and homogeneous Au transducers with similar height. In Fig. 25, we show the measured phase lag  $\varphi$  in two different samples with two different interfaces. In one case, the oxide was removed before fabricating the transducer on top of the germanium substrate, and in the other case the oxide was maintained.

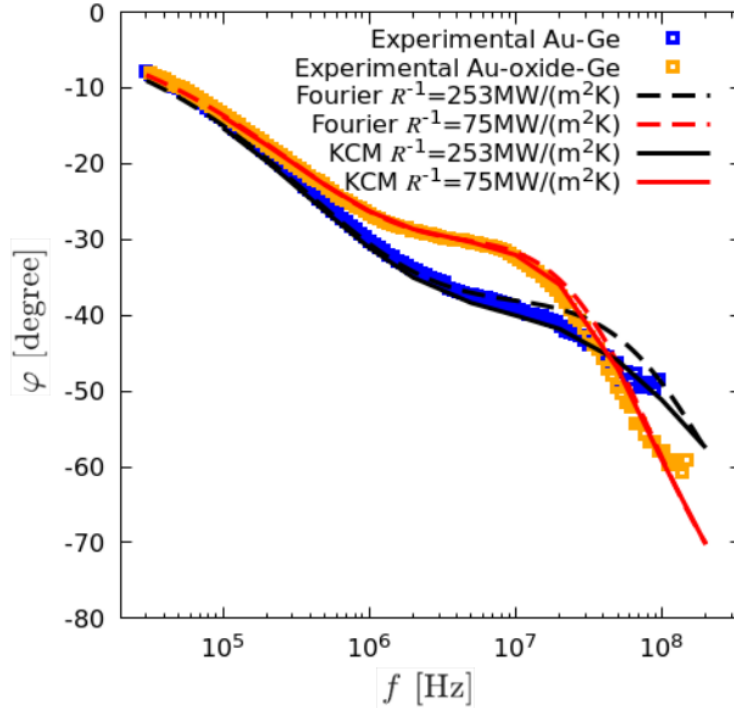


**Figure 25:** Phase shift  $\varphi$  as a function of frequency  $f$  at room temperature. Two sets of experimental data are shown: with (orange dots) and without (blue dots) an oxide interfacial layer. The Fourier (dashed lines) and hydrodynamic (solid lines) predictions using the equation parameters for the Ge substrate and the Au transducer displayed in section 3.5 are shown. The thermal conductances  $R^{-1}$  used are fitted from the low frequency range where the hydrodynamic and the Fourier predictions coincide.

The presence of the oxide layer significantly increases the thermal boundary resistance value. Following the same procedure explained in the previous subsection, we characterize the TBR value in each sample by fitting with a bulk Fourier model at low frequencies with nominal parameter values for all the domains. In the sample containing interfacial oxide, the Fourier model fits the experimental data even at the high frequency range. This is due to the extremely large TBR value dominating the system response, which hinders the non-Fourier effects emerging in the substrate. In consequence, the hydrodynamic and the Fourier modeling are almost equivalent in this case as can be seen in Fig. 25. Conversely, in the sample without oxide, where the TBR value is significantly

reduced, the Fourier modeling clearly fails to describe the measurements at high frequencies using the bulk thermal conductivity, as found for Silicon in the previous subsection. In this case the experimental data is reproduced using the same hydrodynamic modeling with using the appropriate equation parameter values for Germanium (see section 3.5). These results demonstrate the general applicability of the hydrodynamic model for kinetic materials like Silicon or Germanium in this kind of experiments, which provides significant corrections at high frequencies for high quality substrate-transducer interfaces (low  $R$ ).

## 7 1D- and 2D- confined nanostructure cooling in Silicon substrate: EUV-scatterometry technique

In collaboration with Kapteyn-Murnane group (University of Colorado)

In this Chapter we discuss the heat dissipation away from periodic 1D- and 2D-confined heat sources on a silicon substrate using dynamic EUV-scatterometry [57, 91, 92] at room temperature. This is the most illustrative example of the modeling capabilities of the hydrodynamic framework, since a simple analytic expression for the functional form of the heater temperature evolution is provided in terms of geometry and intrinsic material properties.

Both the 1D-confined (nanolines) and 2D-confined (nanodots) heaters were fabricated under identical conditions. As schematically shown in Fig. 26, the time-resolved measurements use an ultrafast infrared pump laser pulse to rapidly excite thermal heating and expansion in the metallic structures. The resulting thermal and elastic surface deformation is monitored by measuring the change in diffraction efficiency of an ultrashort EUV probe pulse. Using this technique, we observe the heat dissipation from nanodot arrays in general geometries without complex fabrication, and of nanoline arrays down to 20nm in size ( $L$ ) and 80nm in spacing ( $P$ ). It is observed that the relaxation of the nanostructures is slower for smaller  $L$ . Furthermore, closely-spaced nanodots or nanolines on a bulk silicon substrate cool faster than widely-spaced ones. Therefore, interpretation of this kind of experiments assuming Fourier's law for substrate heat transport requires the addition of phenomenological effective parameters like a geometry-dependent interfacial TBR [57, 91, 92] or a geometry-dependent substrate thermal conductivity [75]. In contrast, the hydrodynamic model presented in sections 3.3, 3.4, 3.5 provides predictive modeling of the full set of experimental data using fixed parameter values [163]. Furthermore, the hydrodynamic model allows identifying the time scales over which two different transport mechanisms are dominant: one characteristic time dominated by the thermal boundary resistance and another regime that is dominated by hydrodynamic heat transport in the substrate. As it will be shown here, these two distinct mechanisms at work during different time windows lead to a double exponential decay of the heater temperature in some cases. Hence, we are able to identify clear non-Fourier signatures in the present experiment that are fully explained through the inclusion of non-local heat transport effects (see section 4.1). Finally, we develop a two-box model, derived from the hydrodynamic equation 76, which provides physical intuition and specific expressions for the double exponential characteristic decay times and weights.

The sample consists of metallic Ni nanostructure arrays fabricated on the surface of a silicon substrate using an e-beam lithography technique. The nanostructure arrays are  $150 \times 150 \mu\text{m}^2$  areas consisting of both periodic nanolines and nanodots with linewidths ranging from  $1 \mu\text{m}$  down to 20 nm, periods ranging from  $4 \mu\text{m}$  down to 80nm, and average heights of 11.5 nm. The linewidth and period of the nanoline/nanodot arrays is independently controlled in order to

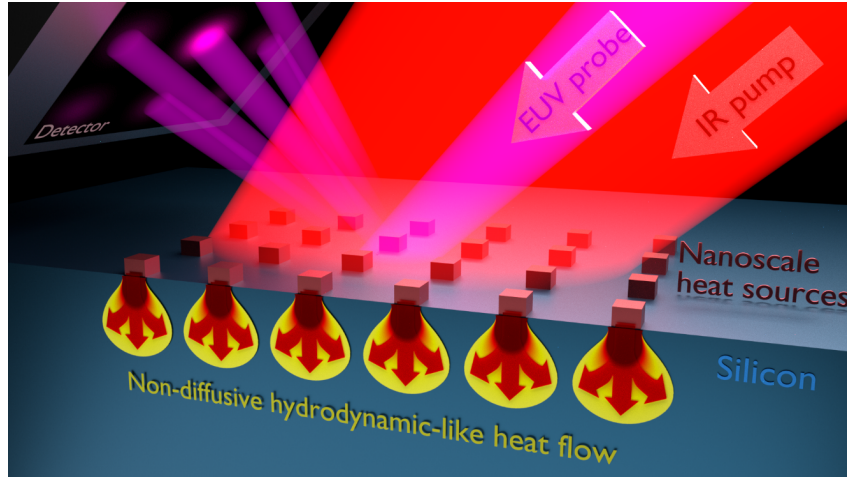


**Figure 26:** *Reproduced from [163].* Schematic of dynamic EUV-scatterometry for probing non-diffusive hydrodynamic-like heat flow. An ultrafast laser pulse rapidly heats the nanostructured transducers, which dissipate the thermal energy by transferring heat to the substrate. The resulting surface deformation of the heated nanostructures and substrate is measured via diffraction of an ultrafast Extreme Ultraviolet (EUV) probe pulse, after a controlled pump-probe time delay. The EUV pulse scatters from the periodic nanostructure arrays into a detector. We reduce the recorded scattering pattern into a single value of diffraction efficiency as a function of time delay between the pump and probe pulses, which precisely tracks the thermal and elastic dynamics in the sample.

separate the effects of size and spacing. The dimensions of the various arrays are characterized using atomic force microscopy. To launch dynamics in the sample, an ultrafast infrared (780 nm wavelength,  $\sim 25$  fs pulse duration) pump beam is incident on the sample with  $\sim 20$  mJ/cm<sup>2</sup> fluence and  $\sim 275$   $\mu$ m spot size. The pump light is preferentially absorbed by the metallic nanostructures which causes rapid heating followed by impulsive thermal expansion in the nanostructures. The coherent excitation of the periodic arrays launches acoustic waves that propagate along the surface of the silicon substrate. As the heated nanostructures cool down by thermal dissipation into the substrate, they relax back to their original profile. An ultrafast, short wavelength probe beam is generated by focusing an ultrafast infrared pulse into an Ar filled glass capillary. A quantum non-linear process called high harmonic generation converts a portion of the infrared light into a coherent short wavelength ( $\sim 30$  nm) ultrashort pulse duration ( $\sim 10$  fs) extreme ultraviolet (EUV) beam [164]. The short wavelength of the probe allows for exquisite picometer sensitivity to the surface displacement and allows for measurements of 10s nm nanostructures [165]. Moreover, these wavelengths interact with core electrons far from the Fermi surface which are not affected by small temperature changes as the photon energies are far from resonances in nickel, [165–167]. The probe beam is scattered from the nanostructure arrays at a set time delay, controlled by a mechanical delay stage, relative to the pump beam and captured on an EUV sensitive CCD camera. Images of the EUV scattering pattern with and without the pump beam are subtracted allowing us to observe

the change in the diffraction pattern. By subtracting the change in intensity of the reflected EUV light from the change in intensity of the diffracted EUV light, we can compute the change in diffraction efficiency. This change in diffraction efficiency is monitored as a function of time delay between the pump and probe beams and can be directly related to the surface deformation of the sample.

To model the experiments, the hydrodynamic heat transport equations including the thermoelastic coupling along with the elastic equations (see section 3.6) are used. The temperature and the heat flux are obtained by solving the energy conservation equation including the thermo-elastic energy exchange term in each domain 100 along with the heat transport equation (Fourier's law for the heaters and Eq. 76 for the substrate). In the heaters, a heat source  $Q$  modeling the laser pulse is introduced in the energy conservation equation. The slip boundary condition 81 is imposed in the interfaces and in the silicon free surfaces. In the free surfaces, thermal insulation 77 is ensured by fixing normal component to zero. In the interfaces, we impose continuity of the heat flux normal component. Finally, the generalized boundary condition for the temperature jump 92 is used. All the thermal parameter values are calculated ab initio and can be found in section 3.5, except the interfacial boundary resistance  $R$  appearing in 92. Using ab initio calculations, we compute a lower bound  $R_{\min}$  for the thermal boundary resistance assuming diffusive phonon reflections and perfect contact area (see section 3.4). However, the nano-gratings fabrication process produces interface defects that increase the actual boundary resistance value. Therefore, a single correcting factor for the boundary parameters is required to predict the thermal decay of all the gratings (1D and 2D). In analogy to the TBR characterization in Chapter 6, the obtained correcting factor is fitted from the thermal decay of the largest experimentally available 1D grating ( $L=1\mu\text{m}$ ), where the hydrodynamic corrections do not play any role (i.e. we obtain the same boundary resistance correction using the hydrodynamic or the Fourier model). Specifically, we obtained a thermal boundary resistance value 3.1 times larger than the lower bound  $R_{\min}$  (see section 3.4). This factor is similar to the one obtained in other experiments for a similarly fabricated metal-semiconductor interface.

The thermal equations are coupled with the classical elastic equation 93 to predict the surface deformation of the system (i.e. the local displacement vector  $\mathbf{u}$ ) in order to compute the resulting change in diffraction efficiency using numerical Fresnel propagation. The mass density  $\rho$  is  $8900 \text{ kg}\cdot\text{m}^{-3}$  and  $2329 \text{ kg}\cdot\text{m}^{-3}$  for Nickel and Silicon, respectively. The stress tensor of the nickel and the silicon includes a linear thermal expansion term. For heaters, we use the standard stress tensor 96 and nominal bulk nickel elastic properties: thermal expansion coefficient  $\alpha_{\text{Ni}}=12.77 \cdot 10^{-6} \text{ K}^{-1}$ , compressibility modulus  $K_{\text{Ni}}=175 \cdot 10^9 \text{ Pa}$ , and shear modulus  $\mu_{\text{Ni}}=76 \cdot 10^9 \text{ Pa}$ . For the substrate, we use an anisotropic stress tensor accounting for the structural defects generated during the fabrication of the nano-gratings on the substrate top surface [136]:

$$\sigma = D : [\nabla \mathbf{u} - \alpha_{\text{Si}}(T - T_0)\mathbb{I}] \quad (114)$$

where  $T_0 = 295\text{K}$  is the reference temperature,  $\alpha_{\text{Si}}=3 \cdot 10^{-6} \text{ K}^{-1}$  is the Silicon coefficient of thermal expansion, and  $D$  is the anisotropic elasticity matrix. In Voigt

notation  $\{yy, xx, zz, xz, yz, zx\}$ , the components of  $D$  read  $D_{11} = 203, D_{12} = 66.5, D_{22} = 173, D_{13} = 36.5, D_{23} = 66.5, D_{33} = 203, D_{14} = 0, D_{24} = 0, D_{34} = 0, D_{44} = 83, D_{15} = 0, D_{25} = 0, D_{35} = 0, D_{45} = 0, D_{55} = 53, D_{16} = 0, D_{26} = 0, D_{36} = 0, D_{46} = 0, D_{56} = 0, D_{66} = 83$  [GPa] to match the simulated geometry that  $y$  is along  $[001]$  and  $x$  (interface normal direction) is along  $[110]$  in the silicon crystal. Finally, the Silicon compressibility modulus and shear modulus are  $K_{\text{Si}}=95 \cdot 10^9$  Pa, and  $\mu_{\text{Si}}=52 \cdot 10^9$  Pa, respectively.

## 7.1 Non-local Effects and Hydrodynamic Region

As discussed in section 4.4, the applicability of Eq. 76 with ab initio parameters is restricted to geometries where edge effects produced by two different boundaries do not overlap, i.e. when boundaries are separated by a distance larger than  $2\ell$ . Here, the distance between heaters is  $P - L$  (see Fig. 27). Thus, Eq. 76 is expected to be valid for nanostructure arrays satisfying  $P - L > 2\ell$ . We term experiments under this condition, where heaters are expected to behave independently, as effectively isolated heat sources, and those with  $P - L < 2\ell$  as close-packed heaters.

We first study effectively isolated heat sources for both 1D-confined (nanolines) and 2D-confined (nanodots) of different sizes and periodicities. Figure 27 compares the experimental results on nanolines and nanodots with theoretical hydrodynamic solutions obtained using COMSOL. We compare both inertial solutions, that include elastic waves generated by the impulsive pump laser excitation (i.e. the full elastic equation 93 is solved), and quasi-static solutions without elastic waves to isolate the effects of the heat flow (i.e. the elastic equation 93 is simplified to the dynamic equilibrium condition  $\nabla \cdot \sigma = 0$ ). The quasi-static solutions capture the deformations just due to thermal expansion and hence can be used to track the temperature evolution of the system [92]. Note that the initial peak obtained in the quasi-static simulations is not observed in experiments because the system needs finite time to expand. To compare the model predictions and the experiments, the predicted diffraction efficiency is scaled by a factor to match the first experimental peak. Since the hydrodynamic model is linear, this is equivalent to scaling the simulated energy density by this factor. The same scaling is used to normalize the quasi-static simulations. This procedure is also applied to the effective Fourier simulations in order to compare Fourier and experiments in Fig. 29. The excellent agreement in Figure 27 between experiment and theory demonstrates a significant advance in modeling - the nanoline thermal decay has already been shown to be highly non-diffusive [57, 92] and the models employing a suppression function are not easily calculable for nanodot geometry [75]. The hydrodynamic model - which is based on only a few key parameters - accurately predicts the thermal transport and elastic waves in both nanolines and nanodots without any geometry-dependent fit parameters, which is beyond the current capabilities of microscopic descriptions.

In the close-packed situation,  $P - L < 2\ell$ , nonlocal effects are expected to yield interaction between heaters, as phonons from a given source are able to

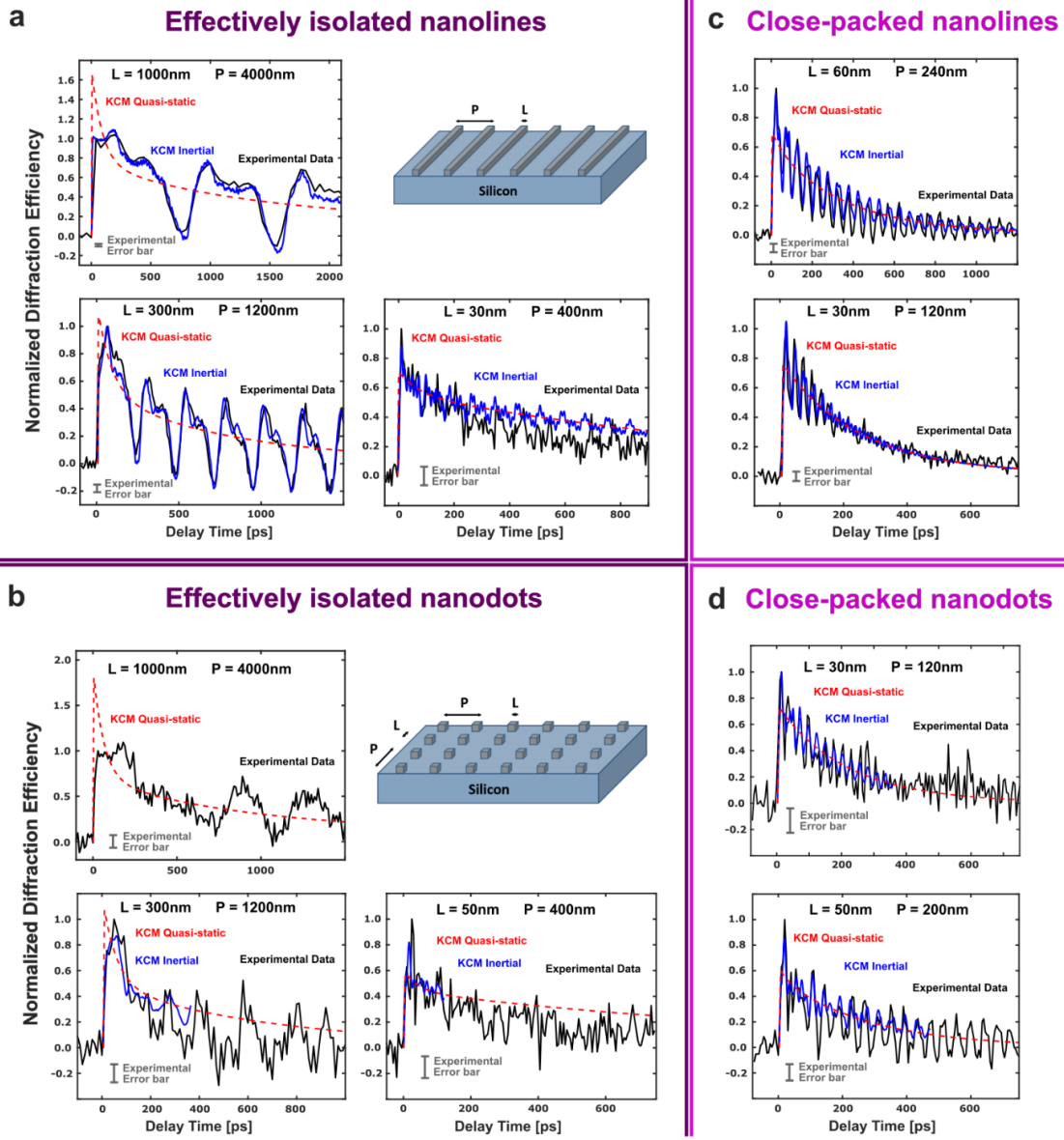


**Figure 27:** *Reproduced from [163].* Experimental and theoretical normalized change in diffraction efficiency as a function of delay time for different sizes  $L$  and periods  $P$  for (a) effectively isolated, i.e. where  $(P - L) > 2\ell$ , nanolines (1D) and (b) nanodots (2D). Black lines denote experimental data where the error is represented by the gray bar. Blue lines indicate the inertial hydrodynamic (KCM) predictions, and red lines denote the hydrodynamic (KCM) quasi-static predictions. Theoretical predictions are computed using the same geometry-independent parameters for all nanostructure sizes and shapes. The theoretical curves are identically normalized in each case so that the initial energy released to the heaters matches experiment. Also shown are the experimental and theoretical changes in diffraction efficiency for close-packed, i.e.  $(P - L) < 2\ell$ , (c) nanolines (1D) and (d) nanodots (2D) of different sizes  $L$  and periods  $P$ . The excellent agreement between KCM and the experimental data for the highly non-diffusive decay for both 1D- and 2D-confined heat source geometries demonstrates the predictive capability of this model.

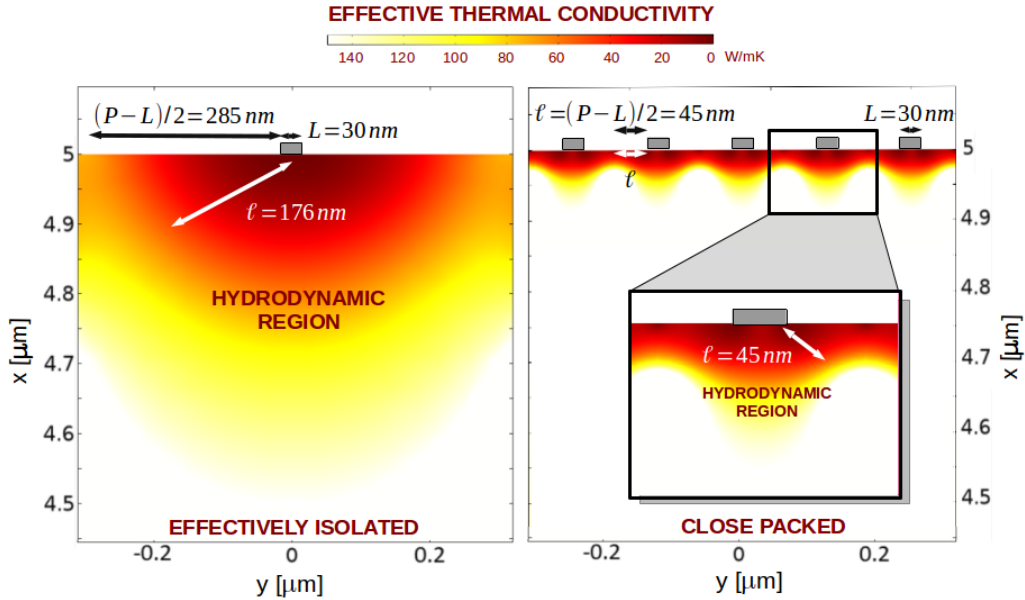


**Figure 28:** *Reproduced from [163].* Hydrodynamic regions in effectively isolated and close-packed situations. Effective thermal conductivity profile on silicon,  $|q|/|\Delta T|$ , predicted by the hydrodynamic model for a nanoheater of width 30 nm at  $t=0.5 \text{ ns}$  for (left) isolated ( $P=600 \text{ nm}$ ) and (right) close-packed ( $P=120 \text{ nm}$ ) configurations. Similar to fluids, a friction-like reduction of thermal transport appears in the regions of the substrate where heat flux gradients are large. Parameter  $\ell$  defines the characteristic size of the region below heaters where these hydrodynamic effects are important (hydrodynamic region). When sources are separated a distance larger than  $2\ell$  (effectively isolated lines) one uses the intrinsic value for  $\ell$ . When this distance is smaller, i.e.  $(P-L) < 2\ell$ , an effective value  $\ell_{\text{eff}} = (P-L)/2 (< \ell)$  is used. The red color indicates regions where the thermal transport has been reduced (compared to diffusion) while the white color represents regions of diffusive transport. In close-packed configurations, the interaction between heaters homogenizes the profile thus reducing viscous effects to a smaller region of size  $\ell_{\text{eff}}$ . As a result, close-packed configurations evacuate heat faster than isolated lines of the same width. The profiles shown do not appreciably change during the timescale of experiments. Note that scales are the same in both panels.



reach neighboring sources before scattering. In this case, one does not expect Eq. 76 to be applicable since higher order derivatives should be included in the transport equation [68] (see section 4.4). To keep the model as simple as possible, we propose that the effects of these higher order terms can be absorbed into a geometry-defined value  $\ell_{\text{eff}}$ , where Eq. 76 is still sufficient to describe the system. We propose the simplest expression that satisfies limiting cases:  $\ell_{\text{eff}} = (P-L)/2 < \ell$ . For this expression, when the period  $P$  tends to the linewidth  $L$ ,  $\ell_{\text{eff}} \rightarrow 0$ . In this limit, the grating tends to a line of infinite linewidth, thus viscous effects should vanish. In the other limit, if  $P-L \rightarrow 2\ell$ , we recover  $\ell_{\text{eff}} \rightarrow \ell$  as constructed. Using this expression for  $\ell_{\text{eff}}$ , we compare hydrodynamic predictions with experimental results for close-packed nanoline (nanodot) heaters in Figure 27c(d). The model predicts that closely-spaced heat sources cool faster than widely-spaced ones, as uncovered in previous experiments [57, 92]. We also experimentally demonstrate that this same counter-intuitive behavior observed in nanoline arrays is universal and manifests in nanodot arrays, since the  $L=50$  nm with  $P=200$  nm nanodot signal is relaxed at 800 ps while  $L=50$  nm with  $P=400$  nm is not. The excellent agreement between the hydrodynamic prediction and experimental results for the close-packed cases shows that the model can capture this behavior with a simple expression for  $\ell_{\text{eff}}$  (without fitting) while the other parameters used are the same used in the isolated cases.

In summary, both nanoline and nanodot experiments can be predicted by the hydrodynamic model using the intrinsic value for  $\ell$  at room temperature (see section 3.5) when sources are separated a distance larger than  $2\ell$  (effectively isolated sources), and a geometry-defined effective value when distances are smaller (close-packed sources). This modification of  $\ell$  for a specific situation allows us to retain both the predictive capability and simplicity of the model.

We interpret now the behavior of the effectively isolated sources from a hydrodynamic viewpoint and compare it to the close-packed sources. For effectively isolated sources, hydrodynamic effects become relevant when linewidth  $L$  is on the same scale as the average phonon mean free paths  $\sim \ell$ ; thus, the non-local terms in Eq. 76 reduce the heat flux, compared to Fourier's law, in agreement with experiments [57, 62, 75, 87, 91, 92]. This phenomenon is analogous to a friction that arises from the large gradients in heat flux that impedes heat flow, referred to as a viscous resistance [120]. In other words, when linewidth  $L$  is on the same scale as  $\sim \ell$ , there is not enough resistive phonon collisions to scatter the heat outward in all directions as diffusion assumes. Instead, the thermal energy is forced straight downward into the substrate over a distance related to  $\sim \ell$  before enough resistive phonon collisions occur to dissipate energy in all directions, shown schematically in Figure 26. These hydrodynamic-like friction effects resulting from a lack of resistive collisions have been described in other formalisms albeit with different interpretations (see section 2.5). For example, models using a phonon suppression function predict heat flow that is less efficient than Fourier's law when linewidth  $L$  is on the same scale as  $\sim \ell$ , similar to the hydrodynamic model; however, this phenomenon is interpreted as a reduced number of carriers due to ballistically traveling phonons [95, 168]. Additionally, models incorporat-

ing anisotropic behavior of thermal conductivity are parallel to the downward flux forcing predicted by our hydrodynamic model [22]. The viscous term in Eq. 76 naturally includes both heat flux reduction and apparent anisotropy observed by experiments. In Figure 28, we visualize these substrate regions where viscous effects are important (hydrodynamic regions) by converting results to a spatially-dependent effective thermal conductivity of silicon. Due to their proximity to the interface, if one tries to apply Fourier's law, hydrodynamic effects might be interpreted either as an increase of the thermal boundary resistance [57] or as a reduction of the thermal conductivity near the heater [75]. Further details about the hydrodynamic region and the process of heat release from a nanostructured heat source towards a semiconductor substrate can be found in section 5. In the effectively isolated case with  $L=30$  nm and  $P=600$  nm, this region has a size of order  $\ell \sim 200$  nm, while in the close-packed case ( $P=120$  nm), it is much smaller and of order  $\ell_{\text{eff}} \sim 50$  nm. Therefore, we hypothesize that the interaction of the nearby heat sources in the close-packed scenario reduces the non-local length, decreasing viscous effects, allowing the system to cool more efficiently than with isolated heaters. Future work should address the microscopic description of this effect.

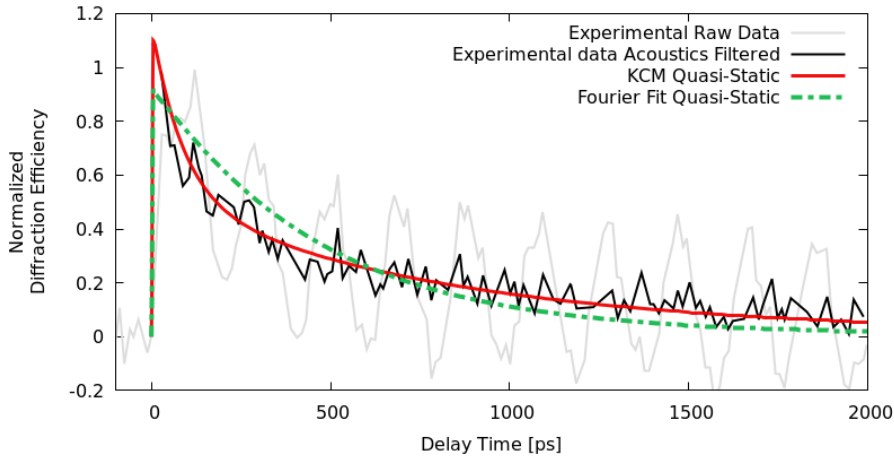


**Figure 29:** *Reproduced from [163].* Experimental and theoretical quasi-static change in diffraction efficiency. Comparison of the thermal relaxation for effectively isolated heater lines of  $L=250$  nm and  $P=1000$  nm. The black (grey) line denotes experimental data without (with) acoustics, the red line is the hydrodynamic (KCM) prediction using intrinsic parameters, while the green line is a Fourier model using an effective thermal boundary resistance value fitted to obtain the best match to data. The Fourier fit overestimates experimental decay at short times and underestimates it at long times. Experimental measurements indicate that the thermal decay of heaters cannot be described by just one characteristic time, like the prediction by Fourier's model; however, the hydrodynamic model captures the decay for all times.

To demonstrate the advantages of our hydrodynamic model over the traditional effective Fourier model with a best-fit boundary resistance, we compare the two theoretical predictions to experimental data for the isolated 250 nm

linewidth case in Figure 29. To emphasize the thermal decay of the system, we compare only the quasi-static calculations and data where the acoustic waves have been subtracted using the matrix pencil method [169, 170]. Although an effective Fourier model can quantify the degree of the non-diffusive nature of the system, one finds that the Fourier model with a fitted TBR fails to describe data at all times, as it overestimates the decay at the beginning and underestimates it at the end. In contrast, the hydrodynamic predictions agree with data at all times. This plot indicates that the experimental results display two characteristic times: a fast one at short times and a slow one at longer times. These two different time scales are also apparent in the other nanostructure sizes shown in Figure 27. Therefore, as diffusive transport in these geometries contains only a single characteristic time scale, the effective Fourier model cannot capture the full nanostructure relaxation and misses the underlying physics, even with fitted intrinsic parameters.

## 7.2 Thermal Decay Analysis: Diffusion vs Hydrodynamics

Here we compare in detail the thermal evolution of the heater according to the Fourier and hydrodynamic models. First consider diffusive heat transport both in the Si substrate and in the Ni heater along with a Kapitza interface boundary condition with resistance  $R$ . We use the bulk thermal properties reported in section 3.5 and we denote the thermal diffusivity of Nickel  $\chi_{\text{Ni}} = \kappa_{\text{Ni}}/c_{\text{Ni}} = 2.2 \cdot 10^{-5} \text{ m}^2 \text{ s}^{-1}$  and of silicon  $\chi_{\text{Si}} = \kappa_{\text{Si}}/c_{\text{Si}} = 9 \cdot 10^{-5} \text{ m}^2 \text{ s}^{-1}$ . For illustration purposes, we discuss this benchmark model considering the specific case of heater height  $h = 10 \text{ nm}$  and width  $L = 20 \text{ nm}$ , with  $R = 1 \cdot 10^{-9} \text{ K m}^2/\text{W}$ . In Figure 30 we show the corresponding temperature evolution of the heater obtained with COMSOL Multiphysics.

The time scale of the thermal evolution in the heater is extremely fast  $h^2/\chi_{\text{Ni}} = 4.5 \text{ ps}$  and hence the temperature in the heater is almost uniform within the time scale of the experiment. In the substrate, at time  $t$ , diffusion has penetrated a region of size  $\sqrt{t\chi_{\text{Si}}}$ . We can quantify an effective thermal resistance due to diffusion  $r(t) = \sqrt{t\chi_{\text{Si}}}/\kappa_{\text{Si}}$ . At early times  $R > r(t)$ , so the thermal decay is dominated by the interface. At times larger than  $R^2\kappa_{\text{Si}}c_{\text{Si}} = 232 \text{ ps}$ , we have  $r(t) > R$  thus the thermal decay is dominated by substrate diffusion:

- For  $t < R^2\kappa_{\text{Si}}c_{\text{Si}}$ : The heat flux in the interface is  $|\mathbf{q}| = \Delta T/R$ , where  $\Delta T$  is the temperature difference between the heater and the substrate across the interface. Moreover, the heat flux leaving the heater can be estimated as  $|\mathbf{q}| \sim c_{\text{Ni}}hR \frac{dT}{dt}$ , and hence  $\Delta T \sim -c_{\text{Ni}}hR \frac{dT}{dt}$ . Therefore, the temperature evolution of the heater is an exponential with characteristic time  $\tau_{\text{F}} = c_{\text{Ni}}hR = 40 \text{ ps}$ .
- For  $t > R^2\kappa_{\text{Si}}c_{\text{Si}}$ : Substrate diffusion has no characteristic time scale (infinite substrate) and hence the thermal decay follows a power law with an exponent depending on the space dimensionality. The thermal evolution in the

region below the heater is instantaneous  $L^2/\chi_{\text{Si}}=4.4$  ps and hence we can consider that the heated region is a point and the temperature evolution is 2D (exponent -1).

In summary, the Fourier model predicts an initial exponential thermal decay with characteristic time  $\tau_F = c_{\text{Ni}}hR = 40\text{ps}$  followed by a power law decay with exponent -1. The transition between both decays is estimated to be at time  $R^2\kappa_{\text{Si}}c_{\text{Si}}=232$  ps.

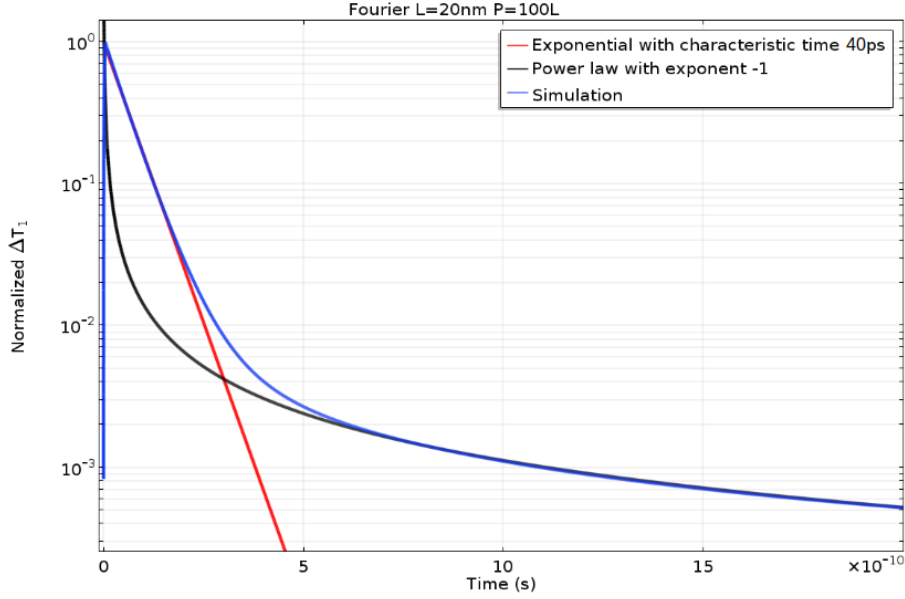


**Figure 30:** Heater temperature evolution for  $h=10$  nm,  $R=1\cdot 10^{-9}\text{K m}^2/\text{W}$ ,  $L=20$  nm and  $P=100L$  according to Fourier model. The initial decay is fitted using an exponential and the long-time decay is fitted using a power-law.

As shown in Figure 29, the functional form of the thermal decay according to Fourier's law is not consistent with the experimental decay from EUV scatterometry measurements, where a double exponential decay with two distinct characteristic times is observed. Care must be taken when comparing our results with those from time-domain thermal reflectance (TDTR) [75], which are two completely different techniques. One key difference is that visible-based probe experiments often need to limit the analysis to the region  $t > 500$  ps due to the challenges separating the contributions of out-of-equilibrium electrons and thermal decay. However, our EUV probe does not suffer from this limitation as we measure the surface deformation through diffraction, which is not altered by the presence of nonequilibrium electrons. If we take EUV scatterometry data and exclude from our analysis the measurements for  $t < 500$  ps, one of the decay times ( $\sim 100$  ps) reported in this work cannot be observed. Consequently, a diffusive model could fit the experimental data by excluding the initial timescales, as done in previous works like [75]. In Figure 31, we show two different fits using Fourier with an effective TBR and an effective substrate conductivity, respectively, restricted to  $t > 500$  ps. Both approaches can reproduce the tail of the

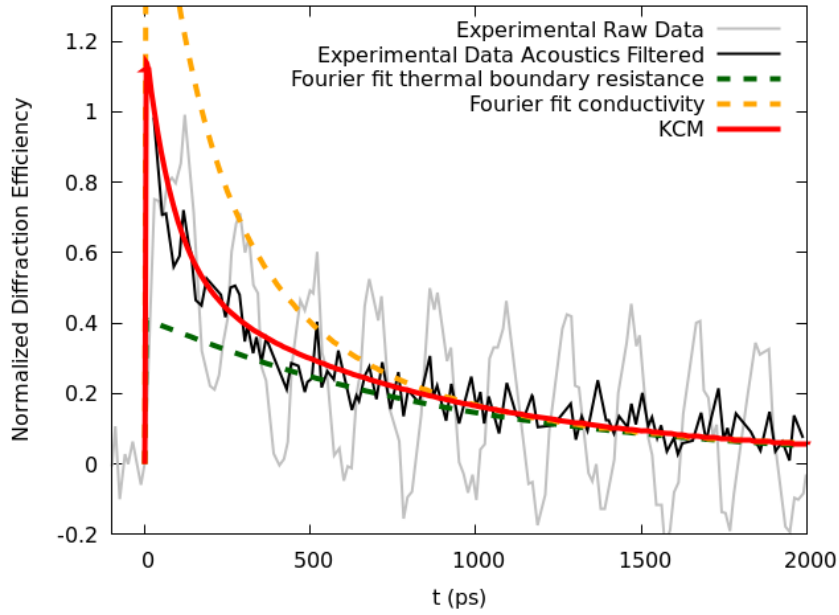


**Figure 31:** Fourier fits to experimental data restricted to  $t > 500$  ps for a heater line of 250 nm. The TBR fit ( $R = 19 \cdot 10^{-9} \text{m}^2 \text{K/W}$ ) using the intrinsic value for the substrate conductivity underpredicts the temperature for  $t < 500$  ps, whereas the conductivity fit ( $\kappa_{\text{fit}} = 0.4 \kappa_{\text{Si}}$ ) using the intrinsic value for the TBR overpredicts it. In both models, the predicted fraction of energy evacuated from the heater is substantially distorted.

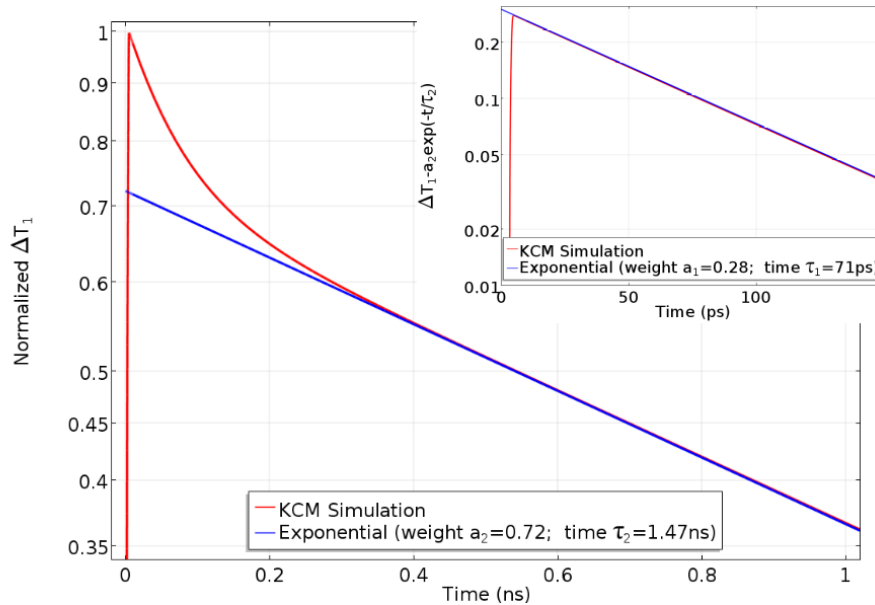


**Figure 32:** Heater temperature evolution for  $L = 30 \text{nm}$  and  $P = 400 \text{nm}$  according to the hydrodynamic model (KCM). The thermal decay is fitted with a double exponential.

decay but fail to reproduce the initial system response. After the first nanosecond, these models are able to reproduce just the last 20% of the signal amplitude but cannot predict the other 80%, i.e. the largest part of the energy dissipation from heaters which is also the most important for applications.

We assume now diffusive heat transport in the heater and hydrodynamic heat transport in the substrate using the hydrodynamic model as explained above. In figure 32, we show an example of the temperature evolution of the heater for  $L=30$  nm and  $P=400$  nm obtained with COMSOL. In contrast to the Fourier model, the hydrodynamic model predicts a slower thermal decay that can be fitted using a double exponential within the time scale of the experiment. We denote as  $\tau_1, \tau_2, a_1, a_2$  the characteristic times and weights of the first and the second exponentials, respectively.

### 7.3 Two-Box Model for Heater Thermal Decay

A distinct advantage of the hydrodynamic model (KCM) is that we can gain deeper insight into the two time scales of thermal relaxation by investigating the role played by hydrodynamics. To do this, we analytically solve the thermal equations in the heater and the substrate for the case  $L < \ell$ . In this range, hydrodynamic effects are dominant: the  $\mathbf{q}$  term in Eq. 76 can be neglected compared to the Laplacian term and the heat flux obeys the (linear) Navier-Stokes equation. The system of equations obtained is:

$$C_1 \frac{dT_1}{dt} = -\frac{T_1 - T_2}{R_1} \quad (115)$$

$$C_2 \frac{dT_2}{dt} = -\frac{T_2 - T_2^\ell}{R_2} + \frac{T_1 - T_2}{R_1} \quad (116)$$

where  $T_1$  is the heater temperature,  $T_2$  the average temperature of the substrate at the interface, and  $T_2^\ell$  the average substrate temperature in the outer part of the hydrodynamic region, i.e. at a depth of order  $\ell$  below the heater.  $C_1 = c_{\text{Ni}}h$  denotes the heat capacity of the heater per unit surface, with  $h$  the height of the heater.  $C_2 = c_{\text{Si}}L(1 + \alpha)/B$  is a heat capacity per unit surface characterizing the substrate, with  $L$  the width of the heater,  $\alpha$  the dimensionless coefficient appearing in equation 76, and  $B$  is a calculated geometric coefficient that for nanolines is 3.0.  $R_1 \equiv R$  is the thermal boundary resistance between the metal and the substrate, and  $R_2 = \frac{B\ell^2}{\kappa_{\text{Si}}L}$  is a size-dependent thermal resistance due to viscous effects. At short times,  $T_2^\ell$  is close to  $T_2^\infty$  as heat has not reached this region and equations 115 and 116 become a linear system with a double-exponential decay:

$$T_1 - T_2^\infty = a_1 \exp\left(-\frac{t}{\tau_1}\right) + a_2 \exp\left(-\frac{t}{\tau_2}\right) \quad (117)$$

with  $\tau_i$  and  $a_i$  the characteristic times and weights, which are determined by  $C_1, C_2, R_1$  and  $R_2$ . Therefore, the hydrodynamic model provides two characteristic

times with specific expressions in terms of the physical properties of the system. Detailed derivation of the previous equation and its coefficients can be found in the next subsection.

Equation 117 can be interpreted intuitively as a two-box model as seen in Figure 33. One box represents the heater, while the other box is a region of order  $L$  in the substrate below the heater (referred to as the dam region). The thermal response of the system begins when the heater is filled with thermal energy from the laser pulse. At short times after the laser pulse, the heater releases the energy into the dam region, which retains the energy and rapidly increases in temperature. The initial rate of this energy transfer is dominated by the intrinsic thermal boundary resistance between the heater and substrate. At larger times, when the dam region has equilibrated with the heater, the dissipation of the thermal energy is dominated by the rate of energy transfer out of the dam region into the rest of the substrate. Therefore, the substrate plays two roles in the thermal response of the system: it acts both as an energy reservoir with heat capacity  $C_2$  and as a thermal resistance  $R_2$ . The rate of energy transfer in these later times is controlled by the viscous resistance, i.e. hydrodynamic effects. The thermal relaxation of the heaters can be described by an equivalent circuit (Figure 33a) and illustrated by a fluid analog (Figure 33c). The predicted temperature evolution of the system as a function of time and position are shown in Figure 33b.

As shown in the next section, for small isolated sources, we find simple expressions for the characteristic times, namely  $\tau_1 = R_1 C_{\text{eq}} = R_1 C_1 C_2 / (C_1 + C_2)$ , and  $\tau_2 = (C_1 + C_2) R_2$ . For nanolines of  $L=50$  nm, these expressions yield  $\tau_1=50$  ps and  $\tau_2=1050$  ps, thus  $\tau_2$  is an order of magnitude larger than  $\tau_1$ . In this limit,  $\tau_1$  depends on the thermal boundary resistance, while the viscous time scale  $\tau_2$  does not depend on the thermal boundary resistance, but mainly on the nonlocal length  $\ell$  and geometry:

$$\tau_2 = \frac{\ell^2 c_{\text{Si}}}{\kappa_{\text{Si}}} \left( 1 + \alpha + B \frac{c_{\text{Ni}} h}{c_{\text{Si}} L} \right). \quad (118)$$

Therefore, for small isolated sources, KCM can provide simple analytical expressions for the two different time scales of the heat transfer, each one associated with a different resistive mechanism. This allows accurate experimental validation of the non-local length value for silicon at room temperature. Additionally, the two-box model Eqs. 115 and 116 can also be applied to close-packed experiments by substituting  $\ell$  by  $\ell_{\text{eff}}$ ; however, the simple expression of Eq. 118 cannot be used in this case (see details in the next section).

Although the two-box model has been derived at small sizes, it also characterizes the non-Fourier behavior for all experimental sizes. To validate the intuition provided by the two-box model, we fit a double-exponential decay 117 to each of our experimental measurements, as shown in Figure 34a. We compare the fits of experiments to fits of numerical hydrodynamic simulations and the analytical two-box model in Figure 34b-d. We find that the experimental fit results agree well with both the hydrodynamic numerical and analytical calculations. Additionally, we confirm the existence of a short time scale ( $\tau_1 \sim 100$  ps) which

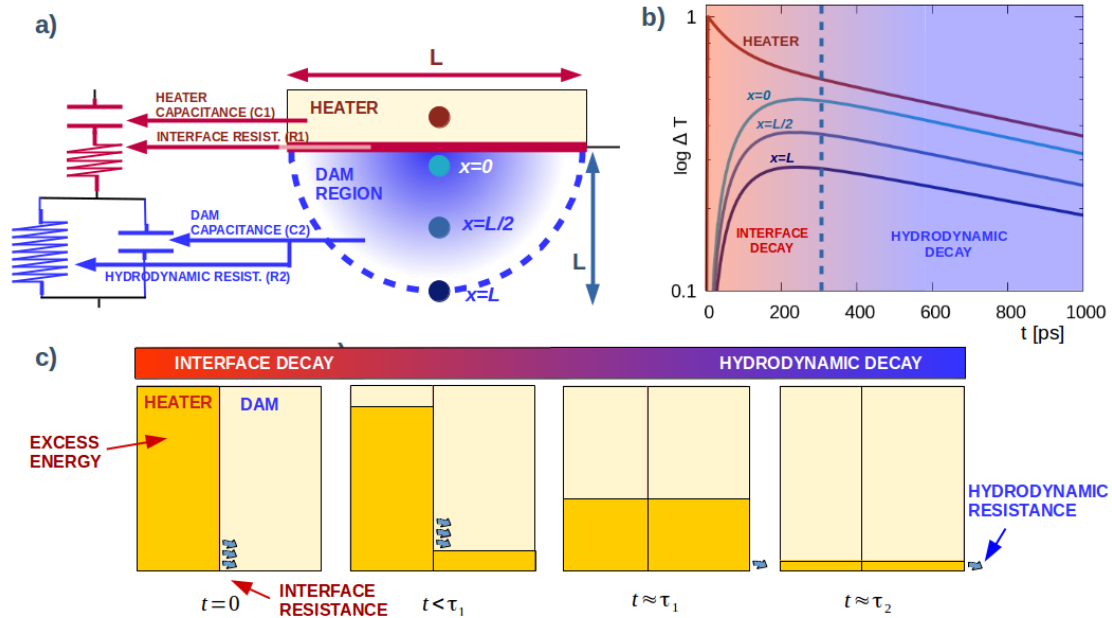


**Figure 33:** Reproduced from [163]. Two-box model for the thermal decay of heaters for  $L < \ell$ . (a) The energy released by the heater (with heat capacity per unit surface,  $C_1$ ) crosses the interface with the substrate at a rate determined by the thermal boundary resistance,  $R_1 \equiv R$ . The thermal response of the substrate is determined by a region of size  $L$  below the heater -the dam region- which acts both as a heat reservoir of capacity  $C_2$ , and as a thermal resistance  $R_2$  due to viscosity from hydrodynamic effects. An analogy to an equivalent electrical circuit is shown. (b) The temperature as a function of time is shown for the positions indicated in (a) from KCM solutions for  $L=30$  nm and  $P=600$  nm. At short times, the dam region retains the energy released by the heater and increases in temperature with a time scale  $\tau_1$  dominated by the interface resistance. At larger times, a slow joint decay of heater and dam temperatures occurs with a characteristic time  $\tau_2$  determined by the hydrodynamic resistance  $R_2$ . (c) Cartoon of the two-box model in analogy with fluids. The two boxes represent the heater and dam with the water level indicating the temperature. For times less than  $\tau_1$ , the excess energy flows out of the heater into the dam through the interface resistance until temperatures equilibrate. For times on scale of  $\tau_2$ , excess energy in heater and dam escapes to the rest of the substrate at a rate ruled by hydrodynamic effects.



is dominated by the intrinsic thermal boundary resistance in Figure 34b and a longer time scale ( $\tau_2 \sim 1$  ns) which is dominated by the hydrodynamic effects in Figure 34c. Figure 34c also displays the splitting of the decay times between effectively isolated and close-packed experiments, i.e. the increase in dissipation efficiency for close-packed heat sources. In Figure 34d, we plot the weight of the hydrodynamic dominated decay,  $a_2$  in 117, which shows a transition from a primarily hydrodynamic decay for small heaters, to a decay ruled by the thermal boundary resistance at large sizes. This is expected as large sizes should converge to the Fourier prediction, which contains a single time scale. Therefore, the size-dependent effective boundary resistance extracted by the effective Fourier model in Refs. [57, 92] can be re-interpreted as capturing the weighted average of the time-scales ( $\tau_1, \tau_2$ ) generated by a size-independent boundary resistance and size-dependent localized hydrodynamic effects. Remarkably, the observation of a second non-Fourier exponential decay with a well-defined characteristic time is an indication of the manifestation of a single length scale governing the substrate diffusion, in good agreement with the generalized hydrodynamic model. This contrasts with alternative descriptions like the BTE/RTA approach (see section 2.5), which introduce multiple length scales to describe heat transport in Silicon.

The information condensed in Figure 34 is more easily understandable by identifying all the double exponential decay coefficients for an specific sample and analyzing the sensitivity of the decay to changes in the hydrodynamic (KCM) parameters values. Here we consider two examples that represent two different situations. On one hand, consider the double exponential decay for isolated small heaters with size  $L = 30\text{nm}$  and periodicity  $P = 400\text{nm}$  ( $\tau_1 = 68\text{ps}$ ,  $\tau_2 = 1470\text{ps}$ ,  $a_2 = 1 - a_1 = 0.7$ ). The thermal evolution for this sample is represented with blue lines in the two top plots of Figure 35. The influence of modifying the non-local length  $\ell$  or the boundary resistance value  $R_1$  is displayed in the left and right plots, respectively. Note that the smaller time  $\tau_1$  is determined by  $R_1$  and the larger one  $\tau_2$  by  $\ell$ , so each decay is associated to a different mechanism. In this case the weight  $a_2 > 0.5$  and the hydrodynamic time is larger than the TBR dominated time ( $\tau_2 > \tau_1$ ). Therefore, the heater thermal evolution is more sensitive to the  $\ell$  value than to the interfacial resistance value  $R_1$ . On the other hand, consider the decay of large heaters with size  $L = 1\mu\text{m}$  ( $\tau_1 = 139\text{ps}$ ,  $\tau_2 = 1840\text{ps}$ ,  $a_2 = 0.09$ ). In this sample the situation is the contrary with respect to the previous case. The hydrodynamic weight is small ( $a_2 < 0.1$ ) and the timescale  $\tau_1$  determined by the TBR dominates. In the bottom plots of Figure 35 the decay for this sample is represented in blue, along with the same sensitivity analysis of the KCM parameters. Notice that the decay is mainly influenced by  $R_1$  while the change of  $\ell$  does not have much effect. This is expected since for large heater sizes the decay is well described by Fourier's law along a Kapitza interfacial resistance.

Therefore, there is a transition from the thermal relaxation dominated by hydrodynamic effects observed for small heater sizes, to the evolution dominated by the interfacial resistance for large sizes. For intermediate sizes, the two mech-

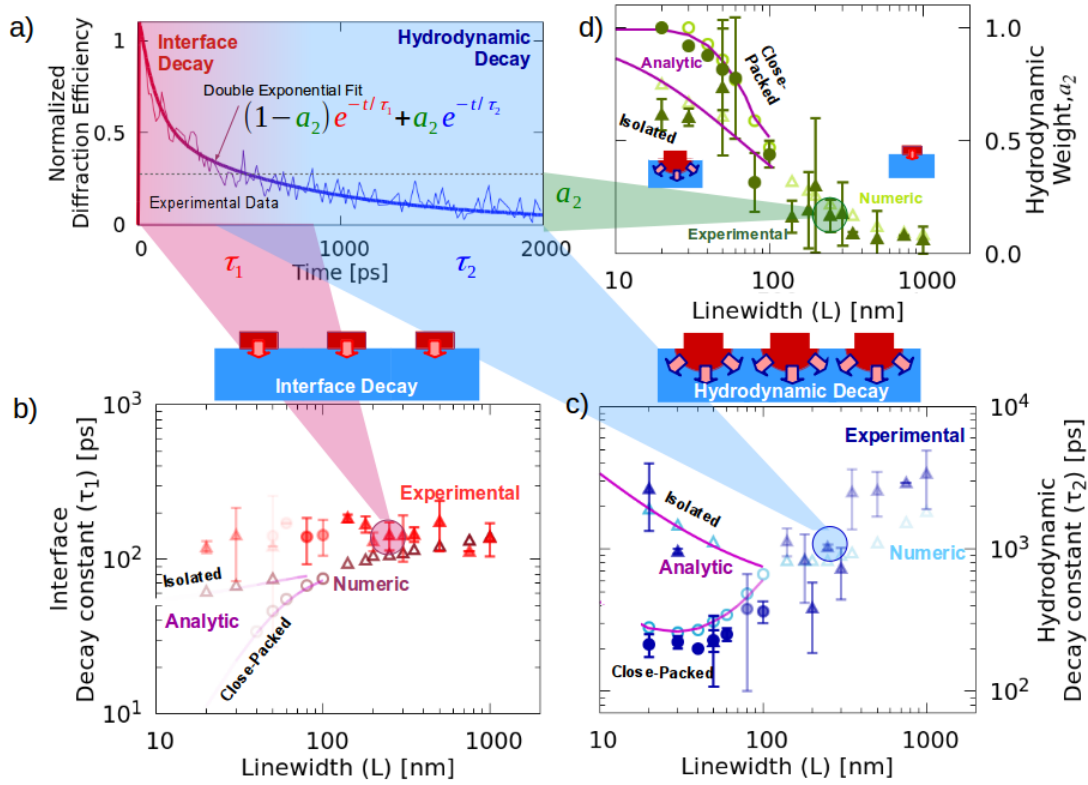


**Figure 34:** *Reproduced from [163].* (a) The experimental change in diffraction efficiency, with oscillations removed, for a heater line of  $L=250$  nm and  $P=1000$  nm (thin line) can be fitted with a double exponential decay (thick line), from which two characteristic times are extracted: a short time scale (red line region,  $\tau_1$ ) and a long time scale (blue line region,  $\tau_2$ ). (b,c) Characteristic time  $\tau_1$  and  $\tau_2$  versus heater linewidths  $L$  for effectively isolated (triangles) and close-packed (circles) experiments. KCM numerical (analytical) results are denoted by open symbols (lines). The color intensity in the symbols indicates the weight of each characteristic time in the overall decay. The short time scale  $\tau_1$  is dominated by the interface resistance, while the long one  $\tau_2$  is ruled by the hydrodynamic effects in the substrate. Additionally, the difference between the dissipation of close-packed versus effectively isolated heat sources is demonstrated. (d) The normalized weight of the hydrodynamic characteristic time in the temperature decay,  $a_2(= 1 - a_1)$ , is displayed versus linewidth for all experiments, showing the transition from interface- to hydrodynamic- dominated decay as source size decreases.

anisms are important and a double exponential decay is evident (see Figure 29). The experimental validation of this transition is displayed in Figure 34d.

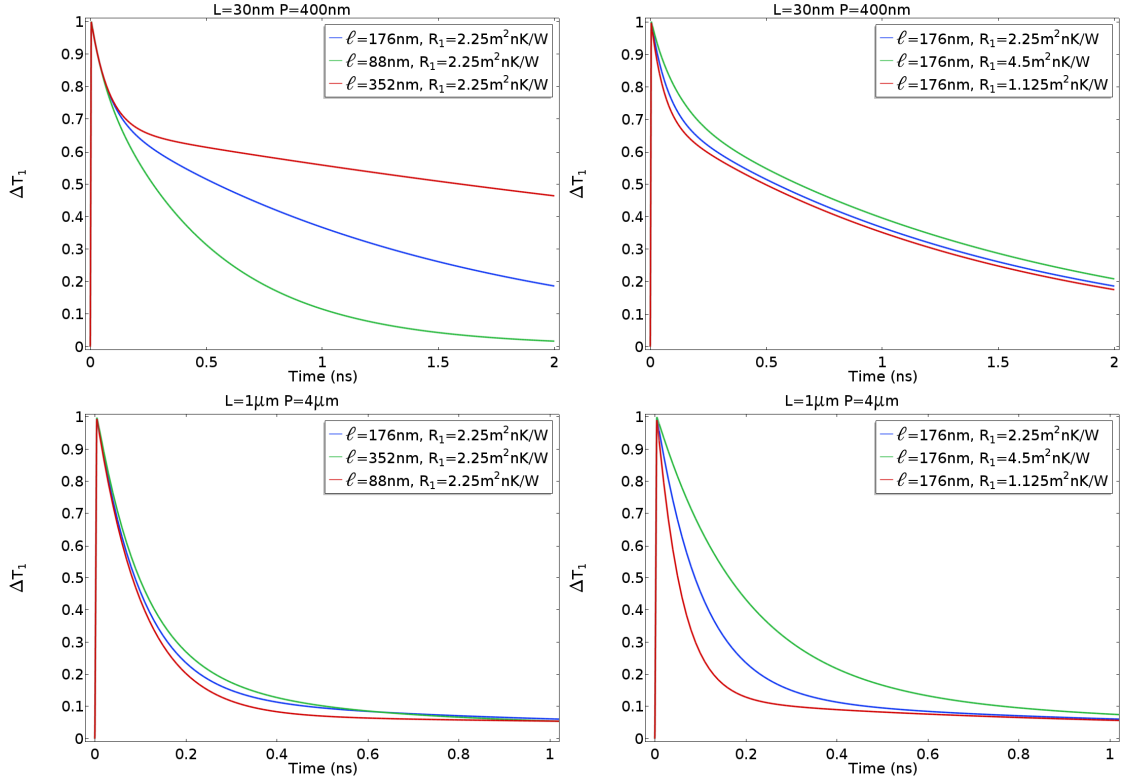


**Figure 35:** Sensitivity of hydrodynamic model parameters. Left Plots: Thermal decay using the values given by ab initio values from section 3.5 (blue line) in comparison with the same system using a non-local length multiplied by two (green) and divided by two (red) times. Right Plots: Analogous comparison is provided but changing the used value of the resistance  $R_1$ . Top: Small heater size ( $L=30\text{ nm}$  and  $P=400\text{ nm}$ ). Bottom: Large heater size ( $L=1\ \mu\text{m}$  and  $P=4\ \mu\text{m}$ ). Notice that the boundary resistance controls the initial decay  $\tau_1$  and the non-Fourier conduction controls the decay at larger times  $\tau_2$ . Moreover, the weight of the second exponential with time  $\tau_2$  increases by decreasing the line-width.

## 7.4 Derivation of the Two-Box Model

Here we provide detailed derivation of the analytical expression for the parameters of the double exponential thermal decay 117 predicted by the hydrodynamic model in the case  $L < \ell$ . We denote  $x$  the cross-plane direction towards the substrate and  $y$  the in-plane direction. The origin of coordinates is the center of the interface.

In KCM, the heat flux in the substrate is described through the hydrodynamic heat transport equation 76 along with the energy conservation equation 75. We neglect the term  $\tau \frac{\partial \mathbf{q}}{\partial t}$  in 76 because it does not play a significant role in the present

experimental conditions. We also neglect the thermo-elastic coupling in the energy conservation for simplicity. We consider the Stokes regime  $L < \ell$  (heat transport dominated by viscosity); then one can neglect the term  $\mathbf{q}$  in (76) close to the heater since we expect  $\ell^2 \nabla^2 \mathbf{q} \sim \frac{\ell^2}{L^2} \mathbf{q}$ . It is worth to note that the heat flux profile saturates after a fast transient and viscosity remains constant during the rest of the experiment. The heat flux profile saturation time can be estimated as  $\ell^2/\chi_{\text{Si}} = 341 \text{ps}$ . To illustrate this, in Figure 36 we show the time evolution of the different terms in equation (76) at  $x = L$  and  $y = 0$  with  $L = 20 \text{nm}$ .

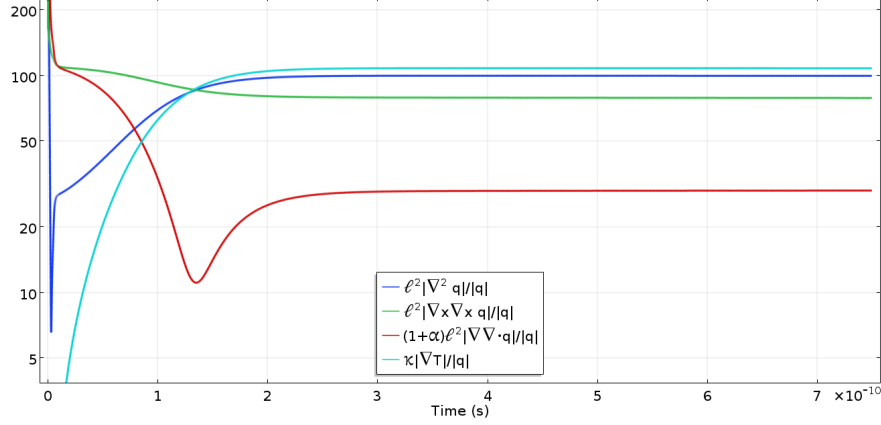


**Figure 36:** Time evolution of the hydrodynamic heat transport equation terms at  $x = L$  and  $y = 0$  with  $L=20 \text{ nm}$ .

We have

$$\frac{\kappa_{\text{Si}}}{\ell^2} \nabla T = \nabla^2 \mathbf{q} + \alpha \nabla (\nabla \cdot \mathbf{q}). \quad (119)$$

Now we perform integration in the region dominated by viscous effects  $x < 2\ell$ :

$$\frac{\kappa_{\text{Si}}}{\ell^2} \int_0^{2\ell} \nabla T dx = -\frac{\kappa_{\text{Si}}}{\ell^2} (T_2 - T_2^{2\ell}) = \int_0^{2\ell} dx \left( \frac{\partial^2 q_x}{\partial x^2} + \frac{\partial^2 q_x}{\partial y^2} \right) + \alpha \int_0^{2\ell} dx \frac{\partial \nabla \cdot \mathbf{q}}{\partial x}, \quad (120)$$

where  $T_2$  is the substrate temperature at the interface  $x = 0$  and  $T_2^{2\ell}$  is the substrate temperature at  $x = 2\ell$ .

At the time scales considered in the experiment  $T_2^{2\ell}$  is constant and close to the initial temperature  $T_2^\infty = T_0$ . Moreover, during the experimental time scale, the heat flux and its derivatives at  $x = 2\ell$  are neglectable in front of the heat flux and its derivatives at the interface  $x = 0$ .

Therefore, we can perform integration of 75 in the hydrodynamic region to obtain

$$\int_0^{2\ell} dx \frac{\partial \nabla \cdot \mathbf{q}}{\partial x} = c_{\text{Si}} \frac{\partial T_2}{\partial t}, \quad (121)$$

or, equivalently,

$$8 \int_0^{2\ell} dx \frac{\partial^2 q_x}{\partial x^2} = c_{\text{Si}} \frac{\partial T_2}{\partial t} + \frac{\partial q_y}{\partial y} \Big|_{x=0}. \quad (122)$$

Introducing 121,122 in 120, we obtain

$$\frac{\kappa_{\text{Si}}}{\ell^2}(T_2 - T_2^\infty) + (1 + \alpha)c_{\text{Si}}\frac{\partial T_2}{\partial t} = - \int_0^{2\ell} dx \frac{\partial^2 q_x}{\partial y^2} - \frac{\partial q_y}{\partial y} \Big|_{x=0}. \quad (123)$$

Now we average equation 123 over all the interface points  $y \in [-L/2, L/2]$ .

$$\frac{\kappa_{\text{Si}}}{\ell^2}(\bar{T}_2 - T_2^\infty) + (1 + \alpha)c_{\text{Si}}\frac{\partial \bar{T}_2}{\partial t} = \frac{B}{L}\bar{q}_x \quad (124)$$

where  $\bar{T}_2, \bar{q}_x$  are the average temperature and heat flux in the interface, respectively, and

$$B = - \frac{\int_0^{2\ell} dx \int_{-L/2}^{L/2} dy \frac{\partial^2 q_x}{\partial y^2}}{\bar{q}_x} - \frac{2q_y \Big|_{y=L/2 \ \& \ x=0}}{\bar{q}_x} \quad (125)$$

is a geometric parameter related with the average heat flux profile in the hydrodynamic region. This parameter saturates because the heat flux profile reach a stationary situation as can be seen in Figure 36. The saturated value can be estimated from the COMSOL simulations. We obtain a constant value for  $L < \ell$  in the 1D geometry:  $B = 3$ .

Diffusion in the heater region is extremely fast and hence the temperature of the heater  $T_1$  is uniform within the time scale of the experiment. Therefore, using the averaged form of a Kapitza interface boundary condition  $\bar{q}_x = \frac{T_1 - \bar{T}_2}{R_1}$  in (124) we obtain the following evolution equation

$$\frac{\tau_S}{R_2} \frac{d\bar{T}_2}{dt} = - \frac{\bar{T}_2 - T_2^\infty}{R_2} + \frac{T_1 - \bar{T}_2}{R_1} \quad (126)$$

where

$$\tau_S = \frac{(1 + \alpha)c_{\text{Si}}\ell^2}{\kappa_{\text{Si}}} \quad (127)$$

and

$$R_2 = \frac{B\ell^2}{\kappa_{\text{Si}}L} \quad (128)$$

is the viscous resistance.

Consider now the energy conservation in the heater  $c_{\text{Ni}}\frac{\partial T_1}{\partial t} = -\nabla \cdot \vec{q}$ . By performing volume integration of this equation with using the Kapitza interface boundary condition and the insulation condition for the other boundaries, we obtain an independent evolution equation

$$c_{\text{Ni}}h\frac{dT_1}{dt} = - \frac{T_1 - \bar{T}_2}{R_1}. \quad (129)$$

Notice that, in the derivation of the evolution equations (126,129), a simplified Kapitza interface condition have been used i.e. the hydrodynamic contributions to the interface boundary condition (92) have been neglected for simplicity. The inclusion of the hydrodynamic contributions to the boundary condition (which

cause only small deviations for extremely small  $L < 50\text{nm}$ ) can be found in the ending notes of this subsection.

The heater temperature  $T_1$  can be obtained from the system of partial differential equations 126,129:

$$T_1 - T_2^\infty = a_1 \exp(-t/\tau_1) + a_2 \exp(-t/\tau_2). \quad (130)$$

In the case of isolated heaters ( $R_1 < R_2$ ), the system 126,129 can be simplified and we obtain

$$\tau_1 = R_1 \frac{c_{\text{Ni}} h \tau_S / R_2}{\tau_S / R_2 + c_{\text{Ni}} h} \equiv R_1 \frac{C_1 C_2}{C_1 + C_2} \equiv R_1 C_{eq} \quad (131)$$

$$\tau_2 = \frac{B c_{\text{Ni}} \ell^2 h}{\kappa_{\text{Si}} L} + \frac{c_{\text{Si}} \ell^2 (1 + \alpha)}{\kappa_{\text{Si}}} = c_{\text{Ni}} h R_2 + \tau_S \equiv (C_1 + C_2) R_2 \quad (132)$$

being  $C_1 = c_{\text{Ni}} h$ ,  $C_2 = \tau_S / R_2$  the heat capacities of the heater and the dam region, respectively. With these definitions, the system 126,129 is equivalent to 115,116 in the main text.

In the case considered here ( $\tau_1 < \tau_2$  i.e.  $R_1 < R_2$ ),

$$a_1 = \frac{\tau_S / R_2}{c_{\text{Ni}} h + \tau_S / R_2} = \frac{C_2}{C_1 + C_2} \quad (133)$$

$$a_2 = \frac{c_{\text{Ni}} h}{c_{\text{Ni}} h + \tau_S / R_2} = \frac{C_1}{C_1 + C_2} \quad (134)$$

If  $R_1 \sim R_2$ , then the system (126,129) needs to be solved with no approximations. This is the case of interest for small  $L$  and  $P = 4L$  (close-packed situation) in which we use a reduced non-local length  $\ell_{\text{eff}}$  (reduced  $R_2$ ). See the ending notes of this section for details.

For illustration, in Figure 37 we show the comparison between the analytical prediction 130 for the heater temperature evolution  $T_1(t)$  with  $L = 20\text{ nm}$  and  $P=800\text{ nm}$  compared with the Finite Elements calculation.

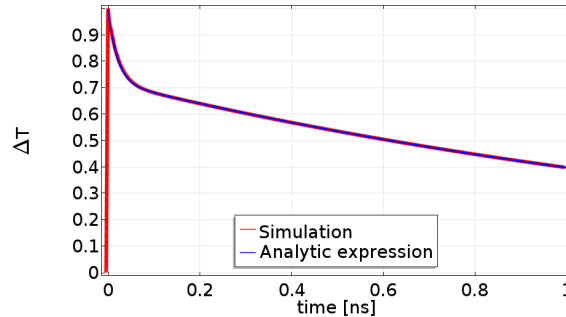


**Figure 37:** Expression 117 with parameters 131,132,133,134 compared with the simulated thermal decay of the heater according to KCM obtained using COMSOL Multiphysics for  $L=20\text{ nm}$  and  $P=800\text{ nm}$ .

**Note I: Solutions of the system of partial differential equations 126,129**

Here we revisit the solutions of the system of partial differential equations (126,129). Exponential solutions  $\exp(tw)$  satisfy

$$w^2 + w\left(\frac{1}{R_1 C_{eq}} + \frac{1}{\tau_S}\right) + \frac{1}{\tau_S C_1 R_1} = 0 \quad (135)$$

being  $w$  the roots of the system characteristic polynomial. There are always two real negative roots  $w_1 = -1/\tau_1$  and  $w_2 = -1/\tau_2$ . In order to find the expressions (131,132) for the characteristic times we assumed  $R_2 > R_1$  and hence we simplified the previous equation to

$$w^2 + w\left(\frac{1}{R_1 C_{eq}}\right) + \frac{1}{\tau_S C_1 R_1} = 0 \quad (136)$$

Regarding the weights of the double exponential, in general we have

$$a_1 = \frac{\tau_1}{C_1 R_1} \frac{\tau_2 - C_1 R_1}{\tau_2 - \tau_1} \quad (137)$$

$$a_2 = \frac{\tau_2}{C_1 R_1} \frac{C_1 R_1 - \tau_1}{\tau_2 - \tau_1} \quad (138)$$

which in the case  $\tau_1 < \tau_2$  simplify to equations (133,134).

Notice that equations (135,137,138) are the general system of equations for the parameters  $\tau_1, \tau_2, a_1, a_2$ . Now consider the two geometrical regimes:

(i) Isolated situation ( $P - L > 2\ell$ ): In this case  $R_2 > R_1$  so that the approximated equation (136) can be used and the explicit analytical expressions (131,132) for  $\tau_1, \tau_2$  are very close to the exact solutions of the general equation (135).

(ii) Close-packed situation ( $P = 4L$  and small  $L$ ): In this case  $\ell_{\text{eff}} = (P - L)/2$  so that  $R_1 \sim R_2$ . In this case the use of the approximated equation (136) is not acceptable and hence we use the exact solutions of the general equation (135) to compare with experiments. It is easy to show that by reducing  $L$  with  $P = 4L$ ,  $a_2$  goes to 1 and  $a_1$  goes to 0;  $\tau_2$  goes to the Fourier decay time  $\tau_F = c_{\text{Ni}} h R_1$  and  $\tau_1$  tends to zero. Therefore, we recover Fourier in this limit and we don't expect a clearly observable double exponential decay. In particular, for  $L < 50\text{nm}$ ,  $P = 4L$  we expect a single exponential decay as in the Fourier-based description. This limit is consistent with experimental observations as shown in Figure 34

**Note II: Inclusion of the hydrodynamic contributions to the interface boundary condition (92) in the two box model.**

Consider the hydrodynamic interface boundary condition (92) instead of the simplified Kapitza condition. We average it along the interface with expressing  $\nabla \cdot \mathbf{q}$  and  $\nabla \mathbf{q}$  as quantities proportional to the interface normal heat flux  $\bar{q}_x$  (this is possible because of the saturation of the heat flux profile close to the interface):

$$(T_1 - \bar{T}_2) = \bar{q}_x \left[ R_1 - \frac{1}{\gamma_{\text{Si}} L} (\beta b_1 - \chi_{xx} b_2 - \chi_{yy} b_3) \right] \quad (139)$$

where

$$b_1 = \frac{\int_{-L/2}^{L/2} dy \nabla \cdot \mathbf{q}}{\bar{q}_x} = 1.5 \quad (140)$$

$$b_2 = \frac{\int_{-L/2}^{L/2} dy \frac{\partial q_x}{\partial x}}{\bar{q}_x} = -1 \quad (141)$$

$$b_3 = \frac{\int_{-L/2}^{L/2} dy \frac{\partial q_y}{\partial y}}{\bar{q}_x} = 2.5 \quad (142)$$

are dimensionless parameters estimated from the corresponding saturated value in the COMSOL simulations.

Now we can input this averaged boundary condition to the  $\bar{T}_2$  evolution equation (124) and the heater energy conservation equation to obtain the two box model system of equations. This system is exactly the same as the one previously obtained (126,129) with a redefined interface boundary resistance  $R'_1$ :

$$R'_1 = R_1 + \frac{1}{\gamma_{Si} L} (-\beta b_1 + \chi_{xx} b_2 + \chi_{yy} b_3). \quad (143)$$

Therefore, by including the hydrodynamic contributions to the boundary condition we obtain a larger thermal resistance which become explicitly geometry dependent. This correction slightly increase the  $\tau_1$  value for small sizes reported in Figure 6 of the main text with respect to the value obtained using the simplified Kapitza boundary resistance. However, for  $L > 50\text{nm}$ , we have  $R_1 \sim R'_1$ .



## 8 Bismuth Telluride nanowire networks for thermoelectric applications

In collaboration with Instituto de Micro y Nanotecnología de Madrid (IMM)

In this Chapter we model the stationary thermal response of a bismuth telluride complex device designed for thermoelectric applications at room temperature. Our aims here are to increase the number of studied materials using the hydrodynamic model, and to show how the model can be used to envision and characterize new devices.

In recent years, great efforts have been devoted to enhance the thermoelectric efficiency of different materials through nanostructuring [143, 144]. For example, the reduction of the effective thermal conductivity observed in systems of nanowire (NW) arrays has driven much attention to this kind of structures [171]. One highly efficient way of obtaining a great number of homogeneous NWs, as far as composition and diameter are concerned, is via electrochemical deposition inside alumina templates [172]. Nevertheless, these structures present drawbacks such as difficulties associated with their characterization and implementation in actual devices, given that the alumina template must be dissolved in most cases, thus producing the collapse of the NW array.

Here, we consider a three-dimensional arrangement of longitudinal NWs of 55 nm in diameter connected by transversal interconnections, or nanocanals (TnC), with approximate dimensions of 40 nm in height and 30 nm in width. The spacing  $P$  between connections is precisely controlled by the previously tailored 3D porous alumina (3D AAO) templates, in which the NWs are deposited by electrodeposition [173]. The NWs are highly oriented along the [110], with the exact Bi<sub>2</sub>Te<sub>3</sub> stoichiometry and high crystallinity. Due to the TnCs, the obtained metamaterial can be made free-standing without destroying its structure (see Fig. 38) by selectively dissolving the alumina template. Since the electrodeposition allows the fabrication over large areas, and the fabricated templates at lab-scale are of the size of several cm<sup>2</sup>, the resulting metamaterial can be measured using conventional thin-film techniques. Furthermore, the 3D-structures exhibit enhanced thermoelectric properties, which depend on the geometrical parameters of the nanostructure. Specifically, we have obtained an increase in the thermoelectric figure of merit,  $zT$  (see eq. 107), in 3D Bi<sub>2</sub>Te<sub>3</sub> metamaterials when compared to Bi<sub>2</sub>Te<sub>3</sub> NWs and films prepared under the same conditions. This increased efficiency is the result of a reduction in the effective thermal conductivity due to nonlocal effects, and a two-fold Seebeck coefficient increase when compared to films and NWs. Importantly, the 3D nanostructuring does not influence the electrical conductivity, for which the measured values are similar to those obtained in the films. We have an electrical conductivity  $\rho^{-1}$  of  $3.0 \cdot 10^4$  S/m in the direction of the NWs, and of  $6.7 \cdot 10^4$  S/m in the transversal directions.

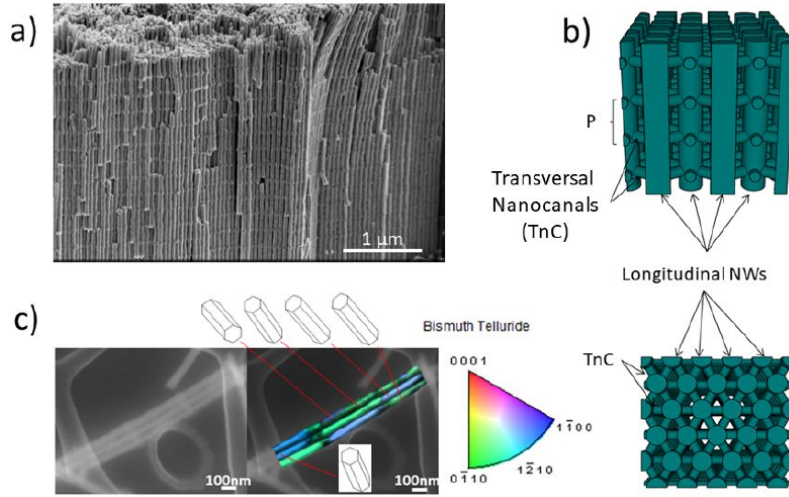


**Figure 38:** a) Scanning electron microscope (SEM) image of a free-standing bismuth telluride scaffold structure obtained after the dissolution of the AAO template. In this image, the transverse interconnections are  $P=220$  nm apart. b) A schematic 3D representation of the scaffold composed of perpendicular interconnected TnCs in lateral view (top), similar to what it can be observed by SEM, and top view (down), where the hexagonal distribution of the longitudinal NWs and their connections can be seen. c) The SEM image and the transmission electron backscatter diffraction (t-EBSD) of a set of three connected nanowires, showing a clear orientation of the c-axis perpendicular to the growth direction in all the structure.

## 8.1 Effective thermal conductivity of the 3D Bi<sub>2</sub>Te<sub>3</sub> nanowire networks

The thermal conductivity values for different intercanal distance  $P$  are shown in Figure 39, along with those obtained for a 1D Bi<sub>2</sub>Te<sub>3</sub> NW array. As it can be seen, by comparing the results of 1D NW arrays of similar diameter inside the 3D porous alumina (green dashed line in figure 2a) to that of the 3D Bi<sub>2</sub>Te<sub>3</sub> scaffolds also inside the alumina, the measured thermal conductivity is lower in the metamaterial (red curve). In Fig. 39b, the curve for the free-standing 3D Bi<sub>2</sub>Te<sub>3</sub> network is shown and compared to one nanowire of similar diameter. As explained in section 3.7, both the lattice and the electronic contributions to the thermal conductivity are significant and are accounted for.

The effective lattice thermal conductivity displayed by the structures can be predicted by solving the hydrodynamic model in a single periodically repeated geometry cell as shown in Fig. 39. First, consider free-standing Bi<sub>2</sub>Te<sub>3</sub> nanowire networks without the oxide. The stationary thermal response in the semiconductor domains is described using conservation of energy 75 and the hydrodynamic heat transport equation 76 using the bulk thermal conductivity and non-local length at room temperature indicated in section 3.5. In all the boundaries except in the nanowires and the TnCs terminals we impose thermal insulation 77 and the slip boundary condition 81 with  $C = 1$  (diffusive phonon-boundary reflec-

tions). In the NW terminals, we fix heat flux periodic boundary conditions with imposing a temperature difference  $\Delta T=1$  K. In each pair of opposed TnC terminals we impose periodic boundary conditions for the heat flux and the temperature. From the resulting steady-state solutions, we calculate the effective lattice thermal conductivity of the free-standing Bi<sub>2</sub>Te<sub>3</sub> structures using expression 108 as done in section 4.2 (see 39b). Since the equations parameter values are intrinsic material properties (i.e. geometry-independent), exactly the same modeling can be used to predict the lattice conductivity of isolated Bi<sub>2</sub>Te<sub>3</sub> NWs (without the TnCs) reported in [174] (see Fig. 40). Note that here we assumed an isotropic thermal conductivity  $\kappa$  in Equation 76, corresponding to the largest component of the bulk anisotropic thermal conductivity tensor. This component corresponds to the direction of the temperature gradient imposed in experiments, which is the longitudinal nanowire direction. To improve the accuracy of the predictions, an anisotropic version of the hydrodynamic heat equation is required. However, we expect the resulting correction to be small because the heat flux mainly flows in the nanowires longitudinal direction. Moreover, note that predicting the effective thermal conductivity in the direction of the TnCs using the presented isotropic model require the use of the adequate thermal conductivity tensor component.

To compare theory and experiments in Fig. 39a, the semiconductor structure is embedded in an oxide matrix. The oxide domains fill all the space which is not occupied by the Bi<sub>2</sub>Te<sub>3</sub> network in each periodically repeated cell. Since the phonon mean free paths in the oxide are much smaller than the geometry characteristic sizes, non-local effects are not expected, and Fourier's law 1 can be used to describe these domains instead of 76. We use nominal thermal conductivity for the oxide alumina  $\kappa_{\text{ox}} = 1.25$  W/mK. In the oxide terminals contiguous to the NW terminals, we impose periodic heat flux boundary conditions along with the corresponding temperature difference  $\Delta T=1$  K. Similarly, in the oxide faces contiguous to opposed TnC terminals we impose periodic boundary conditions for the heat flux and the temperature. Finally, instead of the insulation boundary condition, we impose continuity of the heat flux normal component in the oxide-semiconductor interfaces. It is worth to note that the slip boundary condition (Equation 81) is still required to model the heat flux tangential component in the semiconductor domain. Conversely, this boundary condition is not required in the oxide side. From the resulting steady-state solutions, we calculate the effective lattice thermal conductivity of the Bi<sub>2</sub>Te<sub>3</sub> structures embedded in the oxide matrix using expression 108, considering both the area covered by the NW terminal and by the oxide terminal.

Finally, in Fig. 39a,b we also included the contribution of the electronic thermal conductivity. Using the measured electrical conductivity of the Bi<sub>2</sub>Te<sub>3</sub> NWs from [175] and the Wiedemann-Franz law 106, one can calculate the electronic thermal conductivity,  $\kappa_e$ . Consider the present case of a NW diameter  $D=55$  nm. The corresponding electrical conductivity is  $3 \cdot 10^4$  S/m [175]. The electrical conductivity of the network in the longitudinal direction of the NW is the same as in the isolated NW (the TnCs are not expected to influence electronic transport). Therefore, the electronic thermal conductivity in all the cases under study for

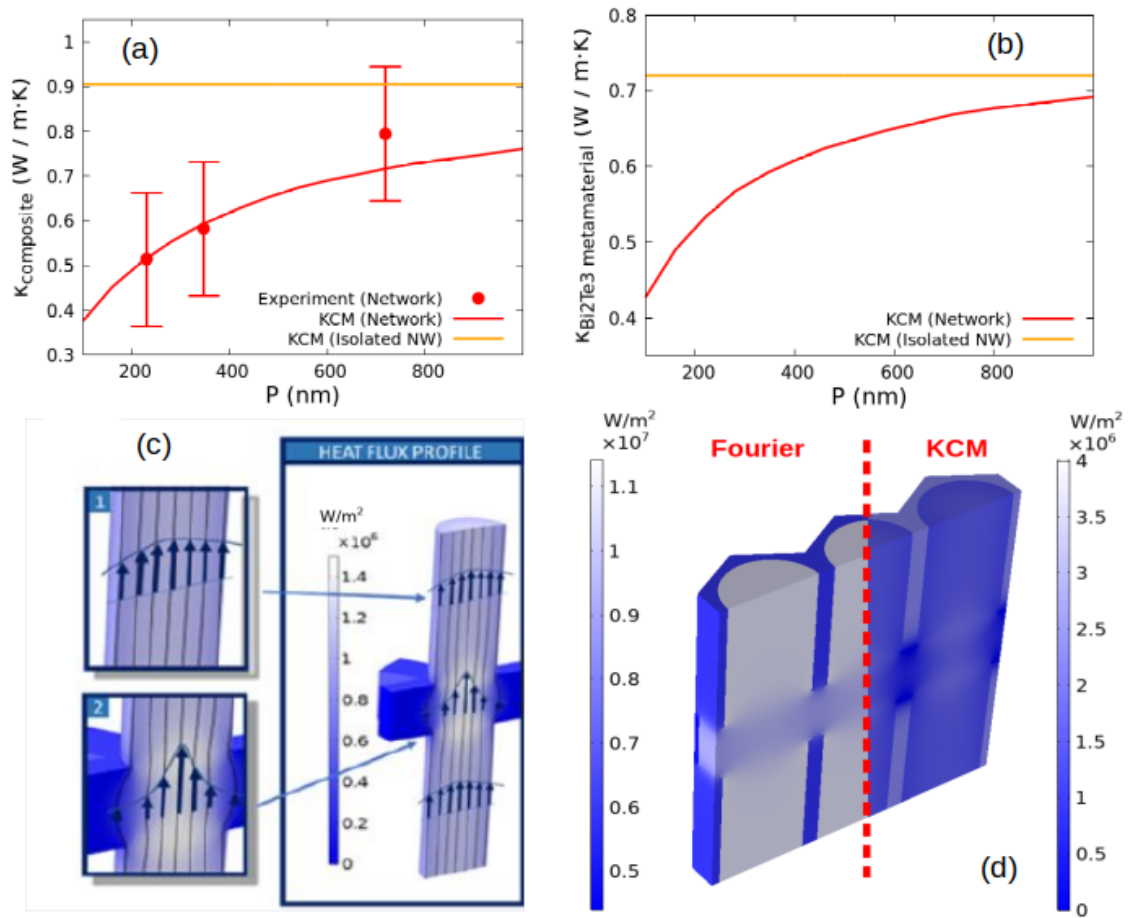


**Figure 39:** a) Thermal conductivity predicted by the hydrodynamic heat transport model considering the lattice and the electronic contributions, as well as the 3D-AAO matrix, along with the experimentally obtained values. The red line represents the thermal conductivity of the composite obtained by the model, and the red points correspond to the measured thermal conductivities obtained for different values of  $P$ . The orange line represents the predicted value for a 55 nm diameter Bi<sub>2</sub>Te<sub>3</sub> nanowire array embedded in the alumina matrix. b) Thermal conductivity predicted by the hydrodynamic heat transport model for the self-supported bismuth telluride metamaterial scaffold, excluding the matrix (red line). The orange line represents the predicted value for a 55 nm diameter nanowire without the alumina template. c) Heat flux steady-state profile according to the hydrodynamic heat transport model for a free-standing 3D network. Two different non-local effects reducing the effective thermal conductivity of the structure can be observed: the inhomogeneous heat flux profile in the nanowire (inset 1) and the curvature of the heat flux streamlines in the regions connected by the TnCs (inset 2). d) Heat flow in the 3D Bi<sub>2</sub>Te<sub>3</sub>/alumina composite taking the values of the bulk material for the nanowires and comparing the hydrodynamic heat transport model and the classical Fourier approach.

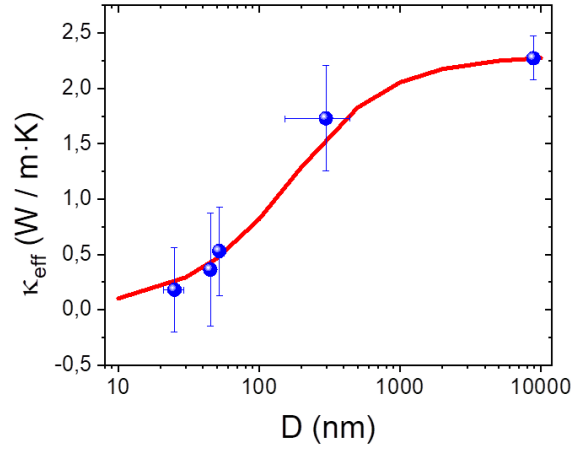


**Figure 40:** Lattice thermal conductivity predicted by the hydrodynamic heat transport model in free-standing Bi<sub>2</sub>Te<sub>3</sub> NW with varying the diameter  $D$ .

the free standing structures is  $\kappa_e=0.22$  W/mK. In Fig. 39a, the electronic thermal conductivity is weighted by the areal density  $x$  covered by the NWs with respect to the full structure including the oxide, so that the contribution of the electronic thermal conductivity is  $x\kappa_e=0.14$  W/mK in the structures embedded in the oxide alumina.

In these complex 3D structures, we can identify two distinct viscous effects according to eq. 76, which contribute to the lattice thermal conductivity reduction observed in experiments. First, the reduction of the heat flux close to the system boundaries as introduced in section 4.2 is also present (see Figure 39c - inset 1). This effect is the responsible of the lattice conductivity reduction in isolated NWs as shown in Figure 40. However, in the network structures, there is an additional and enhanced viscous effect due to the inhomogeneities in the heat flux profile originated in the regions where the TnCs and the longitudinal NWs are connected (see Figure 39c - insert 2). This extra viscous effect is responsible for the further reduction of the thermal conductivity predicted in the network. The higher the number of interconnections (that is, the lower the  $P$ ), the greater the reduction in thermal conductivity is, as it is shown in Figures 39a,b. Moreover, if the alumina is not dissolved from the structure (see Figure 39d), the hydrodynamic effects dramatically modify the Bi<sub>2</sub>Te<sub>3</sub>/alumina relative contribution to the effective thermal conductivity of the composite. According to the hydrodynamic model, the heat flows preferentially through the alumina, since the thermal conductivity of the 3D network becomes smaller than that of the amorphous alumina. In contrast, Fourier's law (bulk) predicts exactly the opposite situation.

Finally, note that, for bismuth telluride, the hydrodynamic model is predictive beyond the applicability condition determined for silicon in Chapter 4. In this case, the non-local length is similar to the NW diameter, and we predict a radial Poiseuille-like heat flux profile in the NWs (see Figure 39c - inset 1) rather than the emergence of non-overlapping boundary layers surrounding the system boundaries as observed in films.

## 8.2 Seebeck coefficient of the 3D Bi<sub>2</sub>Te<sub>3</sub> nanowire networks

The other main difference of the Bi<sub>2</sub>Te<sub>3</sub> NW networks versus electrodeposited thin films or nanowires, is the increase in the measured Seebeck coefficient. Taking into account that the carrier concentration is similar in films and in 3D nanostructured metamaterial, to understand the origin of the Seebeck coefficient increase in the metamaterial, two competing effects may be considered: the crystallinity and the topological surface states. On the one hand, the crystallinity in the 3D nanostructured metamaterial and in the nanowires is higher than in the 20  $\mu\text{m}$ -thick films. It has been observed that the increase in crystallinity increases the Seebeck coefficient. For instance, in Bi<sub>2</sub>Te<sub>3</sub> when the samples are annealed [176] or have a larger grain size [177], the Seebeck coefficient can increase up to tenfold. On the other hand, the influence of the topological surface states (SSs) is known to be detrimental to the Seebeck coefficient. This has been shown in closely related systems, such as Sb<sub>2</sub>Te<sub>3</sub> thin films [178] or Bi(1 -  $x$ )Sb $x$  nanowire arrays [179].

In nanocrystalline, stoichiometric and strongly oriented films grown by the same pulsed deposition method, a Seebeck coefficient of about  $-60 \mu\text{V}\cdot\text{K}^{-1}$  has been measured. For stoichiometric, one dimensional, 55 nm diameter Bi<sub>2</sub>Te<sub>3</sub> nanowires, the Seebeck values measured in the nanowire direction are of the same order of magnitude, around  $-55 \pm 3 \mu\text{V}\cdot\text{K}^{-1}$ . These are among the best values for this nanowire diameter reported in the literature ( $-30 \mu\text{V}\cdot\text{K}^{-1}$ , to  $-57 \mu\text{V}\cdot\text{K}^{-1}$  [180]). Thus, it appears that in the case of 1D nanowires of 55 nm an increase should be observed because of the increase in crystallinity versus the films, but it is not measured because of the influence of the topological surface states at those diameters, which reduce the effective Seebeck coefficient.

However, in 3D Bi<sub>2</sub>Te<sub>3</sub> metamaterial produced similarly as films and 1D wires, we have measured Seebeck values in the in-plane direction (i.e. parallel to the TnCs) which range from  $-103 \pm 5$  to  $-127 \pm 6 \mu\text{V}\cdot\text{K}^{-1}$ . These are more than twice the value found in 1D nanowires or electrodeposited films prepared under similar conditions. It must be stated that no further thermal treatment has been performed on the 3D scaffoldings in order to be compared to the 1D 55 nm nanowire template and films. This startling increase in the Seebeck must be attributed again to the presence of the interconnecting nanocanals. A possible reason for the observed increase in the Seebeck may be the increase in crystallinity versus the films. Another possible reason can be a reduction or disappearance of the negative influence of the topological surface states in the Seebeck coefficient, since the diameter of the TnCs is smaller (between 30 to 40 nm depending on the direction). Indeed, it was experimentally observed that Bi<sub>0.85</sub>Sb<sub>0.15</sub> NWs raised their Seebeck coefficient a factor of 2 when the diameter was reduced to 41 nm from the minimum-Seebeck corresponding to a diameter of 58 nm [179]. This reduction in the detrimental character of SSs was attributed to SS hybridization, where the bulk-extending tails of surface states from opposing boundaries overlap. This opens a gap in the surface states [181, 182], reducing the carrier concentration in the SS and increasing the Seebeck coefficient. Another possible

source of gap opening is that, in a NW configuration, surface states must be antiperiodic when circling the NW perimeter, thus leading to gap formation [183, 184].

To measure the Seebeck, the structure is electrically insulated  $\mathbf{J} \cdot \mathbf{n} = 0$  and a temperature difference  $\Delta T$  is imposed in the direction transversal to the NWs. All the boundaries except the system terminals are thermally insulated [77]. From the resulting electrical potential difference divided by  $\Delta T$ , the Seebeck coefficient of all the structure is obtained. For modeling, the thermal equations should be coupled with the electric current and field using Eq. 105. It is worth to note that if we use the hydrodynamic equation [76] instead of Fourier's law for the Seebeck characterization, the obtained local  $\nabla T$  in the connections between the NWs and the TnCs is increased with respect to the Fourier's description. Consequently, the thermoelectric effect is locally enhanced in the connections and the Seebeck coefficient in these regions influence more the Seebeck in the complete structure. Moreover, note that the hydrodynamic model predicts a reduced heat flux through the structure (consistent with the measured reduction of the effective thermal conductivity). Therefore, the contribution of the phonon drag to the Seebeck coefficient is further reduced in the nanostructures. Nevertheless, the phonon drag contribution is expected to be negligible at room temperature even in bulk situations. Taking into account this remarks, future work should aim to characterize the Seebeck coefficients in each region of the complex structure, and quantize the influence of the topological surface states or the crystallinity in this kind of systems.

Since the Seebeck and the thermal conductivity are measured in different directions, an experimental value for the  $zT$  of the network is not accessible. However, the thermoelectric efficiency of the network operating with thermal gradients along the direction of the TnCs is promising. On one hand, experiments demonstrate a strong increase on the Seebeck coefficient when measured in that direction. On the other hand, according to the hydrodynamic model, the lattice thermal conductivity reduction observed in the NWs longitudinal direction is expected to take place, and even to become enhanced, in the TnCs direction.

## 9 Second sound in Germanium in a rapidly varying temperature field

In collaboration with Institut de Ciència de Materials de Barcelona (ICMAB)

In the previous sections we have shown the influence of non-local effects to describe a variety of experimental observations both in transient and steady-state conditions. In this section we discuss a distinct non-Fourier phenomena, the second sound propagation, which is usually hindered by the dominance of non-local effects but it is included in the generalized hydrodynamic heat transport description. First, we discuss the emergence of this effect from a theoretical point of view, and then we demonstrate its existence in germanium using modified FDTR techniques.

### 9.1 Memory effects

The spatiotemporal propagation of the temperature field in the form of waves is known as second sound, a term that was adopted in analogy to first sound (or simply sound, i.e., mechanical lattice vibrations). Second sound in solids was first experimentally observed in solid He [114]; later in NaF [115], Bi [185], and SrTiO<sub>3</sub> [116]; and most recently highly oriented pyrolytic graphite [48, 186]. Several theoretical works have also recently addressed its occurrence in low-dimensional systems [18, 110, 111]. In all these experimental observations of second sound, the dominance of momentum conserving phonon scattering with respect to resistive phonon scattering was found to be the key mechanism leading to its observation. Second sound was thus observed almost exclusively in the collective regime, i.e. at very low temperatures ( $T < 5$  K), or at higher temperatures (125 K) for samples with low Resistive phonon scattering [48, 186]. A condition for the experimental detection of second sound, based on these experimental observations [48, 114–116], was found to be  $\tau_N < t_{\text{exp}} < t_R$ ; i.e., the typical experimental observation times ( $t_{\text{exp}}$ ) must be larger than Normal phonon scattering times ( $\tau_N$ ) to allow momentum redistribution but smaller than Resistive phonon scattering times ( $\tau_R$ ) to avoid decay of the displaced distribution into the phonon equilibrium distribution. This interpretation is supported by recent experimental evidence, where the emergence of second sound was modeled using the Callaway model (see section 2.2). It is shown that by including the role of the Normal collisions in numerical BTE solutions, the relaxation of an optically induced thermal grating displays an oscillating behavior at low temperatures in graphite, in good agreement with experiments [48]. According to this interpretation, removing the role of the Normal collisions lead to the standard RTA approach and the initial temperature profile exponentially relax back to equilibrium without displaying wave-like behavior. This seems to be consistent with the experiments since the temperature oscillations are shown to be suppressed at high temperatures, where Normal collisions do not dominate. An alternative interpretation of this transition by increasing the temperature is provided below.



The theoretical foundations of second sound were set in the 1960s by M. Chester, R. J. Hardy, C. P. Enz, and co-workers [50, 54, 108, 117], who predicted the existence of Drifting second sound, i.e., a type of wave-like heat transport that is triggered by the dominance of Normal phonon scattering events. This type of second sound was experimentally confirmed in the previously introduced works [48, 114–116]. However, the existence of a Driftless or High-Frequency type, as well as other types of second sound, was also envisioned. In this case, the dominance of Normal scattering events is not a necessary condition for the existence of wave-like heat transport. The key general condition for the wave-like heat transport was shown to be the slow relaxation of the heat flux as compared to the experimental time scales, and the absence of non-local effects. In this section, we discuss in detail these two conditions, and we show how the generalized hydrodynamic model encompasses all the wave-like heat transport processes.

From a mesoscopic perspective, second sound is the transport regime where the time-derivative of the heat flux in the transport equation 76 is non-negligible. This general definition was already introduced by Hardy [50] or Chester [117], and used in many more recent works [187–189]. However, other authors [190], restricted the existence of Second Sound to situations where a complete temperature oscillation could be obtained. The later definition is probably more useful for applications, but in this thesis we use the former definition because we are interested on deviations from purely diffusive transport from a fundamental point of view.

The first natural requirement is that the external perturbation  $Q$  is fast enough to increase the magnitude of the time-derivative of the heat flux in equation 76, thus, unlocking memory effects causing deviations from Fourier. In other words, the characteristic excitation frequency  $f$  should satisfy

$$1 \lesssim f\tau. \quad (144)$$

The second condition for the emergence of second sound is more elusive even though it was already pointed out by Hardy 50 years ago [50]. As introduced in 2.2, the phonon distribution can be written in terms of the eigenvectors of the collision operator of the Boltzmann Transport Equation (the so-called relaxons [15]). The relaxons are linear combinations of phonons that exponentially relax to equilibrium due to collisions with a well-defined relaxation time (the inverse of its associated eigenvalue  $\Omega^\alpha$ ). The relaxons do not diagonalize the drift operator of the BTE, and hence we do not have well-defined velocities for relaxons as we do have for the phonons. Under the drift operator, the relaxons evolve into new combinations of relaxons with complicated transitions relating all the eigenvectors. In the original work by Hardy [50], the second condition for the emergence of second sound can be found in section VI (expression 6.1):

$$q^2 |\langle \theta^1 | D | \theta^\alpha \rangle|^2 < \Omega^{(1)} \Omega^{(a)} \quad (145)$$

where  $q$  is the spatial frequency of the perturbation,  $D$  is the drift operator and  $|\theta^1\rangle$  is the first relaxon. This condition must be satisfied for all relaxon  $|\theta^\alpha\rangle$  except the only one with eigenvalue 0, which generate the local equilibrium part

of the phonon distribution (invariant under collisions). The relaxon  $|\theta^1\rangle$  is defined using the Normal part of the collision operator. If only normal collisions are considered, there is an extra eigenvector with eigenvalue 0 different from the local equilibrium one. This eigenvector generates the displaced distribution and it is associated with the phonon crystal momentum (invariant under normal collisions). The relaxon  $|\theta^1\rangle$  can be obtained from this eigenvector through perturbation theory. The square-root of the left-hand side of condition 145 is the transition rate of a relaxon  $|\theta^\alpha\rangle$  to relaxon  $|\theta^1\rangle$  due to drift within a region of size  $L = q^{-1}$ . Therefore, this condition imposes that the exponential decay of each relaxon due to collisions should be faster than the rate of transitions due to drift. This condition is satisfied in the collective regime, where relaxon  $|\theta^1\rangle$  describes the whole non-equilibrium part of the distribution function (i.e. we have the displaced distribution function) and the other relaxons are not excited. This leads to the Drifting Second Sound. However, condition 145 can be satisfied in more general non-equilibrium situations where the contribution of other relaxons to the non-equilibrium state is relevant. For example, Hardy postulated the existence of one specific kind of Second Sound out of the collective regime, the so-called Driftless Second Sound.

The relaxons can be classified into odd and even. The odd relaxons are the ones that have non-null contribution to the total heat flux. Consequently, if all these relaxons decay to equilibrium independently with a well defined characteristic time (no transitions due to drift) the heat flux will decay exponentially, which is the non-diffusive signature of memory effects as can be described by eq. 76. In accordance with condition 145, this is satisfied when the drift operator can be neglected in front of the collision operator i.e. the non-equilibrium distribution function is spatially homogeneous in a large enough region. In such conditions, non-local effects in equation 76 can be neglected. In conclusion, the general conditions for the appearance of thermal waves are a fast enough external excitation  $Q(q, f)$  that is homogeneous in space i.e. satisfying 144 and 145.

In the absence of non-local effects, the generalized hydrodynamic equation 76 reduces to the Maxwell-Cattaneo equation (along with the energy conservation equation):

$$c \frac{dT}{dt} = -\nabla \cdot \mathbf{q} + Q \quad (146)$$

$$\tau \frac{\partial \mathbf{q}}{\partial t} + \mathbf{q} + \kappa \nabla T = 0 \quad (147)$$

These equations were envisioned long time ago to introduce some inertia in the heat flux, and avoid the causality violation in the establishment of heat fluxes as obtained by Fourier's law [51]. If the thermal gradient is negligible in eq. 147, the main signature of the non-Fourier behavior described by the Maxwell-Cattaneo equation is the exponential relaxation of the heat flux with a characteristic time  $\tau$ . Moreover, this equation describes that a fraction of the thermal energy propagates as waves.

The generalized hydrodynamic model presented in section 3.2, is derived assuming a pseudo-equilibrium distribution in terms of the heat flux and its deriva-

tives, which could in general be written in terms of many different odd relaxons. The election of pseudo-equilibrium distribution function is adequate to describe Second Sound phenomena beyond the Drifting or the Driftless cases, and may resolve an apparent discrepancy between velocities of the different types of Second Sound [50]. According to the model, coefficient  $\tau$  is one order of magnitude larger than the phonon life-time appearing in the thermal conductivity (see section 3.5). Therefore, condition 144 can be satisfied at lower excitation frequencies than previously expected, as discussed for experimental modeling in the next sections of this Chapter.

On the other hand, condition 145 seems to indicate that wave-like heat propagation would be difficult to observe in experiments due to the role of non-locality, which is ubiquitous in many different nanoscale experiments. Interestingly, this interplay between different non-Fourier effects is naturally obtained if using the complete transport equation 76. For example, in Chapter 7, non-local effects dominate the substrate conduction and the memory term proportional to  $\tau$  is negligible. This indicates that when non-local effects emerge, second sound is suppressed, as predicted by condition 145. A simple demonstration that this phenomenology is naturally displayed by equation 76 is shown in Figure 41. Consider the 1D spreading of a Gaussian temperature distribution of size  $L$ . In Figure 41 we show the temperature profile at different times  $t$ . At  $t > \tau$ , Fourier transport is recovered and the heat pulse dissipates diffusely. If  $t \sim \tau$  and  $L > \ell$ , we obtain thermal wave propagation (second sound). However, if  $L < \ell$ , no pulse propagation is observed regardless the observation time  $t$ . Conversely, at early times the initial conditions seems to persist during some transient before diffusion take place. This phenomenology is consistent with the conditions 144 and 145 for the observation of thermal waves. On one hand, condition 144 is only satisfied when the characteristic time scale of the experiment (in this case the observation time) approach  $\tau$ . On the other hand, second sound is only observed for homogenous perturbations

$$\frac{\ell^2}{L^2} < 1 \quad (148)$$

as imposed by 145.

Indeed, using the microscopic definition of  $\ell$  in the collective regime (normal dominant collisions) or in the kinetic regime (Resistive dominant collisions) in the framework of the Kinetic Collective Model (see section 3.2), one can rewrite the condition 145 as 148:

**Collective regime:** If normal collisions dominate, the eigenvector spectrum of the collision operator can be obtained neglecting the Resistive collisions. Therefore, the relaxon  $|\theta^1\rangle$  can be accurately identified with the crystal momentum carried by the phonon distribution. The momentum is relaxed only due to Resistive collisions at the collective (mode-independent) relaxation time  $\Omega^{(1)} = \frac{1}{\tau_C} = \frac{1}{\langle \tau_R^{-1} \rangle^{-1}}$  introduced by Guyer and Krumhansl [6] (see section 2.2), where  $\tau_R$  is the Resistive scattering time and  $\langle \rangle$  stands for the average over the phonon modes. Moreover, the rest of the distribution (and in particular the higher order relaxons) can be relaxed through normal and Resistive collisions. Therefore, in the

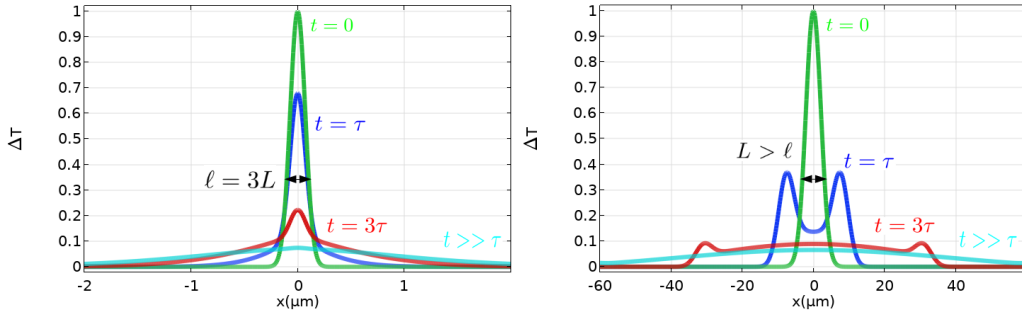


**Figure 41:** Evolution of the initial Gaussian temperature distribution with size  $L$  at different times  $t$  according to equation 76. Second sound i.e. thermal wave propagation is only observed for  $t \sim \tau$  and  $L > \ell$ .

collective regime  $\Omega^{(\alpha)} = \frac{1}{\langle \tau_N \rangle} + \frac{1}{\langle \tau_R \rangle} \approx \frac{1}{\langle \tau_N \rangle}$  for  $\alpha > 1$  ( $\tau_N$  is the normal scattering time). Now using the non-local length for the collective regime derived in the original Guyer and Krumhansl work [6]  $\ell_C^2 = \frac{1}{5} \langle v^2 \tau_N \rangle \langle \tau_R^{-1} \rangle^{-1}$  (see section 2.2) in condition 145, we obtain 148.

**Kinetic regime:** If Resistive collisions dominate, the eigenvector spectrum of the collision operator do not correspond to the one of its Normal part and hence the relaxon  $|\theta^1\rangle$  can not be associated with the distribution crystal momentum. Therefore, all relaxons evolve through Resistive and Normal collisions so that  $\Omega^{(\alpha)} = \frac{1}{\langle \tau_R \rangle} + \frac{1}{\langle \tau_N \rangle} \approx \frac{1}{\langle \tau_R \rangle}$  for  $\alpha > 0$ . Now using the first order approximation presented in section 3.2 for the non-local length in the kinetic regime  $\ell^2 = \frac{1}{5} \langle v^2 \tau_R \rangle \langle \tau_R \rangle$  in condition 145, we obtain 148.

At this point, it is worth to recall that an effectively reduced non-local length  $\ell_{\text{ef}}$  is required for the description of the nanostructure cooling experiment 7 when the distance between heat sources is reduced beyond the applicability condition. Therefore, this kind of geometric constraint in the experimental conditions seems to provide an alternative way to fulfill condition 148 by reducing  $\ell$ . At the moment, a validated model for the effective reduction of  $\ell$  is unavailable. However, the reduction of this parameter due to very abrupt spatial perturbations was previously envisioned in terms of the role of higher order moments of the distribution function [68] (which are not considered in the ab initio derivation of 76). Furthermore, this effect may be used to reinterpret the transition from non-local effects (reduced conductivity) at high temperatures to memory effects (heat waves) at low temperatures in thermal grating relaxation experiments in graphite [48]. In that particular experiment, the non-local length may be smaller than the grating period at high temperatures and non-local effects manifest, whereas it may be effectively reduced at low temperatures due to the increase on the MFPs to sizes much larger than the grating period, thus unlocking second sound. Further understanding and validation of this alternative way to satisfy condition 145 could be key to manipulate second sound for applications.

In the following sections, we consider a Frequency Domain Thermoreflectance experiment with directly heating the semiconductor sample (i.e. without using

a metallic transducer). We first discard the existence of non-local effects in such conditions due to the excited region being one order of magnitude smaller than the intrinsic  $\ell$  (the optical penetration of the laser is extremely small). Hence, we simultaneously satisfy in experiments conditions 144 and 145, which allow measuring memory effects in Germanium even at room temperature.

## 9.2 Frequency Domain Thermorefectance in the absence of metallic transducers

As discussed in the previous section, wave-like heat transport in the presence of a volumetric heat source  $Q$  is described by the combination of the Maxwell-Cattaneo heat equation 147 and the energy conservation equation 146. The model equations can be compactly written as the hyperbolic heat equation (HHE):

$$\tau \frac{\partial^2 T}{\partial t^2} + \frac{\partial T}{\partial t} - \frac{\kappa}{c} \nabla^2 T = \frac{1}{c} \left( Q + \tau \frac{\partial Q}{\partial t} \right). \quad (149)$$

The HHE describes the propagation of a temperature wave with a damping term given by  $\frac{\partial T}{\partial t}$  and a propagation velocity  $v_{ss} = \sqrt{\frac{\kappa}{c\tau}}$ . The solutions of this equation lead to different heat transport regimes, depending on the temporal and spatial length scales under investigation. The usual thermal diffusion (parabolic) equation is obtained by neglecting the terms proportional to  $\tau$ .

Now, we proceed to show that it is possible to observe a type of high-frequency second sound as described using Eq. 149 in natural bulk Ge by driving the system out of equilibrium with a rapidly varying temperature field [191]. Our concept is based on taking advantage of the second-order time derivative in the HHE, Eq. 149, in a frequency-domain experiment. As the driving frequency increases toward the hundreds of megahertz range, the relative weight of this term with respect to the damping term (first-order time derivative) increases proportionally to the frequency upon a harmonic excitation, hence enhancing the non-Fourier memory effect and satisfying the first condition for the observation of second sound 144 discussed in section 9.1. We show that this approach is robust enough to expose second sound independently, to a certain extent, of the phonon scattering rates of the studied material, as well as of temperature. Note that this indicates that it is possible to observe second sound in the high-frequency limit beyond the collective regime (see section 3.1), since heat transport in Ge is dominated by Resistive phonon scattering processes.

Our experiments are based on a frequency-domain optical reflectance pump-and-probe approach based on two lasers with different wavelengths ( $\lambda_{\text{pump}}=405$  nm and  $\lambda_{\text{probe}}=532$  nm) focused onto the surface of a Ge sample to a spot size with radius  $R_{\text{spot}}=5.5$   $\mu\text{m}$ . The studied samples are pieces of a substrate of natural Ge. The experiment is similar to the one discussed in section 6, but instead of using a metallic transducer, the semiconductor substrate is directly heated using the laser excitation and the thermorefectance signal is originated in the Ge surface. The pump laser is modulated between 30 kHz and 200 MHz with a

sinusoidal power output waveform, leading to a dynamic modulation of the optical reflectivity of the surface of the sample, which is also well described by a harmonic waveform. A frequency-dependent phase lag gradually develops, defined as a phase difference between the harmonic thermal excitation,  $Q$ , and the response of the sample,  $T$ , which can be modeled using Eq. 147 in the present experimental conditions. The choice of Ge as a candidate for the observation of second sound is not arbitrary, and it is mostly based on the large optical absorption coefficient of this material for the wavelengths used in this experiment. The optical penetration depth of the pump and probe lasers is  $\delta_{\text{pump}}=15$  nm and  $\delta_{\text{probe}}=17$  nm, respectively. These particular conditions make Ge an ideal material for this study, because the small penetration depth of both lasers ensures that the measured phase lag is local and, thus, accurately describes the oscillations of the thermal waves. The penetration depth of the pump and probe lasers should be compared with the thermal wavelength  $v_{\text{SS}}/f$ . At room temperature and the highest excitation frequency considered,  $v_{\text{SS}}/f=840$  nm, thus considerably larger than the optical penetration depth.

It is worth to remark that we neglect nonlocal effects (i.e. the Laplacian term in Eq. 76) in the hyperbolic heat equation 149 to model the present measurements. Instead, we assume the Maxwell-Cattaneo heat equation 147 which only adds a memory term (i.e the time derivative of the heat flux term) to Fourier's law. The full hydrodynamic equation 76 can not be applied in this experiment due to the non-local length of Ge being much larger than the length scale of the perturbed region ( $\delta_{\text{pump}} < \ell$ ). In fact, the experimental measurements can not be reproduced using Eq. 76 due to the large influence of nonlocal effects even at small heating frequencies, where the experimental data can be reproduced with Fourier's law. Therefore, similarly to the experiments presented in section 7 for close-packed heaters, the non-local length is reduced to very small effective values in the present non-equilibrium conditions (more details about the applicability of the hydrodynamic model can be found in section 4.4). Importantly, the reduction of the non-local length to negligible values allows satisfying the second condition for the observation of second sound 145 discussed in section 9.1. Future work should address the attenuation of nonlocal effects under the present conditions and its influence in the propagation of thermal waves. Indeed, according to the hydrodynamic model, controlling the conditions to suppress non-local effects is key to unlock memory effects (i.e. second sound propagation) as imposed by condition 145 (see Fig. 41 in section 9.1).

### 9.3 Thermorefectance Signal Analysis

In the experiments discussed in section 6, which are also based in the frequency domain thermorefectance technique, the thermorefectance signal comes from the metallic transducer and only depends on the temperature. However, in the present experiments without transducer, the changes  $\Delta R$  of the optical reflectivity of the Ge surface upon the pump laser excitation are also depending on

the modulation  $\Delta n$  of the carrier concentration in the conduction band. The resulting  $\Delta R$  at the energy corresponding to the probe wavelength is provided by the first-order expansion  $\Delta R = \frac{\partial R}{\partial T} \Delta T + \frac{\partial R}{\partial n} \Delta n$  [192]. Interestingly enough, the contribution provided by the variation of the carrier concentration is expected to dominate the way the reflectivity is affected in experiments, like the present ones, involving pulsed laser sources, i.e., for high electronic excitation densities [193, 194]. However, in our excitation conditions, the electronic contribution to the optical reflectivity can be neglected; hence, the optical reflectivity is dominated by the temperature of the lattice  $\Delta T$  for all excitation frequencies as in section 6. We demonstrate this by studying the relative magnitude of  $\frac{\partial R}{\partial T} \Delta T$  and  $\frac{\partial R}{\partial n} \Delta n$ . In particular, we take advantage of the fact that for bulk Ge,  $\frac{\partial R}{\partial T} \simeq 0$  at 220 K for 532 nm of probe wavelength (see Figure 42), whereas  $\frac{\partial R}{\partial n}$  is expected to be temperature almost independent between 220 K and room temperature. Furthermore,  $\frac{\partial R}{\partial T}$  exhibits a sign inversion at this temperature, which is reflected in a change of the phase lag by an angle of  $\pi$ . Figure 42 displays the temperature dependence of  $\Delta R/R$ , as well as the phase lag for low (30 kHz) and high (100 MHz) modulation frequencies  $f$ , and for a constant pump power of  $\sim 10$  mW. The reflectivity signal exhibits a minimum around  $\sim 220$  K, followed by a slow signal recovery at lower temperatures. In the lower temperature range ( $T < 100$  K), the lattice and electronic contributions to the phase lag have opposite signs. Hence, the measured phase lag at high frequency in this range cannot be explained with the electronic contribution to the reflectivity. Moreover, the optical reflectivity extracted from ellipsometry experiments corresponding to  $\Delta T=1$  K is also shown for relative comparison. A similar behavior is observed independently of the excitation frequency, which resembles the ellipsometry data for which  $\Delta n = 0$ , thus indicating that the measured phase lag has a purely thermal origin at room temperature or below 100 K.

To fully confirm that the electronic contribution to the thermoreflectance signal can be neglected in the present experiments, we estimated the electronic contribution to the photoreflectance signal at room temperature as a function of the excitation frequency (see inset of Fig. 42). To calculate the electronic contribution we consider the 3D electron diffusion-recombination equation

$$\frac{\partial n}{\partial t} = D_e \nabla^2 n - \frac{1}{\tau_e} n - g_2 n^2 - g_3 n^3 + Q_e \quad (150)$$

where  $D_e$  is the electron diffusivity,  $\tau_e$  is the linear electron recombination lifetime,  $g_2$  is the quadratic recombination coefficient (usually associated to band-to-band radiative recombination), and  $g_3$  is Auger (cubic) recombination coefficient. Finally,  $Q_e$  is the excited electron density introduced in the sample, which has the shape of the pump laser weighted by the amount of absorbed photons per unit time at a given laser power. In order to provide a conservative estimation of the electron density obtained in experiments, we neglected the non-linear terms in the electron diffusion equation, which in fact amplify the reduction of the amount of excited electrons at high densities. In fact, we have observed that our experimental measurements are independent of the excitation laser power at room temperature, suggesting that the non-linear terms in Eq. 150 are not rele-

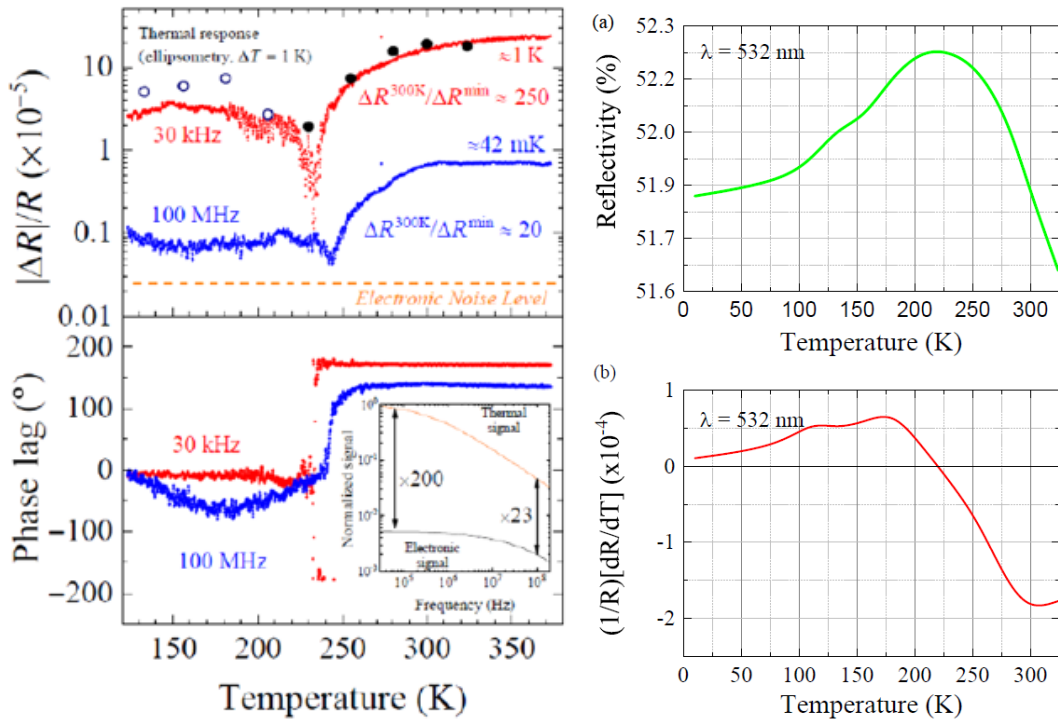


**Figure 42:** Reproduced from [191]. **Left:** Optical reflectivity change as a function of temperature for 30 kHz (red dots) and 100 MHz (blue dots). The black dots are the results obtained from ellipsometry measurements to a temperature rise of 1 K (full symbols  $\rightarrow \partial R/\partial T < 0$ , open symbols  $\rightarrow \partial R/\partial T > 0$ ). The lower panel displays the phase lag of the signal with respect to the pump excitation. Note that the phase lag is directly obtained from measurements i.e. without taking into account the sign of  $\partial R/\partial T$ . This phase lag must be corrected by  $\pm\pi$  to compare to Fig. 43 and 45. The inset displays calculation accounting for the thermal and electronic contributions to the reflectivity at room temperature. **Right:** Thermoreflectance coefficient and reflectivity at 532 nm for a Ge substrate, under normal incidence conditions.



vant to compute the total reflectance signal. We assume an electron diffusivity  $D_e=25 \text{ cm}^2/\text{s}$  and a linear recombination time  $\tau_e=1 \text{ } \mu\text{s}$  [195], which are conservative values at the average excited densities consistent with our experimental conditions. In the inset of Fig. 42 we show the predicted amplitude of the electronic contribution  $\frac{\partial R}{\partial n} \Delta n$  and the temperature contribution  $\frac{\partial R}{\partial T} \Delta T$  according to the 3D electron recombination-diffusion equation 150 and the hyperbolic equation 149, respectively, at a given laser power (i.e. the energy introduced in both simulations is equivalent). Both  $\Delta n$  and  $\Delta T$  are obtained by convolution with the superficial laser probe beam. The thermorefectance coefficient at room temperature is  $\frac{1}{R} \frac{\partial R}{\partial T} = -1.8 \cdot 10^{-4} \text{ K}^{-1}$  as shown in 42. Moreover, the electronic reflectance coefficient is expected to be temperature independent and is solely determined by the probe wavelength used, and can be estimated from experiments by varying the excitation power or the frequency at 220 K, where the thermal contribution is suppressed. We obtained  $\frac{1}{R} \frac{\partial R}{\partial n} = -2 \cdot 10^{-29} \text{ m}^3$ . Thus, the resulting ratio between the thermal and electronic contributions are in good agreement with the measured signals at 220 K (isolated electronic signal) and at 300 K (electronic and thermal signals combined), as displayed in the inset of Fig.42. Whereas the lattice contribution to the optical reflectivity is at least 20-fold larger than the electronic component at the higher frequencies, for lower frequencies, this ratio is substantially increased.

As indicated above, we used a conservative value of the electron diffusivity  $D_e$ . By increasing the diffusivity, the electron density in the surface is further reduced along with its contribution to the reflectance signal. In contrast, the electron reflectance signal is independent of the recombination time  $\tau_e$ . This implies that electron diffusion is the key mechanism reducing the electron density at the observation region, i.e. the surface of the specimens, which cause the corresponding contribution to reflectance to be negligible. Therefore, the higher electron diffusivity with respect to thermal diffusivity in Ge is the main reason why the experimental signal is thermally dominated even at the highest frequencies considered here, which are significantly larger than the electron recombination rates. In conclusion, modelling the temperature evolution of the sample is sufficient to explain the measured thermorefectance signal at room temperature or below 100 K, and no need of introducing the free electron dynamics is required.

## 9.4 Experimental Signatures of Wave-like Heat Transport

The 3D hyperbolic heat equation 149 is solved using Finite Element Methods to calculate the phase lag between the harmonic laser excitation and the temperature response of the system. We impose the insulation condition for the normal component of the heat flux in the boundaries. The laser energy source  $Q$  is restricted to a region defined by the Gaussian function of the pump beam in the radial direction ( $R_{\text{spot}}=5.5 \text{ } \mu\text{m}$ ), and an exponential decay in the cross-plane direction with the characteristic length of the optical penetration ( $\delta_{\text{pump}}=14 \text{ nm}$ ). The temperature oscillations correspond to a weighted average across the sur-

face of the sample computed using the Gaussian function of the probe beam as the weight.

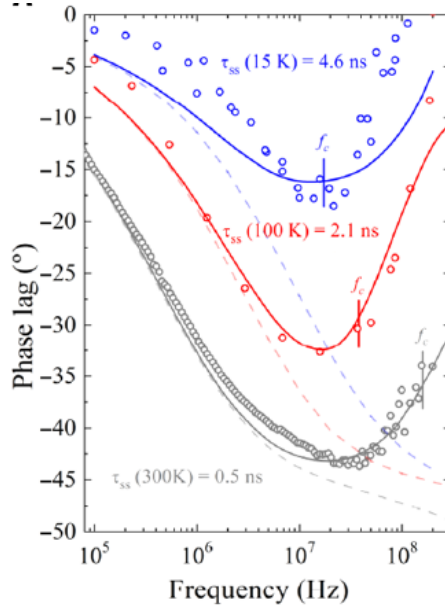


**Figure 43:** *Reproduced from [191].* Phase lag versus frequency for the higher frequency range as a function of temperature with the corresponding fits to the data point using the 3D-HHE. In dashed lines we display the prediction based on Fourier's law at each temperature.

Figure 43 displays the experimental phase lag as a function of frequency between 30 kHz and 200 MHz at different temperatures. The complex thermal response of the specimen was, at first, computed numerically within Fourier's model, solving the parabolic approximation to the three-dimensional (3D) hyperbolic equation 149 (diffusive case). At low frequencies, the agreement between Fourier's solution and the experimental data is good. For high frequencies, the difference between the experimental phase lag and Fourier's predictions is evident. For the higher-frequency range, the experimental data show that the phase lag (absolute value) decreases with increasing frequency. This trend cannot even be qualitatively reproduced by Fourier's model, which predicts that as frequency increases, the phase lag approaches  $-\pi/4$  and even lower values. The full 3D solution of Eq. 149 was used to fit  $\tau$  and  $\kappa/c$  to the experimental data through the entire frequency range, and it is shown in Fig. 43. The observed large reduction of the phase lag with respect to the Fourier prediction indicates the emergence of a more efficient heat transport mechanism as compared to diffusion at high frequencies. We note that the ballistic suppression of phonons [75, 89] discussed in section 2.5 cannot be invoked to rationalize the experimentally observed dependence of the phase lag with frequency. As discussed previously in Chapter 6, a reduction of the thermal conductivity at high frequency would lead to an increase in the phase lag (see fig. 50), rather than a decrease (absolute value), as we observe. Conversely, the observed frequency-dependent phase lag is well

reproduced by the hyperbolic equation 149, i.e., considering the contribution of wave-like heat transport.

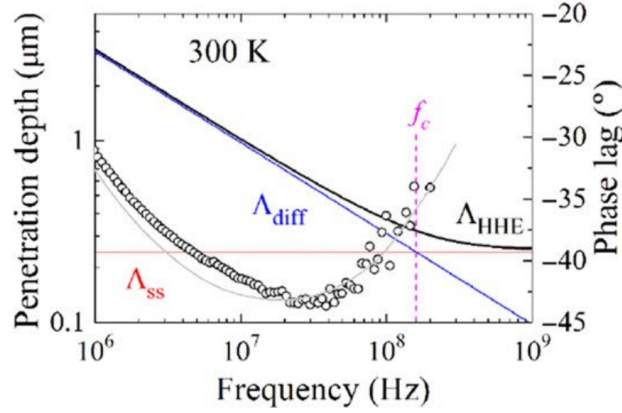


**Figure 44:** *Reproduced from [191].* Frequency dependent thermal penetration depth calculated using the solution of the HHE, the diffusive case, and the penetration depth obtained in the high frequency limit from Eq. 149 at room temperature. The high frequency experimental phase lag is shown for comparison. The crossover between both curves defines the characteristic frequency,  $f_c$ , where  $L_{\text{dif}} = L_{\text{SS}}$ .

The frequency window where second sound is expected can be estimated comparing the thermal penetration depth of the diffusive and wave-like regimes. Figure 44 displays the penetration depth,  $L_{\text{HHE}}$ , as well as the diffusive and wave-like limits,  $L_{\text{dif}} = \sqrt{\frac{\kappa}{c\pi f}}$  and  $L_{\text{SS}} = 2\sqrt{\frac{\kappa\tau}{c}}$ , respectively. A characteristic frequency  $f_c$  is obtained when  $L_{\text{SS}} = L_{\text{dif}}$ , thus providing an estimation of the frequency for which the diffusive and wave-like contributions to heat transport are similar. As temperature decreases, the ratio between the penetration depth of the wave-like and diffusive contributions is  $L_{\text{SS}}/L_{\text{dif}} = \sqrt{4\pi\tau}$ , which implies that lower temperatures favor the spatial propagation of the thermal waves because larger  $\tau$  is expected and indeed experimentally observed for lower temperatures. Wave-like effects are already present below  $f_c$ , as can be observed comparing the experimental data with the corresponding fits using Eq. 149 to the Fourier predictions, as shown in Fig. 42. The onset of wave-like effects is also evidenced by the deviations between  $L_{\text{dif}}$  and  $L_{\text{HHE}}$  as shown in Fig. 44.

The spatial dependence of the temperature field in the parabolic (diffusive) and the hyperbolic (wave-like) cases was simulated in the direction perpendicular to the surface of the sample at an arbitrary time. Figure 45 displays the normalized temperature profiles for 15, 100, and 300 K at the highest experimental excitation frequency of  $\sim 300$  MHz. As expected, the wave-like behavior of the temperature field exhibits a strong temperature dependence.

The complete set of fits using the HHE to the experimental phase lag is shown in Fig. 46, and the resulting temperature-dependent fitted values using the hyperbolic equation 149 for  $\tau$  and  $v_{\text{SS}}$  are shown in Fig. 47. The predicted parameter values according to the generalized hydrodynamic model (see section 3.5)

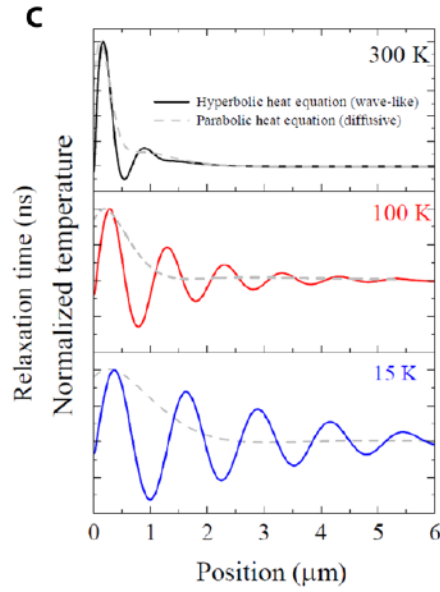


**Figure 45:** *Reproduced from [191].* Finite element simulations of the spatial distribution of the temperature field as a function of temperature in the direction perpendicular to the surface of the sample at the highest excitation frequency of  $\sim 300$  MHz for an arbitrary time. The parabolic and hyperbolic solutions are shown in dashed and full lines, respectively.

are also shown for comparison purposes. The agreement of the predicted values with those obtained from the experiments is remarkable for  $T > 100$  K. Hence, at high temperatures, the hydrodynamic model quantitatively captures memory effects if neglecting non-local effects. Microscopic derivation of the HHE from the BTE within the same generalized hydrodynamic framework (section 3.2) leading to the same values for  $\tau$  can be found in [191]. We note that the mesoscopic modeling based in Eq. 149 is expected to be valid for  $|\Delta T| \ll T$ , where  $|\Delta T|$  is the amplitude of the laser-induced thermal oscillations and  $T$  is the absolute temperature as set by the cryostat. In our experiments,  $|\Delta T|_{\max} < 20$  K; thus, the observed deviations between the theoretical predictions and the measured values at very low temperatures are expected. Finally, some comments about the applicability of the HHE 149 are in order. Some problems have been raised in the literature [196] against the physical plausibility of using the HHE to describe the temperature field, such as the possibility of negative entropy production, energy or temperature. These criticisms, however, are solved in the context of Extended Irreversible Thermodynamics (EIT) (see section 2.4). In Classical Irreversible Thermodynamics, the entropy is the local-equilibrium entropy, and entropy production for a heat flux obeying the Maxwell-Cattaneo equation can yield negative values. However, the generalized entropy of EIT always yields positive definite entropy production. On the other hand, by just looking at the mathematical form of the HHE, negative temperatures might be possible. However, this is avoided when introducing realistic physical constraints such as, e.g,

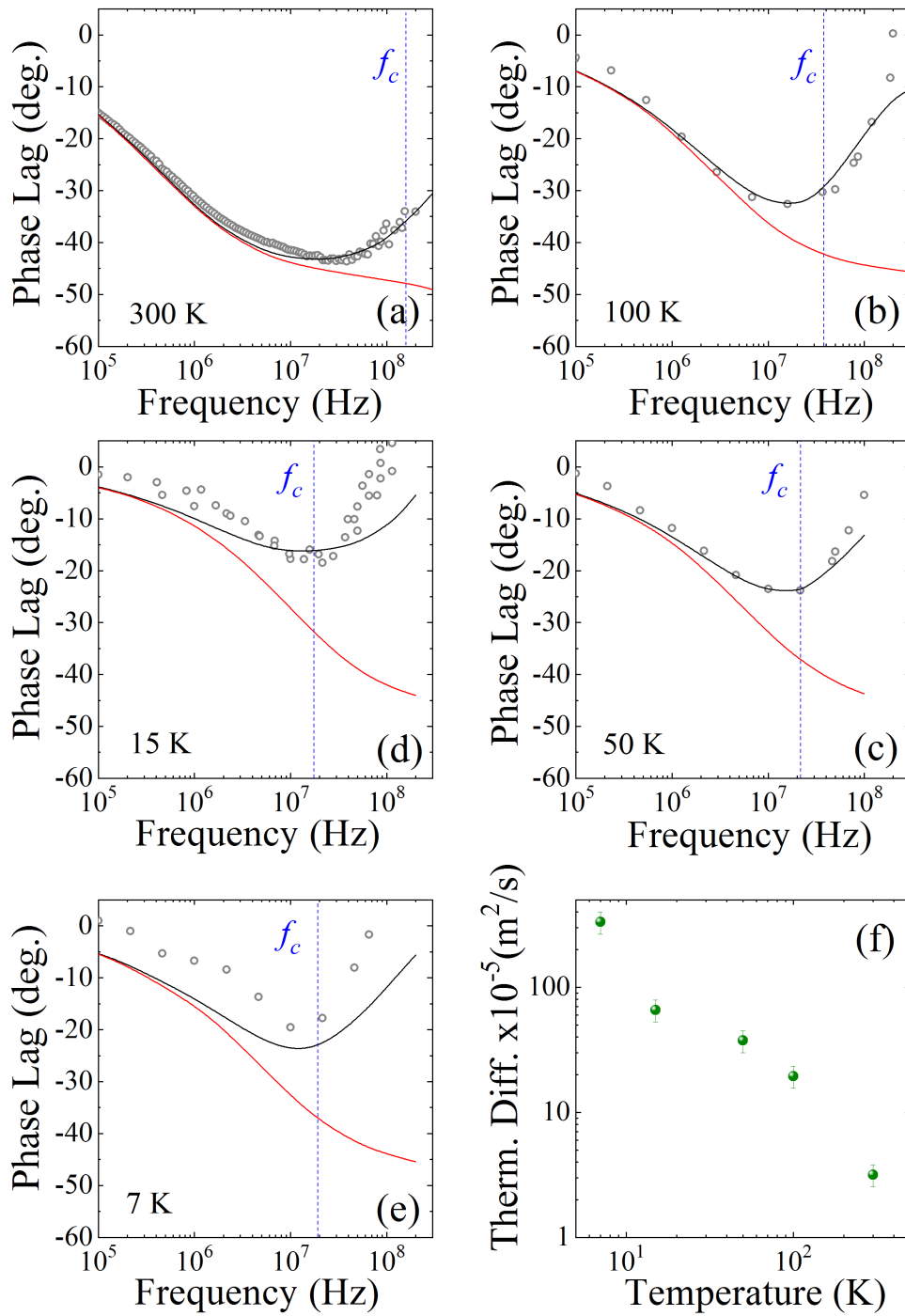


**Figure 46:** *Reproduced from [191].* (a-e) Phase lag as a function vs. frequency for different temperatures. The black lines correspond to fits to the data point using the hyperbolic heat equation 149, where the relaxation time and the thermal diffusivity have been fitted simultaneously, minimizing the error of the fitting procedure. The red curves correspond to the diffusive solution, as given by the prediction based on Fourier's law, using the thermal diffusivity as obtained from the hyperbolic fits. (f) The thermal diffusivity as a function of temperature extracted from the fits to the data using the hyperbolic heat equation.

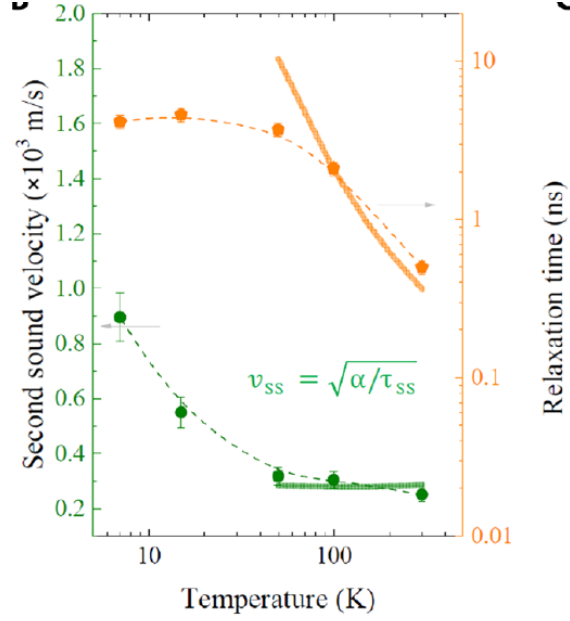


**Figure 47:** *Reproduced from [191].* The experimental relaxation times  $\tau$ , as well as the propagation velocity  $v_{ss}$  are shown as a function of temperature. The dashed lines are guides to the eye. The full lines are the ab initio calculated parameter values shown in section 3.5.

the existence of a maximum heat flux  $|\mathbf{q}|_{\max} \sim c\bar{v}T$  (with  $v$  being the average phonon velocity), which would correspond to the limit situation where all the thermal energy flows in one direction.

## 9.5 Diffusion of Hot Electrons and Influence of the Pump and Probe Penetration Depths

It is worth addressing the heat generation process in Ge which, in the present experiments, takes place through optical excitation of the electronic system. Upon optical excitation with the pump laser at  $E=3.06$  eV vertical transitions are induced from the valence to the conduction band. We recall that the momentum carried by photons is much smaller than the typical momentum of electrons in semiconductors and, thus, the optical excitation must occur with  $|\Delta\mathbf{k}|=0$ . In Ge, the principal optical bandgaps ( $|\Delta\mathbf{k}|$ ) in high symmetry points with high absorption at 3.06 eV correspond to the transition  $L_{3'} \rightarrow L_3$  with an energy band gap of 2 eV. Thus, only electron-hole pairs with  $\Delta E < 3.06$  eV can be excited, with local densities in  $\mathbf{k}$ -space which depend on the joint density of states between the conduction and valence bands. In fact, for  $E=3.06$  eV excitation, the joint density of states is maximum for states at the L point [197]. Although electron-hole pairs can also be excited at the  $\Gamma$  point, the joint density of excited states at this point is much lower as compared to the L point [198], which is also evidenced by the onset of the absorption spectra in Ge at  $E \sim 2$  eV [199]. After the

initial optical excitation process with  $E=3.06$  eV, the hot electrons at the Z point are scattered to the conduction band minimum, which is located at the same Z point. The mechanism which leads to the relaxation of the initially excited electrons is electron-electron scattering, with typical time constants of 100 fs [200]. On the other hand, the comparatively low amount of electrons excited at the  $\Gamma$  point relax towards the Z minimum through inter-valley scattering processes in a few hundreds of femtoseconds [201–203]. The two previous processes, i.e. (i) initial scattering to local minima and (ii) inter-valley scattering towards the Z point, involve the emission of optical and acoustic phonons, hence leading to the production of heat. Note that substantial amount of energy,  $(3.06 \text{ eV} - 0.66 \text{ eV}) = 2.4 \text{ eV}$  per absorbed photon, is transferred to the lattice before the electrons reach local equilibrium at the Z point. After they reach the minimum of the conduction band at the Z point, electrons are already thermalized in the sense that they do not produce the emission of thermal phonons. Their relative energy is reduced to  $E=0.66$  eV, compared to the initial  $E=3.04$  eV. Eventually, after several tens of ps to hundreds of  $\mu\text{s}$ , depending on the temperature of the lattice, these electrons relax, e.g. through the emission of photons and the absorption (anti-Stokes) or emission (Stokes) of a phonon (required for momentum conservation), Auger processes, defects, etc. We remark that the later recombination processes do not produce heat, since the electrons involved are already thermalized. These electrons populate the lowest energy states in the conduction band minimum at the L point. Hence, the probability of electron-phonon scattering events, which is the main heat generation mechanism, largely decreases since no lower energy electronic states are available. This implies that almost not heat is created in the electron-hole final recombination process, independently on its radiative or non-radiative nature. Using the previous values of the relaxation time of the excited electrons, we can estimate an upper limit for the propagation length of the hot electrons, e.g. using the maximum drift velocity in Ge which at 300 K is  $6.5 \cdot 10^4$  m/s [204]. Hence, the maximum estimated diffusion length for the hot electrons is 6.5 nm. Analogous arguments leading to similar results are also valid for holes. The estimated propagation length of the hot electrons/holes can slightly alter the laser penetration depth as estimated from the optical penetration depth of  $\delta_{\text{pump}} \sim 15$  nm.

Therefore, we study the effect of increasing the penetration depth of the pump and probe lasers on the phase lag response. In Figure 48, we show that if hypothetically considering a larger effective pump penetration depth, the phase lag curves would exhibit a correspondingly larger Fourier behavior in thermal transport, i.e. the phase lag approaches  $-\pi/4$  and even lower values. In other words, a larger effective pump penetration depth would mask, and not fictitiously amplify a second sound signature. Indeed, we show that the observation of second sound is not evident when the penetration depth of the heating region exceeds  $\sim 100$  nm. We have performed finite element calculations using the HHE varying the penetration depth of the heated region (pump) and considering as superficial the detection region (probe), as well as varying the penetration depth of the detection region (probe) and considering a 14 nm heating region (pump). Note that the pump region cannot be set to be too superficial due to the energy con-

servation considerations. Figure 48 displays the results from these calculations.

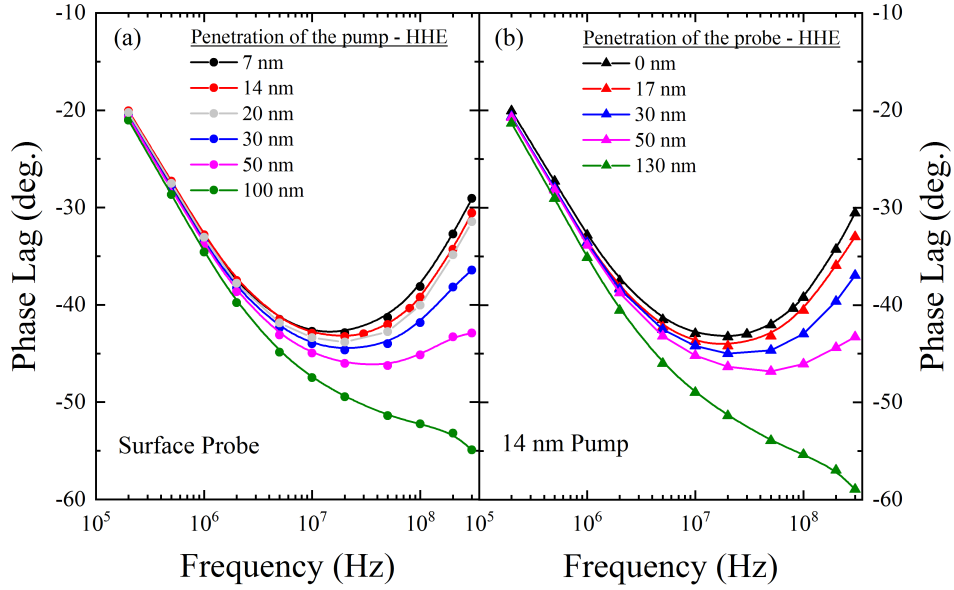


**Figure 48:** Reproduced from [191]. Phase lag response vs excitation frequency simulated using the hyperbolic heat equation (HHE). (a) Influence of different penetration depths of the heating region in the phase lag response studied for the case of surface detection. (b) Influence of increasing the probe region on the phase lag response for heat source with 14 nm penetration depth.

## 9.6 1D-Limit of the HHE and Influence of the Spot Size

As shown in Figure 44, the thermal penetration in the sample  $L_{\text{HHE}}$  is reduced by increasing the excitation frequency. At room temperature and the highest experimentally available frequencies, the thermal penetration is significantly smaller than the pump laser spot radius  $R_{\text{spot}}$ . Therefore, thermal transport is restricted to the cross-plane direction and the system thermal response is 1D. Exploiting this, in this subsection we derive the analytical 1D hyperbolic equation 149 solutions and hence we provide a simple expression for the phase lag at high frequencies and temperatures.

Consider the 1D version of the Maxwell-Cattaneo equation 147 and the energy conservation equation 146 including the heat source induced by the pump laser with characteristic length  $L_{\text{pump}}=14$  nm:

$$c \frac{\partial T}{\partial t} + \frac{\partial q}{\partial x} = \frac{Q_0}{L_{\text{pump}}} \exp\left(\frac{-x}{L_{\text{pump}}}\right) i\omega t, \quad (151)$$

$$q + \tau \frac{\partial q}{\partial t} + \kappa \nabla T = 0, \quad (152)$$



where  $x$  is the cross-plane coordinate,  $Q_0=1$  W and  $w$  is the angular heating frequency. We look for stationary solutions of the form

$$cT(x, t) = F(x) \exp(iwt), \quad (153)$$

$$q(x, t) = G(x) \exp(iwt). \quad (154)$$

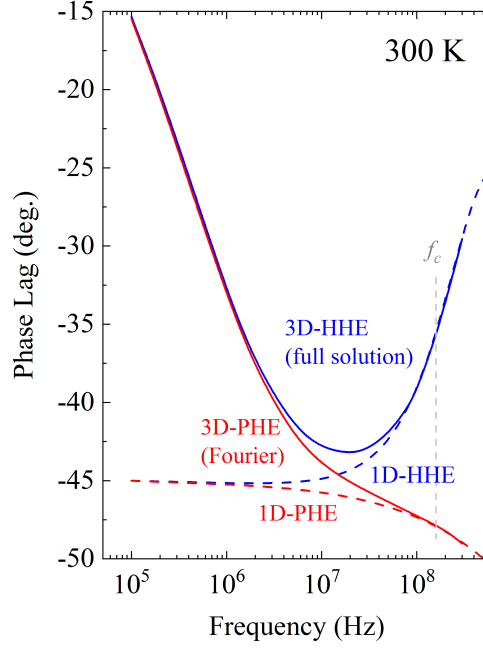


**Figure 49:** *Reproduced from [191].* Phase lag curves calculated using different heat transport models: (i) 3-dimensional hyperbolic heat equation (3D-HHE), (ii) 3-dimensional parabolic heat equation (3D-PHE, diffusive), (iii) 1-dimensional hyperbolic heat equation (1D-HHE), and (iv) 1-dimensional parabolic heat equation (1D-PHE, diffusive).

According to equations 151,152, the functions  $F(x)$  and  $G(x)$  satisfy

$$iwF + G' = \frac{Q_0}{L_{\text{pump}}} \exp\left(\frac{-x}{L_{\text{pump}}}\right), \quad (155)$$

$$(1 + iw\tau)G = -\frac{\kappa}{c}F', \quad (156)$$

where superindex ' denote the time-derivative. By defining

$$\gamma^2(w) = \frac{iw - \tau w^2}{\kappa/c} \quad (157)$$

and combining equations 155 and 156, we obtain the following second order nonhomogeneous differential equation:

$$\gamma^2 G - G'' = \frac{Q_0}{L_{\text{pump}}^2} \exp\left(\frac{-x}{L_{\text{pump}}}\right). \quad (158)$$

The general solution of 158 is the combination of the homogeneous solution with negative exponent (heat flux vanish far away from the semiconductor surface at  $x = 0$ ) and a particular solution

$$G(x) = A \exp(-\gamma x) + G_0 \exp\left(\frac{-x}{L_{\text{pump}}}\right), \quad (159)$$

where  $G_0 = \frac{Q_0}{(\gamma L_{\text{pump}})^2 - 1}$  and  $A$  is a constant depending on the boundary condition. We impose the insulation boundary condition  $0 = q(x = 0, t) = G(x = 0) = A + G_0$  and we obtain

$$G(x) = G_0 \left( \exp\left(\frac{-x}{L_{\text{pump}}}\right) - \exp(-\gamma x) \right). \quad (160)$$

Therefore, from 155,

$$F(x) = \frac{1}{i\omega} \left( G_0 \left( \frac{\exp(-x/L_{\text{pump}})}{L_{\text{pump}}} - \gamma \exp(-\gamma x) \right) + \frac{Q_0}{L_{\text{pump}}} \exp\left(\frac{-x}{L_{\text{pump}}}\right) \right), \quad (161)$$

and the solution for the temperature reads

$$cT(x, t) = \frac{Q_0}{i\omega} \left( \left( \frac{G_0}{Q_0} + 1 \right) \frac{\exp(-x/L_{\text{pump}})}{L_{\text{pump}}} - \gamma \frac{G_0}{Q_0} \exp(-\gamma x) \right) \exp(i\omega t). \quad (162)$$

The thermal penetration depth of the perturbation is then  $L_{\text{HHE}} = 1/\Re(\gamma)$ . At low frequencies  $\omega\tau \ll 1$ , we recover the classical penetration depth  $L_{\text{dif}} = \sqrt{\frac{2\kappa}{c\omega}}$ . By increasing the frequency, the penetration depth deviates from the classical prediction and, in the limit  $\omega\tau \gg 1$ , it becomes frequency-independent  $L_{\text{SS}} = 2\sqrt{\frac{\kappa\tau}{c}}$ . These thermal penetration lengths are shown in Fig 44. Moreover, the wavelength of the thermal oscillations is  $\lambda_{\text{HHE}} = \frac{2\pi}{\Re(\gamma)}$ . Note that at high frequencies we obtain the limit  $\lambda_{\text{SS}} = v_{\text{SS}}/f$  as expected. These characteristic lengths obtained from the 1D-HHE properly characterize the full 3D problem as confirmed by the Finite Elements calculations.

At the surface

$$cT(x = 0, t) = \frac{Q_0}{i\omega L_{\text{pump}}} \left( \frac{G_0}{Q_0} (1 - \gamma L_{\text{pump}}) + 1 \right) \exp(i\omega t). \quad (163)$$

The resulting phase lag between the laser and the temperature oscillation is

$$\arg[T(x = 0, t)] = -\frac{\pi}{2} + \arctan\left(\frac{\sin\theta}{\cos\theta + L_{\text{pump}}|\gamma|}\right), \quad (164)$$

where  $\theta = \arg[\gamma]$ . From 164, it can be seen that by increasing the heating frequency to values close to  $\tau^{-1}$ , the wave-like thermal behavior emerges leading to a non-monotonous behavior of the phase lag. In Figure 49 we show the 1D-HHE solution and the 1D Fourier solution ( $\tau=0$ ) at room temperature compared with the corresponding 3D solutions from both models using FEMs. It can be seen

that the 1D solutions match the 3D numerical solutions for  $f > 30$  MHz. In fact, in this frequency range and at room temperature the thermal penetration depth  $L_{\text{HHE}}$  is one order of magnitude smaller than the laser spot diameter and, thus, the system response is effectively restricted to 1D as expected. Conversely, at lower temperatures the thermal penetration depths are larger and the transition to the 1D behavior is not obtained within the studied frequency range.

Now, we address the influence of the spot size and its relation to the minimum of the phase lag response curve, which, in general, is not observed at the characteristic frequency  $f_c$ . As temperature decreases,  $f_c$  gradually approaches the minimum of the phase lag curve as observed in Figure 43 and 46. However, at room temperature  $f_c$  is not well represented by the minimum. The origin of this effect is the 3D→1D heat flow transition that the system experiences as frequency increases at room temperature. The reduction of the dimensionality causes a shift of the phase lag minimum curve to frequencies smaller than  $f_c$ . Note that this effect is only observed at high temperatures in the present experimental conditions since, for higher frequencies ( $f > 10$  MHz), the penetration depth ( $L_{\text{HHE}} < 1 \mu\text{m}$ ) is much smaller than the diameter of the pump laser spot ( $\sim 11 \mu\text{m}$ ) and, thus, heat transport become 1D. In contrast, this effect is gradually suppressed as temperature decreases since the thermal penetration depth increases, thus, leading to 3D heat transport within all the considered frequency range. In such conditions, the minimum of the phase lag curve is uniquely related to the unlocking of wave-like effects, hence  $f_c$  and the frequency of the minimum coincide. In Figure 50 we show calculations of the phase lag using the HHE in 3D and its 1D limit, and for different spot sizes of the heating region at room temperature. At high frequencies the 3D and 1D solutions of the HHE are equivalent, thus, showing that the system undergoes the mentioned 3D→1D transition. Consistently, at low frequencies the 1D limit of the HHE is not a good approximation to our experiments due to the finite size of the heating spot. However, as the spot size increases the solution at lower frequencies gradually approaches  $-\pi/4$ .

The frequency position of the minimum is dependent on three parameters: the thermal diffusivity of the sample ( $\kappa/c$ ), the heat flux relaxation time ( $\tau$ ), and the size of the heating spot ( $R_{\text{spot}}$ ). Figure 50 displays simulations for different diameters of the heat source, and using the room temperature values of  $\kappa/c = 3 \cdot 10^{-5} \text{ m}^2/\text{s}$  and  $\tau = 500 \text{ ps}$ . As discussed above, by reducing the spot size the 3D→1D transition is shifted to higher frequencies and, hence, the position of the minimum becomes closer to  $f_c$ . On the other hand, the influence of  $\kappa/c$  and  $\tau$  on the position of the minimum is rather easier to qualitatively address. Exploiting the 3D→1D transition, we explain in a simple fashion how the minimum depends on each parameter using the 3D Fourier and the 1D-HHE for the lower and higher frequency range, respectively. Figure 50 displays calculations of the 3D diffusive response (3D-PHE) for different values of  $\kappa/c$ . In addition, we also show the 1D limit of the HHE for different values of  $\tau$ . All calculations were done for a fixed spot size,  $2R_{\text{spot}} = 10 \mu\text{m}$ . Larger values of  $\kappa/c$  imply larger values of the thermal penetration depth, which cause a shift to higher frequencies of the 3D→1D transition and, consequently, the minimum of the phase lag curve is obtained at

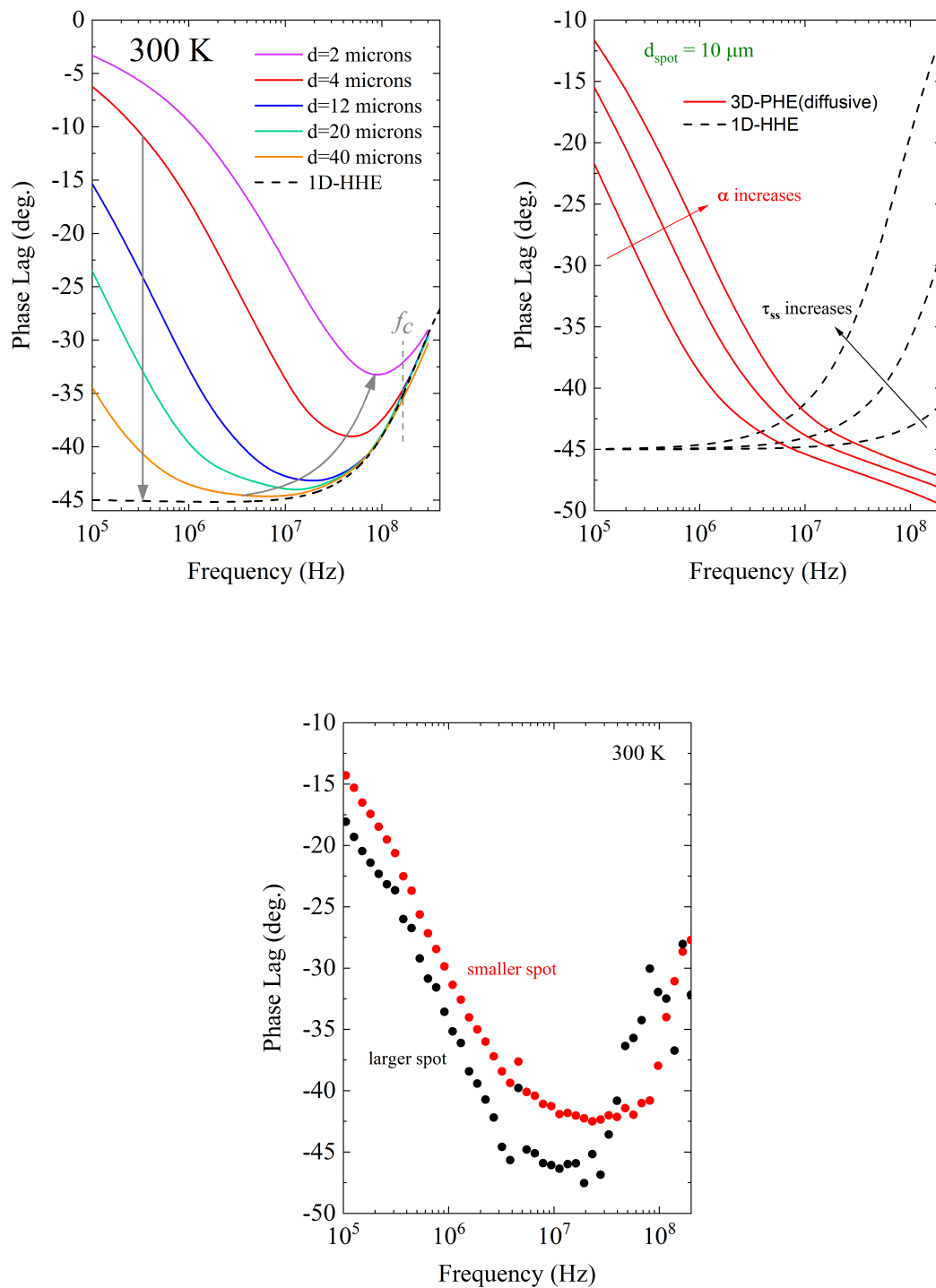


**Figure 50:** *Reproduced from [191]. (Upper-Left):* Numerical simulations on the influence of different spot sizes diameter at room temperature. The dashed line corresponds to the 1D-HHE. **(Upper-Right):** Calculations on the influence of increasing the thermal diffusivity and the heat flux relaxation time on the minimum of the phase lag curve for  $R_{\text{spot}} = 5 \mu\text{m}$ . The approximate position of the minimum is given by the intersection of the 3D-PHE with the 1D-HHE. **(Lower):** Experimental measurements showing the influence of the spot size on the phase lag response.

higher frequencies. Conversely, by increasing the value of  $\tau$  the wave-like effects (i.e. a reduction of the phase lag) are obtained at lower frequencies, which shift the minimum to lower

## 9.7 Influence of Metallic Transducers

Here we compare the present experiments in bare Ge with the data obtained including a thermal interface through the deposition of a gold metallic transducer, which is analyzed in Chapter 6. Figure 51 displays the frequency dependent phase lag at room temperature for the two different interfaces, Ge/oxide/Au and Ge/Au, studied in section 6.3.

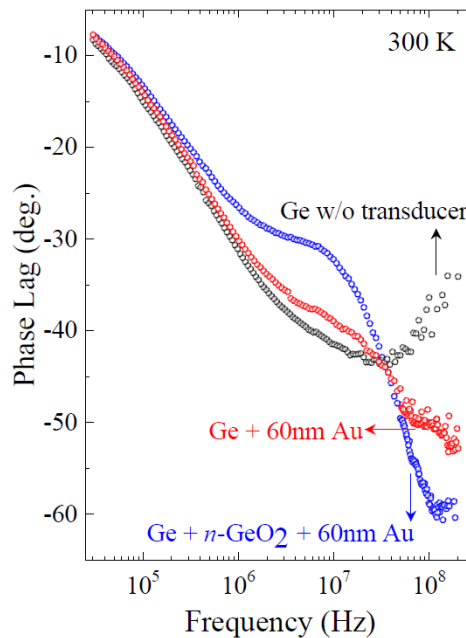


**Figure 51:** *Reproduced from [191].* Influence of the presence of a thermal interface on the frequency-dependent phase lag at room temperature.

It can be seen that the presence of the thermal interface between the Au transducer and the Ge substrate, as well as the Au transducer itself, dominate the system response in the frequency range where wave-like effects are expected. In particular, this becomes the dominant contribution over 100 MHz and the second sound signature (i.e. the non-monotonous trend of the phase lag) is not observed. Recall that the extremely small size of the heated region in bare Ge (smaller than  $\ell$ ) is what suppress non-local effects, thus unlocking memory effects as predicted

by condition 145 (see section 9.1). However, if a transducer is used, the heat is injected through the boundary and no external volumetric heat source is imposed in the semiconductor domain, which cause interfacial and non-local transport effects to play a role as shown in Chapter 6. More work is required to understand the attenuation of nonlocal effects and its interplay with memory effects.

## 10 Computational Experiments

The generalized phonon hydrodynamic framework is capable of predicting the thermal behavior of semiconductor samples under a variety of non-equilibrium situations. This theory describes the evolution of macroscopic quantities like the heat flux and the temperature, which allow easy and direct application to the thermodynamic modeling of complex devices. However, neither the mechanical evolution of the crystal lattice nor the phonon dynamics are directly accessible from the model solutions. In consequence, understanding the fundamental microscopic mechanisms governing the thermal transport at the nanoscale requires the use of alternative approaches. In this Chapter we explore the connections between microscopic models and the hydrodynamic model presented in section 3.2. In particular, we consider a Monte Carlo solver of the BTE [32, 205] and Non-equilibrium Molecular Dynamics simulations of the crystal dynamics [206, 207]. Such comparisons provide deeper understanding of the emergence of phonon hydrodynamic phenomena, and also provide insight to push the limits of applicability of the hydrodynamic model to smaller length and time scales.

### 10.1 Deviational energy Monte Carlo BTE simulations

Provided complete knowledge of the collision operator, it is widely accepted that solving the BTE is the most reliable way to model phonon transport. As explained in section 2.1, significant progress on characterizing the phonon-phonon scattering mechanisms has been achieved with the implementation of Density Functional theory. However, the high computational cost and the introduction of nanoscale energy sources or complex system boundaries has impeded the use of the BTE for direct thermal modeling of electronic devices for long years. Nevertheless, several numerical schemes have been developed to optimize the calculations and to incorporate the influence of the external perturbations. Usually, such models use simplified collision operators based in the RTA or the Callaway approximation (see section 2.2). These numerical methods mainly include the Monte Carlo scheme [32–35, 39], the Lattice Boltzmann Method [36], the Discrete-Ordinate-Method scheme [45, 46], the Finite Volume Method [37], and the Discrete Unified Gas Kinetic Scheme [38]. Due to the use of approximated collision operators, energy conservation should be imposed [30, 32]. Other works aimed to solve the full (non-diagonal) collision operator characterized with DFT using similar numerical schemes [40–42]. Even though the use of the full (and exact) collision operator would guarantee the energy and momentum conservation, numerical uncertainty also forces these solvers to include Lagrange multipliers or similar methods to accurately impose the conservation laws.

The main purpose here is to provide microscopic insight about the phenomenology predicted by the hydrodynamic model and to determine which are the fundamental microscopic constraints required to reproduce the hydrodynamic model predictions. To do so, we implement an energy-based, deviational Monte Carlo solver of the BTE (MC-BTE) [32]. In order to provide an equal footing compari-

son with the hydrodynamic model, we use a single averaged mean free path  $\Lambda$  for all our deviational energy particles. In good agreement with the ab initio expression for the non-local length  $\ell_2$  if considering a single relaxation time, here we assume that  $\Lambda = \sqrt{5}\ell$ . Note that  $\Lambda$  is significantly larger than the usual averaged phonon mean free path weighted by the specific heat [208], as required for experimental modeling (see Chapter 4). Within the Monte Carlo BTE framework, energy conservation is strictly imposed, but the conservation of momentum is not guaranteed during the scattering processes since the out-going particles after scattering have random direction. In contrast, other refined Monte Carlo solvers of the BTE carefully include the role of the Normal collisions and incorporate the interplay between different phonon modes with a variety of MFP [40, 41]. These refined solvers predict the emergence of hydrodynamic heat flux profiles in specific non-equilibrium conditions in 2D materials like graphene [41]. Here, we deliberately neglect the role of Normal collisions in order to demonstrate that the dominance of this kind of collisions is not required to observe hydrodynamic behavior as described by eq. 76.

Similar comparison between eq. 76 and energy-based deviational Monte Carlo simulations of the BTE with a single mean free path and with neglecting the Normal collisions have evidenced good agreement in some specific non-equilibrium situations [16]. Specifically, the thermal conductivity in thin films and the thermal response under frequency-modulated external excitations have been contrasted. Here we focus in a different non-equilibrium situation in which the hydrodynamic equation has shown to successfully predict the experimental observations in section 5 and 7. We consider the process of heat release from a nanoscale heater towards a Silicon substrate at room temperature in steady-state conditions (see schematic of the simulation domain in Fig. 52). In such situation, the heat flux is non-homogeneously injected and the thermal response away from the heater within the average phonon MFP length scale deviate from the diffusive prediction. Our main objective is to demonstrate that the conservation of momentum in this length scale due to the lack of phonon-phonon Resistive collisions cause the heat flux initial direction to persist in the downward direction, and the resulting thermal perturbations are non-locally connected, leading to the appearance of heat vorticity [46] in perfect agreement with eq. 76 predictions.

### Monte Carlo solver

An energy-based deviational Monte Carlo method is used to simulate the Boltzmann Transport Equation [32]. The following implementation and the corresponding simulations were obtained in collaboration with the graduate student Marc Gutiérrez.

While traditional MC methods are meant to obtain the phonon distribution  $f$  by solving the phonon BTE under the RTA

$$\frac{\partial f}{\partial t} + \mathbf{v}\nabla f = \frac{f^{\text{eq}}(T_0) - f}{\tau}, \quad (165)$$



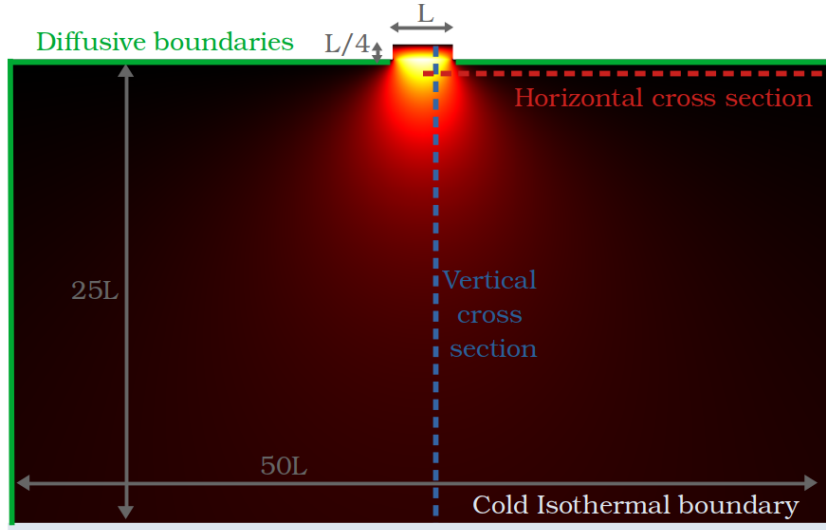


**Figure 52:** The stationary heat flux and temperature profiles are obtained according to Fourier's, the hydrodynamic model, and the MC-BTE. The solutions presented in Figures 53, 54, 55, and 56, are represented along the indicated horizontal and vertical cross-sections.

the energy-based formulation solves the energy projection of the BTE

$$\frac{\partial e}{\partial t} + \mathbf{v}\nabla e = -\frac{e - e^{\text{eq}}(T_0)}{\tau}, \quad (166)$$

being  $\mathbf{v}$  the phonon group velocity,  $\tau = \Lambda/|\mathbf{v}|$  the phonon mode relaxation time, and  $T_0$  a reference temperature. Super-index "eq" denotes the Bose-Einstein equilibrium phonon distribution and its corresponding energy, respectively. The unknown variable is then the energy  $e = \hbar\omega f$ , with  $\omega$  denoting the phonon frequency.

To increase the efficiency of the MC simulations and to accurately compute the resulting local thermodynamic outputs like the heat flux, only the small energy fraction transported by the deviational phonons with respect to the equilibrium at  $T_0$  is simulated. Defining the deviational energy  $e^d = e - e^{\text{eq}}(T_0)$ , the transport equation for  $e^d$  reads

$$\frac{\partial e^d}{\partial t} + \mathbf{v}\nabla e^d = -\frac{e^d}{\tau}. \quad (167)$$

By discretizing the deviational energy in particles with fixed energy, equation (167) can be simulated in our specific experiment with strictly imposing the conservation of energy. For comparison purposes with the hydrodynamic heat transport equation, here we use a gray-model approximation by choosing a mode-independent value for  $\tau$  and  $|\mathbf{v}|$ . The local temperature differences in our numerical experiments is extremely small, so we can use fixed average properties for Silicon at the reference temperature  $T_0 = 300\text{K}$ .

First, we impose the 3D relation between the non-local length calculated for Silicon at room temperature  $\ell=196\text{nm}$  (see section 3.5) and the mean free path

$\Lambda = \tau|\mathbf{v}| = \sqrt{5}\ell = 439 \text{ nm}$  [16, 19]. Moreover, the kinetic definition of the thermal conductivity 13 must be satisfied. In agreement with the single mode RTA:  $\kappa = \frac{1}{3}|\mathbf{v}|\Lambda c = 141 \text{ W/mK}$ , where  $c = 1.63 \cdot 10^6 \text{ J/m}^3\text{K}$  is the specific heat. Therefore, the velocity modulus of our deviational energy particles is  $|\mathbf{v}| = 591 \text{ m/s}$ .

Note that the mean free path  $\Lambda$  (the velocity  $|\mathbf{v}|$ ) is significantly larger (smaller) than the usual averaged values from the phonon population weighting by the specific heat of each mode [208]. We are not simulating the phonon population dynamics here, but the transport of deviational energy, which is properly described with some specific averages that can be derived from the full BTE as discussed in section 3.2. Furthermore, it can be shown that the resulting scattering time for our particles  $\tau = \Lambda/v$  is the characteristic decay time of the heat flux appearing in the hydrodynamic equation 76, as obtained from the first moment projection of the BTE [19].

In the MC-BTE simulation, the computational domain shown in Figure 52 is homogeneously divided into rectangular cells. Initially, an arbitrary temperature distribution is assumed in the system. We study the evolution of the deviational energy with respect to the equilibrium energy at the reference temperature  $T_0 = 300\text{K}$ . Assuming local equilibrium, this deviational energy for a given cell at a certain temperature  $T$  can be calculated as

$$\Delta E = \sum_p \int_{\omega} \hbar\omega D(\omega, p) \left( \frac{1}{\exp\left(\frac{\hbar\omega}{k_B T}\right) - 1} - \frac{1}{\exp\left(\frac{\hbar\omega}{k_B T_0}\right) - 1} \right) d\omega, \quad (168)$$

where  $p$  denotes the phonon branch, and  $D(\omega, p)$  is the density of states.

The deviational energy is discretized in particles with fixed energy  $\varepsilon^d$ , so the initial number of particles in a given cell is  $N_{\pm} = \Delta E/\varepsilon^d$ . The energy of each particle  $\varepsilon^d$  is determined based on a trade-off between variance-reduction and computational cost. Note that depending on the sign of  $\Delta E$ , the particles represent positive or negative energy deviations.

Once the system is initialized imposing random initial direction for all the particles, in a time step of duration  $\Delta t$  the particles are allowed to drift with velocity  $\mathbf{v}$  as indicated by Eq. 167. The  $\Delta t (\ll \tau)$  must be chosen such that the particles can not traverse an entire cell in one time step. After drift, the temperature of a given cell is sampled from its deviational energy

$$\Delta E = \varepsilon^d (N^+ - N^-) \quad (169)$$

by numerically inverting Eq. (168).  $N_j^+$  and  $N_j^-$  refer to the number of positive and negative particles within the cell, respectively. Once the particles are advected, the heat flux inside a given cell can be computed as

$$\mathbf{q} = \frac{\varepsilon^d}{V} \sum_i s(i) \mathbf{v}(i) \quad (170)$$

where  $V$  is the cell volume, and we sum over all the particles  $i$  in the cell, with  $s(i)$  the particles energy sign and  $\mathbf{v}(i)$  the velocities.

Before finishing each time step, we determine the particles that suffered scattering using the scattering probability

$$P = 1 - \exp\left(-\frac{\Delta t}{\tau}\right) \quad (171)$$

as indicated by Eq. (167).

The scattered particles are removed from the system. Then, the minimum amount of particles in each cell to conserve energy is generated; that is, if in one time step  $N^+$  positive particles and  $N^-$  negative particles have scattered in one cell,  $|N^+ - N^-|$  particles in the same cell (positive if  $N^+ > N^-$  and negative otherwise) are introduced. The position and direction of the new particles are chosen randomly inside the cell. Therefore, the energy is locally conserved in each cell during scattering, but the momentum of the particles is destroyed (only Resistive collisions are simulated). Furthermore, note that this process tends to reduce the number of particles as the system approaches the steady-state situation. Thus, the method tends to locally reduce the thermodynamic fluctuations, which is in agreement with the notion of optimum local entropy production [5].

As shown in Figure 52, all the system boundaries except the cold isothermal boundary in the bottom are modeled as diffusive boundaries. The incident particles to this boundaries are randomly reoriented towards the system. This kind of boundary is mesoscopically described in the hydrodynamic model by the slip boundary condition 81 with  $C = 1$  and the insulation one 77 as discussed in section 3.4. In the out-of-plane direction, periodic boundary conditions are used.

To model the nanoscale heat source in Figures 53, 54 and 55 below, in each time step a fixed number of positive particles  $N$  is homogeneously introduced with random direction in the nanoscale structure (width  $L$  and height  $L/4$ ) displayed in Figure 52. Hence, the power density introduced is  $Q = \frac{4\epsilon^d N}{L^2 \Delta t}$ . In the hydrodynamic model, the power density introduced in the heater using the energy conservation equation 75 is exactly  $Q$ . In the Fourier solutions, the power density must be increased by a different factor depending on the Knudsen number to fit the heater temperature obtained in the MC-BTE simulations, which is another indication of the breakdown of the diffusive description.

The isothermal boundary absorb all the incident particles and generate a fixed number of deviational energy particles in each time step with random direction, depending on the imposed temperature  $T_{\text{iso}}$  according to expression (168). This boundary condition is mimicking an interfacial boundary condition contacting the system and a thermal bath at the mesoscopic level of description. Accordingly, a Kapitza boundary condition contacting the system with a thermal bath at fixed temperature  $T_{\text{iso}}$  is used:

$$T - T_{\text{iso}} = -R_{\text{bath}} \mathbf{q} \cdot \mathbf{n}, \quad (172)$$

where the resistance  $R_{\text{bath}} = \frac{1}{4c|\mathbf{v}|} = 2 \cdot 10^{-9} \text{ m}^2 \text{K/W}$ , being  $|\mathbf{v}| = 591 \text{ m/s}$  the velocity of the deviational energy particles used in the MC-BTE simulations, and  $\mathbf{n}$  the boundary normal vector. This is a particular case of the interfacial boundary

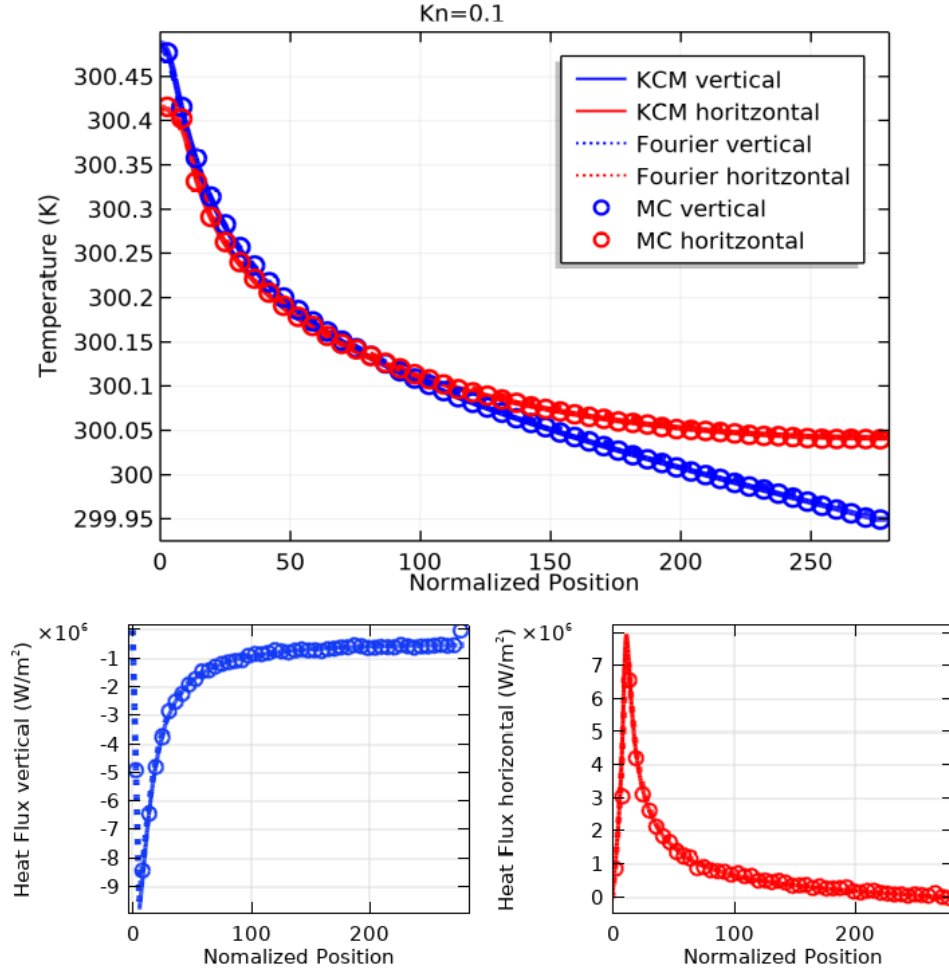


**Figure 53:** The temperature profile (top), the heat flux (low) obtained from the different models along the cross-sections indicated in Figure 52 is compared for  $Kn = 0.1$ . Position is normalized by the non-local length  $\ell$ .

condition 92 derived in section 3.4 with neglecting the non-Kapitza (non-local) terms. Such corrections are shown to have very small impact at room temperature in Silicon and, hence, we neglect it here for simplicity. Note that in Fig. 56 we use this boundary condition to model the nanoscale hot source of size  $L$  instead of introducing a power density to the heater.

## Results

In Figure 53 we show comparison of the temperature and the heat flux profiles as predicted by the hydrodynamic model (eq. 76) and the MC-BTE, when the heater size  $L$  is much larger than the Monte Carlo MFP  $\Lambda$  ( $Kn = \frac{\Lambda}{L} = \frac{\sqrt{5}\ell}{L} < 1$ ). For illustration, the Fourier's law prediction (obtained by neglecting the Laplacian term in Eq. 76) is also shown. As expected, diffusive transport is obtained and, hence, both the MC-BTE and the hydrodynamic predictions coincide with the Fourier results.

In Figure 54 and 55, we show the corresponding results when the heater size is

comparable to the phonon MFP ( $Kn = 1, 2$ , respectively). In such quasi-ballistic situations, the hydrodynamic predictions deviate from the diffusive solution and matches the MC-BTE simulations. Note that, according to the Fourier model in such stationary situation for a given temperature of the heater, substrate heat conduction is described by the equation  $\nabla^2 T = 0$ , which is independent of the thermal conductivity value. Therefore, the MC-BTE temperature profiles can not be reproduced by diffusion even with the use of an effective value of the thermal conductivity. For larger values of the Knudsen number ( $Kn > 2$ ), the hydrodynamic prediction start to deviate from the MC-BTE simulations, showing that the models are not completely equivalent in extremely ballistic situations. This might be attributed to the unavoidable limitations of a mesoscopic description based in continuous variables to describe the stochastic energy particles dynamics with finite mean free path  $\Lambda$ . However, from figures 54 and 55, it is clear that the mechanisms leading to the emergence of non-Fourier transport phenomena at the nanoscale are consistently captured at the two levels of description.

In order to further compare the different models, in Figure 54 and 55 we also compare the heat flux curl  $|\nabla \times \mathbf{q}|$  profile, and the local effective thermal conductivity  $|\nabla \mathbf{q}|/|\nabla T|$ . The boundary conditions both in the hydrodynamic description and in the Monte Carlo simulations generate heat flux vorticity due to the non-homogeneous energy injection to the system. In contrast, the Fourier solutions are irrotational, regardless the boundary conditions used. Furthermore, it can be seen that the existence of a non-null curl of the heat flux in the MC-BTE simulations is quantitatively correlated in space with the reduction of the heat flux (or the local thermal conductivity), in perfect agreement with eq. 76. Consequently, the emergence of heat vorticity and the non-diffusive transport predicted by the present MC-BTE simulations is successfully captured at the mesoscopic level of description by the hydrodynamic model.

The scarcity of Resistive collisions close to the boundaries is thus the necessary condition for this non-Fourier effect to be observed. In other words, what determines the existence of these kind of hydrodynamic-like heat transport in stationary situations is the heater size and the observation region, rather than the existence of intrinsic Normal collisions, which is a compatible but unnecessary condition. Nevertheless, the Normal collisions can reduce the broadness of the MFP spectrum of the phonons that mostly contribute to the energy conduction due to the emergence of collective modes [55]. The presence of such collisions may be then crucial to allow a heat transport description based in a single length scale (i.e. the mean free path and the non-local length in the MC-BTE and the hydrodynamic descriptions, respectively) in materials like Silicon (see section 4.1 for an extended discussion).

At this point, it is worth to note that previous mesoscopic modeling of the MC-BTE simulations [205] demonstrated that the Fourier predictions can be significantly improved by using isothermal nanoscale boundaries instead of introducing a constant power density in nanoscale heaters as considered previously. In Figure 56, we show the MC-BTE simulations with assuming a hot isothermal nanoboundary of size  $L$  instead of the heater, and the corresponding Fourier

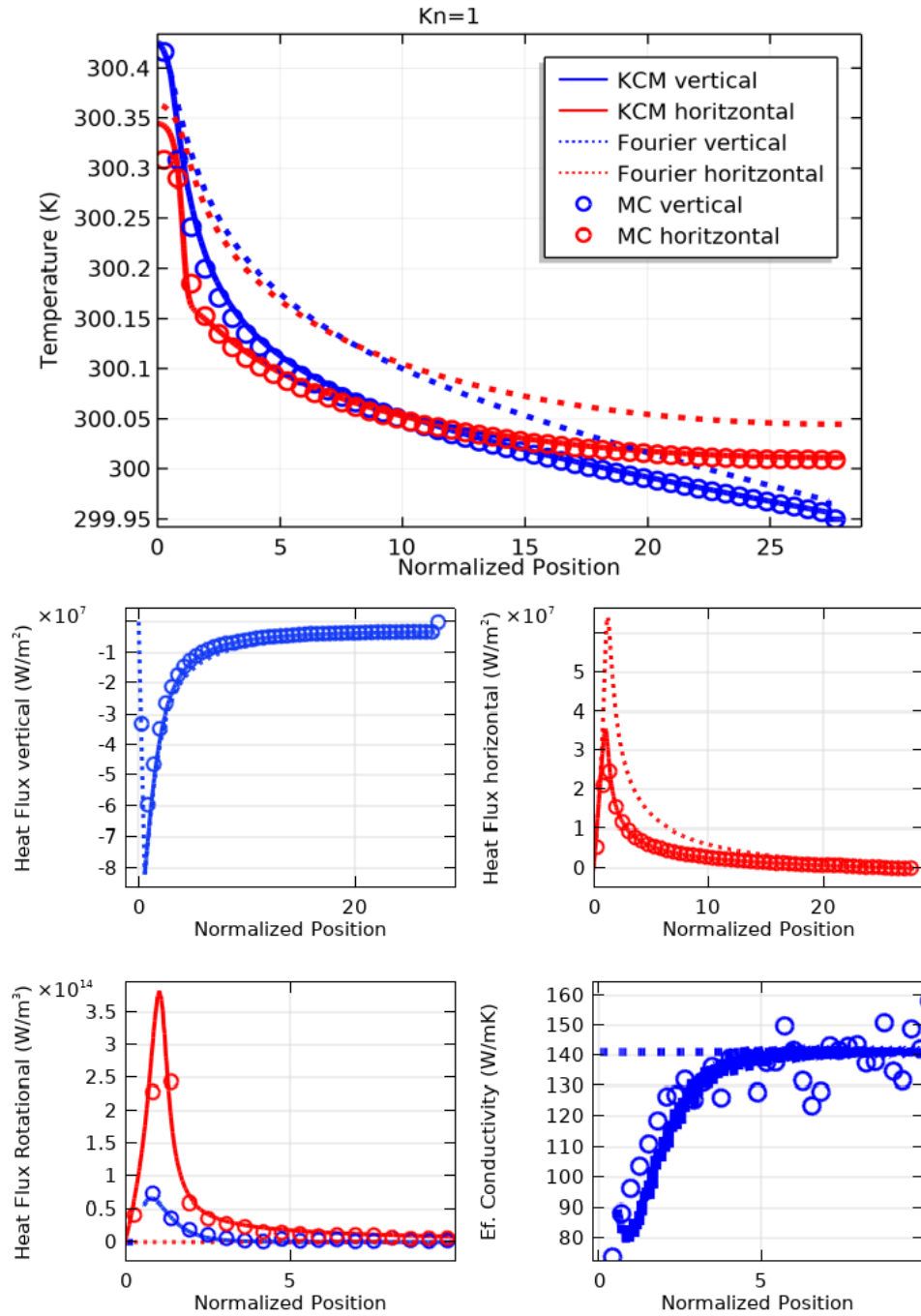


**Figure 54:** The temperature profile (top), the heat flux (mid), the heat flux curl (down-left), and the effective thermal conductivity (down-right), obtained from Fourier, the hydrodynamic model, and the MC-BTE is compared along the cross sections indicated in Figure 52, for  $Kn = 1$ . Position is normalized by the non-local length  $\ell$ .

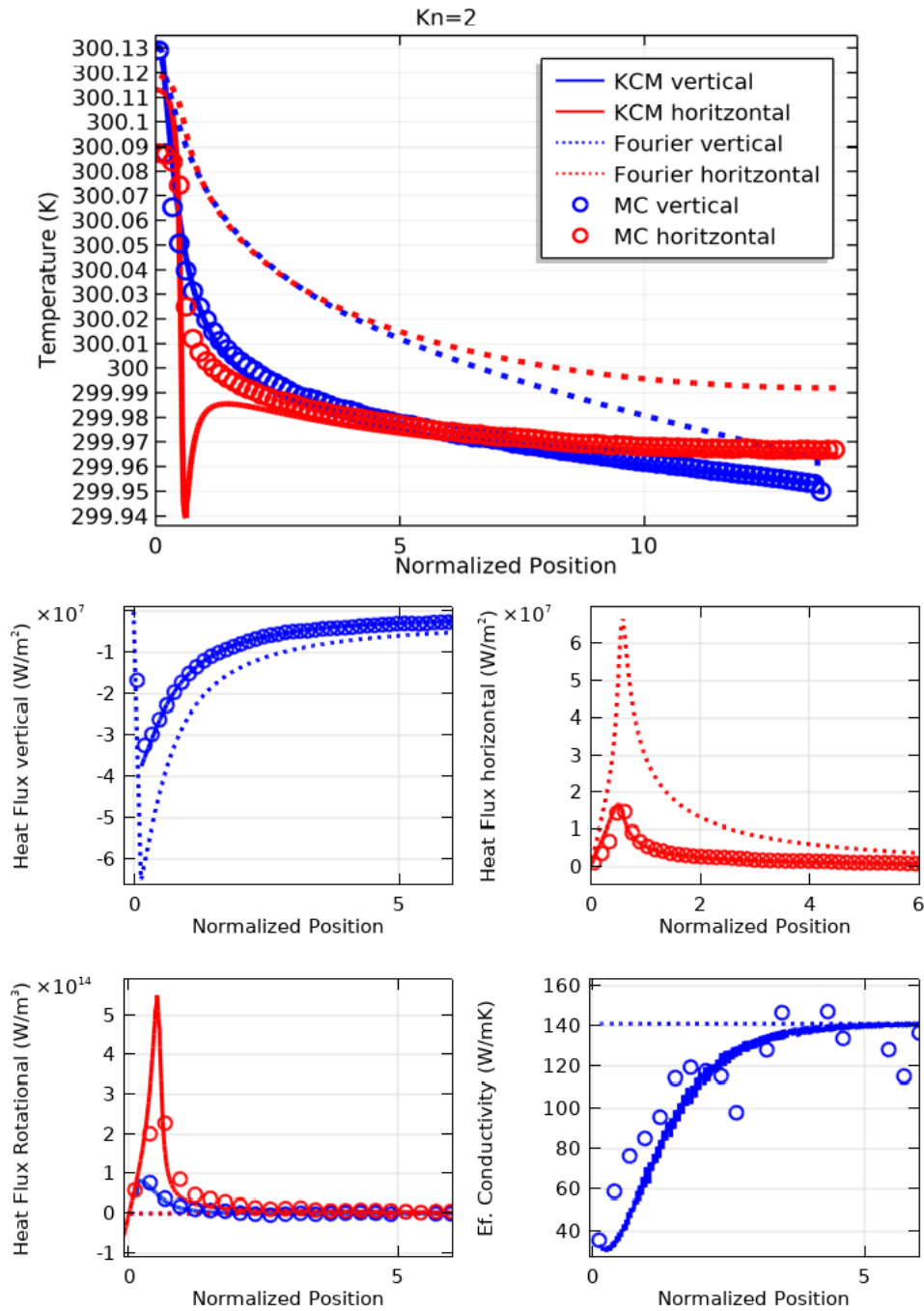


**Figure 55:** The temperature profile (top), the heat flux (mid), the heat flux curl (down-left), and the effective thermal conductivity (down-right), obtained from Fourier, the hydrodynamic model, and the MC-BTE is compared along the cross sections indicated in Figure 52, for  $Kn = 2$ . Position is normalized by the non-local length  $\ell$ .

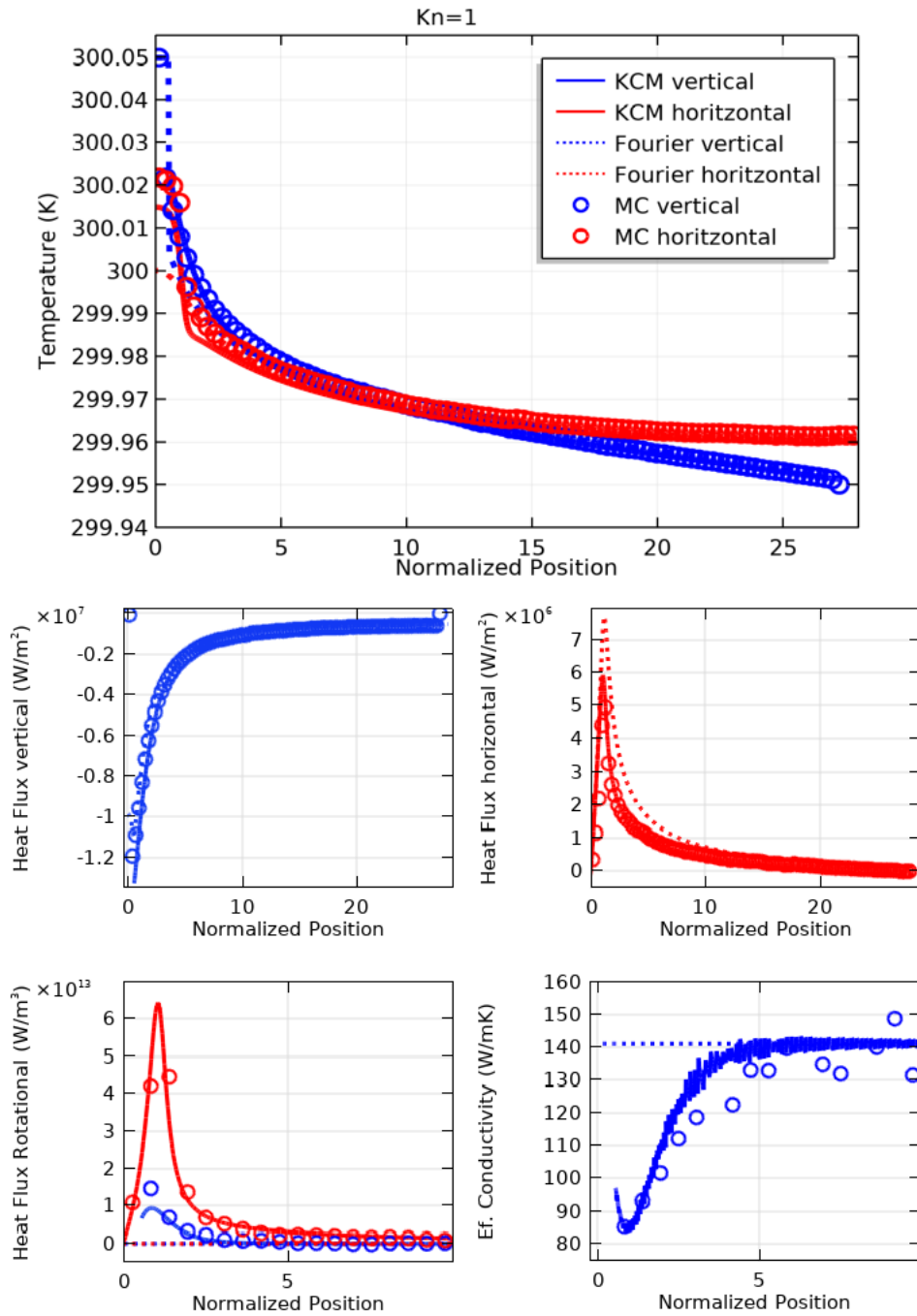


**Figure 56:** The temperature profile (top), the heat flux profiles (mid), the rotational (down-left) and the effective thermal conductivity (down-right) obtained from the different models is compared along the cross sections indicated in Figure 52 for  $Kn=1$ , with using a hot isothermal boundary condition of size  $L$  instead of introducing a fixed power density in the heater. Position is normalized by the non-local length  $\ell$ .



and hydrodynamic predictions using the isothermal 172 boundary condition. It can be seen that the Fourier predictions are significantly improved if using this alternative way to model the experiment. In contrast to the more physical modeling of the heater used in Figures 54 and 55, in this case the injected heat flux is homogeneous in all the hot nanoboundary, which attenuate the vorticity. However, the hydrodynamic prediction is still more accurate than the diffusive one, and the emergence of a non-null heat flux curl, which is a signature of non-Fourier behavior, is still present in the simulations. Therefore, the requirement of refined mesoscopic transport equations is demonstrated, which also allows more flexibility when imposing the boundary conditions to reproduce an specific experimental set up. Nevertheless, as demonstrated in [205], the use of refined mesoscopic boundary conditions is crucial to reproduce the MC-BTE simulations in specific non-equilibrium conditions. In particular, using a nanoscale isothermal boundary source to mimic the fixed energy density on the heater allows to introduce an extra boundary condition that improves the mesoscopic modeling even with maintaining Fourier's law to describe the substrate thermal response.

In conclusion, the dominance of momentum-conserving collisions is not required to observe non-local or hydrodynamic phenomena as predicted by Eq. 76. The lack of collisions within the phonon MFP length scales in the boundary regions also guarantee the momentum conservation required to unlock the non-diffusive behavior in nanoscale heater experiments (i.e. heat vorticity and reduced effective thermal conductivity), which is mesoscopically described through the inclusion of a Laplacian term in the hydrodynamic transport equation. These results are consistent with alternative numerical solvers of the BTE [46], and provide further theoretical justification to the applicability of hydrodynamic-like transport models to standard materials like Silicon at room temperature.

Future work should aim to compare the hydrodynamic model and more refined BTE solvers including more than one characteristic phonon mean free path. Taking into account the hydrodynamic signatures characterized by a single length scale ( $\ell$ ) in experiments (Chapter 4), such multiscale models should also predict transport phenomena characterized by the emergence of a single scale (like characteristic hydrodynamic decay times in Chapter 7). However, this is not what is obtained by state-of-the-art solvers based in multiscale RTA-BTE [75], in which phonon mean free paths much longer than the non-local length  $\ell$  manifest (see section 4.1). Similar to the energy conservation restriction (i.e. the zero order BTE projection) that should be imposed to these solvers [30], it may be hypothesized that proper inclusion of higher-order BTE projections would be required to refine this multiscale microscopic models.

## 10.2 Non-equilibrium Molecular Dynamics

In collaboration with the National Institute of Applied Sciences of Lyon  
(University of Lyon)

It is also possible to directly simulate the lattice dynamics at the atomic structure level through Molecular Dynamics (MD) simulations. The trajectories and the interaction forces of the atoms are explicitly calculated, and hence the BTE and the complexity associated to the phonon collisions is completely avoided. From the atomic evolution, the temperature can be defined in terms of the kinetic energy of the atoms and the heat flux via its velocity and stress [209, 210]. The bulk thermal conductivity can be quantified in equilibrium using the fluctuation dissipation theorem [211], or by simulating a thermal gradient and computing the resulting heat flux [212]. The mechanic equations of motion are classical and, hence, the results are only valid above the Debye temperature, where quantum corrections can be neglected. Remarkably, the thermal properties of bulk Si have been characterized through this method [207], and signatures of non-Fourier transport have been reported [213]. It is important to note that the interatomic potential is approximated since the electron dynamics and interactions are not explicitly simulated. This potential is adjusted so that the bulk thermal conductivity measured experimentally under homogeneous thermal gradients is obtained, but characterization of other transport parameters relevant for more complex non-equilibrium situations, like the non-local length or the heat flux relaxation time, have been received much less attention.

The main aim of the present section is to explore the emergence of non-Fourier phenomena in Silicon by comparing non-equilibrium MD simulations and the generalized hydrodynamic transport model. Specifically, we study the stationary heat flux profile established in nanowires and the emergence of thermal waves under extremely localized pulsed perturbations. These computational experiments are analyzed using effective parameters for the mesoscopic transport equations since the accessible characteristic sizes and times in MD are far beyond the applicability of the *ab initio* model (section 4.4). Nevertheless, it will be shown that the signatures of non-Fourier transport at these extremely small length scales can be still modeled using the hydrodynamic transport equations.

### Heat flux profile in Silicon nanowires

Silicon nanowires are a paradigmatic case of study of non-equilibrium MD due to its technological relevance. Current fabrication techniques have made possible the reduction of its diameter to the tens of nanometers, for which extremely low thermal conductivities have been measured [72]. Such nanosystems are beyond the applicability of the hydrodynamic heat transport model (see section 4.4). However, it is still possible to explore the phenomenology arising in these systems with the use of the hydrodynamic equation 76 with effective parameters.

The goal here is to simulate and interpret the heat flux radial profile established in the steady-state in Silicon nanowires. In MD, the thermal gradient is

generated by using hot (at 320 K) and cold (at 280 K) thermostats in the two terminals of the nanowire [214]. The trajectories of the atoms are computed using Verlet integration scheme, implemented in LAMMPS [215], and the interatomic potentials from Ref. [216] are used. The simulated NWs have a length of 500 Å, and two different radius are considered ( $R = 37.5$  Å and  $R = 50$  Å).

In MD, the heat flux in a volume  $V$  is defined as [209]:

$$\mathbf{q} = \frac{1}{V} \left( \sum_i E_i \mathbf{v}_i + \sigma_i \cdot \mathbf{v}_i \right), \quad (173)$$

with  $E_i$ ,  $\mathbf{v}_i$ ,  $\sigma_i$  being the total energy, the velocity, and the stress of atom  $i$ , respectively. The sum runs over all the atoms inside the considered volume  $V$ . The virial contribution  $\sigma_i \cdot \mathbf{v}_i$  takes into account all the non-negligible interatomic forces acting on atom  $i$ , as discussed in Ref. [217]. The heat flux 173 can be calculated locally and averaged at each radial position.

In Figure 57, the heat flux obtained in MD is shown for two different NW radius, and the profile is fitted using the hydrodynamic transport equations (75 and 76) along with the slip boundary conditions (77 and 81) using effective parameters  $\kappa$ ,  $\ell$ ,  $C$ . The obtained fitted values can be found in Table 3 for  $H=0$  (no amorphous layer). The two different NWs with different radius have exactly the same free-surface quality, so the same fraction of specular phonon-boundary reflections is expected. Consistently, parameter  $C$  does not depend on the radius (see eq. 82). However, the fitted values of  $C$  are smaller than 1, which is not consistent with the interpretation of this coefficient provided in section 3.4. Probably, this indicates that the assumption of thermalization for the phonons undergoing diffusive scattering at the boundary is not precise enough at the extremely reduced length scales simulated here. Moreover, both the thermal conductivity and non-local length are reduced by reducing the nanowire radius, which is expected due to the reduction of the phonon mean free paths in such confined system. Even though the parameter values are well below the ab initio calculated values at room temperature, the heat flux reduction close to the system boundaries can be well reproduced with eq. 76. In other words, the heat flux boundary layers introduced in section 4.2 to explain the thermal conductivity of films are observed in MD. This indicates that, beyond the applicability of the hydrodynamic model, non-local effects are still apparent and can be used to provide phenomenological descriptions.

### **Influence of Amorphous Layers**

In silicon samples exposed to oxygen, a thin amorphous layer surrounding the system boundaries is naturally formed. The typical width  $H$  of these layers is a few nanometers. For system sizes comparable to  $\ell$  ( $\gg H$ ), like the thin films considered in section 4.2, the in-plane effective thermal conductivity is not significantly influenced by these layers. However, at the reduced length scales accessible with Molecular Dynamics simulations, one can explore the influence of these amorphous regions by explicitly including disordered regions [218] surrounding the system contours along with the corresponding crystal-amorphous

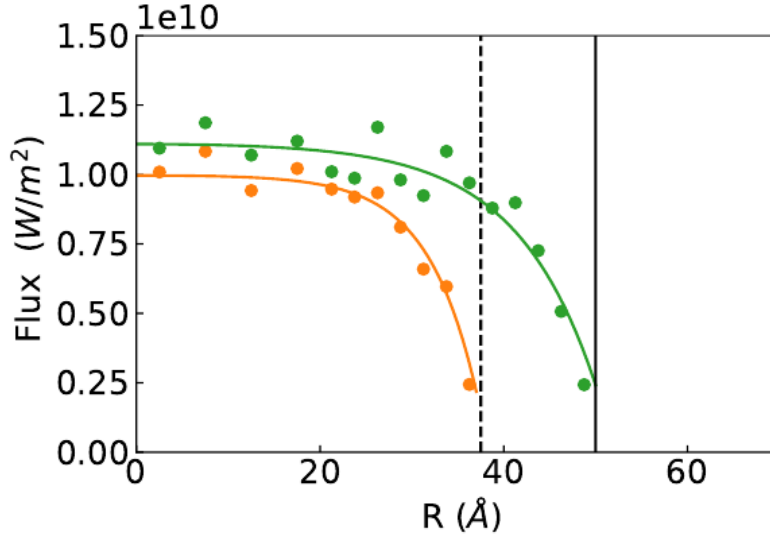


**Figure 57:** Heat flux obtained in MD simulations (dots) at different radial positions for NWs of radius  $R = 37.5 \text{ \AA}$  (orange) and  $R = 50 \text{ \AA}$  (green). The profiles are reproduced using the hydrodynamic model (lines) with effective parameter values shown in Table 3. In both cases, a heat flux boundary layer is observed close to the system boundaries.

interface [219, 220]. The amorphous shell thickness assumed here is  $H = 10 \text{ \AA}$ .

Since the phonon mean free paths are extremely small in the amorphous shell, heat transport can be described using Fourier law in these domains (non-local effects are negligible). The thermal conductivity for the amorphous is  $\kappa_{\text{amorph}} = 1.5 \text{ W/mK}$  as characterized from MD simulations [221]. The amorphous shell free surfaces are insulated 77. Regarding the crystalline-amorphous interface, the slip condition 81 is only required for the crystalline side where hydrodynamic transport is expected, and continuity of the heat flux 84 is used instead of insulation. In Figure 58 we compare the heat flux profile with and without the shell for a crystalline radius of  $R = 37.5 \text{ \AA}$ . The heat flux at the interface and the size of the boundary layer is unmodified, so we obtain the same  $C$  and  $\ell$  fitted values (see table 3). However, the heat flux saturation value in the center of the nanowire is reduced due to the presence of the shell, so the fitted thermal conductivity  $\kappa$  value is reduced. The profile is unmodified by considering larger amorphous shell thickness  $H$ .

In consequence, the amorphous layer does not modify the boundary effects which would reflect in a modification of  $C$  or  $\ell$ , but modifies the intrinsic material properties in the crystalline region since  $\kappa$  is affected. The dispersion relations, density of states and phonon group velocities can be characterized from MD [206], and no influence of the amorphous shell is obtained in the present simulations. Therefore, from the microscopic expression of  $\kappa$  13, it can be concluded that the presence of the amorphous shell reduce the phonon relaxation times in the nanowires. In principle, such modification would also reduce the non-local length according to its microscopic expression 72. However, the mode-dependent weights of the relaxation times in the microscopic expressions for  $\ell$

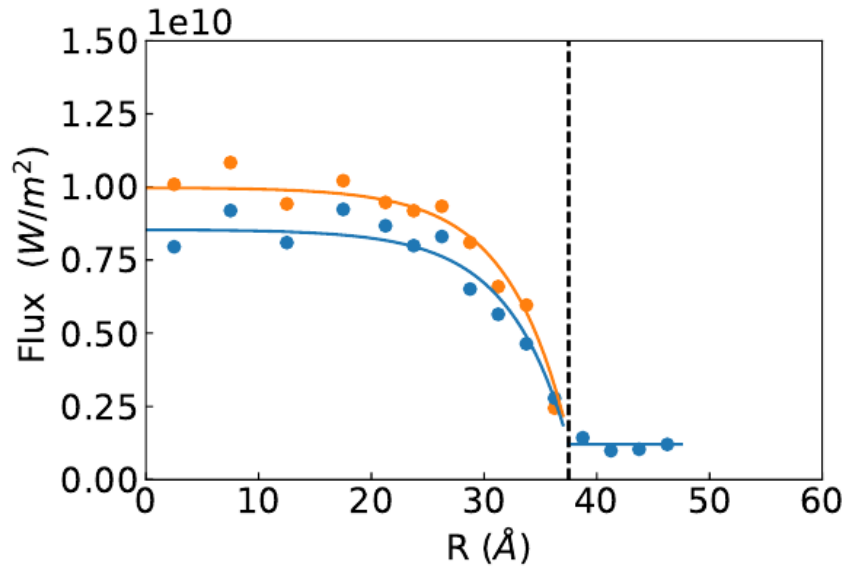


**Figure 58:** Heat flux obtained in MD simulations (dots) at different radial positions for NWs of radius  $R = 37.5 \text{ \AA}$  without shell (orange) and with a shell of thickness  $H=10 \text{ \AA}$  (blue). The profiles are reproduced using the hydrodynamic model (lines) with effective parameter values shown in Table 3. The heat flux saturation value in the centre of the NW is reduced due to the presence of the amorphous shell, which is translated to a reduction of parameter  $\kappa$ .

**Table 3:** Hydrodynamic parameter values fitted to the MD heat flux radial profiles for different NW radius  $R$  and amorphous shell thickness  $H$ .

$R$ [ $\text{\AA}$ ]	$H$ [ $\text{\AA}$ ]	$\kappa$ [W/mK]	$\ell$ [ $\text{\AA}$ ]	$C$
37.5	0	12.5	5	0.3
37.5	10	10.7	5	0.3
50	0	14	8	0.3
50	10	12.3	8	0.3

and  $\kappa$  are not equivalent (see section 3.5. In other words, a reduction of the relaxation time of a specific mode does not necessarily has the same influence on the two different parameters. Then, the obtained fits could be explained by a reduction of the relaxation times of the modes that mostly influence  $\kappa$  (intermediate frequencies) with leaving unaffected the modes that mainly determine  $\ell$  (low frequency modes). Future work should aim verification of this hypothesis by characterizing the mode-dependent phonon relaxation time in MD [222] with/without the shell. Finally, it is known that the presence of the shell modifies the strain in the nanowire, which can influence the thermal conductivity [223]. Hence, future work should also aim to quantitatively explore the influence of the mechanic stress due to the shell.

### Thermal wave propagation in Silicon

In Chapter 9, it is shown that kinetic materials like Germanium (where Nor-

mal collisions are not dominant) can hold wave-like heat transport. Therefore, contrary to common belief, the intrinsic material properties (i.e. the intrinsic phonon-phonon collisions in the bulk) at a given temperature do not univocally determine the kind of non-Fourier behavior expected. Contrarily, the non-equilibrium situation mainly determine the emerging phenomena. In other words, wave-like heat transport is obtained if the excitation and observation times are reduced enough to the scales of the phonon collision times. To further demonstrate this claim, here we show that in MD one can obtain heat pulse propagation in Silicon due to sufficiently fast and localized external perturbations in an infinite crystal (periodic boundary conditions). Furthermore, we show that the local kinetic energy evolution obtained in MD can be modeled using the hydrodynamic equations with effective parameters. In contrast to Chapter 9, where non-local effects are neglected to model second sound, here both memory and non-local effects are shown to be necessary for a proper mesoscopic modeling.

The numerical scheme used for the MD simulations in nanowires in the previous subsections is used here to perform the following computational experiment. We consider an infinite Silicon crystal at equilibrium at 10 K with the use of periodic boundary conditions. This temperature is below the Debye temperature, but analogous results would be obtained at higher temperatures where MD simulations are reliable. Here we use such a low temperature to reduce the background kinetic energy that complicates the identification and tracking of the energy introduced by an external perturbation. A very thin slice of 0.2 Å is perturbed using a force with arbitrary modulus that has a different random direction for each atom in the slice. The perturbation is performed during an initial time window of 0.36ps. The forces exerted on the atoms are weighted by a sinusoidal function with a frequency of 12 THz. Consequently, only a characteristic propagating normal mode is excited. In other words, only one non-equilibrium phonon mode is excited before collisions start to cause transitions to other phonon modes at larger time scales. In consequence, the heat flux relaxation time  $\tau$  would be determined by a single mode, and the relation between mechanical sound  $v_{ms}$  and second sound  $v_{ss}$  become the usual relation  $v_{ms} = \sqrt{3}v_{ss}$  according to the microscopic expression 73.

In Figure 59, the local kinetic energy obtained in MD is compared with the hydrodynamic heat transport model (equations 75 and 76). Mesoscopically, the external perturbation is simulated as a heat source  $Q$  restricted to the excited slice and time window used in MD. In both models, a fraction of the introduced energy propagates as a pulse. The amount of energy transported by the wave (height of the pulses) can be fitted through modifying the heat flux relaxation time, and we obtained  $\tau=3ps$  (for  $\tau=0$  no heat pulse is obtained). In MD, the pulse velocity is  $v_{MD} \sim 2800$  m/s. Hence, the group velocity of the traveling phonons along random directions is  $v_g = \sqrt{3}v_{MD}$ , and the resulting thermal conductivity  $\kappa = cv_g^2\tau/3=1.53 \cdot 10^{-5}$  W/mK. Finally, the width of the pulses is controlled by the non-local length (see Figure 60), and we obtained  $\ell=3nm$ . Since this non-local effect neither modifies the fraction of evacuated energy by the waves nor the waves velocity, it is not required to model a global observable like the phase lag

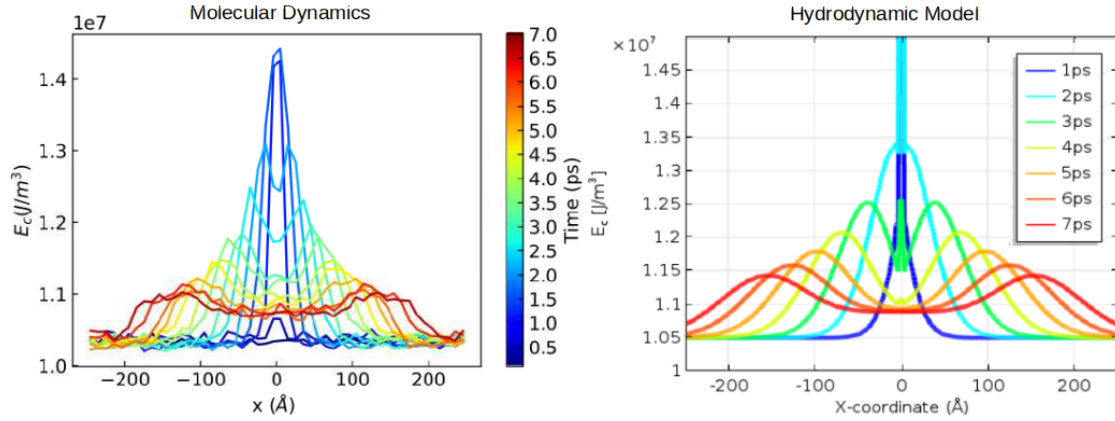


**Figure 59:** Local kinetic energy obtained in MD simulation (left) at different times under the localized external excitation in crystalline Silicon. The profiles are reproduced using the hydrodynamic model (right) with effective parameter values. In both cases, a propagating thermal pulse is obtained.

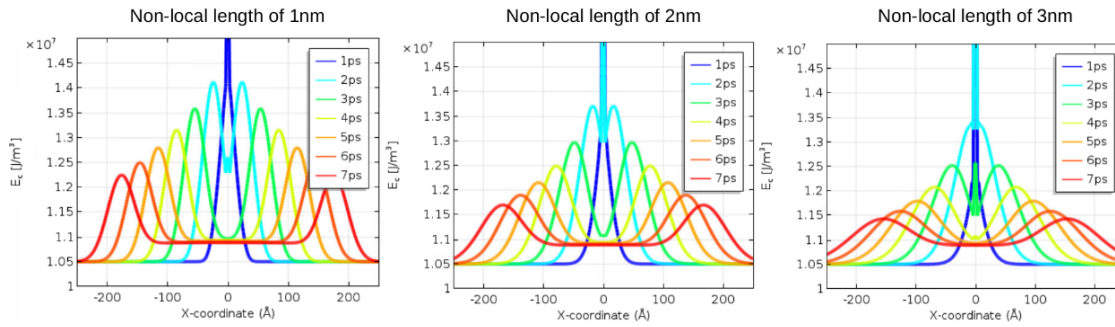


**Figure 60:** The thermal wave propagation according to the hydrodynamic model is shown for three different values for the non-local length  $\ell$ . This parameter determines the width of the propagation pulses, without modifying the velocity or the amount of transported energy by the pulse.

in frequency-domain thermoreflectance experiments (Chapter 9). However, it is necessary to accurately model the shape of the pulses obtained in MD, which are clearly not well described by only considering memory effects as shown in Figure 60. This is the only case where both memory and non-local effects are simultaneously observed within this thesis. Given the crucial relevance of the interplay between these two phenomena on the conditions to unlock second sound (see section 9.1), future work should aim to perform similar experiments using MD and extend the present analysis.

It is also worth to mention that, if a longitudinal excitation is used instead of a random one (i.e. if the direction of the external force is fixed for all atoms in the slice), the external kinetic energy does not thermalize but completely propagates as a mechanical wave. Remarkably, the obtained relation between mechanical and second sound  $v_{\text{ms}} = \sqrt{3}v_{\text{ss}}$  is fulfilled in the present MD simulations. Since we restrict the analysis to an initial time window of 7 ps, no significant transfer between mechanical and thermal energy is observed. The propagation of the mechanical waves due to longitudinal excitations can be successfully modeled

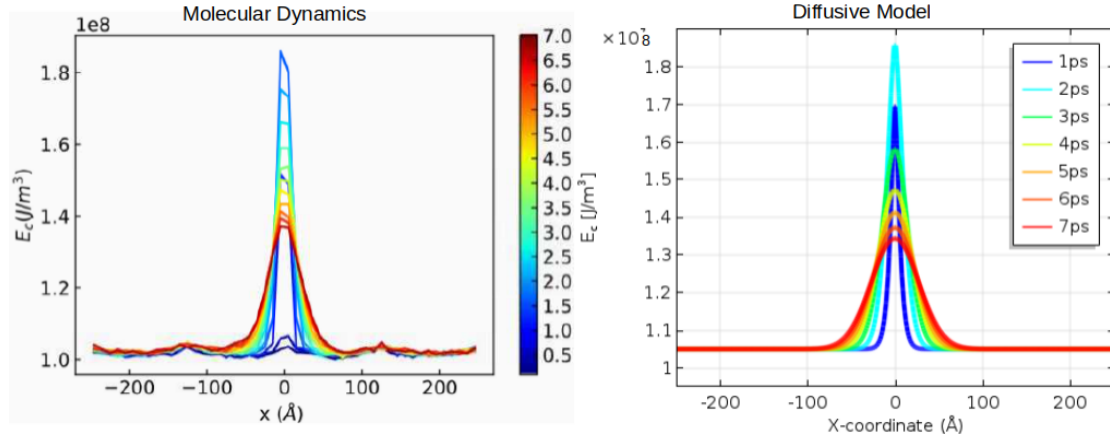


**Figure 61:** Local kinetic energy obtained in MD simulations (left) at different times under the localized external excitation in amorphous Silicon. The profiles are reproduced using the Fourier model (right) with effective parameter values. In both cases, a diffusive relaxation (no heat pulses) are obtained.

using the elastic equations explained in section 3.6.

The same computational experiment using the random excitation can be also performed in an amorphous material. In such situation, Fourier transport is expected due to the drastic reduction of the phonon relaxation times. Consistently, the MD simulations display a diffusive relaxation (no heat pulses) that can be properly fitted using Fourier's law ( $\ell = \tau = 0$ ) as shown in Figure 61.



# 11 Mathematical Methods

## 11.1 Finite Elements

This section shows the Galerkin Method implementation [224] to obtain numerical solutions of equation 75 and 76 with the boundary conditions presented in section 3.4. The resulting weak form of the model equations are implemented using COMSOL Multiphysics (see Figure 62).

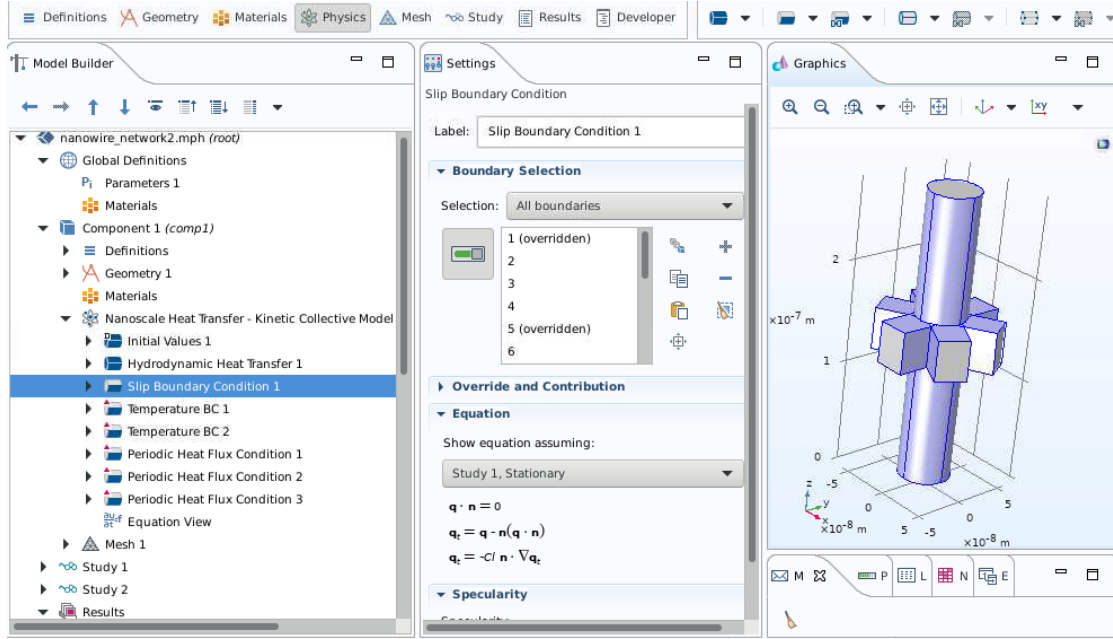


**Figure 62:** COMSOL interface to solve the hydrodynamic heat transport model in arbitrary complex geometries and temperatures.

First step is to obtain the weak form of equation 75 by multiplying by a linear test function  $\hat{T}$  of the temperature and integrating over the volume  $\Omega$ .

$$\int_{\Omega} \hat{T} \left( c \frac{T}{dt} + \nabla \cdot \mathbf{q} - Q \right) d\Omega = 0 \quad (174)$$

In order to obtain the weak form of the hydrodynamic heat transfer equation (76), we define the following tensor  $\sigma$ :

$$\sigma = \ell^2 \nabla \mathbf{q} + \alpha \ell^2 \nabla \cdot \mathbf{q} \mathbb{I} - \kappa T \mathbb{I} \quad (175)$$

where  $\mathbb{I}$  is the identity matrix.

Consider equation (76) in the form

$$\mathbf{q} + \tau \frac{\partial \mathbf{q}}{\partial t} = \nabla \cdot \sigma \quad (176)$$

Now we multiply by a quadratic test function  $\hat{\mathbf{q}}$  of the heat flux and we integrate over the volume by parts

$$\int_{\Omega} \hat{\mathbf{q}}(\mathbf{q} + \tau \frac{\partial \mathbf{q}}{\partial t}) d\Omega = \int_{\Omega} \nabla \cdot (\hat{\mathbf{q}} \cdot \sigma) d\Omega - \int_{\Omega} \nabla \hat{\mathbf{q}} : \sigma d\Omega \quad (177)$$

The first term in the right-hand side of previous expression can be expressed as a surface integral using the Divergence Theorem

$$\int_{\Omega} \hat{\mathbf{q}}(\mathbf{q} + \tau \frac{\partial \mathbf{q}}{\partial t}) d\Omega = \oint_{\Gamma} \hat{\mathbf{q}} \cdot (\mathbf{n} \cdot \sigma) d\Gamma - \int_{\Omega} \nabla \hat{\mathbf{q}} : \sigma d\Omega \quad (178)$$

where  $\Gamma$  is the boundary surface surrounding  $\Omega$ , and  $\mathbf{n}$  is the boundary normal vector.

When approximating  $T$  and  $\mathbf{q}$  by a linear combination of functions in (174) and (178), for each test function in the same Hilbert space we obtain an independent equation. To obtain an approximated solution, the resulting linear system of equations is solved numerically to obtain the coefficients of the linear combinations. The surface integral in (178) is manipulated to impose the boundary conditions (77) and (81) through the Discontinuous Galerkin method [225].

### Insulation and Slip boundary condition

From (178), we identify the Lagrange multiplier  $\lambda = \sigma \cdot \mathbf{n}$ . We want to impose different conditions for the different components of the heat flux. Hence, the surface integral of  $\lambda$  is included as a weak contribution by testing only with the heat flux boundary normal component  $(\hat{\mathbf{q}} \cdot \mathbf{n})\mathbf{n}$

$$\oint_{\Gamma} (\hat{\mathbf{q}} \cdot \mathbf{n})\mathbf{n} \cdot \lambda d\Gamma. \quad (179)$$

Considering  $\lambda$  as a new variable that is also approximated in the boundary by a linear combination of functions, we are able to impose Eq. 77 using the test function of  $\lambda$  in another weak contribution

$$\oint_{\Gamma} (\mathbf{q} \cdot \mathbf{n})\mathbf{n} \cdot \hat{\lambda} d\Gamma = 0. \quad (180)$$

Consider now the tangential component of the heat flux  $\mathbf{q}_t = \mathbf{q} - (\mathbf{q} \cdot \mathbf{n})\mathbf{n}$ . By including only (179) and (180),  $\mathbf{q} = \mathbf{q}_t$  in the boundary and the surface integral of  $\lambda$  tested by the tangential component of the heat flux also appearing in (178) is implicitly fixed to zero. Hence, to impose the boundary condition 81 we simply need to include the tangential heat flux as another weak contribution:

$$- \oint_{\Gamma} \frac{\ell}{C} \hat{\mathbf{q}}_t \cdot \mathbf{q}_t d\Gamma, \quad (181)$$

thus imposing

$$- \oint_{\Gamma} \frac{\ell}{C} \hat{\mathbf{q}}_t \cdot \mathbf{q}_t d\Gamma = \oint_{\Gamma} \hat{\mathbf{q}}_t \cdot \lambda d\Gamma = \oint_{\Gamma} \ell^2 \hat{\mathbf{q}}_t \cdot (\nabla \mathbf{q} \cdot \mathbf{n}) d\Gamma, \quad (182)$$

where we used that  $\hat{\mathbf{q}}_t \cdot \mathbf{n} = 0$ .

For the sake of clarity, let us show that equation (182) is indeed the integral form of the boundary condition (81):

$$-\frac{\ell}{C}\hat{\mathbf{q}}_t \cdot \mathbf{q}_t = -\frac{\ell}{C}|\hat{\mathbf{q}}_t||\mathbf{q}_t| = \ell^2|\hat{\mathbf{q}}_t|\mathbf{t} \cdot (\nabla \mathbf{q} \cdot \mathbf{n}) = \ell^2|\hat{\mathbf{q}}_t|\left(\frac{\partial \mathbf{q}}{\partial x_n} \cdot \mathbf{t}\right) \quad (183)$$

where  $\mathbf{t}$  is the tangential normal vector and  $x_n, x_t$  are the normal and tangential directions, respectively. Now, consider that  $\mathbf{q} = |\mathbf{q}_t|\mathbf{t} + |\mathbf{q}_n|\mathbf{n}$ . Then,

$$-\frac{\ell}{C}|\hat{\mathbf{q}}_t||q_t| = \ell^2|\hat{\mathbf{q}}_t|\left(\frac{\partial |\mathbf{q}_t|}{\partial x_n}\mathbf{t} + |\mathbf{q}_t|\frac{\partial \mathbf{t}}{\partial x_n} + \frac{\partial |\mathbf{q}_n|}{\partial x_n}\mathbf{n} + |\mathbf{q}_n|\frac{\partial \mathbf{n}}{\partial x_n}\right) \cdot \mathbf{t} \quad (184)$$

Recall now that with (180) we imposed  $\mathbf{q}_n = 0$  and hence  $\frac{\partial |\mathbf{q}_n|}{\partial x_t} = 0$ . Moreover,  $\mathbf{t} \cdot \mathbf{n} = 0$  and  $\frac{\partial \mathbf{t}}{\partial x_n} \cdot \mathbf{t} = 0$ . Therefore,

$$|\mathbf{q}_t| = -C\ell\left(\frac{\partial |\mathbf{q}_t|}{\partial x_n}\right) \quad (185)$$

### Stabilization

A weak contribution for stabilization (Penalty Method) is required [225]:

$$-\oint_{\Gamma} \ell^2 O[m](\hat{\mathbf{q}} \cdot \mathbf{n})(\mathbf{q} \cdot \mathbf{n})d\Gamma = 0 \quad (186)$$

where  $O[m]$  is a coefficient depending on the discretization element surface to volume ratio.

### Periodic Boundary Conditions

In many of the studied experimental configurations, periodic heat flux conditions are required to reproduce the whole geometry by simulating only a periodically repeated unit. The procedure is the same as for imposing (77) but averaging between boundaries the Lagrange multiplier and averaging all the components of  $\mathbf{q}$  and  $\hat{\mathbf{q}}$ . Let us denote as 1 and 2 the boundaries in which the periodic condition is imposed. Then the average normal component of  $\sigma$  is

$$\lambda_{av} = \frac{1}{2}(\lambda_1 + \lambda_2) = \frac{1}{2}(\mathbf{n}_1 \cdot \sigma_1 + \mathbf{n}_2 \cdot \sigma_2) \quad (187)$$

where  $\mathbf{n}_1$  and  $\mathbf{n}_2$  are the boundary normal vectors ( $\mathbf{n}_1 = -\mathbf{n}_2$ ). A temperature jump between boundaries 1 and 2 can be imposed by mapping the temperature appearing in  $\sigma_1$  and  $\sigma_2$  with imposing a difference  $\Delta T$ . Half of the required weak contributions including the stabilization one are imposed in each boundary. For  $i=1,2$ :

$$\begin{aligned} & \oint_{\Gamma_i} \lambda_{av} \cdot \frac{1}{2}\hat{\mathbf{q}}_i d\Gamma_i + \oint_{\Gamma_i} \hat{\lambda}_i \cdot \frac{1}{2}(\mathbf{q}_1 - \mathbf{q}_2) d\Gamma_i \\ & - \oint_{\Gamma_i} \ell^2 O[m](\mathbf{q}_1 - \mathbf{q}_2) \cdot \hat{\mathbf{q}}_i d\Gamma_i \end{aligned} \quad (188)$$

### **Isothermal boundary condition**

To fix an homogeneous temperature in a boundary ( $T = T_0$ ), the surface integral appearing in 178 should be imposed as a weak contribution with replacing  $T$  by  $T_0$ .

### **Interfacial boundary conditions**

The boundary conditions for an interface between a metal and a semiconductor connecting Fourier transport and hydrodynamic transport (eqs. 92, 81, 84) are imposed as a constraint instead of using a weak contribution. Hence, an explicit Lagrange multiplier is not required, but implicit Lagrange multipliers are eliminated by the solvers, together with the degrees of freedom being constrained [224].

### **Generalized Slip boundary condition**

To implement the generalized boundary condition 83 for curved surfaces introduced in 3.4, the tensor  $\sigma$  should be redefined as

$$\sigma' = \ell^2 \nabla \mathbf{q} + \ell^2 \nabla \mathbf{q}^T + (\alpha - 1) \ell^2 \nabla \cdot \mathbf{q} \mathbb{I} - \kappa T \mathbb{I}. \quad (189)$$

Notice that equation 76 is also recovered using  $\sigma'$  in 176. However, it can be easily demonstrated that insulation 77 and the generalized slip boundary condition 83 including an extra term are imposed if using exactly the same weak contributions 179,180,181 with replacing  $\sigma$  by  $\sigma'$ .

## **11.2 Analytical solutions and validation**

The generalized hydrodynamic model equations can be analytically solved in some simple situations. In this section we use some of these analytic solutions to validate the Finite Element implementation presented in the previous section.

### **Stationary conditions: Heat conduction in wires**

First, we validate the implementation of the non-local term in steady-state conditions (i.e. the Laplacian term in eq. 76) in a simple geometry like a wire with radius  $R$  and length much larger than the radius. Similar to the analysis in thin films in section 4.2, a temperature difference is imposed between the terminals of the wire and the slip boundary condition is used for the wire contours. We use the analytical solutions derived from the model equations for this situation in [226]. Specifically, we use the effective thermal conductivity 108 normalized by the bulk conductivity reported in expression (16) of [226], that we reproduce here:

$$\frac{\kappa_{\text{ef}}}{\kappa} = 1 - \frac{2\text{Kn}I_1(1/\text{Kn})}{I_0(1/\text{Kn}) + CI_1(1/\text{Kn})}, \quad (190)$$

where  $\text{Kn} = \ell/R$ , and  $I_\nu$  is the modified Bessel function of the first kind of order  $\nu$ . In Fig. 63 we show the normalized conductivity according to the Finite Element solutions and the analytical expression 190 for  $R \ll \ell$ . The reduction of the

effective thermal conductivity with respect to the bulk value is a measure of the predicted non-Fourier response due to non-local effects. Hence, the consistent large reduction of the conductivity obtained in this case through the numerical and analytical calculation methods validates the Finite Element implementation of the Laplacian term in 76 and the slip boundary condition 81.

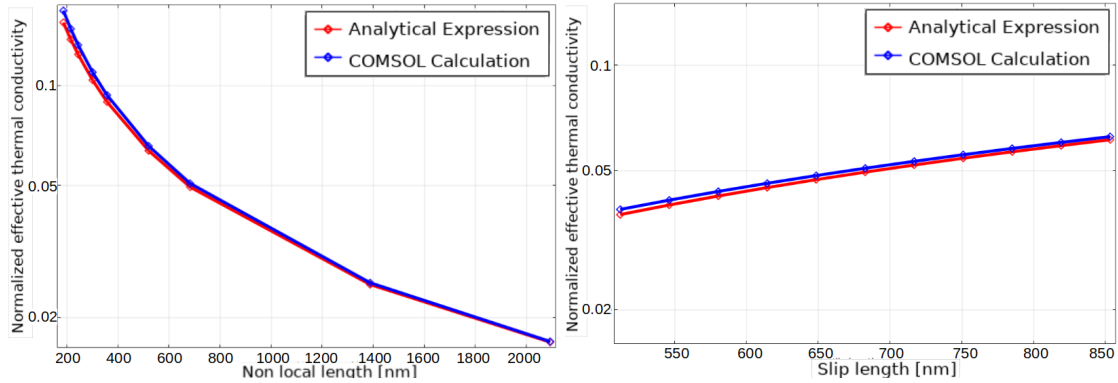


**Figure 63:** Comparison between the normalized conductivity according to the analytical expression 190 and the Finite Element calculations using COMSOL for a given radius  $R$  such that  $\text{Kn} \ll 1$ . In the left-plot, the ab initio non-local length  $\ell$  value is varied from 300 K to 100 K for Silicon with  $C = 1.4$ . In the left-plot, the slip length  $C\ell$  is varied with maintaining the non-local length  $\ell$  value at 150 K.

### Transient conditions: Frequency Domain Thermoreflectance experiments

FDTR experiments (chapters 6 and 9) allow simultaneous measurement of the phase lag and the amplitude of the temperature oscillation. Since these observables are very sensitive to the thermal transport mechanisms at work, these experimental configurations are excellent to accurately validate the non-Fourier behavior displayed by the Finite Element numerical solutions.

The analytical solutions of the model equations in the presence of a metallic transducer and the corresponding interface (see Chapter 6) can be found in Appendix D of [134]. Comparison between the analytical solutions and the Finite Element solutions for the phase lag and the thermal oscillations amplitude at different temperatures can be found in Fig. 21 and Fig. 22, respectively. As explained in Chapter 6, this kind of experiments are dominated by non-local effects in the presence of an interface, so this validation confirms the appropriated Finite Element implementation of the second order spatial derivative terms in eq. 76 along with the interfacial boundary condition 92 in transient situations.

In the case of FDTR experiments with directly heating the semiconductor substrate (i.e. without the presence of a transducer), the 1D solutions neglecting non-local effects ( $\ell = 0$ ) are provided in section 9.6. These solutions are useful to study the high frequency regime, where the thermal penetration depth is significantly smaller than the spot radius, and the thermal transport is restricted to the cross-plane direction (effective 1D transport). Consistently, in Fig. 49, the phase lag at high frequencies calculated from the 3D Finite Element solutions collapses

to the analytical 1D solutions (expression 164). This validation confirms the appropriated Finite Element implementation of the heat flux time-derivative term, which dominate the high frequency response in this specific experimental conditions as discussed in Chapter 9.

## 12 Conclusions

The main conclusion of this thesis is that the generalized phonon hydrodynamic framework, based in a mesoscopic description of heat transport including non-local and memory effects, predicts a variety of experimental observations in Silicon and similar materials. Within a well defined applicability regime of characteristic system sizes and time scales, the model can be used with *ab initio* calculated parameters in complex non-equilibrium situations including metal-semiconductor interfaces in a wide range of conditions. Specifically, for silicon, the *ab initio* model is predictive if and only if the distance between two disconnected boundaries or the size of a volumetric heat source is larger than twice the non-local length. The model captures significant deviations from thermal diffusion, and it is demonstrated to be a valuable tool for engineering next-generation electronic devices. Moreover, the model is shown to provide new interpretations of nanoscale thermal transport, that can be used to analyze other models at other levels of description like Molecular Dynamics simulations.

At odds with current conventional understanding, the present results demonstrate that phonon hydrodynamic phenomena, like the second sound propagation or the Poiseuille heat flux profile, are not restricted to the low temperature regime for some exotic materials where momentum-preserving phonon collisions dominate. Conversely, this kind of phenomena is unlocked in the appropriate non-equilibrium conditions in arbitrary materials and temperatures. Consequently, the hydrodynamic description unifies a variety of experimental observations in materials like silicon or germanium. This conclusion is also supported by the good agreement between the hydrodynamic description and Monte Carlo simulations of the BTE using a single relaxation time and neglecting the role of the Normal collisions.

The same experiments have been traditionally interpreted from a very different perspective, in terms of the ballistic and independent behavior of phonon modes along with the notions of mean free path spectroscopy and spectral thermal conductivity. Hence, special care has been taken here to contrast the hydrodynamic and purely ballistic points of view, which have two main characteristic differences. On one hand, the hydrodynamic model makes use of a single length scale (the non-local length), whereas the independent behavior and suppression of phonons is inherently a multiscale model. On the other hand, phonon hydrodynamics is based in a generalized transport equation at the mesoscopic level of description including memory and non-local effects, whereas the ballistic suppression of phonons rely on an effective form of Fourier's law with a modified thermal conductivity. These differences, in light of the analyzed experiments, allows concluding that Silicon behaves hydrodynamically, and the kinetic description breaks down even at high temperatures:

First, Silicon samples with sizes smaller than a significant fraction of mean free paths are shown to display nearly the bulk thermal conductivity in experiments. This is inconsistent with the suppression of those long MFP phonons, and perfectly consistent with the hydrodynamic model, which predicts the emergence

of boundary effects at significantly smaller sizes (comparable to the non-local length). Second, Fourier's law fails to simultaneously describe all the observables in experiments, even in its effective form. For instance, in Chapter 6, we show that a different effective thermal conductivity is required to describe the amplitude of the thermal oscillations and the phase lag between the external power and the temperature in FDTR experiments; In Chapter 5, we show that a different effective thermal conductivity is required to fit the temperature profile in a nanoscale heater releasing energy to a Silicon substrate, with respect to the conductivity required to fit the temperature in a thermometer close to the heat source. Furthermore, the fitted conductivities not only depend on the heater size but also on its shape. Remarkably, all these inconsistencies are shown to be compactly resolved by the hydrodynamic model with intrinsic parameters. Third, in Chapter 7, we show the emergence of two distinct characteristic decay times during the temperature evolution of a nanoscale heater relaxing towards equilibrium by releasing heat to a Silicon substrate, whereas the effective Fourier framework only predicts the existence of a single characteristic decay time associated to the TBR. The hydrodynamic model explains the emergence of this second time-scale in terms of the geometry-dependent viscous effects in the substrate. Finally, it is worth mentioning that the breakdown of the effective Fourier approach is also supported by other experiments not considered here, like the one reported in [22], where an anisotropic thermal conductivity tensor is required to describe Time Domain Thermoreflectance experiments in an isotropic material like Silicon. As a consequence of these multiple evidences, the independent evolution of the phonon modes with its own mean free path seems to be non-physical for Si and similar materials at the nanoscale. Therefore, the numerical methods directly solving the BTE under the RTA in complex non-equilibrium situations should be revised. The failure of this picture has also implications on alternative approaches beyond RTA [52] which also predicts a Fourier-like transport equation with a reduced thermal conductivity resembling the one predicted by the ballistic suppression of phonons.

The key advantage of the hydrodynamic model is the use of intrinsic (geometry-independent) parameter values for the transport equation along with appropriate boundary conditions. This is possible due to the achieved consistency between the non-equilibrium distribution function, the transport equations and the boundary conditions, which are all related through the BTE. In consequence, the model can be compactly described as shown in sections 3.3, 3.4, 3.5, and may be directly applied by engineers to optimize the thermal response of microelectronic devices, or to envision new devices enabling controlled thermal transport to carry or process information [227]. Furthermore, the model has other advantages, like the simplified modeling of metal-semiconductor interfaces, which are ubiquitous in applications. Specifically, all the experiments are described with the use of intrinsic thermal boundary resistance values very close to the widely accepted DMM, with only introducing small correcting factors to account for unavoidable fabrication defects. The apparently larger and geometry-dependent TBR values used in previous work are thus reinterpreted as a combined effect between the intrinsic TBR and viscous effects close to the interface. This sim-



plicity is a strong point of the phonon hydrodynamic model, which contrasts with alternative modeling of the same experiments requiring orders of magnitude larger TBR values [89]. Moreover, it is worth to note that the present simple modeling of the interface does not seem to be easily conciliated with other models using spectral (phonon mode dependent) interfacial resistances to interpret experimental data [228], so more work is still required.

Beyond the applicability regime, the model has shown to phenomenologically capture the thermal response in experiments by using reduced and effective values for the non-local length. For example, a geometrically-defined non-local length explains the enhanced cooling efficiency observed in close-packed systems of heaters with respect to isolated heaters in Chapter 7. Moreover, an extremely small heating region in FDTR experiments without transducer is shown to eliminate the influence of non-local effects in Chapter 9. Most importantly, we have shown that the vanishing of non-local effects in such conditions is the key to unlock wave-like or memory thermal effects in an unexpected material like germanium.

Nevertheless, this thesis raises more questions than it solves. To mention a few examples, the apparent breakdown of the hydrodynamic model with *ab initio* parameters for alloys like SiGe or InGaAs has not been explored, and the fundamental aspects distinguishing these materials and semiconductors like Silicon have not been clarified. Moreover, the microscopic mechanisms leading to the apparent reduction of the non-local length in experimental conditions beyond the applicability of the *ab initio* model have not been identified. Related to this, a clear picture of the interplay between memory and non-local effects, which is key to manipulate thermal wave-like transport for applications, remains pendant work. Furthermore, establishing stronger connections between mesoscopic interpretations like hydrodynamics and other microscopic perspectives like the Lévy flights is also required. As a final goal, future studies should pave the way to refine the hydrodynamic description of heat transport with *ab initio* calculated parameters and extend the applicability of the model to even smaller length and time scales.

## 13 List of Publications

### **A General and Predictive Understanding of Thermal Transport from 1D- and 2D-Confined Nanostructures: Theory and Experiment**

ALBERT BEARDO<sup>†</sup>, Joshua L. Knobloch<sup>†</sup>, Lluç Sendra, Javier Bafaluy, Travis D. Frazer, Weilun Chao, Jorge N. Hernandez-Charpak, Henry C. Kapteyn, Begona Abad, Margaret M. Murnane, F. Xavier Alvarez, and Juan Camacho, *ACS Nano* 15, 8, 13019–13030 (2021)

### **Observation of Second Sound in a Rapidly Varying Temperature Field in Ge**

ALBERT BEARDO, Miquel López-Suárez, Luis Alberto Pérez, Lluç Sendra, Maria Isabel Alonso, Claudio Melis, Javier Bafaluy, Juan Camacho, Luciano Colombo, Riccardo Rurali, F. Xavier Alvarez, and Juan Sebastián Reparaz, *Science Advances* 7, 27, eabg4677 (2021)

### **Derivation of a Hydrodynamic Heat Equation from the Phonon Boltzmann Equation for General Semiconductors**

Lluç Sendra, ALBERT BEARDO, Pol Torres, Javier Bafaluy, F. Xavier Alvarez, and Juan Camacho, *Physical Review B* 103, L140301 (2021)

### **Geometrical Quasi-ballistic Effects on Thermal Transport in Nanostructured Devices**

Sami Alajlouni<sup>†</sup>, ALBERT BEARDO<sup>†</sup>, Lluç Sendra, Amirkoushyar Ziabari, Javier Bafaluy, Juan Camacho, Yi Xuan, F. Xavier Alvarez, and Ali Shakouri, *Nano Research* 14, 945-952 (2021)

### **Phonon Hydrodynamics in Frequency Domain Thermorefectance Experiments**

ALBERT BEARDO, Matthew Hennessy, Lluç Sendra, Juan Camacho, Tim G. Myers, Javier Bafaluy, and F. Xavier Alvarez, *Physical Review B* 101, 0753033 (2020)

### **Hydrodynamic Heat Transport in Compact and Holey Silicon Thin Films**

ALBERT BEARDO, Marc Calvo-Schwarzwalder, Juan Camacho, Tim G. Myers, Pol Torres, Lluç Sendra, F. Xavier Alvarez, and Javier Bafaluy, *Physical Review Applied* 11, 034003 (2019)

### **Hydrodynamic Thermal Transport in Silicon at Low Temperatures**

ALBERT BEARDO<sup>†</sup>, Sami Alajlouni<sup>†</sup>, Lluç Sendra, Javier Bafaluy, Amirkoushyar Ziabari, Yi Xuan, Juan Camacho, Ali Shakouri, and F. Xavier Alvarez (*submitted*)

### **Metamaterials to Increase the Thermoelectric Efficiency**

Alejandra Ruiz-Clavijo, Olga Caballero-Calero, Cristina V. Manzano, Xavier Maeder, ALBERT BEARDO, Xavier Cartoixà, F. Xavier Alvarez, Marisol Martın-Gonzalez, (*submitted*)

## List of Figures

1	Schematic illustration of transport equations and interface boundary conditions for a semiconductor with a metallic transducer on top. . . . .	46
2	Thermal conductivity and specific heat vs temperature for Ge, Si and Diamond. . . . .	47
3	Non-local length and heat flux relaxation time vs temperature for Ge, Si and Diamond. . . . .	47
4	Heat flux profile for a Silicon thin film at room temperature predicted by Fourier and KCM. . . . .	56
5	Thin films experimental and predicted thermal conductivities versus width at room temperature, and temperature for different widths. . . . .	57
6	Holey films experimental and predicted thermal conductivities versus temperature for different geometric properties. . . . .	58
7	Thermal grating decay rate in a 400nm-thick Silicon film versus hydrodynamic and Fourier predictions. . . . .	60
8	Normalized mean-square displacement of an evolving thermal energy pulse according to the Lévy Flight Formalism . . . . .	65
9	Overview of Thermoreflectance Imaging (TRI) experimental setup and outputs. . . . .	67
10	IVT calibration of the gold thermoreflectance coefficient. . . . .	67
11	Oxide layer and substrate thermal conductivity characterization at room temperature in the largest circular device. . . . .	70
12	Temperature-profile comparisons of TRI measurements, Fourier bulk predictions, and hydrodynamic predictions at room temperature. . . . .	71
13	Normalized effective thermal conductivity, $\kappa_{\text{fit}}/\kappa_{\text{bulk}}$ , required to reproduce the TRI experimental temperature profile at room temperature. . . . .	72
14	Local effective thermal conductivity profiles in circular and linear heater devices. . . . .	73
15	Heat flux profiles in linear heater devices. . . . .	74
16	Effect of the thermostat window on the measurement of thermoreflectance profile at room temperature. . . . .	76
17	Temperature-profile comparisons of TRI measurements, Fourier bulk predictions, and hydrodynamic predictions at low temperature. . . . .	77
18	Normalized effective thermal conductivity, $\kappa_{\text{fit}}/\kappa_{\text{bulk}}$ , required to reproduce the TRI experimental temperature profile at low temperature. . . . .	78

19	Phase shift $\varphi$ and normalized temperature oscillation amplitude $\Delta T$ as functions of the heating frequency at 311 K along with effective Fourier model predictions. . . . .	80
20	Output obtained from the models for $f=100$ MHz at 311 K. . . . .	82
21	Experimental phase shift $\varphi$ as a function of frequency $f$ at different temperatures versus hydrodynamic and Fourier predictions in Silicon. . . . .	84
22	Normalized temperature amplitude $\Delta T$ as a function of frequency $f$ at 311 K versus hydrodynamic and Fourier predictions in Silicon. . . . .	85
23	Phase shift $\varphi$ as a function of frequency $f$ at 311 K versus hydrodynamic and Fourier predictions considering inhomogeneous transducers in Silicon. . . . .	86
24	The thermal penetration depths computed from Fourier and the hydrodynamic models at 311 K and 81 K. . . . .	86
25	Phase shift $\varphi$ as a function of frequency $f$ at room temperature in Germanium. . . . .	87
26	Schematic of dynamic EUV scatterometry for probing non-diffusive hydrodynamic-like heat flow. . . . .	90
27	Direct comparison between EUV scatterometry data and hydrodynamic modeling in 1 and 2D. . . . .	93
28	Hydrodynamic regions in effectively isolated and close-packed situations. . . . .	94
29	Experimental and theoretical quasi-static change in diffraction efficiency. . . . .	96
30	Heater temperature evolution according to Fourier model. . . . .	98
31	Fourier fits to experimental data restricted to $t > 500$ ps for a heater line of 250 nm. . . . .	99
32	Heater temperature evolution for $L=30$ nm and $P=400$ nm according to the hydrodynamic model. . . . .	99
33	Two-box model for the thermal decay of heaters for $L < \ell$ . . . . .	102
34	Two characteristic decay times in thermal relaxation of nanoline (1D) experiments. . . . .	104
35	Sensitivity of hydrodynamic model parameters. . . . .	105
36	Time evolution of the hydrodynamic heat transport equation terms at $x = L$ and $y = 0$ with $L=20$ nm . . . . .	106
37	Two-box model analytical solutions vs Finite Elements solutions. . . . .	108
38	SEM images, schematic representation, and experimental characterization of the 3D Bi <sub>2</sub> Te <sub>3</sub> structures. . . . .	112

39	Thermal conductivity and heat flux profiles predicted by the hydrodynamic heat transport model in 3D Bi <sub>2</sub> Te <sub>3</sub> structure. . . . .	114
40	Lattice thermal conductivity predicted by the hydrodynamic heat transport model in free-standing Bi <sub>2</sub> Te <sub>3</sub> NW. . . . .	115
41	Evolution of the initial Gaussian temperature distribution with size $L$ at different times $t$ according to equation 76. . . . .	122
42	Electronic and thermal contributions to reflectivity signal in Ge substrate. . . . .	126
43	Phase lag versus frequency for the higher frequency range as a function of temperature. . . . .	128
44	Frequency dependent thermal penetration depth calculated using the solution of the HHE, the diffusive case, and the penetration depth obtained in the high frequency limit. . . . .	129
45	Spatial distribution of the temperature field as a function of temperature in the direction perpendicular to the surface of the sample.	130
46	Phase lag versus frequency for the higher frequency range as a function of temperature (full set of data fits). . . . .	131
47	Experimental vs theoretical heat flux relaxation times and second sound velocities. . . . .	132
48	Influence of the pump and probe penetration depths on the phase lag. . . . .	134
49	1D vs 3D parabolic and hyperbolic heat equation solutions. . . . .	135
50	Influence of the laser spot size, the thermal diffusivity and the heat flux relaxation time. . . . .	138
51	Influence of the presence of a thermal interface on the frequency-dependent phase lag at room temperature. . . . .	139
52	Sketch of the Monte Carlo BTE simulation domain. . . . .	143
53	Energy based Monte Carlo BTE simulations vs hydrodynamic predictions for Kn=0.1. . . . .	146
54	Energy based Monte Carlo BTE simulations vs hydrodynamic predictions for Kn=1. . . . .	148
55	Energy based Monte Carlo BTE simulations vs hydrodynamic predictions for Kn=2. . . . .	149
56	Energy based Monte Carlo BTE simulations vs hydrodynamic predictions for Kn=1 with using a hot nanoscale isothermal boundary instead of volumetric heating. . . . .	150
57	Heat flux radial profile in NWs according to non-equilibrium molecular dynamics simulations and the hydrodynamic model. . . . .	154

58	Influence of amorphous shell in the heat flux radial profile of NWs according to non-equilibrium molecular dynamics simulations and the hydrodynamic model. . . . .	155
59	Thermal wave propagation in crystalline Silicon according to non-equilibrium molecular dynamics simulations and the hydrodynamic model. . . . .	157
60	Influence of the non-local length in the thermal wave propagation in crystalline Silicon. . . . .	157
61	Thermal wave propagation in amorphous Silicon according to non-equilibrium molecular dynamics simulations and the hydrodynamic model. . . . .	158
62	COMSOL Interface. . . . .	159
63	Validation of the FEM solutions in wires. . . . .	163

## References

- [1] M. Mitchell Waldrop. "The chips are down for Moore's law". *Nature* (2016).
- [2] Gang Chen. "Nanoscale Energy Transport and Conversion: A Parallel Treatment of Electrons, Molecules, Phonons, and Photons". *Oxford University Press*, New York (2005).
- [3] Keivan Esfarjani, Gang Chen, and Harold T. Stokes. "Heat transport in silicon from first-principles calculations". *Phys. Rev. B* 84 (8 Aug. 2011), p. 085204.
- [4] L. Lindsay, C. Hua, X.L. Ruan, and S. Lee. "Survey of ab initio phonon thermal transport". *Materials Today Physics* 7 (2018), pp. 106–120.
- [5] David Jou, Georgy Lebon, and Jose Casas-Vazquez. "Extended Irreversible Thermodynamics". *Springer Netherlands* (2010).
- [6] R. A. Guyer and J. A. Krumhansl. "Solution of the Linearized Phonon Boltzmann Equation". *Physical Review* 148.2 (Aug. 1966), pp. 766–778.
- [7] Yangyu Guo and Moran Wang. "Phonon hydrodynamics and its applications in nanoscale heat transport". *Physics Reports* 595 (2015). Phonon hydrodynamics and its applications in nanoscale heat transport, pp. 1–44.
- [8] Sangyeop Lee and Xun Li. "Hydrodynamic phonon transport: past, present and prospects". 2053-2563 (2020), 1-1 to 1–26.
- [9] J. M. Ziman. "Electrons and Phonons". *Clarendon Press*, Oxford, United Kingdom (2007).
- [10] R. K. Pathria and Paul D. Beale. "Statistical Mechanics". *Academic Press*, United States of America (2011).
- [11] Zhuomin M. Zhang. "Nanoscale and Microscale Heat Transport". *The McGraw-Hill Companies*, United States of America (2007).
- [12] Henning Struchtrup. "Macroscopic Transport Equations for Rarefied Gas Flows". *Springer*, Berlin, Germany (2005).
- [13] Zhiting Tian, Jivtresh Garg, Keivan Esfarjani, Takuma Shiga, Junichiro Shiomi, and Gang Chen. "Phonon conduction in PbSe, PbTe, and PbTe<sub>1-x</sub>Se<sub>x</sub> from first-principles calculations". *Phys. Rev. B* 85 (18 May 2012), p. 184303.
- [14] David A. Broido, M. Malorny, G. Birner, Natalio Mingo, and D. a. Stewart. "Intrinsic lattice thermal conductivity of semiconductors from first principles". *Applied Physics Letters* 91.23 (Dec. 2007), p. 231922.
- [15] Andrea Cepellotti and Nicola Marzari. "Thermal Transport in Crystals as a Kinetic Theory of Relaxons". *Phys. Rev. X* 6 (4 Oct. 2016), p. 041013.
- [16] Yangyu Guo and Moran Wang. "Phonon hydrodynamics for nanoscale heat transport at ordinary temperatures". *Physical Review B* 97.3 (2018).
- [17] Chengyun Hua, Lucas Lindsay, Xiangwen Chen, and Austin J. Minnich. "Generalized Fourier's law for nondiffusive thermal transport: Theory and experiment". *Physical Review B* 100.8 (2019), pp. 1–11.

- [18] Michele Simoncelli, Nicola Marzari, and Andrea Cepellotti. “Generalization of Fourier’s Law into Viscous Heat Equations”. *Phys. Rev. X* 10 (1 Jan. 2020), p. 011019.
- [19] Lluc Sendra, Albert Beardo, Pol Torres, Javier Bafaluy, F. Xavier Alvarez, and Juan Camacho. “Derivation of a hydrodynamic heat equation from the phonon Boltzmann equation for general semiconductors”. *Phys. Rev. B* 103 (14 Apr. 2021), p. L140301.
- [20] Yangyu Guo, David Jou, and Moran Wang. “Nonequilibrium thermodynamics of phonon hydrodynamic model for nanoscale heat transport”. *Phys. Rev. B* 98 (10 Sept. 2018), p. 104304.
- [21] Amirkoushyar Ziabari, Pol Torres, Bjorn Vermeersch, Yi Xuan, Xavier Carroixà, Alvar Torelló, Je-Hyeong Bahk, Yee Rui Koh, Maryam Parsa, Peide D. Ye, F. Xavier Alvarez, and Ali Shakouri. “Full-field thermal imaging of quasiballistic crosstalk reduction in nanoscale devices”. *Nature Communications* 9.1 (Dec. 2018), p. 255.
- [22] R. B. Wilson and David G. Cahill. “Anisotropic failure of Fourier theory in time-domain thermoreflectance experiments”. *Nature Communications* (2014).
- [23] Tianli Feng, Lucas Lindsay, and Xiulin Ruan. “Four-phonon scattering significantly reduces intrinsic thermal conductivity of solids”. *Phys. Rev. B* 96 (16 Oct. 2017), p. 161201.
- [24] Navaneetha K. Ravichandran and David Broido. “Phonon-Phonon Interactions in Strongly Bonded Solids: Selection Rules and Higher-Order Processes”. *Phys. Rev. X* 10 (2 June 2020), p. 021063.
- [25] Alberto Debernardi, Stefano Baroni, and Elisa Molinari. “Anharmonic Phonon Lifetimes in Semiconductors from Density-Functional Perturbation Theory”. *Phys. Rev. Lett.* 75 (9 Aug. 1995), pp. 1819–1822.
- [26] G. Kresse and J. Furthmüller. “Efficient iterative schemes for ab initio total-energy calculations using a plane-wave basis set”. *Phys. Rev. B* 54 (16 Oct. 1996), pp. 11169–11186.
- [27] Atsushi Togo and Isao Tanaka. “First principles phonon calculations in materials science”. *Scripta Materialia* 108 (2015), pp. 1–5.
- [28] Wu Li, Jesús Carrete, Nebil A. Katcho, and Natalio Mingo. “ShengBTE: A solver of the Boltzmann transport equation for phonons”. *Computer Physics Communications* 185.6 (2014), pp. 1747–1758.
- [29] D. A. Broido, A. Ward, and N. Mingo. “Lattice thermal conductivity of silicon from empirical interatomic potentials”. *Phys. Rev. B* 72 (1 July 2005), p. 014308.
- [30] Bjorn Vermeersch, Jesús Carrete, Natalio Mingo, and Ali Shakouri. “Superdiffusive heat conduction in semiconductor alloys. I. Theoretical foundations”. *Physical Review B - Condensed Matter and Materials Physics* 91.8 (Feb. 2015), p. 085202.



- [31] A. J. Minnich, G. Chen, S. Mansoor, and B. S. Yilbas. “Quasiballistic heat transfer studied using the frequency-dependent Boltzmann transport equation”. *Phys. Rev. B* 84 (23 Dec. 2011), p. 235207.
- [32] Jean-Philippe M. Péraud and Nicolas G. Hadjiconstantinou. “Efficient simulation of multidimensional phonon transport using energy-based variance-reduced Monte Carlo formulations”. *Phys. Rev. B* 84 (20 Nov. 2011), p. 205331.
- [33] Roman Anufriev, Aymeric Ramiere, Jeremie Maire, and Masahiro Nomura. “Heat guiding and focusing using ballistic phonon transport in phononic nanostructures”. *Nature Communications* (2017).
- [34] Yu-Chao Hua and Bing-Yang Cao. “An efficient two-step Monte Carlo method for heat conduction in nanostructures”. *Journal of Computational Physics* 342 (2017), pp. 253–266.
- [35] David Lacroix, Karl Joulain, and Denis Lemonnier. “Monte Carlo transient phonon transport in silicon and germanium at nanoscales”. *Phys. Rev. B* 72 (6 Aug. 2005), p. 064305.
- [36] Yangyu Guo and Moran Wang. “Lattice Boltzmann modeling of phonon transport”. *Journal of Computational Physics* 315 (2016), pp. 1–15.
- [37] Sreekant V.J. Narumanchi, Jayathi Y. Murthy, and Cristina H. Amon. “Sub-micron heat transport model in silicon accounting for phonon dispersion and polarization”. *Journal of Heat Transfer* (2004).
- [38] Zhaoli Guo and Kun Xu. “Discrete unified gas kinetic scheme for multi-scale heat transfer based on the phonon Boltzmann transport equation”. *International Journal of Heat and Mass Transfer* (2016).
- [39] David Lacroix, Karl Joulain, and Denis Lemonnier. “Monte Carlo transient phonon transport in silicon and germanium at nanoscales”. *Phys. Rev. B* 72 (6 Aug. 2005), p. 064305.
- [40] Colin D. Landon and Nicolas G. Hadjiconstantinou. “Deviational simulation of phonon transport in graphene ribbons with ab initio scattering”. *Journal of Applied Physics* 116.16 (2014), p. 163502.
- [41] Xun Li and Sangyeop Lee. “Role of hydrodynamic viscosity on phonon transport in suspended graphene”. *Phys. Rev. B* 97 (9 Mar. 2018), p. 094309.
- [42] Giuseppe Romano. “OpenBTE: A Multiscale Solver for the Phonon Boltzmann Transport Equation”. *APS March Meeting Abstracts*. Vol. 2019. APS Meeting Abstracts. Jan. 2019, T70.321.
- [43] Joseph Callaway. “Model for Lattice Thermal Conductivity at Low Temperatures”. *Physical Review* 113.4 (Feb. 1959), pp. 1046–1051.
- [44] Xiao-Ping Luo, Yang-Yu Guo, Mo-Ran Wang, and Hong-Liang Yi. “Direct simulation of second sound in graphene by solving the phonon Boltzmann equation via a multiscale scheme”. *Phys. Rev. B* 100 (15 Oct. 2019), p. 155401.

- [45] Yangyu Guo and Moran Wang. "Heat transport in two-dimensional materials by directly solving the phonon Boltzmann equation under Callaway's dual relaxation model". *Phys. Rev. B* 96 (13 Oct. 2017), p. 134312.
- [46] Chuang Zhang, Songze Chen, and Zhaoli Guo. "Heat vortices of ballistic and hydrodynamic phonon transport in two-dimensional materials". *International Journal of Heat and Mass Transfer* 176 (2021), p. 121282.
- [47] Yangyu Guo, Zhongwei Zhang, Marc Bescond, Shiyun Xiong, Moran Wang, Masahiro Nomura, and Sebastian Volz. "Size effect on phonon hydrodynamics in graphite microstructures and nanostructures". *Phys. Rev. B* 104 (7 Aug. 2021), p. 075450.
- [48] S. Huberman, R. A. Duncan, K. Chen, B. Song, V. Chiloyan, Z. Ding, A. A. Maznev, G. Chen, and K. A. Nelson. "Observation of second sound in graphite at temperatures above 100 K". *Science* 364.6438 (2019), pp. 375–379.
- [49] Yangyu Guo, Zhongwei Zhang, Masahiro Nomura, Sebastian Volz, and Moran Wang. "Phonon vortex dynamics in graphene ribbon by solving Boltzmann transport equation with ab initio scattering rates". *International Journal of Heat and Mass Transfer* 169 (2021), p. 120981.
- [50] Robert J. Hardy. "Phonon Boltzmann Equation and Second Sound in Solids". *Phys. Rev. B* 2 (4 Aug. 1970), pp. 1193–1207.
- [51] P. Vernotte. "Les paradoxes de la theorie continue de l'équation de la chaleur". *Comptes Rendus* 246.22 (1958), p. 3154.
- [52] Chengyun Hua and Lucas Lindsay. "Space-time dependent thermal conductivity in nonlocal thermal transport". *Phys. Rev. B* 102 (10 Sept. 2020), p. 104310.
- [53] Andrea Cepellotti and Nicola Marzari. "Boltzmann Transport in Nanostructures as a Friction Effect". *Nano Letters* 17.8 (Aug. 2017), pp. 4675–4682.
- [54] R. A. Guyer and J. A. Krumhansl. "Thermal Conductivity, Second Sound, and Phonon Hydrodynamic Phenomena in Nonmetallic Crystals". *Phys. Rev.* 148 (2 Aug. 1966), pp. 778–788.
- [55] C. de Tomas, A. Cantarero, a. F. Lopeandia, and F. X. Alvarez. "From kinetic to collective behavior in thermal transport on semiconductors and semiconductor nanostructures". *Journal of Applied Physics* 115.16 (Apr. 2014), p. 164314.
- [56] P. Torres, A. Torelló, J. Bafaluy, J. Camacho, X. Cartoixà, and F. X. Alvarez. "First principles kinetic-collective thermal conductivity of semiconductors". *Physical Review B* 95.16 (Apr. 2017), p. 165407.

- [57] Kathleen M. Hoogeboom-Pot, Jorge N. Hernandez-Charpak, Xiaokun Gu, Travis D. Frazer, Erik H. Anderson, Weilun Chao, Roger W. Falcone, Ronggui Yang, Margaret M. Murnane, Henry C. Kapteyn, and Damiano Nardi. "A new regime of nanoscale thermal transport: Collective diffusion increases dissipation efficiency". *Proceedings of the National Academy of Sciences* 112.16 (Mar. 2015), p. 4846.
- [58] C. W. Chang, D. Okawa, H. Garcia, A. Majumdar, and A. Zettl. "Breakdown of Fourier's Law in Nanotube Thermal Conductors". *Phys. Rev. Lett.* 101 (7 Aug. 2008), p. 075903.
- [59] LUDWIG BOLTZMANN. "Further Studies on the Thermal Equilibrium of Gas Molecules". *The Kinetic Theory of Gases*, pp. 262–349.
- [60] S. Chapman and T.G. Cowling. "The Mathematical Theory of Non-uniform Gases". *Cambridge University Press*, Cambridge, United Kingdom (1991).
- [61] Harold Grad. "On the kinetic theory of rarefied gases". *Communications on Pure and Applied Mathematics* 2.4 (1949), pp. 331–407.
- [62] Xiangwen Chen, Chengyun Hua, Hang Zhang, Navaneetha K. Ravichandran, and Austin J. Minnich. "Quasiballistic Thermal Transport from Nanoscale Heaters and the Role of the Spatial Frequency". *Phys. Rev. Applied* 10 (5 Nov. 2018), p. 054068.
- [63] David Jou, Georgy Lebon, and Jose Casas-Vazquez. "Understanding Non-equilibrium Thermodynamics". *Springer Berlin, Germany* (2008).
- [64] S.R. de Groot and P. Mazur. "Non-Equilibrium Thermodynamics". *Dover Publications*, New York (1984).
- [65] D. Jou, C. Pérez-García, L. S. García-Colín, M. López de Haro, and R. F. Rodríguez. "Generalized hydrodynamics and extended irreversible thermodynamics". *Phys. Rev. A* 31 (4 Apr. 1985), pp. 2502–2508.
- [66] Peter Galenko and David Jou. "Diffuse-interface model for rapid phase transformations in nonequilibrium systems". *Phys. Rev. E* 71 (4 Apr. 2005), p. 046125.
- [67] F. X. Alvarez and D. Jou. "Memory and nonlocal effects in heat transport: From diffusive to ballistic regimes". *Applied Physics Letters* 90.8 (2007), p. 083109.
- [68] F. X. Alvarez and D. Jou. "Size and frequency dependence of effective thermal conductivity in nanosystems". *Journal of Applied Physics* 103.9 (2008), p. 094321.
- [69] F. X. Alvarez, D. Jou, and a. Sellitto. "Phonon hydrodynamics and phonon-boundary scattering in nanosystems". *Journal of Applied Physics* 105.1 (2009), p. 014317.
- [70] Wieslaw Larecki and Zbigniew Banach. "Influence of nonlinearity of the phonon dispersion relation on wave velocities in the four-moment maximum entropy phonon hydrodynamics". *Physica D: Nonlinear Phenomena* 266 (2014), pp. 65–79.

- [71] Zbigniew Banach and Wieslaw Larecki. "Nine-moment phonon hydrodynamics based on the maximum-entropy closure: one-dimensional flow". *Journal of Physics A: Mathematical and General* 38.40 (Sept. 2005), pp. 8781–8802.
- [72] Deyu Li, Yiyang Wu, Philip Kim, Li Shi, Peidong Yang, and Arun Majumdar. "Thermal conductivity of individual silicon nanowires". *Applied Physics Letters* 83.14 (2003), pp. 2934–2936.
- [73] Martin Maldovan. "Micro to nano scale thermal energy conduction in semiconductor thin films". *Journal of Applied Physics* 110.3 (2011).
- [74] Jeremy A. Johnson, A. A. Maznev, John Cuffe, Jeffrey K. Eliason, Austin J. Minnich, Timothy Kehoe, Clivia M. Sotomayor Torres, Gang Chen, and Keith A. Nelson. "Direct Measurement of Room-Temperature Nondiffusive Thermal Transport Over Micron Distances in a Silicon Membrane". *Physical Review Letters* 110.2 (Jan. 2013), p. 025901.
- [75] Yongjie Hu, Lingping Zeng, Austin J. Minnich, Mildred S. Dresselhaus, and Gang Chen. "Spectral mapping of thermal conductivity through nanoscale ballistic transport". *Nature Nanotechnology* 10 (8 June 2015), pp. 701–706.
- [76] D. Y. Tzou. "A Unified Field Approach for Heat Conduction From Macro- to Micro-Scales". *Journal of Heat Transfer* 117.1 (Feb. 1995), pp. 8–16.
- [77] Da Yu Tzou. "Experimental support for the lagging behavior in heat propagation". *Journal of Thermophysics and Heat Transfer* 9.4 (1995), pp. 686–693.
- [78] D. Y. Tzou. "Nanoscale Energy Transport and Conversion: A Parallel Treatment of Electrons, Molecules, Phonons, and Photons". *John Wiley and Sons*, New York (2014).
- [79] Marco Gandolfi, Claudio Giannetti, and Francesco Banfi. "Temperonic Crystal: A Superlattice for Temperature Waves in Graphene". *Phys. Rev. Lett.* 125 (26 Dec. 2020), p. 265901.
- [80] Bing-Yang Cao and Zeng-Yuan Guo. "Equation of motion of a phonon gas and non-Fourier heat conduction". *Journal of Applied Physics* 102.5 (2007), p. 053503.
- [81] Cao Bing-Yang Dong Yan and Guo Zeng-Yuan. "Generalized heat conduction laws based on thermomass theory and phonon hydrodynamics". *Journal of Applied Physics* 110.6 (2011), p. 063504.
- [82] Hai-Dong Wang, Bing-Yang Cao, and Zeng-Yuan Guo. "Heat flow choking in carbon nanotubes". *International Journal of Heat and Mass Transfer* 53.9 (2010), pp. 1796–1800.
- [83] H.B.G. Casimir. "Note on the conduction of heat in crystals". *Physica* 5.6 (1938), pp. 495–500.
- [84] J. S. Heron, T. Fournier, N. Mingo, and O. Bourgeois. "Mesoscopic Size Effects on the Thermal Conductance of Silicon Nanowire". *Nano Letters* 9.5 (2009). PMID: 19435377, pp. 1861–1865.

- [85] Amy M. Marconnet, Mehdi Asheghi, and Kenneth E. Goodson. "From the Casimir Limit to Phononic Crystals: 20 Years of Phonon Transport Studies Using Silicon-on-Insulator Technology". *Journal of Heat Transfer* 135.6 (May 2013). 061601.
- [86] Keith T. Regner, Justin P. Freedman, and Jonathan A. Malen. "Advances in Studying Phonon Mean Free Path Dependent Contributions to Thermal Conductivity". *Nanoscale and Microscale Thermophysical Engineering* 19.3 (2015), pp. 183–205.
- [87] Lingping Zeng, Kimberlee C. Collins, Yongjie Hu, Maria N. Luckyanova, Alexei A. Maznev, Samuel Huberman, Vazrik Chiloyan, Jiawei Zhou, Xiaopeng Huang, Keith A. Nelson, and Gang Chen. "Measuring Phonon Mean Free Path Distributions by Probing Quasiballistic Phonon Transport in Grating Nanostructures". *Scientific Reports* 5. August (Nov. 2015), p. 17131.
- [88] John Cuffe, Jeffrey K. Eliason, A. A. Maznev, Kimberlee C. Collins, Jeremy A. Johnson, Andrey Shchepetov, Mika Prunnila, Jouni Ahopelto, Clivia M. Sotomayor Torres, Gang Chen, and Keith A. Nelson. "Reconstructing phonon mean-free-path contributions to thermal conductivity using nanoscale membranes". *Phys. Rev. B* 91 (24 June 2015), p. 245423.
- [89] Keith T. Regner, Daniel P. Sellan, Zonghui Su, Cristina H. Amon, Alan J. H. McGaughey, and Jonathan A. Malen. "Broadband phonon mean free path contributions to thermal conductivity measured using frequency domain thermoreflectance". *Nature Communications* 4 (Mar. 2013), p. 1640.
- [90] Samuel Huberman, Vazrik Chiloyan, Ryan A. Duncan, Lingping Zeng, Roger Jia, Alexei A. Maznev, Eugene A. Fitzgerald, Keith A. Nelson, and Gang Chen. "Unifying first-principles theoretical predictions and experimental measurements of size effects in thermal transport in SiGe alloys". *Phys. Rev. Materials* 1 (5 Oct. 2017), p. 054601.
- [91] Mark E Siemens, Qing Li, Ronggui Yang, Keith a KA Keith A Nelson, Erik H Anderson, Margaret M Murnane, and Henry C Kapteyn. "Quasiballistic thermal transport from nanoscale interfaces observed using ultrafast coherent soft X-ray beams." *Nature materials* 9.1 (Jan. 2010), pp. 26–30.
- [92] Travis D Frazer, Joshua L Knobloch, Kathleen M Hoogeboom-Pot, Damiano Nardi, Weilun Chao, Roger W Falcone, Margaret M Murnane, Henry C Kapteyn, and Jorge N Hernandez-Charpak. "Engineering Nanoscale Thermal Transport: Size- and Spacing-Dependent Cooling of Nanostructures". *Phys. Rev. Applied* 11.2 (Feb. 2019), p. 24042.
- [93] A. J. Minnich. "Determining Phonon Mean Free Paths from Observations of Quasiballistic Thermal Transport". *Phys. Rev. Lett.* 109 (20 Nov. 2012), p. 205901.

- [94] Vazrik Chiloyan, Lingping Zeng, Samuel Huberman, Alexei A. Maznev, Keith A. Nelson, and Gang Chen. “Variational approach to solving the spectral Boltzmann transport equation in transient thermal grating for thin films”. *Journal of Applied Physics* 120.2 (2016).
- [95] A. A. Maznev, Jeremy A. Johnson, and Keith A. Nelson. “Onset of non-diffusive phonon transport in transient thermal grating decay”. *Phys. Rev. B* 84 (19 Nov. 2011), p. 195206.
- [96] Gang Chen. “Ballistic-Diffusive Heat-Conduction Equations”. *Phys. Rev. Lett.* 86 (11 Mar. 2001), pp. 2297–2300.
- [97] Gang Chen. “Ballistic-Diffusive Equations for Transient Heat Conduction From Nano to Macroscales”. *Journal of Heat Transfer* 124.2 (Aug. 2001), pp. 320–328.
- [98] Housseem Rezgui, Faouzi Nasri, Mohamed Fadhel Ben Aissa, Hafedh Belmabrouk, and Amen Allah Guizani. “Modeling Thermal Performance of Nano-GNRFET Transistors Using Ballistic-Diffusive Equation”. *IEEE Transactions on Electron Devices* 65.4 (2018), pp. 1611–1616.
- [99] Mojtaba Forghani and Nicolas G. Hadjiconstantinou. “Comparison on two ways of phonon spectral property reconstruction from thermal spectroscopy experiment”. *International Journal of Heat and Mass Transfer* 175 (2021), p. 121119.
- [100] Bjorn Vermeersch, Amr M. S. Mohammed, Gilles Pernot, Yee Rui Koh, and Ali Shakouri. “Superdiffusive heat conduction in semiconductor alloys. II. Truncated Lévy formalism for experimental analysis”. *Physical Review B* 91.8 (Feb. 2015), p. 085203.
- [101] Amr M S Mohammed, Yee Rui Koh, Bjorn Vermeersch, Hong Lu, Peter G. Burke, Arthur C. Gossard, and Ali Shakouri. “Fractal Lévy Heat Transport in Nanoparticle Embedded Semiconductor Alloys”. *Nano Letters* 15.7 (Feb. 2015), pp. 4269–4273.
- [102] Ralf Metzler and Joseph Klafter. “The random walk’s guide to anomalous diffusion: a fractional dynamics approach”. *Physics Reports* 339.1 (2000), pp. 1–77.
- [103] György Trefán, Elena Floriani, Bruce J. West, and Paolo Grigolini. “Dynamical approach to anomalous diffusion: Response of Lévy processes to a perturbation”. *Phys. Rev. E* 50 (4 Oct. 1994), pp. 2564–2579.
- [104] Zhiwei Ding, Jiawei Zhou, Bai Song, Vazrik Chiloyan, Mingda Li, Te-Huan Liu, and Gang Chen. “Phonon Hydrodynamic Heat Conduction and Knudsen Minimum in Graphite”. *Nano Letters* 18.1 (2018). PMID: 29236507, pp. 638–649.
- [105] V. L. Gurevich. “Transport in phonon systems”. *Elsevier Science Publishers, Amsterdam* (1986).
- [106] P. Ván, A. Berezovski, T. Fulop, Gy. Gróf, R. Kovács, Á. Lovas, and J. Verhás. “Guyer-Krumhansl type heat conduction at room temperature”. *EPL (Europhysics Letters)* 118.5 (June 2017), p. 50005.

- [107] A. Sellitto, F. X. Alvarez, and D. Jou. “Second law of thermodynamics and phonon-boundary conditions in nanowires”. *Journal of Applied Physics* 107.6 (2010), p. 064302.
- [108] J A Sussmann and A Thellung. “Thermal Conductivity of Perfect Dielectric Crystals in the Absence of Umklapp Processes”. *Proceedings of the Physical Society* 81.6 (June 1963), pp. 1122–1130.
- [109] Robert J. Hardy and Dennis L. Albers. “Hydrodynamic approximation to the phonon Boltzmann equation”. *Phys. Rev. B* 10 (8 Oct. 1974), pp. 3546–3551.
- [110] Andrea Cepellotti, Giorgia Fugallo, Lorenzo Paulatto, Michele Lazzeri, Francesco Mauri, and Nicola Marzari. “Phonon hydrodynamics in two-dimensional materials”. *Nature Communications* 6.1 (Dec. 2015), p. 6400.
- [111] Sangyeop Lee, David A. Broido, Keivan Esfarjani, and Gang Chen. “Hydrodynamic phonon transport in suspended graphene.” *Nature communications* 6 (Jan. 2015), p. 6290.
- [112] Koichi Izawa, Atsushi Miyake, Yo Machida, Masashi Tokunaga, Kazuto Akiba, Alaska Subedi, Kamran Behnia, and Yuichi Akahama. “Observation of Poiseuille flow of phonons in black phosphorus”. *Science Advances* 4.6 (2018), eaat3374.
- [113] Valentina Martelli, Julio Larrea Jiménez, Mucio Continentino, Elisa Baggio Saitovitch, and Kamran Behnia. “Thermal Transport and Phonon Hydrodynamics in Strontium Titanate”. *Phys. Rev. Lett.* 120 (12 Mar. 2018), p. 125901.
- [114] C. C. Ackerman, B. Bertman, H. A. Fairbank, and R. A. Guyer. “Second Sound in Solid Helium”. *Phys. Rev. Lett.* 16 (18 May 1966), pp. 789–791.
- [115] T. F. McNelly, S. J. Rogers, D. J. Channin, R. J. Rollefson, W. M. Goubau, G. E. Schmidt, J. A. Krumhansl, and R. O. Pohl. “Heat Pulses in NaF: Onset of Second Sound”. *Phys. Rev. Lett.* 24 (3 Jan. 1970), pp. 100–102.
- [116] Akitoshi Koreeda, Ryuta Takano, and Seishiro Saikan. “Second Sound in SrTiO<sub>3</sub>”. *Phys. Rev. Lett.* 99 (26 Dec. 2007), p. 265502.
- [117] Marvin Chester. “Second Sound in Solids”. *Phys. Rev.* 131 (5 Sept. 1963), pp. 2013–2015.
- [118] R. Kovács and P. Ván. “Generalized heat conduction in heat pulse experiments”. *International Journal of Heat and Mass Transfer* 83 (2015), pp. 613–620.
- [119] M. J. Fryer and H. Struchtrup. “Moment model and boundary conditions for energy transport in the phonon gas”. *Continuum Mech. Therm* 26.26 (Sept. 2014), pp. 593–618.
- [120] P. Torres, A. Ziabari, A. Torelló, J. Bafaluy, J. Camacho, X. Cartoixà, A. Shakouri, and F. X. Alvarez. “Emergence of hydrodynamic heat transport in semiconductors at the nanoscale”. *Physical Review Materials* 2.7 (2018), p. 076001.

- [121] Pol Torres, Amr Mohammed, Àlvar Torelló, Javier Bafaluy, Juan Camacho, Xavier Cartoixà, Ali Shakouri, and F. Xavier Alvarez. “Collective thermal transport in pure and alloy semiconductors”. *Phys. Chem. Chem. Phys.* 20 (10 2018), pp. 6805–6810.
- [122] A. Beardo, M. Calvo-Schwarzwälder, J. Camacho, T.G. Myers, P. Torres, L. Sendra, F.X. Alvarez, and J. Bafaluy. “Hydrodynamic Heat Transport in Compact and Holey Silicon Thin Films”. *Phys. Rev. Applied* 11 (3 Mar. 2019), p. 034003.
- [123] Dietrich Einzel, Peter Panzer, and Mario Liu. “Boundary condition for fluid flow: Curved or rough surfaces”. *Phys. Rev. Lett.* 64 (19 May 1990), pp. 2269–2272.
- [124] D. A. Lockerby, J. M. Reese, R. W. Barber, and D. R. Emerson. “Geometric and constitutive dependence of Maxwell’s velocity slip boundary condition”. *AIP Conference Proceedings* 762.1 (2005), pp. 725–730.
- [125] Henning Struchtrup. “Maxwell boundary condition and velocity dependent accommodation coefficient”. *Physics of Fluids* 25.11 (2013), p. 112001.
- [126] Yu-Chao Hua and Bing-Yang Cao. “Slip Boundary Conditions in Ballistic–Diffusive Heat Transport in Nanostructures”. *Nanoscale and Microscale Thermophysical Engineering* 21.3 (2017), pp. 159–176.
- [127] Manuel Torrilhon and Henning Struchtrup. “Boundary conditions for regularized 13-moment-equations for micro-channel-flows”. *Journal of Computational Physics* 227.3 (2008), pp. 1982–2011.
- [128] Navaneetha K. Ravichandran and Austin J. Minnich. “Role of thermalizing and nonthermalizing walls in phonon heat conduction along thin films”. *Phys. Rev. B* 93 (3 Jan. 2016), p. 035314.
- [129] Puqing Jiang, Lucas Lindsay, Xi Huang, and Yee Kan Koh. “Interfacial phonon scattering and transmission loss in um thick silicon-on-insulator thin films”. *Phys. Rev. B* 97 (19 May 2018), p. 195308.
- [130] G. Chen. “Size and Interface Effects on Thermal Conductivity of Superlattices and Periodic Thin-Film Structures”. *Journal of Heat Transfer* 119.2 (May 1997), pp. 220–229.
- [131] George Karniadakis, Ali Beskok, and Narayan Aluru. “Microflows and Nanoflows”. *Springer*, United States of America (2000).
- [132] E T Swartz and R O Pohl. “Thermal resistance at interfaces”. *Applied Physics Letters* 51.26 (1987), pp. 2200–2202.
- [133] Ashutosh Giri and Patrick E. Hopkins. “A Review of Experimental and Computational Advances in Thermal Boundary Conductance and Nanoscale Thermal Transport across Solid Interfaces”. *Advanced Functional Materials* 30.8 (2020), p. 1903857.
- [134] A. Beardo, M. G. Hennessy, L. Sendra, J. Camacho, T. G. Myers, J. Bafaluy, and F. X. Alvarez. “Phonon hydrodynamics in frequency-domain thermoreflectance experiments”. *Phys. Rev. B* 101 (7 Feb. 2020), p. 075303.



- [135] L.D. Landau and E.M. Lifshitz. "Theory of Elasticity: Vol. 7 of Course of Theoretical Physics". *Pergamon Press*, Oxford, United Kingdom (1970).
- [136] Damiano Nardi, Marco Travaglini, Mark E. Siemens, Qing Li, Margaret M. Murnane, Henry C. Kapteyn, Gabriele Ferrini, Fulvio Parmigiani, and Francesco Banfi. "Probing thermomechanics at the nanoscale: Impulsively excited pseudosurface acoustic waves in hypersonic phononic crystals". *Nano Letters* 11.10 (2011), pp. 4126–4133.
- [137] R. Kronig. "On the hydrodynamics of non-viscous fluids and the theory of helium ii. part III". *Physica* 19.1 (1953), pp. 535–544.
- [138] J Gooth, F Menges, N Kumar, V Süß, C Shekhar, Y Sun, U Drechsler, R Zierold, C Felser, and B Gotsmann. "Thermal and electrical signatures of a hydrodynamic electron fluid in tungsten diphosphide". *Nature Communications* 9.1 (2018), p. 4093.
- [139] Joseph A Sulpizio, Lior Ella, Asaf Rozen, John Birkbeck, David J Perello, Debarghya Dutta, Moshe Ben-Shalom, Takashi Taniguchi, Kenji Watanabe, Tobias Holder, Raquel Queiroz, Alessandro Principi, Ady Stern, Thomas Scaffidi, Andre K Geim, and Shahal Ilani. "Visualizing Poiseuille flow of hydrodynamic electrons". *Nature* 576.7785 (2019), pp. 75–79.
- [140] Daniel Champier. "Thermoelectric generators: A review of applications". *Energy Conversion and Management* 140 (2017), pp. 167–181.
- [141] Conyers Herring. "Theory of the Thermoelectric Power of Semiconductors". *Phys. Rev.* 96 (5 Dec. 1954), pp. 1163–1187.
- [142] A. Miele, R. Fletcher, E. Zaremba, Y. Feng, C. T. Foxon, and J. J. Harris. "Phonon-drag thermopower and weak localization". *Phys. Rev. B* 58 (19 Nov. 1998), pp. 13181–13190.
- [143] G Jeffrey Snyder and Eric S Toberer. "Complex thermoelectric materials". *Nature Materials* 7.2 (2008), pp. 105–114.
- [144] M. S. Dresselhaus, G. Chen, M. Y. Tang, R. G. Yang, H. Lee, D. Z. Wang, Z. F. Ren, J.P. Fleurial, and P. Gogna. "New Directions for Low-Dimensional Thermoelectric Materials". *Advanced Materials* 19.8 (2007), pp. 1043–1053.
- [145] Changwook Jeong, Supriyo Datta, and Mark Lundstrom. "Thermal conductivity of bulk and thin-film silicon : A Landauer approach". *Journal of Applied Physics* 093708 (2012).
- [146] M. Asheghi, M. N. Touzelbaev, K. E. Goodson, Y. K. Leung, and S. S. Wong. "Temperature-Dependent Thermal Conductivity of Single-Crystal Silicon Layers in SOI Substrates". *Journal of Heat Transfer* 120.1 (1998), p. 30.
- [147] W. Liu and M. Asheghi. "Phonon-boundary scattering in ultrathin single-crystal silicon layers". *Applied Physics Letters* 84.19 (2004), pp. 3819–3821.
- [148] Puqing Jiang, Lucas Lindsay, and Yee Kan Koh. "Role of low energy phonons with mean free paths 0.8 um in heat conduction in silicon". *Journal of Applied Physics* 110.24 (2016), p. 245705.

- [149] David Song and Gang Chen. "Thermal conductivity of periodic microporous silicon films". *Applied Physics Letters* 84.5 (2004), pp. 687–689.
- [150] Navaneetha K. Ravichandran, Hang Zhang, and Austin J. Minnich. "Spectrally Resolved Specular Reflections of Thermal Phonons from Atomically Rough Surfaces". *Phys. Rev. X* 8 (4 Oct. 2018), p. 041004.
- [151] Roman Anufriev, Sergei Gluchko, Sebastian Volz, and Masahiro Nomura. "Quasi-Ballistic Heat Conduction due to Lévy Phonon Flights in Silicon Nanowires". *ACS Nano* 12.12 (2018), pp. 11928–11935.
- [152] Sami Alajlouni, Albert Beardo, Lluc Sendra, Amirkoushyar Ziabari, Javier Bafaluy, Juan Camacho, Yi Xuan, F Xavier Alvarez, and Ali Shakouri. "Geometrical quasi-ballistic effects on thermal transport in nanostructured devices". *Nano Research* 14.4 (2021), pp. 945–952.
- [153] Amirkoushyar Ziabari, Maryam Parsa, Yi Xuan, Je-Hyeong Bahk, Kazuaki Yazawa, F. Xavier Alvarez, and Ali Shakouri. "Far-field thermal imaging below diffraction limit". *Opt. Express* 28.5 (Mar. 2020), pp. 7036–7050.
- [154] M Farzaneh, K Maize, D Luerßen, J A Summers, P M Mayer, P E Raad, K P Pipe, A Shakouri, R J Ram, and Janice A Hudgings. "CCD-based thermorefectance microscopy: principles and applications". *Journal of Physics D: Applied Physics* 42.14 (June 2009), p. 143001.
- [155] T. Favaloro, J.-H. Bahk, and A. Shakouri. "Characterization of the temperature dependence of the thermorefectance coefficient for conductive thin films". *Review of Scientific Instruments* 86.2 (2015), p. 024903.
- [156] F Warkusz. "The size effect and the temperature coefficient of resistance in thin films". *Journal of Physics D: Applied Physics* 11.5 (Apr. 1978), pp. 689–694.
- [157] A. Ziabari, J. H. Bahk, Y. Xuan, P. D. Ye, D. Kendig, K. Yazawa, P. G. Burke, A. C. Lu H.; Gossard, and A. Shakouri. "Sub-diffraction limit thermal imaging for HEMT devices." *Proceedings of the 31st Thermal Measurement, Modeling and Management Symposium (SEMI-THERM)* (2015), pp. 82–87.
- [158] K. T. Regner, S. Majumdar, and J. A. Malen. "Instrumentation of broadband frequency domain thermorefectance for measuring thermal conductivity accumulation functions". *Review of Scientific Instruments* (2013).
- [159] Yee Kan Koh and David G. Cahill. "Frequency dependence of the thermal conductivity of semiconductor alloys". *Physical Review B* 76.7 (Aug. 2007), p. 075207.
- [160] Jeffrey L. Braun, David H. Olson, John T. Gaskins, and Patrick E. Hopkins. "A steady-state thermorefectance method to measure thermal conductivity". *Review of Scientific Instruments* 90.2 (2019), p. 024905.
- [161] David Rodin and Shannon K. Yee. "Simultaneous measurement of in-plane and through-plane thermal conductivity using beam-offset frequency domain thermorefectance". *Review of Scientific Instruments* 88.1 (2017), p. 014902.

- [162] Jun Liu, Jie Zhu, Miao Tian, Xiaokun Gu, Aaron Schmidt, and Ronggui Yang. “Simultaneous measurement of thermal conductivity and heat capacity of bulk and thin film materials using frequency-dependent transient thermoreflectance method”. *Review of Scientific Instruments* 84.3 (2013), p. 034902.
- [163] Albert Beardo, Joshua L. Knobloch, Lluc Sendra, Javier Bafaluy, Travis D. Frazer, Weilun Chao, Jorge N. Hernandez-Charpak, Henry C. Kapteyn, Begoña Abad, Margaret M. Murnane, F. Xavier Alvarez, and Juan Camacho. “A General and Predictive Understanding of Thermal Transport from 1D- and 2D-Confined Nanostructures: Theory and Experiment”. *ACS Nano* 15.8 (2021). PMID: 34328719, pp. 13019–13030.
- [164] Andy Rundquist, Charles G. Durfee, Zenghu Chang, Catherine Herne, Sterling Backus, Margaret M. Murnane, and Henry C. Kapteyn. “Phase-Matched Generation of Coherent Soft X-rays”. *Science* 280.5368 (1998), pp. 1412–1415.
- [165] Ra’anan I. Tobey, Mark E. Siemens, Oren Cohen, Margaret M. Murnane, Henry C. Kapteyn, and Keith A. Nelson. “Ultrafast extreme ultraviolet holography: dynamic monitoring of surface deformation”. *Opt. Lett.* 32.3 (Feb. 2007), pp. 286–288.
- [166] F. Bencivenga et al. “Nanoscale transient gratings excited and probed by extreme ultraviolet femtosecond pulses”. *Science Advances* 5.7 (2019).
- [167] D. Naumenko, R. Mincigrucci, M. Altissimo, L. Foglia, A. Gessini, G. Kurdi, I. Nikolov, E. Pedersoli, E. Principi, A. Simoncig, M. Kiskinova, C. Masciovecchio, F. Capotondi, and F. Bencivenga. “Thermoelasticity of Nanoscale Silicon Carbide Membranes Excited by Extreme Ultraviolet Transient Gratings: Implications for Mechanical and Thermal Management”. *ACS Applied Nano Materials* 2.8 (2019), pp. 5132–5139.
- [168] Kimberlee C. Collins, Alexei A. Maznev, Zhiting Tian, Keivan Esfarjani, Keith A. Nelson, and Gang Chen. “Non-diffusive relaxation of a transient thermal grating analyzed with the Boltzmann transport equation”. *Journal of Applied Physics* 114.10 (2013), p. 104302.
- [169] Y. Hua and T. K. Sarkar. “Matrix Pencil Method to Estimate the Parameters of Exponentially Damped/Undamped Sinusoids in Noise”. *IEEE Trans. Acoust., Speech, Signal Process.* 38 (1990), pp. 814–824.
- [170] T. K. Sarkar and O. Pereira. “Using the Matrix Pencil Method to Estimate the Parameters of a Sum of Complex Exponentials”. *IEEE Antennas and Propagation Mag.* 37 (1995), pp. 48–55.
- [171] Allon Hochbaum, Renkun Chen, Raul Diaz Delgado, Wenjie Liang, Erik Garnett, Mark Najarian, Arun Majumdar, and Peidong Yang. “Enhanced thermoelectric performance of rough silicon nanowires”. *Nature* 451.7175 (2008), pp. 163–167.

- [172] Alejandra Ruiz, Olga Caballero, and Marisol Martin. "Revisiting anodic alumina templates: from fabrication to applications". *Nanoscale* 13 (4 2021), pp. 2227–2265.
- [173] Jaime Martín, Marisol Martin, Jose Francisco Fernández, and Olga Caballero. "Ordered three dimensional interconnected nanoarchitectures in anodic porous alumina". *Nature Communications* 5.1 (2014), p. 5130.
- [174] Miguel Muñoz Rojo, B. Abad, C. V. Manzano, P. Torres, X. Cartoixa, F. X. Alvarez, and M. Martín Gonzalez. "Thermal conductivity of Bi<sub>2</sub>Te<sub>3</sub> nanowires: how size affects phonon scattering". *Nanoscale* 9 (20 2017), pp. 6741–6747.
- [175] Miguel Muñoz Rojo, Yingjie Zhang, Cristina V Manzano, Raquel Alvaro, Johannes Gooth, Miquel Salmeron, and Marisol Martin-Gonzalez. "Spatial potential ripples of azimuthal surface modes in topological insulator Bi<sub>2</sub>Te<sub>3</sub> nanowires". *Scientific Reports* 6.1 (2016), p. 19014.
- [176] Cheng-Lung Chen, Yang-Yuan Chen, Su-Jien Lin, James C. Ho, Ping-Chung Lee, Chii-Dong Chen, and Sergey R. Harutyunyan. "Fabrication and Characterization of Electrodeposited Bismuth Telluride Films and Nanowires". *The Journal of Physical Chemistry C* 114.8 (2010), pp. 3385–3389.
- [177] Farbod Amirghasemi and Sam Kassegne. "Effects of RF Magnetron Sputtering Deposition Power on Crystallinity and Thermoelectric Properties of Antimony Telluride and Bismuth Telluride Thin Films on Flexible Substrates". *Journal of Electronic Materials* 50.4 (2021), pp. 2190–2198.
- [178] Nicki F. Hinsche, Sebastian Zastrow, Johannes Gooth, Laurens Pudewill, Robert Zierold, Florian Rittweger, Tomás Rauch, Jurgen Henk, Kornelius Nielsch, and Ingrid Mertig. "Impact of the Topological Surface State on the Thermoelectric Transport in Sb<sub>2</sub>Te<sub>3</sub> Thin Films". *ACS Nano* 9.4 (2015). PMID: 25826737, pp. 4406–4411.
- [179] M. Cassinelli, S. Müller, K.O. Voss, C. Trautmann, F. Völklein, J. Gooth, K. Nielsch, and M. E. Toimil-Molares. "Influence of surface states and size effects on the Seebeck coefficient and electrical resistance of BiSb nanowire arrays". *Nanoscale* 9 (9 2017), pp. 3169–3179.
- [180] Cristina V. Manzano and Marisol Martin-Gonzalez. "Electrodeposition of V-VI Nanowires and Their Thermoelectric Properties". *Frontiers in Chemistry* 7 (2019), p. 516.
- [181] R. Egger, A. Zazunov, and A. Levy Yeyati. "Helical Luttinger Liquid in Topological Insulator Nanowires". *Phys. Rev. Lett.* 105 (13 Sept. 2010), p. 136403.
- [182] L. Brey and H. A. Fertig. "Electronic states of wires and slabs of topological insulators: Quantum Hall effects and edge transport". *Phys. Rev. B* 89 (8 Feb. 2014), p. 085305.
- [183] D. Bercioux, J. Cayssol, M. Garcia Vergniory, and Reyes Calvo. "Topological Matter". *Lectures from the Topological Matter School 2017* (2017).

- [184] Kedar Hippalgaonkar, Ying Wang, Yu Ye, Diana Y. Qiu, Hanyu Zhu, Yuan Wang, Joel Moore, Steven G. Louie, and Xiang Zhang. “High thermoelectric power factor in two-dimensional crystals of MoS<sub>2</sub>”. *Phys. Rev. B* 95 (11 Mar. 2017), p. 115407.
- [185] V. Narayanamurti and R. C. Dynes. “Observation of Second Sound in Bismuth”. *Phys. Rev. Lett.* 28 (22 May 1972), pp. 1461–1465.
- [186] Jihoon Jeong, Xun Li, Sangyeop Lee, Li Shi, and Yaguo Wang. “Transient Hydrodynamic Lattice Cooling by Picosecond Laser Irradiation of Graphite”. *Phys. Rev. Lett.* 127 (8 Aug. 2021), p. 085901.
- [187] R. Kovács and P. Ván. “Second sound and ballistic heat conduction: NaF experiments revisited”. *International Journal of Heat and Mass Transfer* 117 (2018), pp. 682–690.
- [188] Claudio Melis, Giorgia Fugallo, and Luciano Colombo. “Room temperature second sound in cumulene”. *Phys. Chem. Chem. Phys.* 23 (28 2021), pp. 15275–15281.
- [189] S.L. Sobolev. “On hyperbolic heat-mass transfer equation”. *International Journal of Heat and Mass Transfer* 122 (2018), pp. 629–630.
- [190] Marco Gandolfi, Giulio Benetti, Christ Glorieux, Claudio Giannetti, and Francesco Banfi. “Accessing temperature waves: A dispersion relation perspective”. *International Journal of Heat and Mass Transfer* 143 (2019), p. 118553.
- [191] Albert Beardo, Miquel López-Suárez, Luis Alberto Pérez, Lluç Sendra, Maria Isabel Alonso, Claudio Melis, Javier Bafaluy, Juan Camacho, Luciano Colombo, Riccardo Rurali, Francesc Xavier Alvarez, and Juan Sebastián Reparaz. “Observation of second sound in a rapidly varying temperature field in Ge”. *Science Advances* 7.27 (2021).
- [192] Robert E Wagner and Andreas Mandelis. “Nonlinear photothermal modulated optical reflectance and photocurrent phenomena in crystalline semiconductors: II. Experimental”. *Semiconductor Science and Technology* 11.3 (Mar. 1996), pp. 300–307.
- [193] L. Wang, R. Cheaito, J. L. Braun, A. Giri, and P. E. Hopkins. “Thermal conductivity measurements of non-metals via combined time- and frequency-domain thermoreflectance without a metal film transducer”. *Review of Scientific Instruments* 87.9 (2016), p. 094902.
- [194] Jiawei Zhou, Hyun D Shin, Ke Chen, Bai Song, Ryan A Duncan, Qian Xu, Alexei A Maznev, Keith A Nelson, and Gang Chen. “Direct observation of large electron–phonon interaction effect on phonon heat transport”. *Nature Communications* 11.1 (2020), p. 6040.
- [195] J. Vanhellefont and E. Simoen. “Brother Silicon, Sister Germanium”. *Journal of The Electrochemical Society* 154.7 (2007), H572.
- [196] T. J. Bright and Z. M. Zhang. “Common Misperceptions of the Hyperbolic Heat Equation”. *Journal of Thermophysics and Heat Transfer* 23.3 (2009), pp. 601–607.

- [197] Carola Emminger, Farzin Abadizaman, Nuwanjula S. Samarasingha, Thomas E. Tiwald, and Stefan Zollner. "Temperature dependent dielectric function and direct bandgap of Ge". *Journal of Vacuum Science & Technology B* 38.1 (2020), p. 012202.
- [198] Michael Zürich, Hung-Tzu Chang, Lauren J Borja, Peter M Kraus, Scott K Cushing, Andrey Gandman, Christopher J Kaplan, Myoung Hwan Oh, James S Prell, David Prendergast, Chaitanya D Pemmaraju, Daniel M Neumark, and Stephen R Leone. "Direct and simultaneous observation of ultrafast electron and hole dynamics in germanium". *Nature Communications* 8.1 (2017), p. 15734.
- [199] H. R. Philipp and E. A. Taft. "Optical Constants of Germanium in the Region 1 to 10 eV". *Phys. Rev.* 113 (4 Feb. 1959), pp. 1002–1005.
- [200] Stefan Zollner, Sudha Gopalan, Miquel Garriga, Josef Humlicek, Luis Viña, and Manuel Cardona. "Ultrafast initial relaxation of hot electrons and holes in tetrahedral semiconductors via deformation potential interaction: Theory and experiment". *Applied Physics Letters* 57.26 (1990), pp. 2838–2840.
- [201] Koichiro Tanaka, Hideyuki Ohtake, and Tohru Suemoto. "Determination of intervalley scattering time in germanium by subpicosecond time-resolved Raman spectroscopy". *Phys. Rev. Lett.* 71 (12 Sept. 1993), pp. 1935–1938.
- [202] G. Mak and W. W. Rühle. "Femtosecond carrier dynamics in Ge measured by a luminescence up-conversion technique and near-band-edge infrared excitation". *Phys. Rev. B* 52 (16 Oct. 1995), R11584–R11587.
- [203] X. Q. Zhou, H. M. van Driel, and G. Mak. "Femtosecond kinetics of photoexcited carriers in germanium". *Phys. Rev. B* 50 (8 Aug. 1994), pp. 5226–5230.
- [204] C. Jacoboni, F. Nava, C. Canali, and G. Ottaviani. "Electron drift velocity and diffusivity in germanium". *Phys. Rev. B* 24 (2 July 1981), pp. 1014–1026.
- [205] Jean-Philippe M. Péraud and Nicolas G. Hadjiconstantinou. "Extending the range of validity of Fourier's law into the kinetic transport regime via asymptotic solution of the phonon Boltzmann transport equation". *Phys. Rev. B* 93 (4 Jan. 2016), p. 045424.
- [206] Martin T. Dove. *Introduction to Lattice Dynamics*. Cambridge Topics in Mineral Physics and Chemistry. Cambridge University Press, 1993.
- [207] Sebastian G. Volz and Gang Chen. "Molecular-dynamics simulation of thermal conductivity of silicon crystals". *Phys. Rev. B* 61 (4 Jan. 2000), pp. 2651–2656.
- [208] Han-Ling Li, Junichiro Shiomi, and Bing-Yang Cao. "Ballistic-Diffusive Heat Conduction in Thin Films by Phonon Monte Carlo Method: Gray Medium Approximation Versus Phonon Dispersion". *Journal of Heat Transfer* 142.11 (Sept. 2020). 112502.

- [209] Robert J. Hardy. “Energy-Flux Operator for a Lattice”. *Phys. Rev.* 132 (1 Oct. 1963), pp. 168–177.
- [210] Donatas Surblys, Hiroki Matsubara, Gota Kikugawa, and Taku Ohara. “Application of atomic stress to compute heat flux via molecular dynamics for systems with many-body interactions”. *Phys. Rev. E* 99 (5 May 2019), p. 051301.
- [211] Ryogo Kubo. “Statistical-Mechanical Theory of Irreversible Processes. I. General Theory and Simple Applications to Magnetic and Conduction Problems”. *Journal of the Physical Society of Japan* 12.6 (1957), pp. 570–586.
- [212] P. K. Schelling, S. R. Phillpot, and P. Keblinski. “Phonon wave-packet dynamics at semiconductor interfaces by molecular-dynamics simulation”. *Applied Physics Letters* 80.14 (2002), pp. 2484–2486.
- [213] Sebastian Volz, Jean-Bernard Saulnier, Michel Lallemand, Bernard Perrin, Philippe Depondt, and Michel Mareschal. “Transient Fourier-law deviation by molecular dynamics in solid argon”. *Phys. Rev. B* 54 (1 July 1996), pp. 340–347.
- [214] Patrick K. Schelling, Simon R. Phillpot, and Pawel Keblinski. “Comparison of atomic-level simulation methods for computing thermal conductivity”. *Phys. Rev. B* 65 (14 Apr. 2002), p. 144306.
- [215] Steve Plimpton. “Fast Parallel Algorithms for Short-Range Molecular Dynamics”. *Journal of Computational Physics* 117.1 (1995), pp. 1–19.
- [216] J. Tersoff. “Empirical interatomic potential for silicon with improved elastic properties”. *Phys. Rev. B* 38 (14 Nov. 1988), pp. 9902–9905.
- [217] Zheyong Fan, Luiz Felipe C. Pereira, Hui-Qiong Wang, Jin-Cheng Zheng, Davide Donadio, and Ari Harju. “Force and heat current formulas for many-body potentials in molecular dynamics simulations with applications to thermal conductivity calculations”. *Phys. Rev. B* 92 (9 Sept. 2015), p. 094301.
- [218] A. Tlili, V. M. Giordano, Y. M. Beltukov, P. Desmarchelier, S. Merabia, and A. Tanguy. “Enhancement and anticipation of the Ioffe–Regel crossover in amorphous/nanocrystalline composites”. *Nanoscale* 11 (44 2019), pp. 21502–21512.
- [219] R.L.C. Vink, G.T. Barkema, W.F. van der Weg, and Normand Mousseau. “Fitting the Stillinger–Weber potential to amorphous silicon”. English. *Journal of Non-Crystalline Solids* 282.2-3 (2001), pp. 248–255.
- [220] Arthur France-Lanord, Samy Merabia, Tristan Albaret, David Lacroix, and Konstantinos Termentzidis. “Thermal properties of amorphous/crystalline silicon superlattices”. *Journal of Physics: Condensed Matter* 26.35 (Aug. 2014), p. 355801.
- [221] Paul Desmarchelier, Alice Carré, Konstantinos Termentzidis, and Anne Tanguy. “Ballistic Heat Transport in Nanocomposite: The Role of the Shape and Interconnection of Nano-inclusions”. *Nanomaterials* 11.8 (2021).

- [222] Paul Desmarchelier, Anne Tanguy, and Konstantinos Termentzidis. “Thermal rectification in asymmetric two-phase nanowires”. *Phys. Rev. B* 103 (1 Jan. 2021), p. 014202.
- [223] Xiaobo Li, Kurt Maute, Martin L. Dunn, and Ronggui Yang. “Strain effects on the thermal conductivity of nanostructures”. *Phys. Rev. B* 81 (24 June 2010), p. 245318.
- [224] Olek Zienkiewicz, Robert Taylor, and J. Z. Zhu. *The Finite Element Method: its Basis and Fundamentals: Seventh Edition*. 2013.
- [225] O. C. Zienkiewicz, R. L. Taylor, and J. Sherwin S. J. aRnd Peiró. “On discontinuous Galerkin methods”. *International Journal for Numerical Methods in Engineering* 58.8 (2003), pp. 1119–1148.
- [226] M. Calvo-Schwarzwälder, M.G. Hennessy, P. Torres, T.G. Myers, and F.X. Alvarez. “A slip-based model for the size-dependent effective thermal conductivity of nanowires”. *International Communications in Heat and Mass Transfer* 91 (2018), pp. 57–63.
- [227] Nianbei Li, Jie Ren, Lei Wang, Gang Zhang, Peter Hänggi, and Baowen Li. “Colloquium: Phononics: Manipulating heat flow with electronic analogs and beyond”. *Rev. Mod. Phys.* 84 (3 July 2012), pp. 1045–1066.
- [228] Chengyun Hua, Xiangwen Chen, Navaneetha K. Ravichandran, and Austin J. Minnich. “Experimental metrology to obtain thermal phonon transmission coefficients at solid interfaces”. *Phys. Rev. B* 95 (20 May 2017), p. 205423.